



UNIVERSITÀ DEGLI STUDI DI TRIESTE

XXXII CICLO DEL DOTTORATO DI RICERCA IN INGEGNERIA INDUSTRIALE E DELL'INFORMAZIONE

Borsa finanziata da NIDEC INDUSTRIAL SOLUTIONS

EFFICIENT METHODS FOR THE STUDY OF EDDY-CURRENTS EFFECTS IN MEDIUM- VOLTAGE ROTATING ELECTRICAL MACHINES

Settore scientifico-disciplinare: ING-IND/32 Convertitori, Macchine ed Azionamenti Elettrici

DOTTORANDO
MATTEO OLIVO

COORDINATORE
Prof. FULVIO BABICH

SUPERVISORE DI TESI
Prof. ALBERTO TESSAROLO

CO-SUPERVISORE
Ing. FABIO LUISE

ANNO ACCADEMICO 2018/2019

Efficient Methods for the Study of Eddy-Currents Effects in Medium-Voltage Rotating Electrical Machines

Matteo Olivo

ABSTRACT

The efficient computation of eddy-current effects in medium voltage electric machines is discussed in this dissertation. Two particular cases are considered.

Firstly, the effects of shaft eddy-currents on two-pole induction motor performance is addressed, with special focus on the power factor. In the second part of the thesis the start-up calculation of a large synchronous motor with solid rotor is analyzed.

For each application a special calculation procedure is introduced. These procedures adopt a set of suitable finite-element models to properly compute the machine equivalent circuit parameters that are mainly influenced by eddy-current-related phenomena. By suitably choosing finite-element models boundary conditions and excitations their geometry is simplified to the maximum possible extent, in order to reduce the computational burden.

The results of the new calculation methods are compared with experimental data and with analogous results obtained from commonly-adopted calculation procedures. The comparison proves that the proposed approaches can lead to high accuracy levels with very remarkable computational savings.

Lo scopo di questa tesi è presentare alcuni metodi efficienti (dal punto di vista computazionale) per il calcolo degli effetti dovuti alle correnti parassite (eddy currents) in macchine elettriche rotanti in media tensione. Due applicazioni in particolare sono state considerate nel dettaglio.

Inizialmente viene analizzato il fenomeno delle correnti parassite indotte nell'albero di motori asincroni a due poli e il conseguente effetto sulle prestazioni della macchina, focalizzandosi in particolare sul fattore di potenza. La seconda parte della tesi concentra la sua attenzione sullo studio dell'avviamento da rete di motori sincroni con rotore massiccio.

Per ciascuna applicazione vengono introdotte alcune procedure di calcolo, facenti uso di opportuni modelli numerici basati sul metodo degli elementi finiti, per mezzo delle quali vengono adeguatamente calcolati i parametri dei circuiti equivalenti di macchina, tenendo conto degli effetti legati alle correnti parassite. I modelli numerici sono opportunamente definiti, in modo tale da ridurre al massimo la complessità delle geometrie e il conseguente onere computazionale.

I risultati delle procedure innovative qui proposte sono confrontati con i dati provenienti da prove sperimentali sulle macchine oggetto di studio e con analoghi risultati di calcolo dedotti tramite le procedure comunemente utilizzate. Il confronto fra questi dati ha dimostrato che gli approcci di calcolo introdotti in questa tesi permettono di ottenere risultati con un elevato livello di accuratezza e una netta riduzione dell'onere computazionale.

CONTENTS

Introduction

I EFFECTS OF SHAFT CURRENTS IN TWO-POLE INDUCTION MACHINES

1	PROBLEM OVERVIEW	9
1.1	Shaft eddy-currents in induction motors	9
1.2	Experimental investigation	11
1.2.1	Test equipment description	11
1.2.2	Test results	11
1.3	Literature review	13
2	INDUCTION MOTOR EQUIVALENT CIRCUIT CALCULATION	17
2.1	Motor geometry and main dimensions	17
2.2	Resistances	24
2.2.1	Stator resistance	24
2.2.2	Rotor resistance	24
2.3	Leakage reactances	24
2.3.1	Slot leakage	25
2.3.2	End-winding leakage	25
2.3.3	Air-gap leakage	26
2.4	Magnetization and no-load losses	27
2.4.1	Magnetization characteristics	28
2.4.2	Magnetizing reactance	35
2.4.3	Core losses	36
2.4.4	Mechanical losses	37
2.5	Performance calculation	37
3	SHAFT EFFECTS CALCULATION METHODS	41
3.1	Standard Finite-Element Method	41
3.1.1	Notable PDEs for electric machine analysis	42
3.1.2	2D modeling of an induction motor	43
3.1.3	Solution procedure for steady-state analysis	48
3.2	Improved Equivalent Circuit Method	52
3.2.1	Overall procedure description	52
3.2.2	Reduced model for induction motor analysis	54
4	METHODS COMPARISON	57
4.1	Real-motors performance calculation	57
4.2	Discussion	59

II STARTING PERFORMANCE OF DOL SYNCHRONOUS MOTORS

5	SYNCHRONOUS MOTORS WITH SOLID ROTOR	67
5.1	Synchronous motor rotor geometry	67
5.2	Experimental study of rotor-groove impact	71
5.2.1	Testing procedure description	71
5.2.2	Example of grooving impact investigation	73
6	TWO-AXIS MODEL FOR START-UP	77

6.1	Synchronous machine modeling	77
6.1.1	Clarke-Park Transformation	77
6.1.2	Standard dq dynamic model for synchronous motors	80
6.1.3	Quasi-stationary dq model for motor starting	83
6.1.4	Starting performance calculation	85
6.1.5	Per-unit reduction	88
6.2	Model identification from stand-still tests	89
6.2.1	Stationary dq model at stand-still	89
6.2.2	Axis admittance identification	91
7	STARTING MODEL CALCULATION	95
7.1	Method outline	95
7.1.1	Three-phase excited model	96
7.1.2	Single-phase excited model	99
7.1.3	Model comparison	101
7.2	Model set-up	101
7.2.1	Excitation and boundary conditions	101
7.2.2	Materials properties correction	104
7.3	Model equivalence check	106
8	METHOD VALIDATION	109
8.1	Start-up rotor parameter calculation	109
8.1.1	Field winding resistance calculation	111
8.1.2	Static parameters	112
8.1.3	Iterative calculation	113
8.2	Start-up performance calculation	113
8.3	Results	114
8.3.1	Reference solid salient pole machine	114
8.3.2	Results comparison	117

Conclusions

Appendices

A	END-WINDING LEAKAGE CALCULATION	127
A.1	Method outline	127
A.1.1	End-winding inductance for a multi-phase winding	129
A.1.2	End-winding inductance for a single-phase winding	131
A.2	Coil geometry model	131
A.2.1	Stator-winding geometry	131
A.2.2	Rotor-winding geometry	134
A.3	Neumann integrals calculation	135
A.3.1	Neumann integral between finite segments	136
A.3.2	Self-inductance of a finite segment	141
A.3.3	Neumann integral between infinite segments	142
B	MMF AND FLUX-LINKAGE CALCULATION	147
B.1	Winding Function expression	147
B.1.1	Winding structure	147
B.1.2	Winding function expression	148
B.1.3	Flux-linkage expression	151
B.2	Rotating system of MMF and flux linkage	153
B.2.1	Extention to a generic three-phase system	155

B.3 Pulsating system of MMF and flux-linkage	157
C PER-UNIT BASE QUANTITIES	159
Bibliography	
General bibliography	161
Publications by author	166

ACRONYMS & SYMBOLS

ACRONYMS

AC Alternating Current

BC Boundary Condition

CCW Counter-Clock-Wise

CPT Clarke-Park Transformation

CW Clock-Wise

DC Direct Current

DOL Direct-On-Line

ECM Equivalent Circuit Method

EMF Electro-Motive Force

FE Finite-Element

FEA Finite-Element Analysis

FEM Finite-Element Method

IEC International Electrotechnical Commission

IEEE Institute of Electrical and Electronics Engineers

IM Induction Machine, Induction Motor

LP Lumped Parameter

LRC Locked-Rotor Current

LRT Locked-Rotor Torque

MMF Magneto-Motive Force

MVP Magnetic Vector Potential

PDE Partial Differential Equation

PF Power Factor

RMS Root-Mean Square

SG Synchronous Generator

SM Synchronous Machine, Synchronous Motor

TEFC Totally-Enclosed Fan-Cooled

TH Time-Harmonic

VFD Variable Frequency Drive

SYMBOLS

α	Angle Electric angle Temperature coefficient for resistance
α_{end}	End-winding angular half-width
A	Magnetic vector potential
\mathcal{B}_{gap}	Air-gap flux-density distribution
B	Flux-density
B_1	Fundamental of air-gap flux-density
B_{fund}	Fundamental of air-gap flux-density
B_g	Air-gap flux density
$B_{g,\text{max}}$	Maximum value of air-gap flux density
B_h	Peak of the h -th air-gap flux-density harmonic
$b_{\text{ins,rtu}}$	Rotor inter-turn insulation thickness
$b_{\text{ins,scs}}$	Stator ground-wall insulation double-thickness
$b_{\text{ins,sew}}$	Stator elementary wire insulation double-thickness
$b_{\text{ins,stu}}$	Stator turn insulation double-thickness
χ	Coil-to-pole ratio (coil pitch shortening)
$\cos \varphi$	Power factor
δ	Mass density
δ_{ps}	Pole-shoe center offset
D_{gap}	Air-gap average diameter
$D_{\text{r,base}}$	Rotor diameter at pole base (salient rotors)
$D_{\text{r,inn}}$	Rotor inner diameter
$D_{\text{r,out}}$	Rotor outer diameter
$D_{\text{r,yk}}$	Rotor yoke average diameter
$D_{\text{rng,avg}}$	Rotor ring average diameter
$D_{\text{rng,inn}}$	Rotor ring inner diameter
$D_{\text{rng,out}}$	Rotor ring outer diameter
$D_{\text{s,inn}}$	Stator inner diameter
$D_{\text{s,out}}$	Stator outer diameter
$D_{\text{s,yk}}$	Stator yoke average diameter
d_{pwr}	Pole-to-winding distance in the radial direction
d_{pwt}	Pole-to-winding distance in the tangential direction
d_{wwt}	Winding inter-layer distance in the tangential direction

E	Electric field
	EMF for generators
	Back-EMF for motors
e	Basis for the natural logarithm
$\vec{e}_r, \vec{e}_\theta, \vec{e}_z$	Fundamental directions for a cylindrical reference frame
$\vec{e}_x, \vec{e}_y, \vec{e}_z$	Fundamental directions for a cartesian reference frame
Φ_h	Elementary flux for the h -th flux-density spatial harmonic
Φ_p	Flux per pole
φ	Phase angle
	Impedance characteristic angle
F_0	MMF drop in the gap+teeth region
F_{gap}	MMF drop across the air-gap
F_{mag}	Magnetizing MMF (Total MMF drop)
$F_{\text{mag},0}$	No load MMF drop across stator yoke, air-gap and teeth
F_{rt}	MMF drop across the rotor teeth
F_{ry}	MMF drop across the rotor yoke
F_{st}	MMF drop across the stator teeth
F_{sy}	MMF drop across the stator yoke
f	Force per unit surface
f	Frequency
f_0	Rated frequency
g	Air-gap radial length
g'	Air-gap equivalent length
g_{avg}	Average air-gap length
g_{max}	Maximum air-gap length
g_{min}	Minimum air-gap length
g_q	Air-gap length on quadrature axis
η	Efficiency
H	Magnetic field intensity
h	Harmonic order
h_{bar}	Rotor bar height
h_G	Groove depth
h_{pb}	Pole-body height
h_{ps}	Pole-shoe height
h'_{ps}	Pole-shoe side height
h_{rew}	Rotor elementary wire thickness
h_{rng}	Rotor ring radial height

$h_{\text{rsl,bot}}$	Rotor slot height on yoke side
$h_{\text{rsl,pre}}$	Rotor pre-slot height
$h_{\text{rsl,top}}$	Rotor slot height on gap side
$h_{\text{rsl,tot}}$	Rotor slot total height
h_{ryk}	Rotor yoke height
h_{scs}	Stator coil-side height
h_{sew}	Stator elementary wire thickness
$h_{\text{ssl,pre}}$	Stator pre-slot height
$h_{\text{ssl,tot}}$	Stator slot total height
$h_{\text{ssl,wed}}$	Stator wedge slot height
h_{syk}	Stator yoke height
I	Current RMS Line current
I_1	Positive sequence current
I_2	Negative sequence current
I_{avg}	RMS of line current at fundamental frequency
I_{d}	Direct axis stator current
I_{f}	Field winding current, referred to stator
I_{kd}	Direct axis damper winding current, referred to stator
I_{kq}	Quadrature axis damper winding current, referred to stator
I_{m}	Magnetizing current
I_{n}	Rated current
I_{pul}	RMS of line current fluctuation
I_{q}	Quadrature axis stator current
I_{r}	Rotor current (referred to stator)
I_{s}	Stator current
i	Per-unit value of line currents
J	Current density Moment of inertia
j	Imaginary unit
K_{f}	Torque friction factor
K_{fw}	Friction and windage loss factor
$K_{\text{L,t}}$	Core-loss manufacturing factor for teeth
$K_{\text{L,y}}$	Core-loss manufacturing factor for yokes
K_{rng}	Rotor end-winding leakage factor
K_{sym}	Symmetry multiplier for reduced FE models

K_{Ψ}	Flux-linkage factor
$k_{C,rcd}$	Carter factor for radial cooling ducts on rotor and stator
$k_{C,rsl}$	Carter factor for rotor slots
$k_{C,scd}$	Carter factor for radial cooling ducts on stator only
$k_{C,ssl}$	Carter factor for stator slots
$k_{C,tot}$	Carter factor for stator and rotor slots
$k_{r2s,Z}$	Rotor-to-stator transformation factor for impedances
k_{rst}	Rotor stacking factor
k_{sat}	Saturation factor for air-gap flux-density
k_{sst}	Stator stacking factor
k_w	Stator winding factor for the fundamental
$k_{w,h}$	Stator winding factor for the h -th harmonic
λ_{rsl}	Rotor slot permeance factor
λ_{ssl}	Stator slot permeance factor
L	Inductance Self-inductance
L_{ad}	Direct axis three-phase mutual inductance (magnetizing inductance)
L_{aq}	Quadrature axis three-phase mutual inductance (magnetizing inductance)
L_f	Field winding leakage inductance, referred to stator
L_{kd}	Direct axis damper winding leakage inductance, referred to stator
L_{kq}	Quadrature axis damper winding leakage inductance, referred to stator
L_s	Stator phase leakage inductance
l	Axial length
l_{bar}	Rotor bar length
l_{end}	End-winding average line total length
$l_{end,eye}$	End-winding axial length, eye part
$l_{end,hel}$	End-winding axial length, helicoidal part
$l_{end,str}$	End-winding axial length, straight part
l_G	Groove width
l_{gap}	Air-gap equivalent axial length
$l_{r,net}$	Net rotor axial length
$l_{r,tot}$	Total rotor axial length
l_{rcd}	Rotor radial cooling ducts width
l_{rng}	Rotor ring thickness
l_{rtu}	Rotor average turn length
$l_{s,net}$	Net stator axial length

$\ell_{s,tot}$	Total stator axial length
ℓ_{scd}	Stator radial cooling ducts width
ℓ_{stu}	Stator average turn length
μ	Magnetic permeability
μ_0	Vacuum magnetic permeability
N_G	Number of grooves
N_p	Number of poles
N_{pc}	Number of parallel circuits per phase
N_{pp}	Number of pole-pairs
N_{rcd}	Number of rotor radial cooling ducts
N_{rew}	Number of rotor elementary wires per turn
N_{rsl}	Number of rotor slots
N_{rtc}	Number of turns per rotor pole
$N_{rtc,h}$	Number of overlaid turns per rotor coil (pole)
$N_{rtc,w}$	Number of adjacent turns per rotor coil (pole)
N_{scd}	Number of stator radial cooling ducts
$N_{sew,h}$	Number of overlaid elementary wires per stator turn
$N_{sew,w}$	Number of adjacent elementary wires per stator turn
N_{ssl}	Number of stator slots
N_{tc}	Number of turns per coil
N_{tph}	Number of turns per phase
n_0	Synchronous speed (rpm)
n	Speed (rpm)
Ω	Mechanical rotational speed
Ω_0	Synchronous speed
$\check{\omega}$	Phase shift operator
ω	Angular frequency
ω_0	Rated angular frequency
\mathcal{P}	Clarke-Park transformation matrix
P	Power
	Active power
	Mechanical power
P_{Fe}	Core losses
P_{fw}	Friction and windage (mechanical) losses
P_{in}	Input power
$P_{j,r}$	Rotor joule loss

$P_{j,s}$	Stator joule loss
P_n	Rated power
P_{out}	Output power
p	Specific loss
p_{Fe}	Specific core loss
Q	Reactive power
q	Number of slots per pole per phase
ρ	Electrical resistivity
R	Resistance
R_{bar}	Rotor bar resistance
R_{Fe}	Core losses resistance
R_f	Field winding resistance, referred to stator
R_{kd}	Direct axis damper winding resistance, referred to stator
R_{kq}	Quadrature axis damper winding resistance, referred to stator
R_r	Rotor equivalent resistance referred to stator
R_{rng}	Rotor ring resistance
R_s	Stator AC phase resistance
$R_{s,DC}$	Stator DC phase resistance
r	Per-unit value of resistances
$r_{end,inn}$	End-winding inner radius
$r_{end,out}$	End-winding outer radius
r_{ps}	Pole-shoe radius
σ	Electric conductivity
S	Apparent power Cross-section area
S_{bar}	Rotor bar cross-section area
S_n	Sizing power
S_{rew}	Rotor elementary wire cross-section area
S_{rng}	Rotor ring cross-section area
S_{rtu}	Rotor turn cross-section area
S_{sew}	Stator elementary wire cross-section area
S_{stu}	Stator turn cross-section area
s	Slip
ϑ	Electrical angular position of the rotor
ϑ_r	Mechanical angular position of the rotor
τ_G	Grooving axial pitch

τ_p	Air-gap pole pitch
T	Torque
\hat{T}	Per-unit value of torque
T'	Torque from FE model
T_{avg}	Average torque
T_{em}	Electromagnetic torque
T_{load}	Load torque
T_{pul}	Peak of torque pulsation
t	Time
U	Phase voltage
U_1	Positive sequence phase voltage
U_2	Negative sequence phase voltage
U_d	Direct axis stator voltage
U_f	Field winding voltage
U_n	Rated phase voltage
U_q	Quadrature axis stator voltage
U-V-W	Phase sequence in a three-phase direct system
u	Per-unit value of phase voltage
\mathcal{V}	Volume
V	Voltage RMS Line voltage
V_n	Rated voltage
v	Per-unit value of line voltage
W	Energy
w	Specific energy
w_{pb}	Pole-body width
w_{ps}	Pole-shoe width
w_{rew}	Rotor elementary wire width
$w_{\text{rsl,bot}}$	Rotor slot width on yoke side
$w_{\text{rsl,pre}}$	Rotor pre-slot width
$w_{\text{rsl,top}}$	Rotor slot width on gap side
w_{sew}	Stator elementary wire width
w_{scs}	Stator coil-side width
$w_{\text{ssl,tot}}$	Stator slot width
$w_{\text{ssl,wed}}$	Stator wedge slot width
ζ	Reduced conductor height

X	Reactance (at grid frequency and referred to stator)
X_{ad}	Direct axis three-phase magnetizing reactance
X_{aq}	Quadrature axis three-phase magnetizing reactance
X_f	Field winding leakage reactance
X_{kd}	Direct axis damper winding leakage reactance
X_{kq}	Quadrature axis damper winding leakage reactance
X_m	Magnetizing reactance
$X_{m,uns}$	Unsaturated magnetizing reactance
X_r	Rotor phase leakage reactance
$X_{r,end}$	Rotor end-winding leakage reactance
$X_{r,gap}$	Rotor gap leakage reactance
$X_{r,rsl}$	Rotor slot leakage reactance
X_s	Stator phase leakage reactance
$X_{s,end}$	Stator end-winding leakage reactance
$X_{s,gap}$	Stator gap leakage reactance
$X_{s,ssl}$	Stator slot leakage reactance
x	Per-unit value of reactance
Ψ	Flux linkage Fundamental flux-linkage
Ψ'	Flux linkage from FEM
Ψ_d	Direct axis stator flux-linkage
Ψ_f	Field winding flux-linkage
Ψ_h	Flux linkage for the h -th flux-density spatial harmonic
Ψ_{kd}	Direct axis damper winding flux-linkage
Ψ_{kq}	Quadrature axis damper winding flux-linkage
Ψ_{tot}	Total flux-linkage
Ψ_q	Quadrature axis stator flux-linkage
Y	Admittance
Y_C	Common mode admittance
Y_Δ	Differential mode admittance
Y_d	Direct axis admittance
Y_q	Quadrature axis admittance
Z	Impedance
Z_0	No-load (core) impedance
Z_d	Direct axis operatorial impedance
Z_{eq}	Equivalent impedance

Z_q	Quadrature axis operatorial impedance
Z_r	Rotor impedance
Z_s	Stator impedance
z	Per-unit value of impedance

MATH SYMBOLS AND OPERATORS

x	Real number Scalar
\bar{z}	Complex number Phasor
\vec{v}	Vector
\mathbf{A}	Array Matrix Tensor
$\langle X \rangle$	m -uple of phase quantities \bar{X} in a m -phase system
$ x $	Absolute value for scalars Magnitude for complex numbers and phasors ¹
$\angle \bar{z}$	Argument of complex numbers Initial phase of phasors
\bar{z}^*	Complex conjugate
$\text{Re} \{ \bar{z} \}$	Real part
$\text{Im} \{ \bar{z} \}$	Imaginary part
$\ \vec{v} \ $	Vector euclidean norm (magnitude)
$\vec{u} \cdot \vec{v}$	Scalar product (dot product)
$\vec{u} \times \vec{v}$	Vector product (cross product)
$\vec{u} \perp \vec{v}$	Orthogonal vectors
$\vec{u} \parallel \vec{v}$	Parallel vectors
\dot{x}	Time derivative
$\vec{\nabla} x$	Gradient
$\vec{\nabla} \cdot \vec{x}$	Divergence
$\vec{\nabla} \times \vec{x}$	Curl
$\nabla^2 x$	Laplacian
\mathbf{A}^T	Transposed matrix
\mathbf{A}^{-1}	Inverse matrix

¹ For complex numbers and phasors the magnitude of \bar{z} is also indicated as simply z

MATH FUNCTIONS

arccos	Inverse cosine
arcsin	Inverse sine
arctan	Inverse tangent
arg	Argument (same as \angle)
cos	Cosine
cosh	Hyperbolic cosine
cot	Cotangent
dist	Geometric distance
ln	Natural logarithm
log	Base-10 logarithm
mod	Modulus (remainder)
sin	Sine
sinh	Hyperbolic sine
tan	Tangent
tanh	Hyperbolic tangent

LIST OF FIGURES

Figure 1.1	Rotors of two-pole induction motors	10	
Figure 1.2	Magnetic maps of an induction motor in different loading conditions	10	
Figure 1.3	Impact of the increased magnetizing current on the motor power factor	11	
Figure 1.4	Test equipment used for investigating shaft eddy-currents impact on the magnetizing current	12	
Figure 1.5	Magnetization characteristics obtained from experimental investigation	14	
Figure 1.6	Magnetic quantities trend inside the shaft and rotor for an induction motor	15	
Figure 2.1	Induction motor main dimensions and geometry sketches		18
Figure 2.2	Reference geometry for the teeth region MMF drop computation	30	
Figure 2.3	Determination of the air-gap saturated flux-density wave from the B-vs-MMF characteristic of air-gap and teeth region	32	
Figure 2.4	Calculation of the MMF drop across a yoke	33	
Figure 2.5	Induction motor standard equivalent circuit	39	
Figure 3.1	Finite-Element modelling of an induction motor	45	
Figure 3.2	FEA analysis of the steady-state operation of an induction motor	48	
Figure 3.3	Improved equivalent circuit method for induction motor steady-state analysis	53	
Figure 3.4	Reduced FE model for on load MMF drop computation.	55	
Figure 3.5	Plots of the air-gap flux-density and MVP in induction motor	56	
Figure 4.1	Experimental and calculated data for two-pole IMs		58
Figure 4.2	Magnetizing current from no-load test and from on-load improved equivalent circuit	59	
Figure 4.3	Computation time requested to evaluate induction motor working point	60	
Figure 5.1	Rotor geometric sketch of a salient-pole synchronous motor	68	
Figure 5.2	Example of manufactured salient-pole solid rotor		68
Figure 5.3	Air-gap variation for a salient-pole rotor	69	
Figure 5.4	Experimental set for the investigation of rotor grooving impact	72	
Figure 5.5	Different type of grooving for experimental investigation	73	
Figure 5.6	Results from experimental assessment of grooving efficacy	74	

Figure 6.1	Synchronous machine dynamic circuits	81
Figure 6.2	Synchronous machine circuits for slow start-up	86
Figure 6.3	Synchronous machine circuits for still-rotor condition	90
Figure 7.1	Flux-density complex distribution for a three-phase (rotating) system	97
Figure 7.2	Flux-density complex distribution for a single-phase (pulsating) system	100
Figure 7.3	Logic simplification of synchronous machine FE modeling	102
Figure 7.4	FE models for cage parameters calculation	103
Figure 7.5	Locked-rotor parameters calculated with different methods	107
Figure 8.1	Calculation procedure for DOL-SM circuit	110
Figure 8.2	Field winding resistance look-up table	112
Figure 8.3	Block diagram of the synchronous machine at start-up	115
Figure 8.4	Synchronous motor with DOL-starting capability	116
Figure 8.5	Current traces from SM starting	118
Figure 8.6	Voltage traces from SM starting	119
Figure 8.7	Torque traces from SM starting	120
Figure 8.8	Starting diagrams for synchronous machine	122
Figure A.1	Image method applied to end-coils mutual inductance computation	128
Figure A.2	Detail of a stator end-coil geometry	132
Figure A.3	Detail of a rotor end-coil geometry	134
Figure A.4	Reference nomenclature for the calculation of Neumann integral between two non-intesecting finite segments	136
Figure A.5	Calculation of Neumann integral for two aligned and not overlapping finite segments	139
Figure A.6	Computation of the self inductance associated with a finite straight segment	141
Figure A.7	Reference nomenclature for the calculation of Neumann integral between a segment and a pair of parallel infinite segments	143

LIST OF TABLES

Table 1.1	Prototype data for eddy-currents effect investigation	12
Table 2.1	Three-phase induction motors main dimensions	19
Table 2.2	Physical properties of commonly used materials	23
Table 2.3	Magnetic properties of commonly used steel	23
Table 2.4	Values of K_{fw} for different machine types	37
Table 3.1	Equivalence between motor and 2D-model quantities	47
Table 4.1	Sample IMs for experimental validation	57
Table 4.2	Power factor estimation errors	59
Table 4.3	Computational statistics	60
Table 5.1	Salient-pole rotor characteristic data	69
Table 5.2	Solid rotor data for grooving investigation	73
Table 7.1	Excitation systems for FE models	102
Table 7.2	Current point distributions for different models	104
Table 7.3	Correction factors for finite length effects	105
Table 7.4	Locked rotor test calculation results and statistics	107
Table 8.1	Static dq parameters for the reference DOL machine	113
Table 8.2	Circuit parameters for start-up at rated voltage	114
Table 8.3	Synchronous motor characteristic data	116
Table 8.4	Calculation times for dq half pole models	121
Table A.1	Characteristic points of a stator end-coil	133
Table A.2	Characteristic points of a rotor end-coil	135

INTRODUCTION

Eddy currents are current loops that arise in any conductor that experiences a variable magnetic field, i.e. practically any metallic part of any rotating electrical machine.

Their study is a crucial aspect in the electric machine design process, for many reasons:

- a large amount of the losses that occur in a rotating machine are related to eddy currents arising in both active or auxiliary parts of the machine;
- eddy currents arising in windings are the main cause of AC resistance increase, because of skin and proximity effects;
- similarly, eddy currents arising in conductive regions of the machine magnetic circuit would partially reject the flux lines, causing a change in the machine magnetic working point and, thus, its performance;
- some applications are based on eddy currents, such as in the case of solid-rotor synchronous machine direct-on-line starting.

These aspects are crucial in all machine typologies, from the traditional ones, like induction motors, to the most recent, like permanent-magnet machines.

The eddy current calculation is not a trivial task, because several aspects have to be taken into account simultaneously. In fact eddy-currents arise in conductors because of the variation in the magnetic field but, on the other hand, the magnetic field distribution is modified by the eddy current too. This problem can be formalized in terms of a Partial Differential Equation (PDE), which generally does not admit a closed-form solution. The machine non-linearities, due to iron cores saturation, have to be taken into account as well.

Numerical methods, such as Finite-Element Method (FEM), are usually employed to deal with the eddy current calculation issue. This method is indeed the most accurate tool that machine designers can adopt to cope with such challenging problems, because it allows to represent complex geometries and model the machine physics without the need for simplifying hypotheses and simplifications on which analytical methods rely. The main drawback of numerical methods is their computational burden, which slows down the design process and sometimes may not be acceptable, for instance when the design optimization through genetic algorithms is needed.

This PhD dissertation presents a collection of computationally-efficient methods to deal with the eddy-currents analysis for designing medium-voltage rotating machines. The effectiveness of these methods is the limited use of finite-element models, in combination with analytical approaches derived from rotating machine and electromagnetic field theory, in order to limit the computational burden. The simulation time is further reduced by

exploiting the machine symmetries and limiting the models to minimal geometries, in which the eddy current phenomenon is being investigated.

The thesis is subdivided into two parts, each covering a different aspect of eddy-current related issues, as summarized next.

- Part I focuses on the eddy currents arising inside the shaft of two-pole induction motors; this has a detrimental effect on the machine performance, especially as regards its power factor. This part is organized as follows:
 - chapter 1 gives an insight on the phenomenon, qualitatively describing it at first and then quantitatively assessing its impact on the magnetizing current through some laboratory tests;
 - chapter 2 is a compendium of literature methods to analytically compute the induction machine (IM) performance; these methods are based on the calculation of the machine equivalent circuit;
 - chapter 3 focuses on the shaft eddy-currents calculation through FEM. A new calculation procedure, based on a shaft-focused model used to properly compute the motor magnetizing reactance, is introduced. The standard FEM applied to the complete geometry is described as well;
 - chapter 4 presents the results of the performance calculation for seven real medium-voltage induction machines, adopting the methods presented in chapters 2 and 3. The results are compared with the machines acceptance tests and a discussion on computational performance is given.
- Part II presents a beneficial effect of eddy-currents, i.e. their use in the Direct-On-Line (DOL) starting of a large synchronous machine (SM) with solid rotor; this construction is the most effective and reliable solution to realize the SM self-starting. The eddy currents induced in the rotor core realize a fictitious squirrel cage, which creates an accelerating torque, until the synchronous speed is reached. This part presents the calculation of the starting performance prediction and it is organized as follows
 - chapter 5 summarizes the main features for the solid-rotor structure of synchronous motors;
 - chapter 6 describes the two-axis circuit model employed for the SM start-up performance calculation and its identification from stand-still tests;
 - chapter 7 presents a new method for the computation of the equivalent rotor cage parameters, based on FEM. It is shown as, by properly defining the model, the numerical investigation can be limited to just half of the rotor pole, and an experimental assessment on the computation time saving is also given;
 - an iterative method, based on the reduced model described in the previous chapter, is used in chapter 8 to compute the starting performance of a large solid salient-pole synchronous motor;

the calculation results are compared to the experimental data and to the analogous results coming from a standard Finite-Element Analysis (FEA). A comparative discussion on the computational burden is finally given.

Part I

EFFECTS OF SHAFT CURRENTS IN
TWO-POLE INDUCTION MACHINES

Induction motors have been the most widespread option in the industrial electric drive field for several decades [1]. They can be preferable to SMs thanks to their high reliability [2] and low cost, but suffer for a relatively poor efficiency and power factor (PF) [3–5].

PF plays a key role in determining an IM performance as it closely relates to its electric power consumption over time [5]. An accurate prediction of full-load PF is an essential task in IM design also because international standards prescribe tight tolerances on its measured value with respect to specifications [6].

Many industrial experiences suggest that significant error in the machine performance prediction occur in the case of two-pole IMs. This phenomenon is justified by the fact that the machine magnetic configuration is changed when passing from no-load to full load condition. In fact the flux-lines that normally cross the motor shaft do not produce any effect at no load, when the air-gap magnetic field rotates at the same speed of the rotor; on the other hand, when the motor is loaded, the rotor slows down and so eddy current arise in the shaft. The main consequence of this fact is the flux being rejected from the shaft to the rotor yoke, resulting in a higher saturation of the latter. As a further implication, a greater magnetizing current is absorbed by the machine and this is detrimental for the machine on-load performance, especially as regards PF. These considerations explain why there is such discrepancy between experimental results and calculation prediction, because the motor performance is usually computed (in the design stage) through the Equivalent Circuit Method (ECM) and the magnetizing reactance is calculated referring to the no-load magnetic state.

The efficient on-load PF computation problem is analyzed in the following chapters. First of all, the shaft-to-yoke magnetic flux rejection phenomenon in IMs is studied and quantified through laboratory tests in chapter 1; chapter 2 is an overview of literature methods to implement the ECM for power factor calculation, whereas chapter 3 presents numeric methods applied to PF computation. More in detail, two methods have been considered:

- standard FEM method applied to the complete motor geometry;
- a hybrid numerical-analytical method, which make use of a simplified FEA to properly correct the motor equivalent circuit, taking into account the on-load magnetizing reactance modification

Finally, chapter 4 presents the application of PF calculation methods discussed above to a set of real IMs, comparing the results with data obtained from machine acceptance test.

The research presented in this part has been submitted for publication by author [P8].

1

PROBLEM OVERVIEW

In this chapter an insight into the shaft eddy currents physics is given (section 1.1) and the impact of this phenomenon on machine magnetizing current is quantified through some experiments (section 1.2). Finally, a general overview of the problem as seen by technical literature is provided (section 1.3).

1.1 SHAFT EDDY-CURRENTS IN INDUCTION MOTORS

The shaft of electric machines is usually not classified as an active part, but rather treated as an electromagnetically passive mechanical component. However, for medium-voltage two-pole IMs, which typically include a laminated rotor core and a large solid-steel shaft (figure 1.1), the situation is different.

In these machines, when operated at no load, the main flux tends to cross the shaft as illustrated in figure 1.2a, encountering a relatively low reluctance and requiring a given magnetizing current. When the motor is loaded, instead, the relative motion between the rotating field and the rotor causes eddy currents in the shaft as shown in figure 1.2c; these tend to partly reject the flux lines into the laminated rotor yokes (figure 1.2d) causing an increase in their magnetic saturation as it can be observed by comparing figure 1.2b and figure 1.2e. As a consequence, the main flux encounters a higher reluctance at full load on crossing the rotor and requires a larger magnetizing current than at no load. Such variation in the magnetizing current as a function of the slip (from no-load to loaded conditions) is usually neglected in the performance calculation of IMs [7–10], while it may have a significant entity as experimentally investigated in the section 1.2.

The main impact of this increased magnetizing current on the motor overall performance regards its PF. In fact, as shown in figure 1.3, the magnetizing current amplitude (I_m) is directly related to the phase lag (φ) between the total stator current (I_s) and the phase voltage (U). It can be noticed how, assuming that the torque-producing component of the motor current (I_r) is invariant with respect to the shaft flux rejection phenomenon, the stator voltage is almost unchanged whether the flux is rejected or not, whereas there is a notably difference between the current phase lag in the two cases. For this reason the actual PF value measured from test is worse than expected, calculated assuming the magnetizing current always equal to the no-load value.



Figure 1.1: Rotors of MV two-pole squirrel-cage IMs with laminated core and solid-steel shaft (courtesy of Nidec ASI, Monfalcone, Italy)

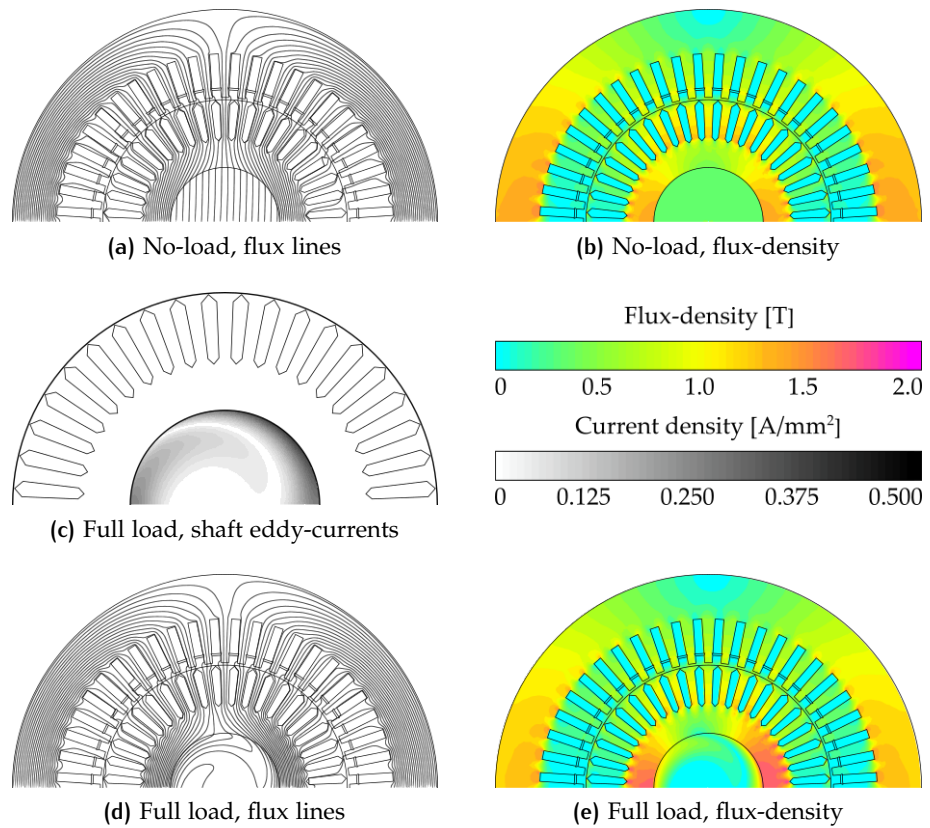


Figure 1.2: Magnetic maps of an induction motor in different loading conditions

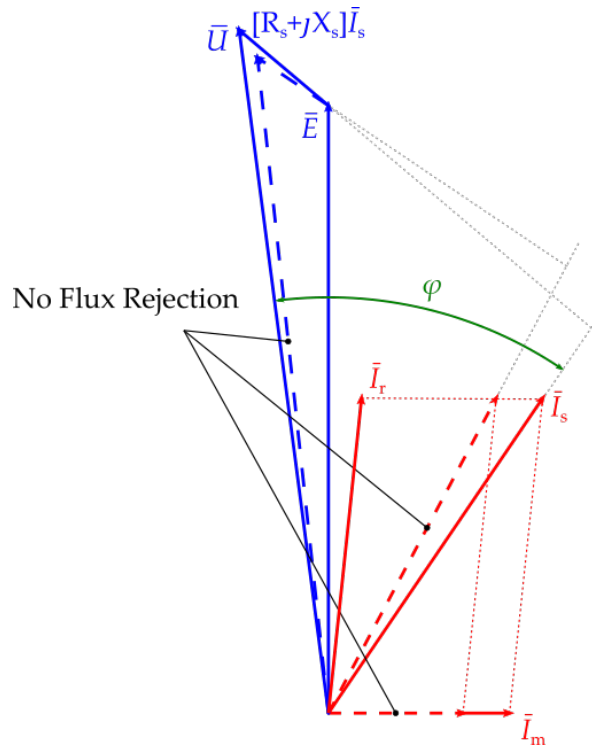


Figure 1.3: Impact of the increased magnetizing current on the motor power factor

1.2 EXPERIMENTAL INVESTIGATION

1.2.1 Test equipment description

Some laboratory tests have been carried out, using the equipment shown in figure 1.4, on a special electric machine prototype having a solid steel shaft and a laminated rotor core without any kind of squirrel cage or winding. The main prototype data are given in table 1.1. The stator has a usual design with a three-phase winding fed from a 50 Hz adjustable-voltage source. The rotor is coupled to a Variable Frequency Drive (VFD) through which its speed can be changed. Due to the absence of rotor circuits, the machine mainly absorbs its magnetizing current at steady state, except for a small active current component required to sustain core and mechanical losses.

By adjusting the rotor speed through the VFD, the prototype has been forced to operate at different slips and, for any given slip, the voltage-versus-current characteristic have been measured by varying the stator supply voltage.

1.2.2 Test results

The experimental results are shown in figure 1.5a for slip values between 0 and 1.2%. It can be noticed how, as the slip increases, the magnetizing current drawn for a given voltage (i.e. motor flux) grows. The fact can be more clearly observed by plotting the current-versus-slip characteristics for different voltages as shown in figure 1.5b. For instance, it can be seen that the magnetizing current for a terminal voltage of 400 V grows by 23% as

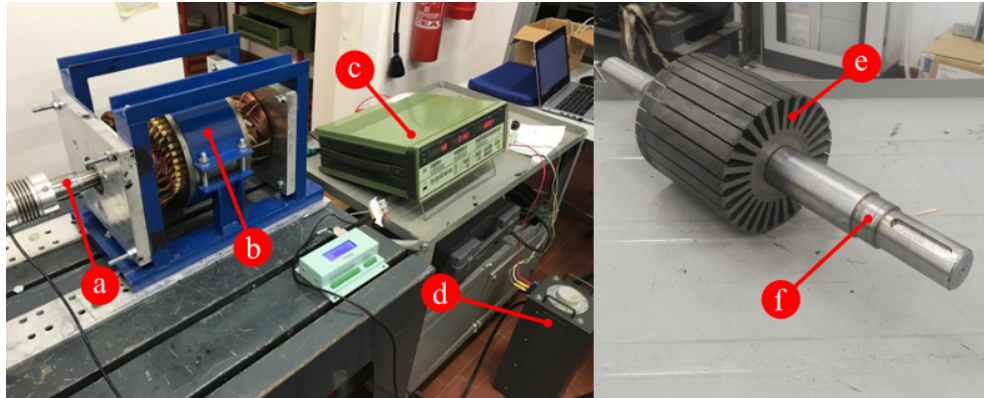


Figure 1.4: Test equipment used for investigating shaft eddy-currents impact on the magnetizing current **a)** variable-speed driven shaft **b)** special prototype for test **c)** digital wattmeter **d)** adjustable electric power supply **e)** prototype rotor laminated core **f)** prototype solid steel shaft

Table 1.1: Prototype data for the investigation of shaft eddy-currents on magnetizing current.

Stator outer diameter	240.0 mm
Stator inner diameter	148.0 mm
Air-gap width	0.5 mm
Rotor yoke thickness	20.2 mm
Stack length	150.0 mm
Shaft diameter	38.0 mm
Number of poles	2
Number of stator slots	36
Number of rotor slots	28
Number of turns per phase	60
Number of parallel paths per phase	1
Stator coil pitch	5/6
Stator phase connection	Y
Laminations material	M530 – 65A ^(a)
Shaft material	C40 ^(b)

^(a) see standard in [11]

^(b) see standard in [12]

the slip increases from 0 to 1%. The growth is less pronounced for lower terminal voltages (i.e. weaker fluxes) because saturation effects in the rotor yoke are reduced.

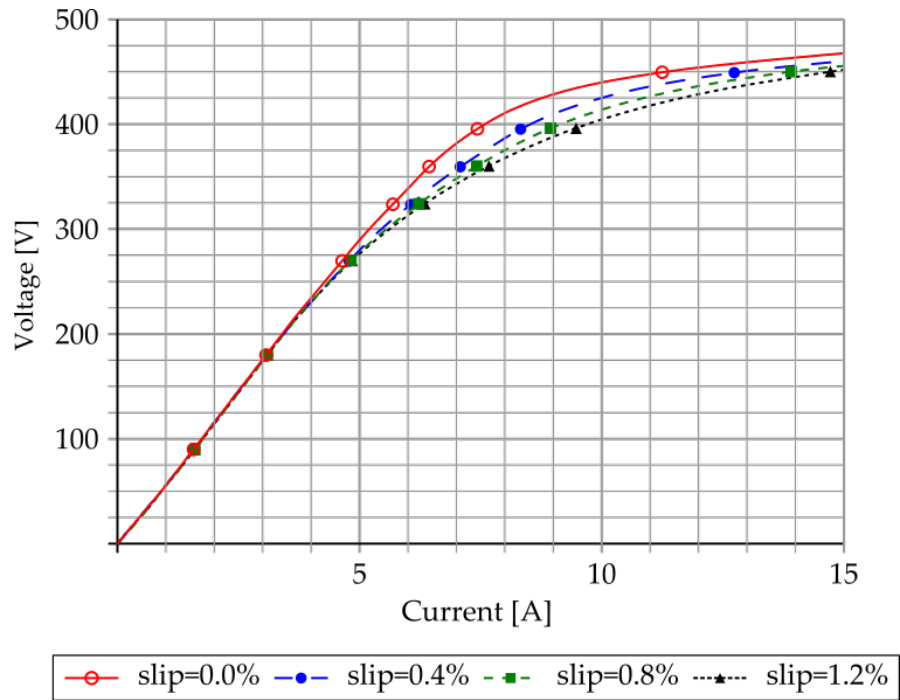
In conclusion, the experimental tests had confirmed that, for a two-pole IM, a significant change may occur in the magnetizing current as a function of the slip due to the physical phenomenon qualitatively described in section 1.1. A relatively traditional way to consider this fact in IM full-load PF prediction employs time-harmonic FEAs performed on a relatively complete motor model as discussed in chapter 3.

1.3 LITERATURE REVIEW

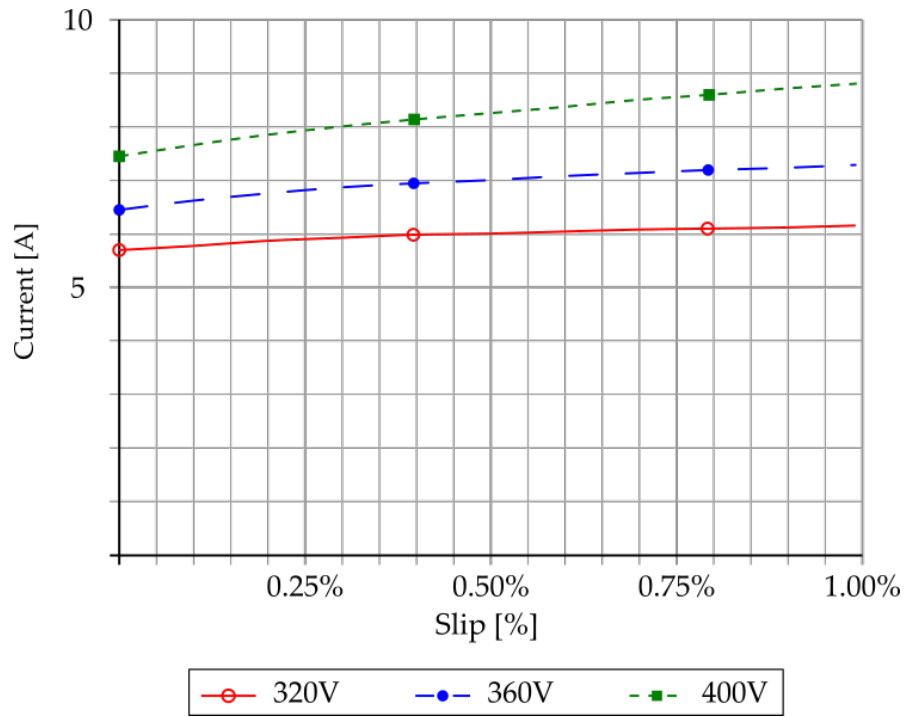
Shaft eddy-currents and their effect on rotor magnetic field distribution have been already investigated in the literature, using both FEAs of the entire motor [13] and analytical methods [14, 15].

Finite-Element (FE)-based approaches suffer from the known drawback of being time-consuming, so they are not conveniently applicable, for instance, in the case of IM design optimization [16]. The most efficient way to imply FEM for IMs design is using several FEAs to identify the motor equivalent circuit parameters [10]. However, this method does not allow to properly taking into account the magnetizing current variation, so a complete simulation of the motor working point is needed, as presented in section 3.1 and [17].

On the other hand analytical techniques, though fast, rely on simplifying heuristic assumptions that may compromise their accuracy and generality. For instance, they are typically incapable of accounting for axial cooling vents in the rotor core [13] or for strongly non-uniform flux-density distributions in the rotor yoke and shaft [14, 15]. As an example consider figure 1.6. In this diagram the observer position versus flux-density, field strength, current density and magnetic permeability are reported. The observer position is expressed as a percentage with respect to the rotor yoke outer radius. It can be noticed how the magnetic permeability inside the yoke is strongly non-uniform.



(a) Voltage-versus-Current for different slips



(b) Current-versus-Slip for different voltages

Figure 1.5: Magnetization characteristics obtained from experimental investigation

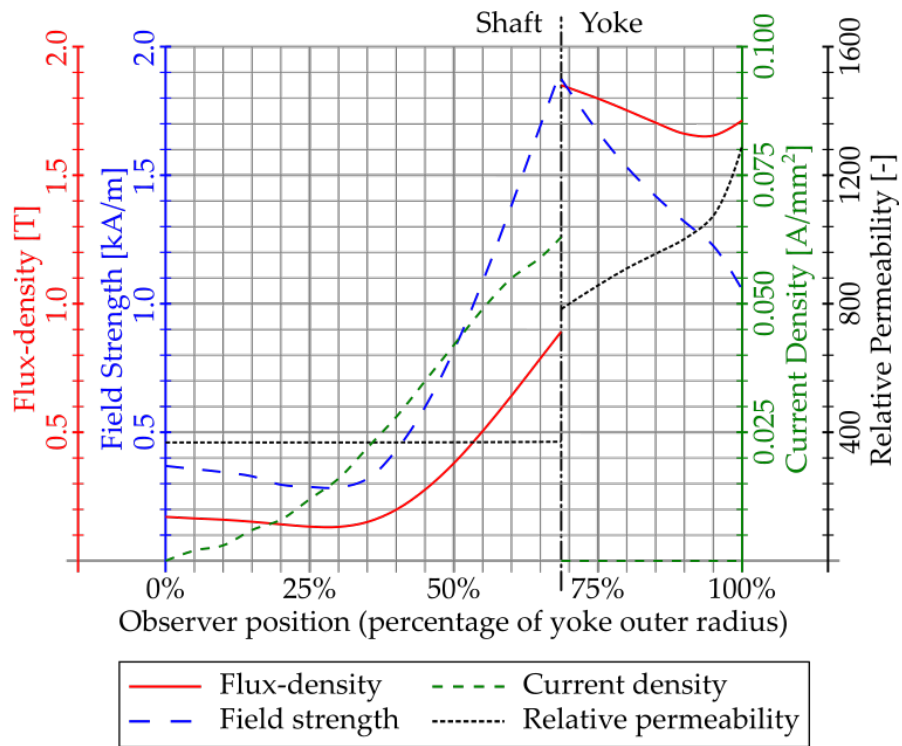


Figure 1.6: Magnetic quantities trend inside the shaft and rotor for an induction motor

2

INDUCTION MOTOR EQUIVALENT CIRCUIT CALCULATION

This chapter is a compendium of literature methods adopted to calculate the equivalent circuit of a large-size medium-voltage IM. These methods are herein collected for the sake of completeness and they will be adopted in combination with FEM in chapter 3.

Starting with the motor main geometry (section 2.1) the resistances, leakage reactances and no-load parameters calculation methods are illustrated (sections 2.2, 2.3 and 2.4 respectively). The determination of motor performance through ECM is finally presented (section 2.5).

2.1 MOTOR GEOMETRY AND MAIN DIMENSIONS

Figure 2.1 sketches the typical sections of a medium-voltage IM, with power ratings varying from ≈ 100 kW up to ≈ 5000 kW. The main dimensions and the geometrical relations between them are collected in table 2.1.

It is worth noticing that these type of machines adopt embridicated pre-formed windings, so it is important to know the end-winding geometry (figure 2.1d) to properly compute the average turn length and the end-winding leakage reactance.

This work is focused on squirrel-cage motors, but it can be easily extended to wound-rotor IMs. Two slot types have been considered (figure 2.1c):

1. rectangular semi-closed slots, usually adopted for copper cages;
2. diamond-shaped closed slots, usually adopted for aluminium cages.

The magnetic cores of both stator and rotor are laminated. Most of the machines addressed in this work are cooled through closed circuit ventilation, with the motor internal air blown through a separate heat exchanger (for instance with cooling codes IC511, IC611 and so on [18]). In this kind of machines the magnetic stacks are not continuous, but they are made by several elementary packs of laminations interspersed with radial cooling ducts (see figure 2.1b). If there are radial cooling ducts in both stator and rotor then the latter must have also axial cooling vents, through which the air is blown by axial fans. However, in two-pole machines, these axial cooling vents would reduce the yoke section, so it is preferable to not realize them, in order to prevent the rotor core saturation; thus the radial cooling ducts are missing as well and the rotor is a continuous stack of laminations. The stator has always the radial cooling ducts, except in the case of Totally-Enclosed Fan-Cooled (TEFC) motors.

Table 2.2 collects some useful physical properties adopted for the machine modeling in the following, whereas table 2.3 shows the magnetic properties for typical electrical and structural steels.

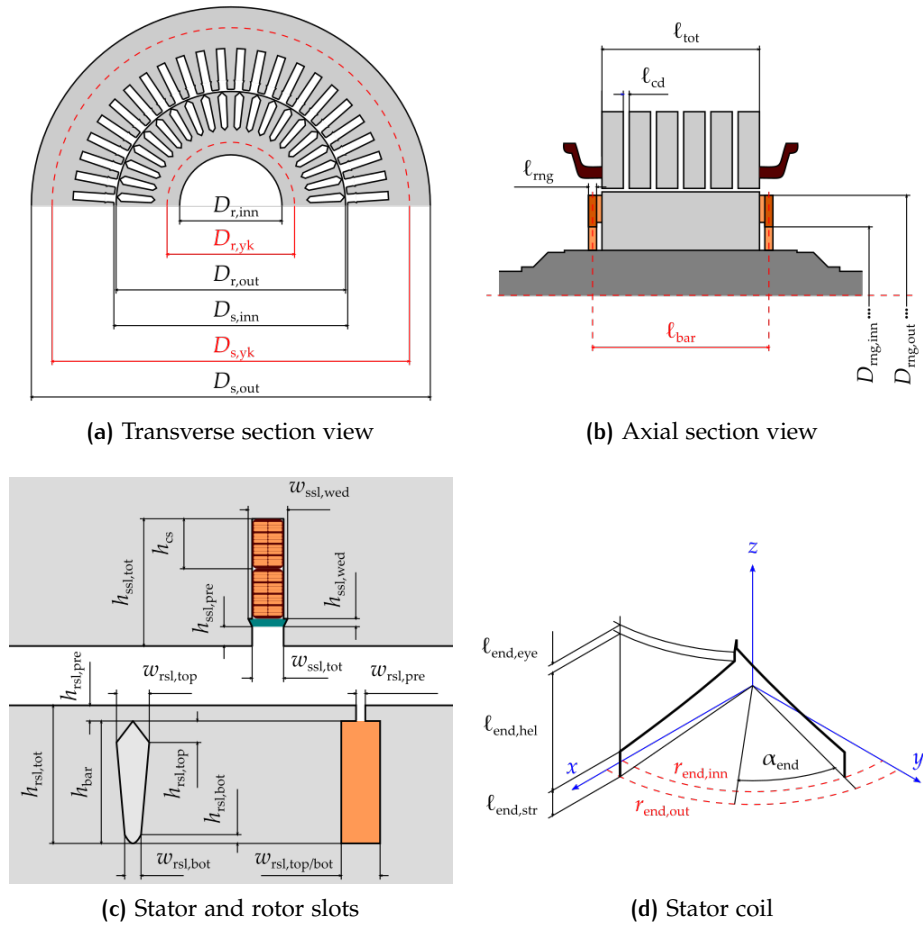


Figure 2.1: Induction motor main dimensions and geometry sketches

Table 2.1: Three-phase induction motors main dimensions

Quantity	Symbol	Notes
NAMEPLATE DATA		
Rated line voltage	V_n	
Rated phase voltage	U_n	¹
Rated current	I_n	
Rated power	P_n	²
Apparent power	S_n	³
Input active power	P_{in}	
Efficiency	η	⁴
Power factor	$\cos \varphi$	⁵
Frequency	f_0	
Angular frequency	ω_0	⁶
Number of pole pairs	N_{pp}	⁷
Synchronous speed [rpm]	n_0	⁸
Synchronous speed [rad/s]	Ω_0	⁹
Rotor speed [rpm]	n	
Rotor speed [rad/s]	Ω	
Slip	s	¹⁰
Torque	T	¹¹
STATOR STACK DATA		
Outer diameter	$D_{s,out}$	
Inner diameter	$D_{s,inn}$	
<i>(continued)</i>		

¹ Assuming a star-connection for the stator phases then $U = V/\sqrt{3}$.

² This is the rated output power, i.e. the mechanical power.

³ $S_n = \sqrt{3}V_n I_n$

⁴ $\eta = P_{mec}/P_{ele}$

⁵ $\cos \varphi = P_{ele}/S_{ele}$

⁶ $\omega_0 = 2\pi f_0$

⁷ Clearly, the number of poles is $N_p = 2 N_{pp}$.

⁸ $n_0 = 60f_0/N_{pp}$

⁹ $\Omega_0 = \omega_0/N_{pp}$

¹⁰ $s = 1 - n/n_0 = 1 - \Omega/\Omega_0$

¹¹ $T = 30/\pi P_{mec}/n$

<i>(continued)</i>		
Yoke average diameter	$D_{s,yk}$	12
Yoke height	h_{syk}	13
Total axial length	$\ell_{s,tot}$	
Number of radial cooling ducts	N_{scd}	
Cooling ducts width	ℓ_{scd}	
Net axial length	$\ell_{s,net}$	14
Stacking factor	k_{sst}	
Number of slots	N_{ssl}	
STATOR SLOT DATA		
Slot total height	$h_{ssl,tot}$	
Pre-slot height	$h_{ssl,pre}$	
Wedge height	$h_{ssl,wed}$	
Slot width	$w_{ssl,tot}$	
Wedge width	$w_{ssl,wed}$	
STATOR WINDING DATA		
Number of turns per coil	N_{tc}	
Number of parallel circuits per phase	N_{pc}	
Number of turns per phase	N_{tph}	15
Number of slots per-pole per-phase	q	16
Coil-to-pole pitch ratio	χ	
Winding factor	k_w	17
Number of overlaid elementary wires per turn	$N_{sew,h}$	
Number of adjacent elementary wires per turn	$N_{sew,w}$	
Elementary wire width	w_{sew}	
Elementary wire thickness	h_{sew}	
Elementary wire insulation double-thickness	$b_{ins,sew}$	
<i>(continued)</i>		

$$12 \quad D_{s,yk} = (D_{s,out} + D_{s,inn} + 2h_{ssl,tot}) / 2$$

$$13 \quad h_{syk} = (D_{s,out} - D_{s,inn}) / 2 - h_{ssl,tot}$$

$$14 \quad \ell_{s,net} = \ell_{s,tot} - N_{scd} \ell_{scd}$$

$$15 \quad \text{For a two-layer winding } N_{tph} = N_{ssl} / 3 \cdot N_{tpc} / N_{pcp}$$

$$16 \quad q = N_{ssl} / N_p / 3$$

$$17 \quad \text{See (2.21)}$$

<i>(continued)</i>		
Elementary wire cross-section area	S_{sew}	
Turn insulation double-thickness	$b_{\text{ins,stu}}$	
Turn cross-section area	S_{stu}	18
Ground-wall insulation double thickness	$b_{\text{ins,scs}}$	
Coil-side height	h_{scs}	19
Coil-side width	w_{scs}	20
End-winding axial length, straight part	$\ell_{\text{end,str}}$	
End-winding axial length, helicoidal part	$\ell_{\text{end,hel}}$	
End-winding axial length, eye part	$\ell_{\text{end,eye}}$	21
End-winding outer radius	$r_{\text{end,out}}$	22
End-winding inner radius	$r_{\text{end,inn}}$	23
End-winding angular half-width	α_{end}	24
End-winding average line total length	ℓ_{end}	25
Average turn length	ℓ_{stu}	26
AIR-GAP DATA		
Air-gap radial length	g	27
Air-gap average diameter	D_{gap}	28
Average pole pitch	τ_{p}	29
ROTOR STACK DATA		
Outer diameter	$D_{\text{r,out}}$	
Inner diameter	$D_{\text{r,inn}}$	30
Yoke average diameter	$D_{\text{r,yk}}$	31
<i>(continued)</i>		

$$18 \quad S_{\text{stu}} = N_{\text{sew,w}} N_{\text{sew,h}} S_{\text{sew}}$$

$$19 \quad h_{\text{scs}} = (h_{\text{ssl,tot}} - h_{\text{ssl,pre}} - h_{\text{ssl,wed}})$$

$$20 \quad w_{\text{scs}} = w_{\text{ssl,tot}}$$

$$21 \quad \ell_{\text{end,eye}} \approx h_{\text{cs}}$$

$$22 \quad r_{\text{end,out}} = D_{\text{s,inn}}/2 + h_{\text{ssl,tot}} - h_{\text{cs}}/2$$

$$23 \quad r_{\text{end,inn}} = r_{\text{s,out}} - h_{\text{cs}}$$

$$24 \quad \alpha_{\text{end}} = \chi\pi/N_{\text{pp}}$$

$$25 \quad \ell_{\text{end}} = 2\ell_{\text{end,str}} + \pi\ell_{\text{end,eye}} + \sqrt{\ell_{\text{end,hel}}^2 + r_{\text{end,inn}}^2 \alpha_{\text{end}}^2} + \sqrt{\ell_{\text{end,hel}}^2 + r_{\text{end,out}}^2 \alpha_{\text{end}}^2}$$

$$26 \quad \ell_{\text{tur}} = 2(\ell_{\text{end}} + \ell_{\text{s,tot}})$$

$$27 \quad g = (D_{\text{s,inn}} - D_{\text{r,out}})/2$$

$$28 \quad D_{\text{gap}} = (D_{\text{s,inn}} + D_{\text{r,out}})/2$$

$$29 \quad \tau_{\text{p}} = \pi D_{\text{gap}}/N_{\text{p}}$$

30 This is the shaft outer diameter.

$$31 \quad D_{\text{r,yk}} = (D_{\text{r,inn}} + D_{\text{r,out}} - 2h_{\text{rsl,tot}})/2$$

<i>(continued)</i>		
Yoke height	h_{ryk}	32
Total axial length	$\ell_{r,tot}$	33
Number of radial cooling ducts	N_{rcd}	34
Cooling ducts width	ℓ_{rcd}	
Net axial length	$\ell_{r,net}$	35
Stacking factor	k_{rst}	
Number of slots	N_{rsl}	
ROTOR SLOT DATA 36		
Slot total height	$h_{rsl,tot}$	
Pre-slot height	$h_{rsl,pre}$	
Special slot height, gap side	$h_{rsl,top}$	37
Special slot height, yoke side	$h_{rsl,bot}$	
Pre-slot width	$w_{rsl,pre}$	38
Slot width, gap side	$w_{rsl,top}$	
Slot width, yoke side	$w_{rsl,bot}$	39
ROTOR CAGE DATA		
Bar total height	h_{bar}	40
Bar cross section area	S_{bar}	41
Bar length	ℓ_{bar}	
Ring outer diameter	$D_{rng,out}$	
Ring inner diameter	$D_{rng,inn}$	
Ring average diameter	$D_{rng,avg}$	42
<i>(continued)</i>		

$$32 \quad h_{syk} = (D_{r,out} - D_{r,inn}) / 2 - h_{rsl,tot}$$

33 Usually this is equal to the stator total length.

34 The number of cooling ducts in the rotor can be lower than the stator one.

$$35 \quad \ell_{r,net} = \ell_{r,tot} - N_{rcd} \ell_{rcd}$$

36 The nomenclature here presented allows to represent both of the slot shapes shown in figure 2.1c.

37 For a rectangular slot it is $h_{rsl,top} = h_{rsl,bot} = 0$.

38 Of course it results $w_{rsl,pre} = 0$ in a closed slot, like the aluminium cage here examined.

39 For a rectangular slot it is $w_{rsl,top} = w_{rsl,bot}$; for a diamond-shaped slot it is $w_{rsl,top} > w_{rsl,bot}$.

$$40 \quad h_{bar} = h_{rsl,tot} - h_{rsl,pre}$$

$$41 \quad S_{bar} = w_{rsl,top} (h_{rsl,tot} - h_{rsl,bot}) / 2 + w_{rsl,bot} (h_{rsl,tot} - h_{rsl,top}) / 2$$

$$42 \quad D_{rng,avg} = (D_{rng,out} + D_{rng,inn}) / 2$$

(continued)

Ring height	h_{rng}	43
Ring thickness	ℓ_{rng}	
Ring cross-section area	S_{rng}	44

Table 2.2: Physical properties of commonly used materials

Material	ρ (20 °C) [$\Omega \text{ mm}^2/\text{m}$]	α [$^{\circ}\text{C}^{-1}$]	δ [kg/dm^3]
Copper	0.0172	0.00393	8.94
Aluminium	0.0265	0.00390	2.70
Brass	0.0464	0.00017	8.55
Electrical steel	–	–	7.60
Structural steel	0.1420	0.00094	7.87

Table 2.3: Magnetic properties of commonly used steel

B [T]	Electrical steel		Shaft steel	
	H [kA/m]	p [W/kg] 50 Hz	p [W/kg] 60 Hz	H [kA/m]
0.10	0.07	0.013	0.017	0.24
0.20	0.09	0.052	0.067	0.48
0.30	0.10	0.117	0.151	0.71
0.40	0.12	0.208	0.268	0.94
0.50	0.14	0.325	0.420	1.16
0.60	0.16	0.468	0.604	1.38
0.70	0.19	0.637	0.822	1.59
0.80	0.21	0.832	1.074	1.81
0.90	0.24	1.053	1.359	2.01
1.00	0.29	1.300	1.678	2.22
1.10	0.34	1.573	2.030	2.42
1.20	0.43	1.872	2.416	2.60
1.30	0.55	2.197	2.836	2.72
1.40	0.81	2.548	3.289	2.89
1.50	1.31	2.925	3.776	3.33
1.60	3.22	3.328	4.296	5.56
1.70	10.11	3.757	4.849	9.21
1.80	32.30	4.212	5.437	15.00
1.90	76.75	4.693	6.058	24.76
2.00	135.97	5.200	6.712	43.00

43 $h_{\text{rng,avg}} = (D_{\text{rng,out}} - D_{\text{rng,inn}}) / 2$ 44 $S_{\text{rng}} = h_{\text{rng}} \ell_{\text{rng}}$

2.2 RESISTANCES

The stator and rotor resistance calculation is taken from [19].

2.2.1 Stator resistance

The DC resistance of a stator phase is simply given by:

$$R_{s,DC} = \rho_{Cu,75^\circ C} \frac{N_{tph} \ell_{stu}}{N_{pc} S_{stu}} \quad (2.1)$$

and the AC value is obtained through:

$$R_s = \left[1 + \frac{2}{9} \frac{\ell_{s,net}}{\ell_{stu}} (16 N_{tc}^2 N_{sew,h}^2 - 0.2) \zeta^4 \right] R_{s,DC} \quad (2.2)$$

with

$$\zeta = h_{sew} \sqrt{\frac{\mu_0 \omega_0}{2 \rho_{Cu,75^\circ C}} \frac{N_{sew,w} w_{sew}}{w_{ssl,tot}}} \quad (2.3)$$

2.2.2 Rotor resistance

In a squirrel cage motor the rotor resistance is calculated as the equivalent resistance of a bar and the corresponding ring portion, referred to the stator by means of a proper transformation coefficient:

$$k_{r2s,Z} = \frac{12 k_w^2 N_{stu}^2}{N_{rsl}} \quad (2.4)$$

The ohmic resistance of the bar is simply given by:

$$R_{bar} = \rho_{bar} \frac{\ell_{bar}}{S_{bar}} \quad (2.5)$$

whereas the ring resistance expression is slightly complicated, because the phase difference between two adjacent bars must be taken into account:

$$R_{rng} = \rho_{bar} \frac{\pi D_{rng,avg}}{2 N_{rsl} S_{rng} \sin^2 \left(N_p \frac{\pi}{N_{rsl}} \right)} \quad (2.6)$$

Since the rotor frequency at rated speed is close to zero the AC-resistance effect can be neglected, so the rotor equivalent resistance is finally given by:

$$R_r = k_{r2s,Z} (R_{bar} + R_{rng}) \quad (2.7)$$

2.3 LEAKAGE REACTANCES

For both stator and rotor the flux leakage can be classified into three contributions:

1. slot leakage;

2. end-winding leakage;
3. air-gap leakage.

Each of these contributions corresponds to a reactance, whose calculations are reported below. The phase leakage reactances are finally given by:

$$X_s = X_{s,sl} + X_{s,end} + X_{s,gap} \quad (2.8)$$

$$X_r = k_{r2s,Z} (X_{r,sl} + X_{r,end} + X_{r,gap}) \quad (2.9)$$

with $k_{r2s,Z}$ obtained from (2.4).

2.3.1 Slot leakage

According to [20] the slot leakage reactance of a double-layer three-phase winding is given by:

$$X_{s,sl} = 12 \mu_0 \omega_0 \ell_{s,net} \frac{N_{tph}^2}{N_{ssl}} \lambda_{ssl} \quad (2.10)$$

whereas, for a single rotor bar it is:

$$X_{r,sl} = \mu_0 \omega_0 \ell_{r,net} \lambda_{rsl} \quad (2.11)$$

The factors λ_{ssl} and λ_{rsl} that appear in (2.10) and (2.11) respectively are the slot permeance factors, defined accordingly to the slot geometry. For a rectangular stator slot we have:

$$\lambda_{ssl} = \frac{2}{3} \left(\frac{1}{4} + \frac{3}{4} \chi \right) \frac{h_{scs} - b_{ins,scs}}{w_{ssl,tot}} + \chi \left(\frac{b_{ins,scs}}{2 w_{ssl,tot}} + \frac{h_{ssl,pre}}{w_{ssl,tot}} \right) + \frac{b_{ins,scs}}{4 w_{ssl,tot}} \quad (2.12)$$

For a rectangular rotor slot the permeance factor becomes:

$$\lambda_{rsl} = \frac{h_{bar}}{3 w_{rsl,top}} + \frac{h_{rsl,pre}}{w_{rsl,pre}} \quad (2.13)$$

and, finally, for a diamond-shaped rotor slot we have:

$$\lambda_{rsl} = \frac{h_{bar} - h_{rsl,top} - h_{rsl,bot}}{3 w_{rsl,top}} + \frac{h_{rsl,pre}}{0.35 w_{rsl,pre}} + 0.66 \quad (2.14)$$

2.3.2 End-winding leakage

The end-winding leakage reactance calculation is not a trivial task, because of the complicated three-dimensional geometry. The approach presented in [21, 22] is adopted in appendix A for the stator end-winding leakage computation, whereas the rotor case is analyzed according to [20], giving:

$$X_{r,end} = \frac{2}{3} \mu_0 \omega_0 \frac{N_{rsl}}{N_p} \left[\frac{\ell_{bar} - \ell_{r,net}}{2} + K_{rng} \frac{\pi D_{rng,avg}}{N_p} \right] \quad (2.15)$$

where $K_{rng} = 0.18$ for a two-pole machine, $K_{rng} = 0.36$ otherwise.

2.3.3 Air-gap leakage

In appendix B it is shown that, for a three-phase double-layer distributed winding, the air-gap flux-density distribution is a function of time and electric angle:

$$\mathcal{B}_{\text{gap}}(\alpha, t) = B_1 \cos(\omega t - \alpha) + \sum_{k=1}^{+\infty} \sum_{\kappa=\pm 1} B_{6k+\kappa} \cos(\omega_0 t - \kappa(6k + \kappa)\alpha)$$

with

$$B_h = \mu_0 \frac{6\sqrt{2}}{h\pi} \frac{k_{w,h} N_{\text{tph}}}{N_p} \frac{I}{g'} \quad (2.16)$$

where the winding factor for the h -th harmonic is defined:

$$k_{w,h} = \sin\left(h\chi \frac{\pi}{2}\right) \frac{\sin\left(h \frac{\pi}{6}\right)}{q \sin\left(\frac{h \pi}{6}\right)} \quad (2.17)$$

and g' is the equivalent air-gap radial length, defined as explained in section 2.4.1. From the flux-density h -th harmonic the corresponding flux-per-pole is obtained:

$$\Phi_h = \frac{2}{\pi} B_h \frac{\tau_p}{h} \ell_{\text{gap}}^{45} \quad (2.18)$$

and, finally, the total flux-linkage is obtained:

$$\Psi_{\text{tot}} = k_{w,1} N_{\text{tph}} \Phi_1 + \sum_{h=6k\pm 1} k_{w,h} N_{\text{tph}} \Phi_h \quad (2.19)$$

It is worth noticing that, for every spatial harmonic order, the flux-linkage components in (2.19) are pulsating at the grid frequency ω_0 . The first component in (2.19) is the fundamental flux, i.e. the flux-linkage producing the motor back-EMF:

$$\Psi = \Psi_1 = k_{w,1} N_{\text{tph}} \Phi_1 = k_w N_{\text{tph}} \Phi_p \quad (2.20)$$

where:

- k_w is the fundamental winding factor

$$k_w = k_{w,1} = \sin\left(\chi \frac{\pi}{2}\right) \frac{\sin\left(\frac{\pi}{6}\right)}{q \sin\left(\frac{\pi}{6q}\right)} \quad (2.21)$$

- Φ_p is the main flux-per-pole:

$$\Phi_p = \Phi_1 = \frac{2}{\pi} B_1 \tau_p \ell_{\text{gap}} \quad (2.22)$$

- B_1 is the fundamental of air-gap flux-density:

$$B_1 = \mu_0 \frac{6\sqrt{2}}{\pi} \frac{k_w N_{\text{tph}}}{N_p} \frac{I}{g'} \quad (2.23)$$

⁴⁵ ℓ_{gap} is the air-gap equivalent axial length, calculated as presented in section 2.4.1

The fundamental flux-linkage is proportional to the stator current according to the unsaturated magnetizing inductance, i.e. the reactance corresponding to the magnetic energy stored in the air-gap only (see section 2.4.1). Combining (2.20), (2.22) and (2.23) together the unsaturated magnetizing reactance is obtained:

$$X_{m,uns} = \omega_0 \frac{\Psi}{\sqrt{2}I} = \mu_0 \omega_0 \frac{6}{\pi^2} (k_w N_{tph})^2 \frac{\tau_p \ell_{gap}}{N_{pp} g'} \quad (2.24)$$

By subtracting the fundamental flux linkage (2.20) from the total flux linkage (2.19) the stator-related air-gap leakage flux is obtained. The leakage reactance is then defined as:

$$X_{s,gap} = \omega_0 \frac{\Psi_{tot} - \Psi_1}{I} = \sum_{h=6k\pm 1} k_{w,h} N_{tph} \omega_0 \frac{\Phi_h}{I} \quad (2.25)$$

This expression can be simplified if (2.16) and (2.18) are rewritten in term of the fundamentals quantities:

$$B_h = \frac{k_{w,h}}{h k_w} B_1 \quad (2.26)$$

$$\Phi_h = \frac{k_{w,h}}{h^2 k_w} \Phi_p \quad (2.27)$$

so (2.25) becomes:

$$X_{s,gap} = \sum_{h=6k\pm 1} k_{w,h} N_{tph} \frac{k_{w,h}}{h^2 k_w} \omega_0 \frac{\Phi_p}{I}$$

and finally, considering (2.20) and (2.24), it results:

$$X_{s,gap} = \frac{X_{m,uns}}{k_w^2} \sum_{h=6k\pm 1} \left(\frac{k_{w,h}}{h} \right)^2 \quad (2.28)$$

The rotor-related air-gap leakage reactance is obtained as by[20]:

$$X_{r,gap} = \frac{X_{m,uns}}{k_{r2s,Z}} \sum_{h=1}^{+\infty} \left(\frac{1}{h} \right)^2 \quad (2.29)$$

2.4 MAGNETIZATION AND NO-LOAD LOSSES

The no-load parameters of an IM equivalent circuit are the magnetizing reactance X_m and the equivalent resistance accounting for the iron-core losses R_{Fe} . These parameters are, generally, variable with the motor back-EMF, because of the magnetic core saturation. Furthermore, the friction-and-windage mechanical losses P_{fw} have to be computed and considered.

In this section the approach given in [8] is adopted to determine the machine magnetization characteristic (section 2.4.1), which is then used to calculate the magnetizing reactance (section 2.4.2) and the core-losses resistance (section 2.4.3). Finally, the mechanical losses are computed (section 2.4.4) accordingly to [23].

2.4.1 Magnetization characteristics

The magnetizing current needed to sustain a certain voltage E is not known *a priori*, because of the non-linearity of ferro-magnetic core. The approach followed in [8] is determining the total Magneto-Motive Force (MMF) drop in the magnetic circuit for any arbitrary amount of air-gap flux density. This allows to define, for any flux-density – MMF pair, the machine magnetizing characteristic.

Air-gap MMF drop

The air-gap MMF drop to sustain a given amount of flux-density B is simply given by:

$$F_{\text{gap}}(B) = \frac{B}{\mu_0} k_{C,\text{tot}} g \quad (2.30)$$

where $k_{C,\text{tot}}$ is the Carter factor [24], introduced to take into account the fringing effect due to open slot. The general expression for the Carter factor is:

$$k_C = \frac{\tau/w}{\tau/w - \frac{w/g}{5 + w/g}} = \frac{\tau}{\tau - \frac{w^2}{w + 5g}}$$

with τ as the slot pitch and w as the slot opening. Using the nomenclature from table 2.1 the Carter factors for stator and rotor are obtained:

$$k_{C,\text{ssl}} = \frac{\pi D_{\text{gap}}}{\pi D_{\text{gap}} - \frac{N_{\text{ssl}} w_{\text{ssl}}^2}{w_{\text{ssl}} + 5g}} \quad (2.31)$$

$$k_{C,\text{rsl}} = \frac{\pi D_{\text{gap}}}{\pi D_{\text{gap}} - \frac{N_{\text{rsl}} w_{\text{rsl,pre}}^2}{w_{\text{rsl,pre}} + 5g}} \quad (2.32)$$

and, finally, the total Carter factor is simply given by:

$$k_{C,\text{tot}} = k_{C,\text{ssl}} k_{C,\text{rsl}} \quad (2.33)$$

It is worth noticing that the Carter factor is always not lower than one, because the denominators in (2.31) and (2.32) are always not greater than the numerator. In particular $k_{C,\text{rsl}}$ is equal to one if and only if $w_{\text{rsl,pre}} = 0$, i.e. for closed slots. From (2.30) it is observed that the Carter factor in (2.33) produces an increase of the air-gap actual length, so the equivalent air-gap length is defined as:

$$g' = k_{C,\text{tot}} g \quad (2.34)$$

Tooth MMF drop

The tooth MMF drop computation must take into account for the flux lines crossing the air regions because of the tooth saturation. Figure 2.2 shows the reference geometry for the tooth MMF drop computation. The approach is the same for the stator and rotor, so the procedure is presented considering a

generic laminated core, having N_{sl} slots (and N_{sl} teeth), with stacking factor k_{st} and net length ℓ_{net} .

Let us consider a generic tooth and the surrounding slot, as shown in figure 2.2. This region is divided into K elementary slices; each slot and tooth slice has a width denoted by s_k and t_k respectively and it is placed at a distance r_k from the machine center; h_k is the radial thickness of the elementary slice. Since the slice shape is a generic trapezoid, the widths s_k and t_k have to be considered as the average width of the elementary slice. It is assumed that each tooth-slice is axially made of both ferromagnetic material (laminated core) and air (insulation between two elementary laminations). Thus, the total axial length of the ferromagnetic part is $k_{st}\ell_{net}$, whereas the axial length of the slot part is ℓ_{net} . The axial length of the inter-lamination insulations is $1 - k_{st}\ell_{net}$.

The cooling ducts are not considered for the computation of tooth axial length and neither it is for the slot, because it is assumed that the fringing effect does not occur inside the core. Conversely, their presence must be taken into account for the air-gap region equivalent axial length. The latter is calculated accordingly to [25]:

$$\ell_{gap} = \frac{\ell_{s,tot} + \ell_{r,tot}}{2} + 2g - k_{C,scd}(N_{scd} - N_{rcd})\ell_{scd} - k_{C,rcd}N_{rcd}\frac{\ell_{scd} + \ell_{rcd}}{2} \quad (2.35)$$

with $k_{C,scd}$ the Carter factor for cooling ducts on the stator only:

$$k_{C,scd} = \frac{\ell_{scd}}{5g + \ell_{scd}} \quad (2.36)$$

and $k_{C,rcd}$ the Carter factor for cooling ducts on both stator and rotor:

$$k_{C,rcd} = \frac{\ell_{scd} + \ell_{rcd}}{5g + \ell_{scd} + \ell_{rcd}} \quad (2.37)$$

Equation (2.35) assumes that the rotor has at most as many cooling ducts as the stator.

If the magnetic core is unsaturated the elementary flux entering a slot-tooth pair entirely flows through the iron cross section, thus we can write:

$$B \frac{\pi D_{gap}}{N_{sl}} \ell_{gap} = \hat{B}_{t,k} t_k k_{st} \ell_{net} \quad (2.38)$$

where $\hat{B}_{t,k}$ is the ideal flux-density value for the k -th elementary tooth slice. This quantity is obtained by solving (2.38):

$$\hat{B}_{t,k} = \frac{\pi D_{gap}}{N_{sl} t_k} \frac{\ell_{gap}}{k_{st} \ell_{net}} B \quad (2.39)$$

The actual flux balance equation must take into account the amount of flux crossing the air regions:

$$B \frac{\pi D_{gap}}{N_{sl}} \ell_{gap} = B_{t,k} t_k k_{st} \ell_{net} + B_{a,k} [t_k(1 - k_{st})\ell_{net} + s_k \ell_{net}] \quad (2.40)$$

It is worth noticing that the second term on the right hand side of (2.40) accounts for the total air radial cross-section area, which is the actual slot area plus the inter-lamination area.

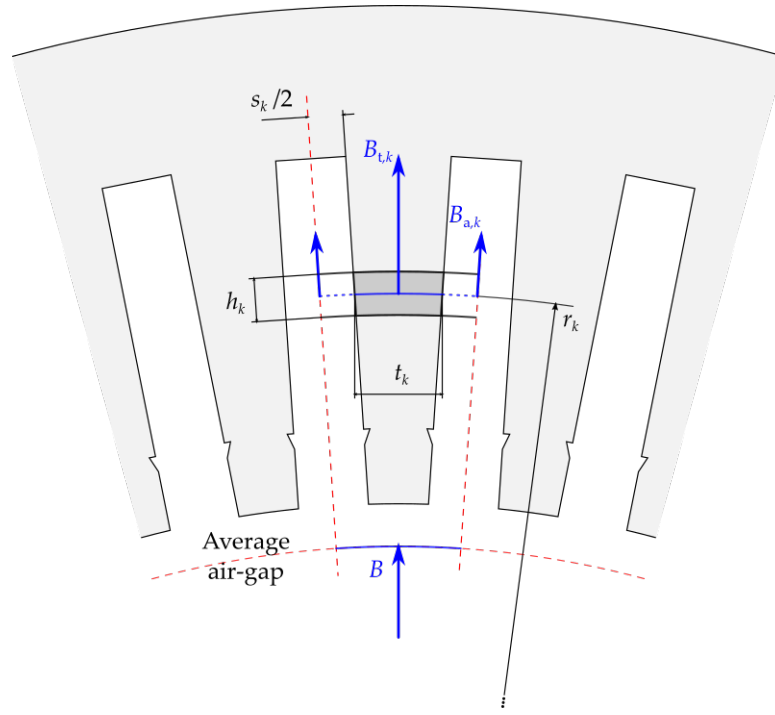


Figure 2.2: Reference geometry for the teeth region MMF drop computation

Combining (2.38) and (2.40) we can write:

$$\hat{B}_{t,k} = B_{t,k} + \frac{(1 - k_{st}) + s_k/t_k}{k_{st}} B_{a,k} \quad (2.41)$$

The only unknown terms in (2.41) are the actual flux-density value in the iron and in the air region, $B_{t,k}$ and $B_{a,k}$. These quantities are linked by the magnetic field intensity H_k , that can be assumed equal to the two regions, because the MMF drop is the same across the whole slot-tooth elementary slice. The iron flux-density depends on H_k through the non-linear magnetizing characteristic (table 2.3), whereas the analogous relationship is linear for the air region:

$$B_{t,k} \rightarrow B_t(H_k) \quad B_{a,k} \rightarrow \mu_0 H_k$$

so (2.41) becomes

$$\hat{B}_{t,k} = B_t(H_k) + \mu_0 \frac{(1 - k_{st}) + s_k/t_k}{k_{st}} H_k \quad (2.42)$$

We need to bear in mind that the term $\hat{B}_{t,k}$ depends on the air-gap flux-density B according to (2.39), so equation (2.42) can be written (and solved) for any value of B and for any k -th elementary slice.

Solving (2.42) for any k finally allows to determine H_k and, thus, to compute the total MMF drop along the tooth, by summing all the drops in the elementary slices:

$$F_t(B) = \sum_{k=1}^K H_k h_k \quad (2.43)$$

The tooth MMF drop can be computed as a function of the air-gap flux-density using the following procedure:

1. the air-gap flux-density (maximum) value B is fixed;
2. the tooth is subdivided into K elementary segments and, for every $k = 1, 2, \dots, K$ the ideal tooth flux-density value $\hat{B}_{t,k}$ is calculated accordingly to (2.39). Solving the non-linear equation in (2.42) the magnetic field intensity H_k is determined as well;
3. the tooth MMF drop is calculated accordingly to (2.43).

Iterating this procedure for any value of B the $F_t(B)$ characteristic is determined.

Saturated air-gap flux-density wave

The MMF drop in the air-gap and teeth region allows to determine the saturated air-gap flux-density wave, i.e. the actual flux-density spatial wave in the air-gap which sustains the magnetizing flux.

Firstly the MMF drop across the air-gap and the stator and rotor teeth has to be determined. The MMF drop computation is made for several values of the air-gap flux-density, so that the flux-density vs MMF drop plot in figure 2.3 is determined. The calculation procedure is summarized as follows:

1. the air-gap flux-density value B is given;
2. the air-gap MMF drop is determined, according to (2.30);
3. the stator tooth MMF drop is computed according to (2.43);
4. the rotor tooth MMF drop is calculated in the same way as the stator tooth;
5. the total MMF drop is simply given adding the three elementary drops:

$$F_0(B) = F_{rt}(B) + F_{gap}(B) + F_{st}(B) \quad (2.44)$$

At this point the saturated flux-density wave is determined as follows (figure 2.3):

1. the air-gap maximum flux-density $B_{g,max}$ is fixed ;
2. the MMF needed to sustain $B_{g,max}$ is determined according to the B-vs-MMF characteristic of the air-gap and teeth region previously calculated. Let $F_{0,max}$ be the MMF value;
3. $F_{0,max}$ is the peak value of the air-gap MMF fundamental wave. Therefore, the air-gap MMF as a function of the electric angle α is given by $F_0(\alpha) = F_{0,max} \cos \alpha$;
4. for any α the air-gap flux-density $B_g(\alpha)$ is calculated, reverting the B-vs-MMF characteristic of the air-gap and teeth region;

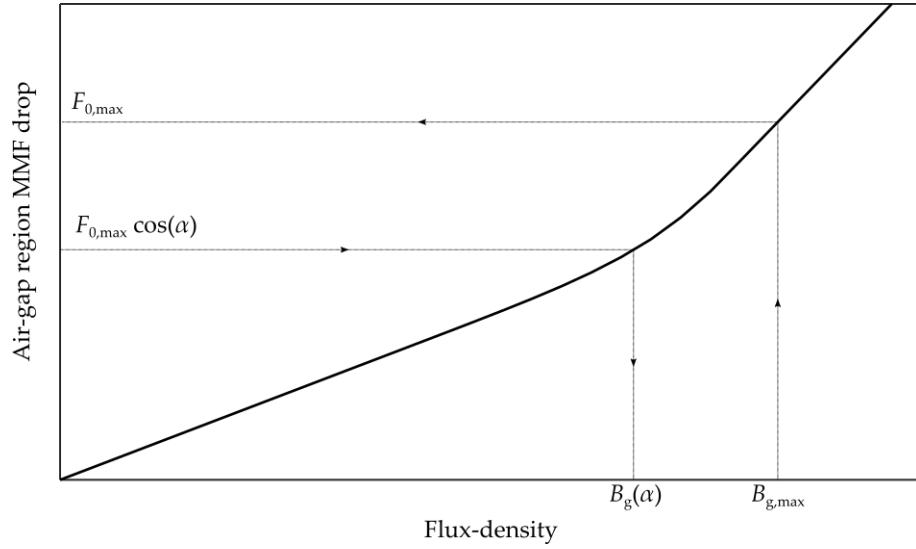


Figure 2.3: Determination of the air-gap saturated flux-density wave from the B-vs-MMF characteristic of air-gap and teeth region

5. the fundamental of the air-gap flux-density wave is determined:

$$B_{\text{fund}} = \frac{1}{\pi} \int_0^{2\pi} B_g(\alpha) \cos \alpha d\alpha \quad (2.45)$$

This value gives the main flux in (2.22); the saturation factor is also introduced, given by:

$$k_{\text{sat}}(B_{g,\text{max}}) = \frac{B_{\text{fund}}}{B_{g,\text{max}}} \quad (2.46)$$

The saturation factor is equal to 1 if the wave is unsaturated, otherwise becomes greater than 1.

An example of saturated flux-density wave is given in figure 2.4, where it is adopted to compute the yoke MMF drop. Before moving to this calculation it is worth saying that the procedure for the saturated flux-density wave determination can be iterated for several values of $B_{g,\text{max}}$, obtaining the corresponding flux-density fundamental $B_{\text{fund}}(B_{g,\text{max}})$ and the saturation factor $k_{\text{sat}}(B_{g,\text{max}})$. This allows one to introduce a new machine characteristic curve, i.e. the $B_{g,\text{max}}$ -vs- B_{fund} characteristic or, equivalently, the B_{fund} -vs- k_{sat} characteristic.

Yoke MMF drop

The calculation of the MMF drop in the machine yokes is illustrated in figure 2.4. As for the teeth case, the procedure is the same for both the stator and the rotor yokes, so the method will be explained considering a generic laminated yoke, having net length ℓ_{net} and stacking factor k_{st} . The yoke radial height is h_{yk} and is calculated accordingly to what presented in table 2.1. For symmetry reasons the MMF drop calculation is limited to half a pole, i.e. an electric angle of 90° . It is assumed that the yoke starts at a pole axis and ends at an inter-pole axis, covering half of a pole pitch. The yoke is subdivided into N elementary segments. The number of segments

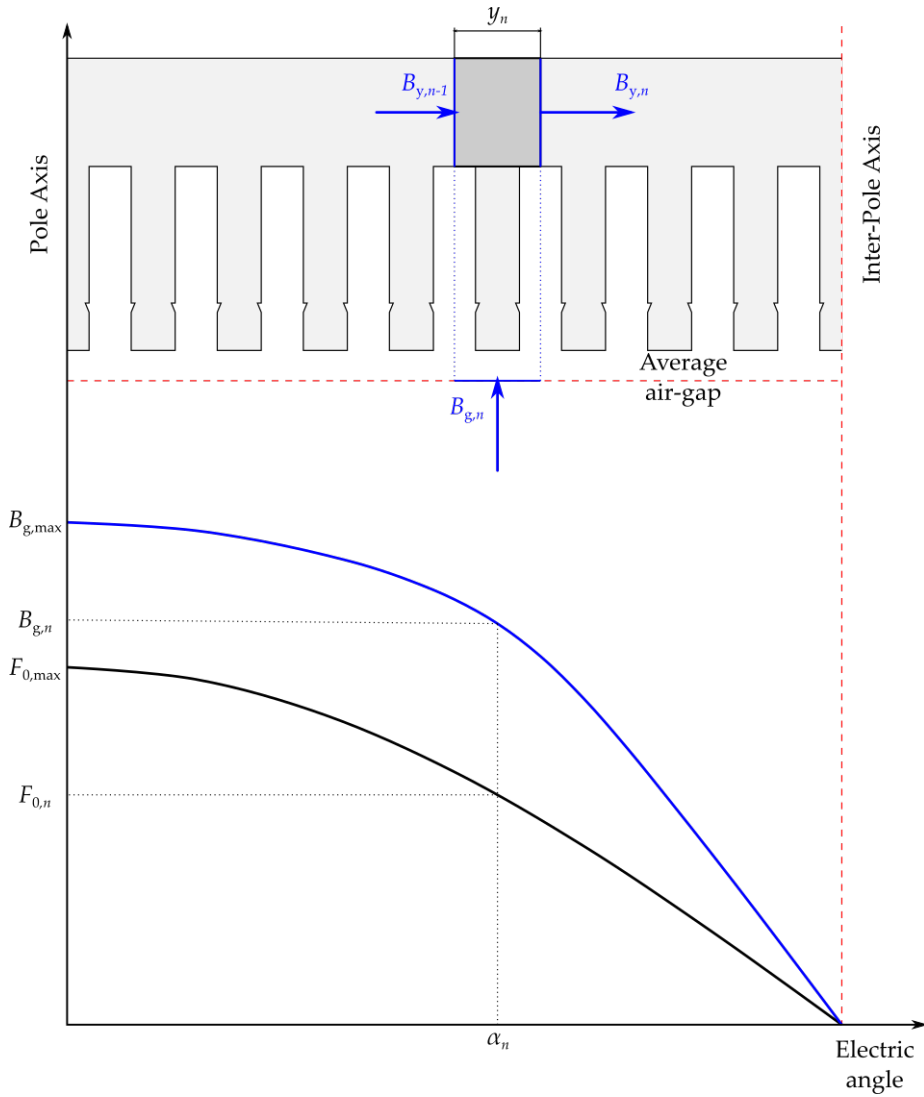


Figure 2.4: Calculation of the MMF drop across a yoke. This figure also shows the air-gap MMF wave (sinusoidal) and the saturated air-gap flux-density wave

should be close to the number of slots. The average between N_{ssl} and N_{rsl} is usually a good choice. Each segment has an elementary width equal to y_n and is placed at an electric angle α_n with respect to the pole axis. The axial length of the iron section for each elementary segment is, of course, $k_{st}\ell_{net}$ and this is the only section that experiences magnetic flux, i.e. the effect of air-crossing considered for the teeth is not assumed in this case, because of the reduced level of saturation that usually occurs in the yokes.

The flux-balance equation for the n -th segment has to take into account the contribution of flux coming from the air-gap and from the adjacent yoke segment. Thus it can be written:

$$B_{y,n-1} h_{yk} k_{st} \ell_{net} + B_{g,n} \frac{\tau_p}{2N} \ell_{gap} = B_{y,n} h_{yk} k_{st} \ell_{net} \quad (2.47)$$

where $B_{y,n}$ is the flux-density in the n -th yoke segment and $B_{a,n}$ is the air-gap value of the flux-density at angle α_n , calculated as described in 2.3; since this procedure depends on the arbitrary value of maximum air-gap flux-density, equation (2.47) can be written for any given $B_{g,max}$. It is worth noticing

that (2.47) is valid for any n , except for $n = 1$; in this case the flux coming from the previous segment is not defined, because, there is no segment 0. However, for symmetry reasons, the total flux entering this segment comes from the air-gap only, i.e. we can assume:

$$B_{y,0} = 0$$

From (2.47) the flux-density in the yokes can be calculated recursively, for $n = 1, 2, \dots, N$:

$$B_{y,n} = B_{y,n-1} + B_{g,n} \frac{\tau_p}{2N h_{yk}} \frac{\ell_{gap}}{k_{st} \ell_{net}} \quad \text{with } B_{y,0} = 0 \quad (2.48)$$

Once the flux-density is determined, the magnetic field intensity $H_{y,n}$ is obtained from the material BH curve (table 2.3) and, finally, the MMF drop:

$$F_y(B_{g,max}) = \sum_{n=0}^N H_{y,n}(B_{y,n}) y_n \quad (2.49)$$

At this point the $B_{g,max}$ -vs- F_y characteristic can be determined as follows:

1. the maximum air-gap flux density $B_{g,max}$ is fixed;
2. the saturated air-gap flux-density wave is determined, applying the procedure described at page 31;
3. the flux-density profile along the yoke is calculated recursively using (2.48);
4. the MMF drop in the yoke is determined accordingly to (2.49).

Total magnetization characteristic

The MMF calculation procedures presented above can be combined to determine the final magnetization characteristic of the whole machine. This characteristic will be used, in the next section, to determine the magnetizing reactance of the IM. It is convenient to express the magnetization characteristic in terms of a E -vs- F_{mag} curve, being E the motor back-EMF and F_{mag} the total magnetizing MMF, i.e. the total MMF drop.

The characteristic is determined as follows:

1. the root-mean square (RMS) value of back-EMF E is fixed;
2. the flux-per-pole is calculated

$$\Phi_p = \frac{\sqrt{2}E}{\omega_0 k_w N_{tph}} \quad (2.50)$$

3. the fundamental of air-gap flux-density is determined inverting (2.22)

$$B_{fund} = \frac{\pi}{2} \frac{\Phi_p}{\tau_p \ell_{gap}} \quad (2.51)$$

4. the corresponding maximum value of the saturated flux-density wave is determined reverting the $B_{\text{fund}}\text{-vs-}k_{\text{sat}}$ characteristic:

$$B_{g,\text{max}} = \frac{B_{\text{fund}}}{k_{\text{sat}}} \quad (2.52)$$

5. the value of $B_{g,\text{max}}$ determined from (2.52) is used in the B-vs-MMF characteristics previously evaluated in (2.44) and (2.49) to determine the total MMF drop:

$$F_{\text{mag}} = F_0(B_{g,\text{max}}) + F_{\text{sy}}(B_{g,\text{max}}) + F_{\text{ry}}(B_{g,\text{max}}) \quad (2.53)$$

Iterating this procedure for any E the $F_{\text{mag}}(E)$ characteristic is finally determined.

2.4.2 Magnetizing reactance

Expression (B.23) in appendix B, limited to the first harmonic, gives the relationship between the magnetizing MMF and the RMS value of the magnetizing current:

$$F_{\text{mag}} = \frac{6\sqrt{2} k_w N_{\text{tph}}}{\pi N_p} I_m \quad (2.54)$$

Since the magnetizing MMF must equal the MMF drop in the whole magnetic circuit that has been calculated before, this expression can be inverted determining the magnetizing current needed to sustain a certain F_{mag} :

$$I_m = \frac{\pi N_p}{6\sqrt{2} k_w N_{\text{tph}}} F_{\text{mag}} \quad (2.55)$$

It is worth noticing that the peak of magnetizing MMF wave is actually evaluated by the drop along half of the magnetic circuit (as presented in section 2.4.1), because the drop along the remaining half is substained by the MMF wave in the adjacent pole.

The magnetizing reactance is simply given by the ratio E/I_m ; however, since the magnetizing MMF in (2.53) is defined as a function of the back-EMF, the magnetizing reactance is defined as a function as well:

$$X_m(E) = \frac{E}{I_m(E)} = \frac{6\sqrt{2} k_w N_{\text{tph}}}{\pi N_p} \frac{E}{F_{\text{mag}}(E)} \quad (2.56)$$

If the magnetizing MMF is limited to the air-gap amount then the unsaturated magnetizing reactance is obtained. The fundamental value of B should be used to evaluate F_{gap} in this case. Since the air-gap MMF is linearly dependent on the back-EMF, the unsaturated reactance is a constant parameter:

$$X_{m,\text{uns}} = \frac{6\sqrt{2} k_w N_{\text{tph}}}{\pi N_p} \frac{E}{F_{\text{gap}}(B_{\text{fund}})} \quad (2.57)$$

2.4.3 Core losses

Core losses are due to hysteresis and eddy currents. Most of the laminated electric steel suppliers provide, along with the BH curve, the material loss characteristic, expressed as a specific power loss (W/kg) at different given values of frequency and flux-density (see table 2.3). Using the flux-density distributions in the teeth and in the yokes evaluated in 2.4.1 the total core loss can be calculated from this specific loss.

The procedure is applied to the stator parts only; in fact the rotor core loss is usually neglected, because of the low frequency that this part of the machine experiences in its normal operation. The specific loss of an elementary volume is related to the maximum value of flux-density that it experiences during an electric cycle. Therefore:

- for the teeth we need to consider the flux-density distribution determined for a tooth placed on the pole axis;
- for the yoke it is sufficient considering the flux-density value on the inter-pole axis.

The specific losses provided by material suppliers are obtained from laboratory tests on normalized specimens. Because of the manufacturing process of the electric machine the actual losses are generally larger than the supplier-provided values. This fact can be taken into account considering the following core loss factors, different for yoke and teeth:

- for the yoke it can be considered a factor $K_{L,y} = 1.25-1.50$
- for the teeth the factor is higher, say $K_{L,t} = 1.75-2.00$

Because of the saturation the core loss varies non-linearly with the machine back-EMF. Thus, as done for the magnetizing characteristic, the procedure has to be iterated for several values of E to determine the voltage-vs-loss characteristic, i.e. the function $p_{Fe}(E)$. The calculation procedure is the following:

1. the RMS value of back-EMF E is fixed;
2. the maximum value of air-gap flux density $B_{g,max}$ is determined as explained in the procedure at page 35;
3. the tooth flux-density distribution $B_{st,k}$ and the maximum yoke flux-density $B_{sy,N}$ are determined as described at page 30 and 34 respectively;
4. the tooth and yoke specific losses are given by:

$$p_{Fe,t}(E) = \sum_{k=1}^K p_{Fe}(B_{st,k}) t_k h_k \quad (2.58)$$

$$p_{Fe,y}(E) = p_{Fe}(B_{sy,N}) \pi D_{s,yk} h_{syk} \quad (2.59)$$

being $p_{Fe}(B)$ the specific loss of the ferromagnetic material at the flux-density value B and for the rated machine frequency;

Table 2.4: Values of K_{fw} for different machine types

TEFC motors	$15 \text{ W s}^2 \text{ m}^{-4}$
Open circuit cooling machines	$10 \text{ W s}^2 \text{ m}^{-4}$
Large induction motors	$8 \text{ W s}^2 \text{ m}^{-4}$
Turbogenerators	$5 \text{ W s}^2 \text{ m}^{-4}$

5. the total core loss is finally given by:

$$P_{Fe}(E) = \delta [K_{L,y} p_{Fe,y}(E) + K_{L,t} N_{ssl} p_{Fe,t}(E)] \ell_{net} \quad (2.60)$$

From (2.60) the core equivalent resistance can be obtained as well.

$$R_{Fe}(E) = \frac{E^2}{P_{Fe}(E)} \quad (2.61)$$

2.4.4 Mechanical losses

The mechanical losses depend on friction and windage, i.e. the bearings losses and the friction between the rotating surfaces of the rotor and its surrounding gas (air). In addition, the self-consumption of the ventilator using for machine self-cooling has to be taken into account as well. The following empirical relation can be used:

$$P_{fw,0} = K_{fw} \frac{D_{r,out} (\ell_{r,tot} + 0.6\tau_p)}{N_p^2} \omega_0^2 \quad (2.62)$$

where K_{fw} is a loss coefficient, depending on machine type, accordingly to table 2.4.

The expression in (2.62) is referred to synchronous speed n_0 ; at a generic speed $n < n_0$ the value given by (2.62) has to be reduced. Since most of the loss is due to windage and the mechanical characteristic of the rotor is approximately a quadratic torque-vs-speed curve (as a fan), the total loss is almost cubic-proportional to the speed, i.e. it can be written:

$$P_{fw}(s) = P_{fw,0}(1-s)^3 \quad (2.63)$$

being s the slip associated to speed n .

2.5 PERFORMANCE CALCULATION

Figure 2.5 shows the standard equivalent circuit for an induction motor. The parameters R_s , X_s , R_{Fe} , X_m , R_r and X_r are determined according to what has been presented in sections 2.2, 2.3 and 2.4. The motor performance at a rated voltage V_n and power output P_n is determined through the following procedure:

1. the phase voltage U_n is calculated:

$$U_n = \begin{cases} \frac{V_n}{\sqrt{3}} & \text{for star-connected motors} \\ V_n & \text{for delta-connected motors} \end{cases}$$

2. a first guess pair (\tilde{E}, \tilde{s}) is fixed for back-EMF and slip;
3. the motor impedances are given by:

$$\bar{Z}_s = R_s + jX_s \quad (2.64a)$$

$$\bar{Z}_0 = \frac{R_{Fe}(\tilde{E}) jX_m(\tilde{E})}{R_{Fe}(\tilde{E}) + jX_m(\tilde{E})} \quad (2.64b)$$

$$\bar{Z}_r = \frac{R_r}{\tilde{s}} + jX_r \quad (2.64c)$$

and the equivalent impedance is:

$$\bar{Z}_{eq} = \bar{Z}_s + \frac{\bar{Z}_0 \bar{Z}_r}{\bar{Z}_0 + \bar{Z}_r} \quad (2.65)$$

4. the stator current is:

$$\bar{I}_s = \frac{\bar{U}_n}{\bar{Z}_{eq}} \quad (2.66)$$

where it is assumed $\bar{U} = U$, i.e. the phase voltage is chosen as reference for the phasors arguments. The rotor current is given as well:

$$\bar{I}_r = \bar{I}_s \frac{\bar{Z}_0}{\bar{Z}_0 + \bar{Z}_r} \quad (2.67)$$

5. the back-EMF is:

$$\bar{E} = \bar{Z}_r \bar{I}_r \quad (2.68)$$

whereas the power output is:

$$\bar{P}_{out} = 3R_r \frac{1 - \tilde{s}}{\tilde{s}} |\bar{I}_r|^2 - P_{fw,0} (1 - \tilde{s})^3 \quad (2.69)$$

6. the values of E from (2.68) has to be compared with the first guess chosen at point 2; similarly \bar{P}_{out} obtained from (2.69) has to be compared to the rated power. If the difference is above the acceptable tolerance the first guess pair (\tilde{E}, \tilde{s}) has to be updated and the procedure from point 2 to here has to be repeated. A good choice for the back-EMF is $|\bar{E}|$ from (2.68), whereas for the slip it can be used the fact that the power output is almost linear with the slip:

$$\tilde{s}_{new} = \frac{P_n}{\bar{P}_{out}} \tilde{s}_{old}$$

Once the convergence is reached the remaining parameters are calculated. The motor losses are given by:

- stator joule losses

$$P_{j,s} = 3R_s |\bar{I}_s|^2 \quad (2.70)$$

- core losses

$$P_{Fe} = 3 \frac{|E|^2}{R_{Fe}} \quad (2.71)$$

- rotor joule losses

$$P_{j,r} = 3R_r |\bar{I}_r|^2 \quad (2.72)$$

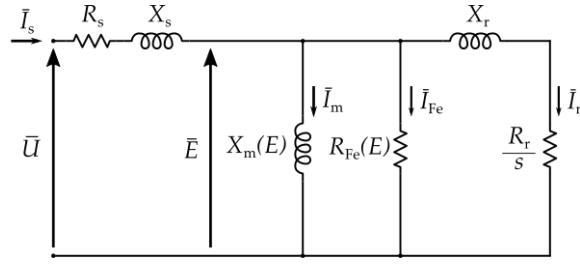


Figure 2.5: Induction motor standard equivalent circuit

- mechanical losses accordingly to (2.63).

The input complex power is:

$$\bar{S}_{\text{in}} = 3\bar{U}_n \bar{I}^* \quad (2.73)$$

and so the active and reactive power are, respectively:

$$P_{\text{in}} = \text{Re} \{ \bar{S}_{\text{in}} \} \quad (2.74)$$

$$Q_{\text{in}} = \text{Im} \{ \bar{S}_{\text{in}} \} \quad (2.75)$$

and the power factor is:

$$\cos \varphi = \frac{P_{\text{in}}}{|\bar{S}_{\text{in}}|} \quad (2.76)$$

Subtracting the losses from the input power the output power is obtained:

$$P_{\text{out}} = P_{\text{in}} - (P_{j,s} + P_{\text{Fe}} + P_{j,r} + P_{\text{fw}}) \quad (2.77)$$

so the motor efficiency is:

$$\eta = \frac{P_{\text{out}}}{P_{\text{in}}} \quad (2.78)$$

and, finally, the motor speed and torque:

$$n = (1 - s)n_0 \quad (2.79)$$

$$T = \frac{60P_{\text{out}}}{2\pi n} \quad (2.80)$$

3

SHAFT EFFECTS CALCULATION METHODS

In this chapter the problem of determining the motor performance for two-pole IMs is investigated. In fact, as said before, the ECM presented in chapter 2 is not accurate for those machine whose shaft experiences a variable magnetic field and, thus, eddy currents arise inside of it. Numerical methods have to be involved to take into account this complex phenomenon. Two methods are detailed here:

1. in section 3.1 the standard, classic FEM applied to the whole motor model is considered; the modeling hypotheses and the analysis procedure are presented and discussed;
2. the FE model detailed in section 3.1 is drastically simplified in section 3.2; this elementary FE model is used to present an innovative method, i.e. an improved version of the ECM detailed in the previous chapter. More in detail, this innovative method is an hybrid numeric-analytical method, which uses a set of FEAs to properly take into account the effect of shaft eddy currents on the motor equivalent circuit magnetizing reactance.

The two methods here presented, together with the ECM from chapter 2, will be applied to some real motors in chapter 4.

3.1 STANDARD FINITE-ELEMENT METHOD

Finite-Element Method is a standard, well-known method applied to many complex engineering problems involving PDEs, like structural analysis, heat transfer, fluid-flow, mass transport and so on. Technical literature is full of publications that apply this method to electromagnetic analysis as well, with particular focus on the low-frequencies and electrical machine analysis [9, 10, 16, 17]. Notable PDE problems for electric machines are detailed in section 3.1.1.

Time-stepping FE simulations are certainly a possible way to compute the full-load power factor of two-pole IMs with a solid-steel shaft [15]. However, they are known to be very time consuming. A faster but sufficiently accurate alternative, described in this section, is an extension of the hybrid approach proposed in [9] such that analytical equivalent-circuit-based calculations are combined with 2D Time-Harmonic (TH) FE simulations performed on the complete machine cross section model at the slip frequency, taking shaft eddy-current effects into account. Section 3.1.2 presents the strategies adopted to simplify the motor in order to fit it into a planar model. The solution procedure is detailed in section 3.1.3.

3.1.1 Notable PDEs for electric machine analysis

The low-frequency formulation for the Maxwell equation is given [26]:

$$\vec{\nabla} \cdot \vec{B} = 0 \quad (3.1a)$$

$$\vec{\nabla} \times \vec{H} = \vec{J} \quad (3.1b)$$

$$\vec{\nabla} \times \vec{E} = -\dot{\vec{B}} \quad (3.1c)$$

subject to the constitutive relations:

$$\vec{B} = \mu \vec{H} \quad (3.2a)$$

$$\vec{E} = \rho \vec{J} \quad (3.2b)$$

The three equations in (3.1) can be combined into a single one by means of the Magnetic Vector Potential (MVP) \vec{A} defined so that:

$$\vec{\nabla} \times \vec{A} = \vec{B} \quad (3.3a)$$

$$\vec{\nabla} \cdot \vec{A} = 0 \quad (3.3b)$$

Equation (3.3a) always guarantees a solution for (3.1a). Substituting (3.3a) into (3.1c) it can be shown that:

$$\vec{E} = -\dot{\vec{A}} - \vec{\nabla}\phi \quad (3.4)$$

being ϕ a scalar potential depending on external excitations, introduced for generality. Reverting (3.2b) it is also obtained:

$$\vec{J} = \sigma \vec{E} = -\sigma \dot{\vec{A}} - \sigma \vec{\nabla}\phi \quad (3.5)$$

and, plugging (3.3) into (3.1b) the fundamental equation is obtained:

$$\vec{\nabla} \times (\mu^{-1} \vec{\nabla} \times \vec{A}) + \sigma \dot{\vec{A}} + \sigma \vec{\nabla}\phi = 0 \quad (3.6)$$

This equation is valid for region subjected to eddy-currents. If there are only source (external) currents (or no current at all) (3.6) can be simplified into

$$\vec{\nabla} \times (\mu^{-1} \vec{\nabla} \times \vec{A}) = \vec{J} \quad (3.7)$$

The solution of (3.6) or (3.7) with respect to \vec{A} allows to determine the remaining quantities through the definition in (3.3a), the constitutive relations in (3.2) and the relation (3.5).

Most of the problems addressed in the electrical machine design admit a planar solution. This means that the magnetic field vectors \vec{B} and \vec{H} lie on a plane, whereas \vec{J} , \vec{E} , \vec{A} and $\vec{\nabla}\phi$ are normal to this plane, so they can be considered as scalars. Equations (3.6) and (3.7) become scalar equations as well:

$$\vec{\nabla} \cdot (\mu^{-1} \vec{\nabla} A) - \sigma \dot{A} = 0 \quad (3.8a)$$

$$\vec{\nabla} \cdot (\mu^{-1} \vec{\nabla} A) + J = 0 \quad (3.8b)$$

The flux-density components are given by:

$$B_x = \frac{\partial A}{\partial y} \quad (3.9a)$$

$$B_y = -\frac{\partial A}{\partial x} \quad (3.9b)$$

or, in polar coordinates:

$$B_r = \frac{1}{r} \frac{\partial A}{\partial \theta} \quad (3.10a)$$

$$B_\theta = -\frac{\partial A}{\partial r} \quad (3.10b)$$

A further simplification derives if the material is magnetically linear and isotropic:

$$\nabla^2 A - \mu\sigma \dot{A} = 0 \quad (3.11a)$$

$$\nabla^2 A + \mu J = 0 \quad (3.11b)$$

Equation (3.8b) and its particular case (3.11b) are classified as *Poisson's equations* and, in the specific case of rotating electrical machines, are the theoretical reference for synchronous-state operation. The FE problem of these equation is called *magnetostatic FE problem*.

The equations (3.8a) or (3.11a) are called *diffusion equations*; their solution is more complex and, generally, might require a time-discretization, so the corresponding FE problems are called *Time-Stepping problems*. However, if the time-dependency is sinusoidal, i.e. the AC steady-state of a machine is being investigated, the equation can be furtherly transformed and simplified.

If ω is the system angular frequency then all the electro-magnetical quantities in (3.8a) can be represented as complex phasors rotating at speed ω , so the time derivative is expressed as $\dot{A} = j\omega \bar{A}$ and the explicit time-dependency can be eliminated, giving:

$$\vec{\nabla} \cdot (\boldsymbol{\mu}^{-1} \vec{\nabla} \bar{A}) - j\omega\sigma \bar{A} = 0 \quad (3.12)$$

and, for linear and homogeneous materials:

$$\nabla^2 \bar{A} - j\omega\mu\sigma \bar{A} = 0 \quad (3.13)$$

The current density is obtained from the MVP accordingly to (3.5):

$$\vec{J} = -j\omega\sigma \bar{A} \quad (3.14)$$

Equations (3.12) and (3.13) are classified as *Helmholtz equations* and the corresponding FE formulation is called *Time-Harmonic problem*.

3.1.2 2D modeling of an induction motor

The steady-state operation of an induction motor can be analyzed by means of a TH-FEA at slip frequency [10]. The FE model for a two-pole

machine is sketched in figure 3.1. The motor geometry is modeled assuming a polar system of coordinate, i.e. each point in the motor is identified through the pair of coordinates (r, θ) , as shown in figure 3.1a. Thanks to the motor symmetry the model can be limited to a single pole, so the domain of definition for the coordinates is

$$(r, \theta) \in [0, D_{s,out}/2] \times [0, \pi]$$

As shown in (3.12) the problem is solved once the MVP A is determined inside of this domain. To guarantee the uniqueness of the solution a suitable set of Boundary Conditions (sBCs) have to be set on the model border. More in detail:

- on the stator external diameter the MVP is assumed as zero (*Dirichlet's BC*):

$$A(D_{s,out}/2, \theta) = 0 \quad \forall \theta \in [0, \pi]$$

- on the radial axis a *anti-periodic BC* is assumed:

$$A(r, 0) = -A(r, \pi) \quad \forall r \in [0, D_{s,out}/2]$$

The FEM solution is based on the *meshing*, i.e. the discretization of the geometric model. As shown in figure 3.1b the mesh size is thinner in the regions where there is a high variation rate of the magnetic field (such as in the air-gap) and in the regions subjected to eddy currents, like the cage and the shaft.

The simplification of modeling a 3D object as a 2D surface implies that all the machine parts are assumed to have the same length. In fact the 2D modeling of the flux that passes from the stator to the rotor through the air-gap, for instance, is realized considering the flux-density distribution inside each of these model region and multiplying it for the corresponding pole surface; each pole surface has the same length for the model, but they actually are different in the motor. As a consequence, the fields inside certain parts of the motor model are not the actual fields in the corresponding parts of the real machine. This fact can be partially corrected by properly adjusting the physical properties of the materials included in the model, similarly to what is suggested in [27].

Let us consider two adjacent regions of the motor, having axial length ℓ_0 and ℓ respectively. The flux is preserved when passing from one region to the other, thus we can write:

$$B_0 \ell_0 dx = B \ell dx \tag{3.15}$$

being dx the width of the interface between the two regions on the cross-plane. The motor is modeled assuming as a reference the length of the first region, so $\ell' = \ell_0$. The flux balance equation becomes:

$$B_0 \ell' dx = B' \ell' dx \tag{3.16}$$

The left hands in (3.15) and (3.16) are the same, so the right hands must be equal as well:

$$B \ell = B' \ell' \tag{3.17}$$

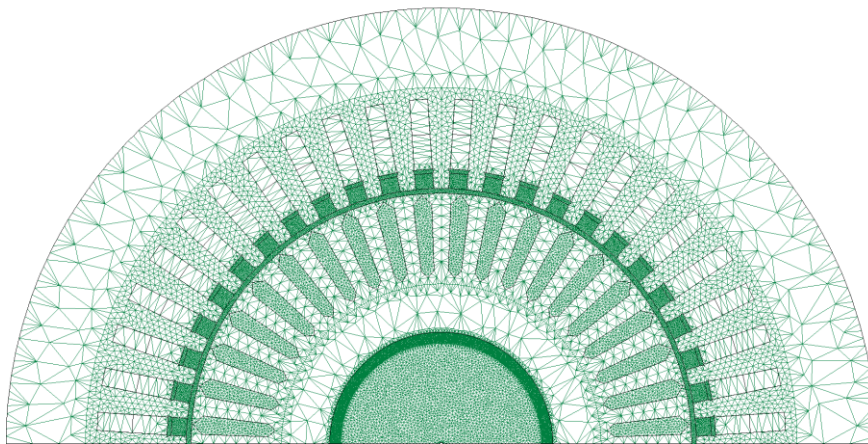
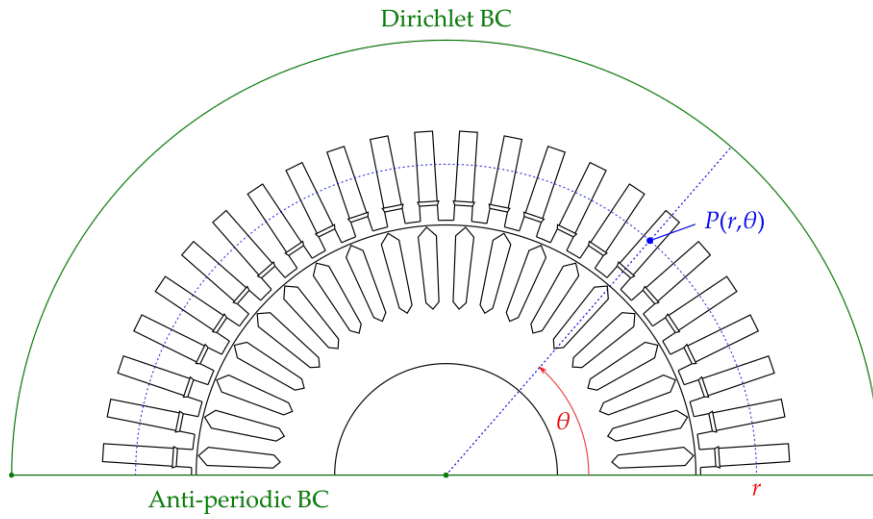


Figure 3.1: Finite-Element modelling of an induction motor

Using the constitutive relationship for magnetic field this expression can be rewritten as follows:

$$\mu H \ell = \mu' H' \ell' \quad (3.18)$$

It can be assumed that $H = H'$, because the field H depends only on the MMF (source currents) and on the dimensions of the cross-section. Therefore, equation (3.18) leads to:

$$\mu' = \frac{\ell}{\ell'} \mu \quad (3.19)$$

This correction on the model permeability guarantees the preservation of MMF, accordingly to (3.18). From (3.17) the relation between the actual and the model flux-density is also derived:

$$B' = \frac{\ell}{\ell'} B \quad (3.20)$$

The introduction of (3.19) requires an additional condition on material resistivity, in order to preserve the penetration depth in the regions subjected to eddy-currents. Since the penetration depth is:

$$\delta = \sqrt{\frac{2\rho}{\omega\mu}} \quad (3.21)$$

the latter is preserved if the resistivity is adjusted in the same way of the permeability, i.e.:

$$\rho' = \frac{\ell}{\ell'} \rho \quad (3.22)$$

or, equivalently:

$$\sigma' = \frac{\ell'}{\ell} \sigma \quad (3.23)$$

As regards the transformation of the remaining fields from the system to the model we can observe that the MVP is proportional to the flux density through a geometric operator (planar curl, see (3.9) or (3.10)) that is invariant when switching from the motor to the model, so the mapping condition for the potential modeling is analogous to the flux-density one:

$$A' = \frac{\ell}{\ell'} A \quad (3.24)$$

The source currents preservation is the basis of the model equivalence; the eddy currents are actually preserved as well, because considering (3.14), (3.23) and (3.24) it can be written:

$$J' = -\sigma' \dot{A}' = -\frac{\ell'}{\ell} \sigma \frac{\ell}{\ell'} \dot{A} = -\sigma \dot{A} = J \quad (3.25)$$

Finally, few considerations about the macroscopic and energetic quantities. The flux in the radial direction is preserved, as directly follows from (3.20):

$$\left. \begin{array}{l} \Phi' \propto B' \ell' \\ \Phi \propto B \ell \end{array} \right\} \longrightarrow \frac{\Phi'}{\Phi} = \frac{B' \ell'}{B \ell} = 1 \quad (3.26)$$

From (3.26) the preservation of voltages directly follows as well, whereas the preservation of current is the initial hypothesis; thus the impedances,

Table 3.1: Equivalence between motor and 2D-model quantities

Quantity	Motor	2D Model
GEOMETRIC QUANTITIES		
Axial length	$\ell = \kappa \ell'$	ℓ'
Cross-section area	S	$S' = S$
Volume	\mathcal{V}	$\mathcal{V}' = \mathcal{V}/\kappa$
Permeability	μ	$\mu' = \kappa\mu$
Resistivity	ρ	$\rho' = \kappa\rho$
Conductivity	σ	$\sigma' = \sigma/\kappa$
FIELD QUANTITIES		
Flux-density	B	$B' = \kappa B$
Magnetic field intensity	H	$H' = H$
Magnetic vector potential	A	$A' = \kappa A$
Current density	J	$J' = J$
Electric field	E	$E' = \kappa E$
MACROSCOPIC QUANTITIES		
Flux	Φ	$\Phi' = \Phi$
Flux linkage	Ψ	$\Psi' = \Psi$
Voltage	U	$U' = U$
Current	I	$I' = I$
Resistance	R	$R' = R$
Inductance	L	$L' = L$
ENERGETIC QUANTITIES		
Specific energy	w	$w' = \kappa w$
Total energy	W	$W' = W$
Specific loss	p	$p' = \kappa p$
Total loss	P	$P' = P$
Torque	T	$T' = T$

resistances and inductances are preserved too. The specific energy (energy-per-volume) is given by:

$$w' = \frac{1}{2} \mu' H'^2 = \frac{1}{2} \frac{\ell}{\ell'} \mu H^2 = \frac{\ell}{\ell'} w \quad (3.27)$$

and, therefore, since the volume is scaled as $\mathcal{V}' = \ell'/\ell \mathcal{V}$ the total energy is preserved. Similar relations are obtained as regards the specific power loss ($p = \rho J^2$), the total power and the torque.

All the notable motor-model equivalences are collected in table 3.1. The motor 2D model is defined according to the geometry correction provided in this table, considering the model "depth" equal to the air-gap length defined in (2.35). All the post-processed quantities are evaluated according to this length and to the relations in table 3.1.

As regards the rotor cage representation, since the bar only can be modeled in the FE geometry (see figure 3.1a) the bar material resistivity is corrected taking into account the contribution of the end-rings portions corre-

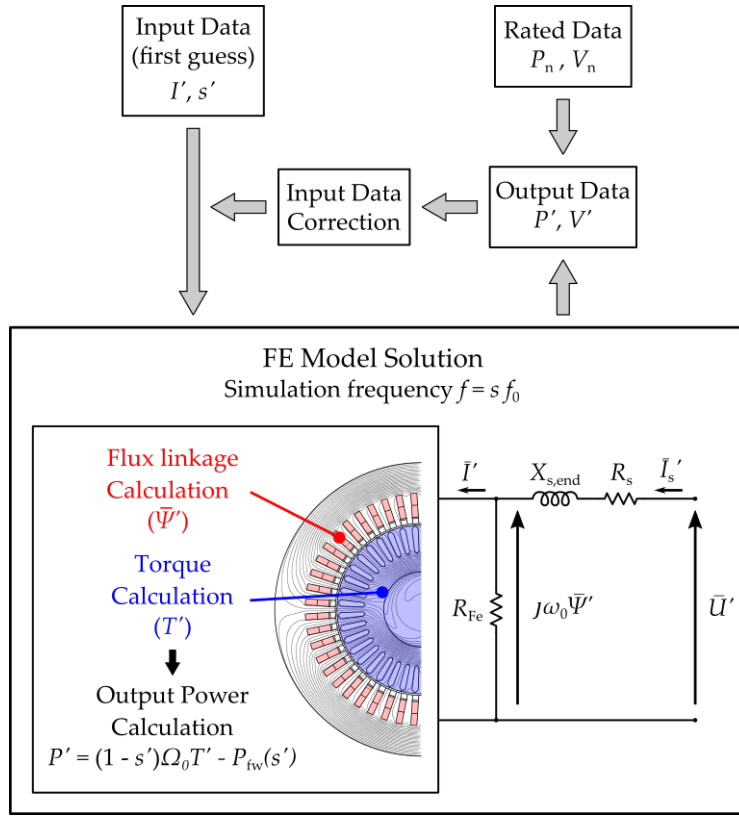


Figure 3.2: Schematic flow chart for the steady-state analysis of an induction motor through FEM, using a current-fed model

sponding to each bar as well. Considering the actual bar and ring resistance from (2.5) and (2.6) respectively the equivalence is expressed as:

$$\rho' \frac{\ell_{\text{gap}}}{S_{\text{bar}}} = \rho \left[\frac{\ell_{\text{bar}}}{S_{\text{bar}}} + \frac{\pi D_{\text{rng,avg}}}{2N_{\text{rsl}} S_{\text{rng}} \sin^2 \left(\frac{N_p}{N_{\text{rsl}}} \pi \right)} \right]$$

where ρ is the actual cage resistivity and ρ' its model equivalent, which is finally calculated as:

$$\rho' = \rho \left[\frac{\ell_{\text{bar}}}{\ell_{\text{gap}}} + \frac{\pi}{2N_{\text{rsl}} \sin^2 \left(\frac{N_p}{N_{\text{rsl}}} \pi \right)} \frac{D_{\text{rng,avg}} S_{\text{bar}}}{\ell_{\text{gap}} S_{\text{rng}}} \right] \quad (3.28)$$

3.1.3 Solution procedure for steady-state analysis

The computation procedure is represented by the flowchart in 3.2. It aims at determining the IM power factor during operation at rated voltage, power and frequency. For this purpose, an iterative process similar to that proposed in [17] is employed as described next.

The model is excited with a balanced three-phase current system of amplitude I' and frequency $f' = s' f_0$, being I' and s' first-guess values for rated current and rated slip respectively. From the TH-FE model solution the stator flux linkage complex phasor $\bar{\Psi}'$ and the electromagnetic torque T' are determined as follows:

- the phase flux linkage is obtained from the vector potential in the slots. In fact, from Kelvin-Stokes theorem [28] the flux of the field's curl through a surface is equal to the circulation of the field along the outer border of the surface:

$$\phi = \iint_{\Omega} \vec{B} \cdot d\vec{\sigma} \stackrel{(3.3a)}{=} \iint_{\Omega} \vec{\nabla} \times \vec{A} \cdot d\vec{\sigma} \stackrel{\text{KST}}{=} \oint_{\partial\Omega} \vec{A} \cdot d\vec{\ell} \quad (3.29)$$

For a 2D model the flux calculation is even simpler to calculate. Let us consider an elementary turn having the coilsides placed at points $C^+ = [r^+, \theta^+]$, $C^- = [r^-, \theta^-]$ in the cross-plane polar reference frame from figure 3.1a. Since the MVP is always normal to this plane and it is independent of the axial coordinate, then the line integral from (3.29) is computed just along the two coil-sides, giving:

$$\phi = [A(r^+, \theta^+) - A(r^-, \theta^-)] \ell \quad (3.30)$$

being ℓ the coil axial dimension. The flux linkage of a phase is calculated extending the calculation in (3.30) to every coilside belonging to that phase. It is assumed that the midpoints of a phase positive coilsides are placed in $[r_k^+, \theta_k^+]$, with $k = 1, 2, \dots, N_{\text{ssl}}/3$, whereas the negative ones are in $[r_k^-, \theta_k^-]$. If the model is reduced to $1/K_{\text{sym}}$ -th of the machine (like in figure 3.1, where $K_{\text{sym}} = 2$) then some of the points $[r_k^{\pm}, \theta_k^{\pm}]$ might be outside of the model domain, so such points must be ignored in that case. Taking into account the number of turns per coil and the number of parallel circuits per phase the total flux linkage is finally given:

$$\Psi' = \frac{K_{\text{sym}} N_{\text{tc}}}{N_{\text{pc}}} \sum_{k=1}^{N_{\text{ssl}}/3} [\bar{A}(r_k^+, \theta_k^+) - \bar{A}(r_k^-, \theta_k^-)] \ell_{\text{gap}} \quad (3.31)$$

- the torque is calculated applying the *Maxwell's stress tensor* [28], that gives the force per unit surface in air:

$$\vec{f} = \frac{1}{\mu_0} \left[(\vec{B} \cdot \vec{n}) \vec{B} - \frac{1}{2} \|\vec{B}\|^2 \vec{n} \right] \quad (3.32)$$

where \vec{n} is a unit vector normal to the surface. Integrating (3.32) on a cylindrical surface surrounding the rotor (having radius $r_0 = D_{\text{gap}}/2$) the electromagnetic torque is obtained:

$$T_{\text{em}} = \vec{e}_z \cdot \iint \vec{r} \times \vec{f} \cdot d\sigma = \frac{D_{\text{gap}}^2 \ell_{\text{gap}}}{4\mu_0} \int_0^{2\pi} B_r B_{\theta} d\theta \quad (3.33)$$

If the model is symmetry-reduced, (3.33) becomes:

$$T_{\text{em}} = K_{\text{sym}} \frac{D_{\text{gap}}^2 \ell_{\text{gap}}}{4\mu_0} \int_0^{2\pi/K_{\text{sym}}} B_r B_{\theta} d\theta \quad (3.34)$$

This expression is valid for the magnetostatic problems, when B_r and B_{θ} are real and time-independent. In dynamics, expression (3.34) should be applied to the instantaneous distribution of flux-density, obtaining

the instantaneous torque. However, taking advantage of the AC steady-state condition, the instantaneous torque components can be computed from the complex flux-density distribution. In fact, considering the trigonometric expression for the flux-density components, it can be written:

$$\begin{cases} B_r(t) = |\bar{B}_r| \cos(\omega t + \angle \bar{B}_r) \\ B_\theta(t) = |\bar{B}_\theta| \cos(\omega t + \angle \bar{B}_\theta) \end{cases}$$

so the instantaneous torque expression becomes:

$$T_{em}(t) = K_{sym} \frac{D_{gap}^2 \ell_{gap}}{4\mu_0} \int_0^{2\pi/K_{sym}} |\bar{B}_r| |\bar{B}_\theta| \cos(\omega t + \angle \bar{B}_r) \cos(\omega t + \angle \bar{B}_\theta) d\theta$$

and then, applying the prosthaphaeresis formulas [29]:

$$T_{em}(t) = K_{sym} \frac{D_{gap}^2 \ell_{gap}}{4\mu_0} \int_0^{2\pi/K_{sym}} \left[\frac{|\bar{B}_r| |\bar{B}_\theta|}{2} \cos(\angle \bar{B}_r - \angle \bar{B}_\theta) + \frac{|\bar{B}_r| |\bar{B}_\theta|}{2} \cos(2\omega t + \angle \bar{B}_r + \angle \bar{B}_\theta) \right] d\theta$$

Therefore the torque is composed of a static component (at zero frequency) and a fluctuating one, pulsating at double the model frequency, respectively given by:

$$T_{em,0} = K_{sym} \frac{D_{gap}^2 \ell_{gap}}{8\mu_0} \int_0^{2\pi/K_{sym}} \text{Re} \{ \bar{B}_r \bar{B}_\theta^* \} d\theta \quad (3.35a)$$

$$\bar{T}_{em,2\omega} = K_{sym} \frac{D_{gap}^2 \ell_{gap}}{8\mu_0} \int_0^{2\pi/K_{sym}} \bar{B}_r \bar{B}_\theta d\theta e^{j2\omega t} \quad (3.35b)$$

Since the steady-state operation is being investigated the torque from the FE model is the static one, i.e. $T' = T_{em,0}$.

The actual motor working point is deduced from the model quantities $\bar{\Psi}'$ and T' including the external effects not included in the FE model from figure 3.1:

1. the voltage drop on the phase resistance R_s and on the stator end-winding reactance $X_{s,end}$;
2. the core losses, dissipated on the equivalent resistance R_{Fe} ;
3. the mechanical losses at the working slip $P_{fw}(s')$

All these parameters are calculated according to what has been presented in chapter 2. The motor back-EMF is approximately given by the derivative of the flux-linkage from the FE model¹:

$$\bar{E}' = j\omega_0 \bar{\Psi}' \quad (3.36)$$

It is worth noticing that this expression considers the stator frequency, not the model one².

¹ In fact the proper motor back-EMF comes from the air-gap fundamental flux-linkage, whereas Ψ' from (3.31) also includes the slot and gap flux leakages.

² An explanation of this fact will be given in part ii

The total stator current is obtained from the model current $\bar{I}' = I'$ considering the active contribution for compensating core losses:

$$\bar{I}'_s = I' + \frac{\bar{E}'}{R_{\text{Fe}}(|\bar{E}'|)} \quad (3.37)$$

and finally the phase and line voltage are obtained:

$$\bar{U}' = \bar{E}' + (R_s + jX_{s,\text{end}})\bar{I}'_s \quad (3.38)$$

$$V' = \begin{cases} \sqrt{3}|\bar{U}'| & \text{if the stator is star-connected} \\ |\bar{U}'| & \text{if the stator is delta-connected} \end{cases} \quad (3.39)$$

The output power is obtained considering that the gap electromagnetic power $\Omega_0 T'$ is dissipated on the resistance R_r/s from circuit in 2.5:

$$\Omega_0 T' = 3 \frac{R_r}{s'} I_r'^2$$

and, according to (2.69):

$$P' = 3R_r \frac{1-s'}{s'} I_r'^2 - P_{\text{fw}}(s')$$

with $P_{\text{fw}}(s) = P_{\text{fw},0}(1-s)^3$. Combining these two expression it is finally obtained:

$$P' = (1-s')\Omega_0 T' - P_{\text{fw}}(s') \quad (3.40)$$

The output data estimated from (3.39) and (3.40) are compared to the IM rated voltage and power. If the difference is larger than a suitable tolerance, the excitation current I' and the slip s' of the FE model are adjusted using a quasi-Newton algorithm [30]. The problem of determining the rated working point of the IM is reduced to the solution of a non-linear vector equation:

$$\begin{vmatrix} P'_{\text{out}}(I', s') \\ V'(I', s') \end{vmatrix} = \begin{vmatrix} P_n \\ V_n \end{vmatrix}$$

Letting I'_k , s'_k , P'_k and V'_k the current, the slip, the output power and the line voltage for the k -th solution of the FE model then, assuming:

$$\mathbf{x}_k = \begin{vmatrix} I'_k \\ s'_k \end{vmatrix} \quad \mathbf{y}_k = \begin{vmatrix} P'_k \\ V'_k \end{vmatrix} \quad \mathbf{y}_n = \begin{vmatrix} P_n \\ V_n \end{vmatrix}$$

then the next model excitation is given by:

$$\mathbf{x}_{k+1} = \mathbf{x}_k - \mathbf{J}_k^{-1}(\mathbf{y}_k - \mathbf{y}_n)$$

where \mathbf{J}_k^{-1} is the jacobian matrix at the k -th iteration, given by:

$$\mathbf{J}_k^{-1} = \begin{bmatrix} \frac{\partial P'}{\partial I'}(\mathbf{x}_k) & \frac{\partial P'}{\partial s'}(\mathbf{x}_k) \\ \frac{\partial V'}{\partial I'}(\mathbf{x}_k) & \frac{\partial V'}{\partial s'}(\mathbf{x}_k) \end{bmatrix}^{-1}$$

The jacobian matrix must be evaluated numerically, assuming a slight variation of each of the FEM inputs separately and calculating the corresponding

output and variations rate. The reference in [30] allows to update the jacobian matrix from the previously solved steps:

$$\mathbf{J}_k^{-1} = \mathbf{J}_{k-1}^{-1} + \frac{\delta \mathbf{x}_k - \mathbf{J}_{k-1}^{-1} \delta \mathbf{y}_k}{\delta \mathbf{x}_k^T \mathbf{J}_{k-1}^{-1} \delta \mathbf{y}_k} \delta \mathbf{x}_k^T \mathbf{J}_{k-1}^{-1}$$

with $\delta \mathbf{x}_k = \mathbf{x}_k - \mathbf{x}_{k-1}$ and $\delta \mathbf{y}_k = \mathbf{y}_k - \mathbf{y}_{k-1}$.

The FE model excitations are updated using this method and the calculation procedure is repeated. The iteration loop ends when the percent error between rated and estimated power and voltage values is below the chosen threshold. The IM power factor at rated conditions is finally computed as:

$$\cos \varphi' = \cos(\angle \bar{U}' - \angle \bar{I}'_s) \quad (3.41)$$

3.2 IMPROVED EQUIVALENT CIRCUIT METHOD

The computation procedure described in section 3.1.3, even if faster than a time-stepping FE simulation, suffers from a relatively poor computational performance because it implies solving time-consuming non-linear TH-FEAs of a complete model. Instead, the new proposed approach to the problem, presented in this section, employs a reduced IM 2D model, which will be shown to yield remarkable savings in terms of computation time without significant loss of accuracy. The general procedure is firstly described in 3.2.1 and an insight on the reduced model is given in 3.2.2.

3.2.1 Overall procedure description

The proposed procedure is illustrated in figure 3.3. As in sections 2.5 and 3.1, the objective is to determine the IM working point (and, in particular, the power factor) in rated conditions, i.e. with voltage V_n , frequency f_0 and output power P_n , considering shaft eddy-current effects as well.

As a starting point, it is assumed that the IM operates with a first-guess flux per pole Φ and slip s . From the flux-per pole the first-guess value of the back-EMF and the maximum air-gap flux-density are also determined, accordingly to (2.50), (2.51) and (2.52). The MMF drop across the contour MPQ shown in figure 3.4 is analytically estimated, as presented in section 2.4.1. It can be noticed how the contour MPQ crosses half of the stator yoke, the stator and rotor teeth and the air-gap, so it is simply given by:

$$F_{\text{mag},0} = \int_{\text{MPQ}} \vec{H} \cdot d\vec{\ell} = F_0(B_{g,\text{max}|\Phi}) + F_{\text{sy}}(B_{g,\text{max}|\Phi}) \quad (3.42)$$

where $B_{g,\text{max}|\Phi}$ is the maximum air-gap flux-density corresponding to the flux per pole Φ . It is assumed that the MMF drop from (3.42) is the same in both no-load and full-load conditions. This is a reasonable hypothesis because the shaft eddy currents arising at full load produce a flux density increase in the rotor yoke but do not significantly alter the flux density (and hence the magnetic field H) in the other IM cross-section regions, as can be seen in figure 1.2.

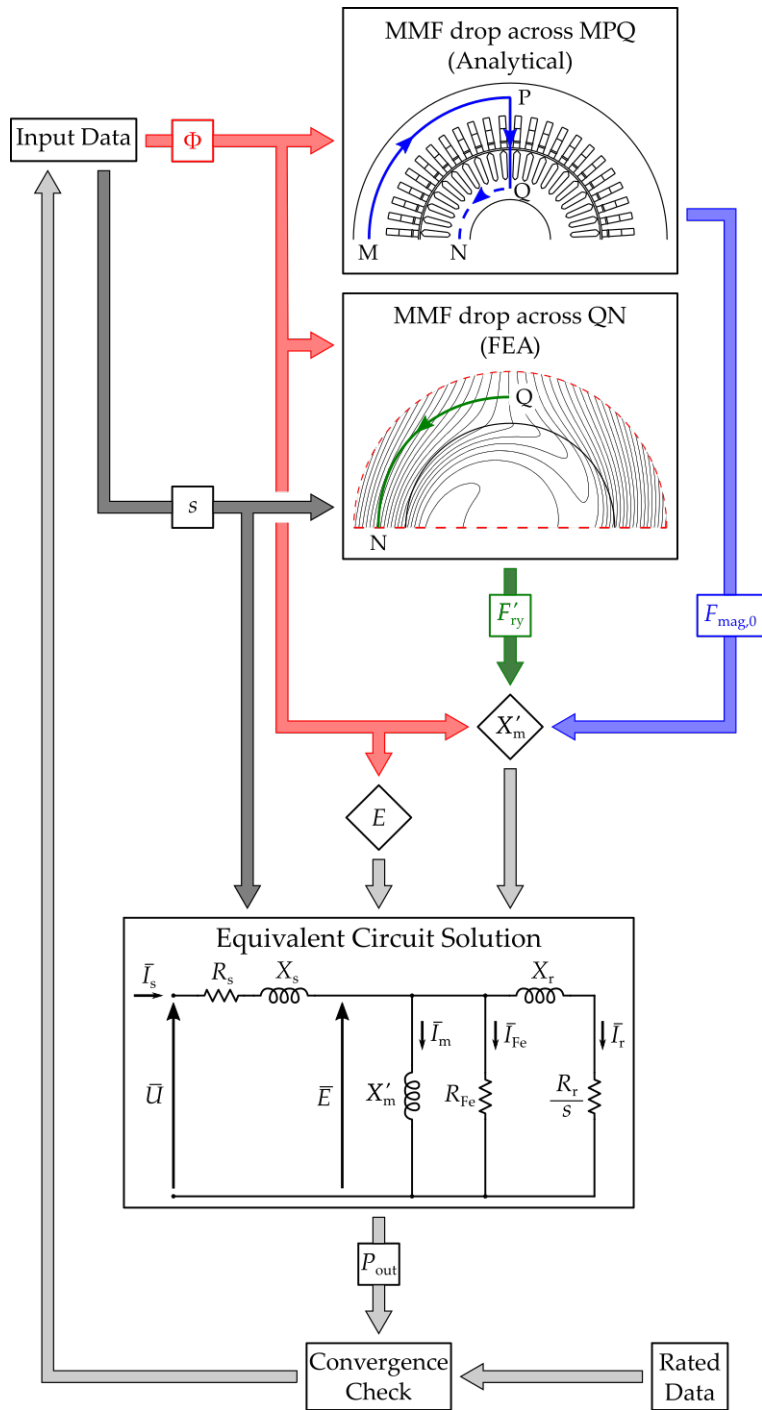


Figure 3.3: Schematic flow chart for the steady-state analysis of an induction motor through an improved equivalent circuit method. The FEM is limited to a reduced model for the calculation of the on-load magnetizing reactance

What varies with rotor slip s (hence from no-load to loaded conditions) is, instead, the MMF drop across the arc QN placed inside the rotor yoke (figure 3.4). In fact it has to be borne in mind that the MMF drop from (2.49) is obtained in no-load conditions, i.e. ignoring the shaft flux rejection due to shaft eddy currents. For an accurate and sufficiently fast computation of the correct value of this MMF drop, it is herein proposed to perform a time-harmonic FE simulation of the very simple semi-circular model shown in figure 3.4 in order to reproduce the behavior of the rotor yoke and shaft in full load conditions (rated slip). The details on how such reduced model is built and solved will be separately provided in section 3.2.2 for the sake of clarity.

After the rotor yoke MMF drop F'_{ry} and the no-load drop $F_{mag,0}$ are calculated, it is possible to estimate the IM full-load magnetizing current I'_m and, from it, the full-load magnetizing reactance X'_m , accordingly to (2.55) and (2.56):

$$I'_m = \frac{\pi}{6\sqrt{2}} \frac{N_p}{k_w N_{tph}} (F_{mag,0} + F'_{ry}) \quad (3.43)$$

$$X'_m = \frac{6}{\pi} \omega_0 k_w^2 N_{tph}^2 \frac{\Phi}{N_p (F_{mag,0} + F'_{ry})} \quad (3.44)$$

The value of magnetizing reactance obtained from (3.44) is inserted into the equivalent circuit from figure 2.5 in place of the reactance from (2.56); the remaining circuit parameters are the same as presented in chapter 2. The circuit is solved as presented in section 2.5 and the output power is determined. The latter is compared with the rated one (and the actual flux per pole from circuit solution is compared with the first-guess value); if the difference is above the chosen tolerance threshold the input data is adjusted and the whole method is repeated until the convergence is obtained. The PF is finally calculated accordingly to (2.76).

3.2.2 Reduced model for induction motor analysis

This section describes the definition of the reduced model which needs to be solved by TH-FEM at any iteration of the procedure described in section 3.2.1. The model is shown in bottom of figure 3.4. The reduced model is obtained from the complete model shown in figure 3.1a, limiting the geometric dominion to:

$$(r, \theta) \in [0, r_{max}] \times [0, \pi]$$

with r_{max} the rotor yoke outer radius, given by:

$$r_{max} = \frac{D_{r,inn}}{2} + h_{r,yk} \quad (3.45)$$

The same considerations made for the standard model in section 3.1.2 are valid for the simplified model. The model frequency is the slip frequency $s f_0$, with s the slip being investigated in the procedure illustrated in figure 3.3. As regards the boundaries, the anti-periodic condition is still valid for the radial axis:

$$\bar{A}(r, 0) = -\bar{A}(r, \pi) \quad \forall r \in [0, r_{max}]$$

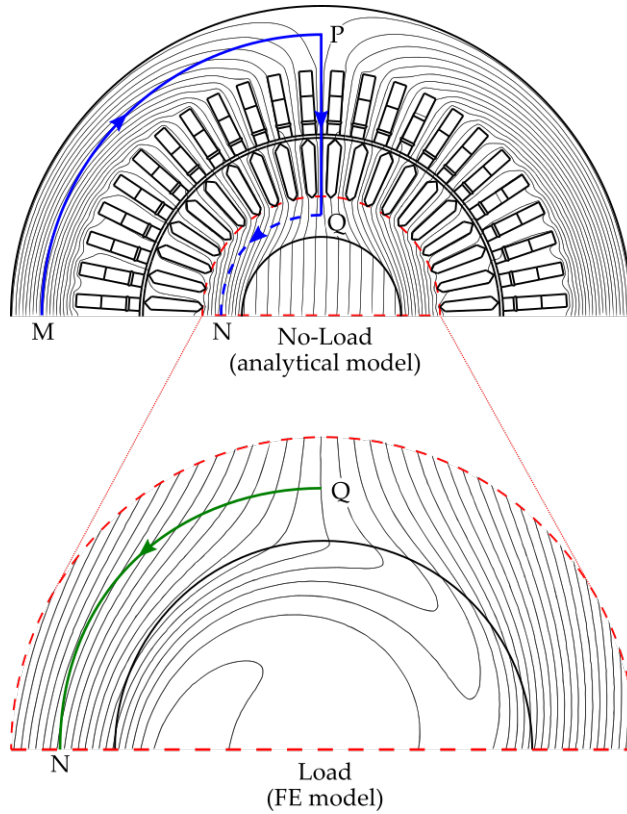


Figure 3.4: Reduced FE model for on-load MMF drop computation. This model is obtained by extracting a sub-domain from the complete FE model in figure 3.1, limited to the shaft and the rotor yoke

whereas a suitable condition involving vector potential must be defined on the outer radius.

In fact, since this model does not have any source of field defined inside it, the condition on outer radius must provide the model excitation, representing the effects of the field source that are located outside of this model, i.e. the air-gap flux-density distribution. The hypothesis is made that the fundamental flux-density (and hence the vector potential) has a sinusoidal spatial distribution along the outer radius (see fig. 3.5), thus it can be written (see also (B.26) in appendix B):

$$A(r_{\max}, \theta, t) = A_{\max} \cos(N_{\text{pp}}\theta - s\omega_0 t) = \text{Re} \left\{ A_{\max} e^{j(N_{\text{pp}}\theta - s\omega_0 t)} \right\}$$

or, using the phasor notation:

$$\bar{A}(r_{\max}, \theta) = A_{\max} e^{jN_{\text{pp}}\theta} \quad \forall \theta \in [0, \pi] \quad (3.46)$$

It is worth noticing that in these expressions the number of pole-pairs have been introduced, to take into account the fact that θ is a mechanical angle, whereas expressions like (B.26) have been so far written for electric angles only. However, in the particular case of a two-pole motor, this detail is purely formal, since $N_{\text{pp}} = 1$.

The constant A_{\max} in (3.46) is determined observing that the flux per pole along the mean air-gap circumference is the same as the flux per pole enter-

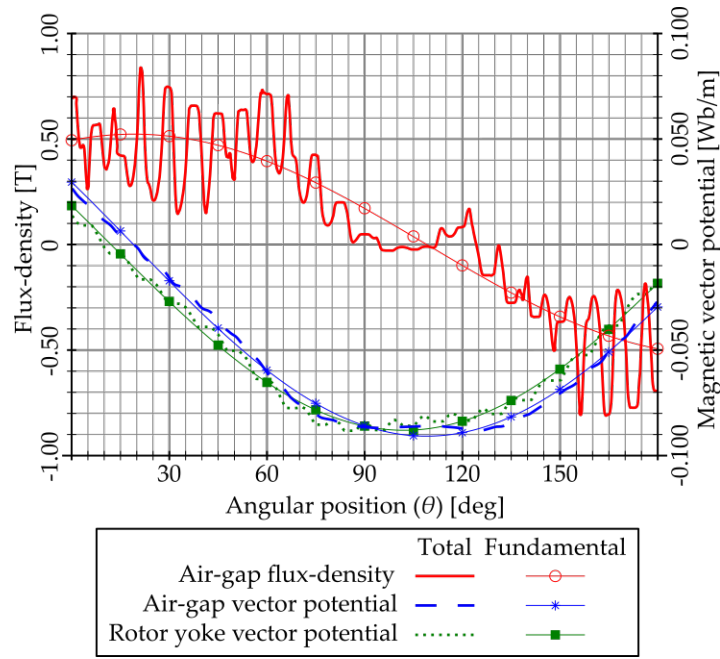


Figure 3.5: Plots of the air-gap flux-density and MVP obtained from FE solution of figure 3.1. It can be noticed how the potential along the yoke mean line is almost the same of air-gap mean line

ing the rotor yoke across the model outer radius. Thanks to relation in (3.30) we can write:

$$\Phi = [\bar{A}(r_{\max}, \pi) - \bar{A}(r_{\max}, 0)]\ell_{\text{gap}} = -2A_{\max}\ell_{\text{gap}} \quad (3.47)$$

This relation is valid in the 2D model (and so is (3.46)), because the model (air-gap) length is used as axial length (see also table 3.1). Hence, solving (3.47) the condition in (3.46) becomes:

$$\bar{A}(r_{\max}, \theta) = -\frac{\Phi}{2\ell_{\text{gap}}}e^{jN_{\text{pp}}\theta} \quad \forall \theta \in [0, \pi] \quad (3.48)$$

Once boundary conditions are set based on the estimated value of the flux per pole Φ , the model is solved through a time-harmonic FEA at the estimated slip frequency sf_0 . From the solution the rotor yoke on-load MMF-drop is calculated (see figure 3.4):

$$F'_{\text{ry}} = \int_Q^N \vec{H} \cdot d\vec{\ell} \quad (3.49)$$

and used to calculate the on-load magnetizing reactance in (3.44).

4

METHODS COMPARISON

In the previous chapters three methods to deal with the problem of evaluating the on-load performance in two pole motors have been presented:

1. the "Classic" Equivalent Circuit Method (C-ECM), which is an analytical method (chapter 2);
2. the Finite-Element Method (FEM), which is a numerical method (section 3.1);
3. the "Improved" Equivalent Circuit Method (I-ECM), which is a hybrid of the two previous methods (section 3.2)

In order to assess the validity of the I-ECM and compare it with the standard methods a set of real medium-voltage IMs is considered and the three calculations methods are applied (section 4.1) and the results are examined and commented (section 4.2)

4.1 REAL-MOTORS PERFORMANCE CALCULATION

In order to assess the validity of the proposed calculation method a set of built and tested medium-voltage two-pole induction motors of different sizes is considered. Their ratings and some characteristic dimensions are given in table 4.1.

All motors are for S1 service [6] and have insulation class F [31]. They have all undergone a full factory test according to [32]. Load tests have been conducted at rated load, except for motor M6, which has been tested at 75% of its rated load.

The full-load performance for all the IMs in table 4.1 is also computed with the three calculations methods presented in the previous chapters; for

Table 4.1: Sample IMs for experimental validation

Machine label		M1	M2	M3	M4	M5	M6	M7
Shaft height	[mm]	315	355	400	450	500	630	710
Rated power	[kW]	250	450	360	1150	1560	2980	2550
Rated voltage	[V]	4000	4000	6600	4000	4000	4000	11000
Rated current	[A]	42	75	37	187	257	485	154
Rated frequency	[Hz]	60	60	50	60	60	60	50
Rated PF	[-]	0.883	0.892	0.882	0.902	0.899	0.899	0.885
Total mass	[kg]	1700	2400	3500	5000	6900	9400	12500
Core length	[mm]	420	420	420	600	600	950	950
Outer diameter	[mm]	546	620	700	780	865	970	1080

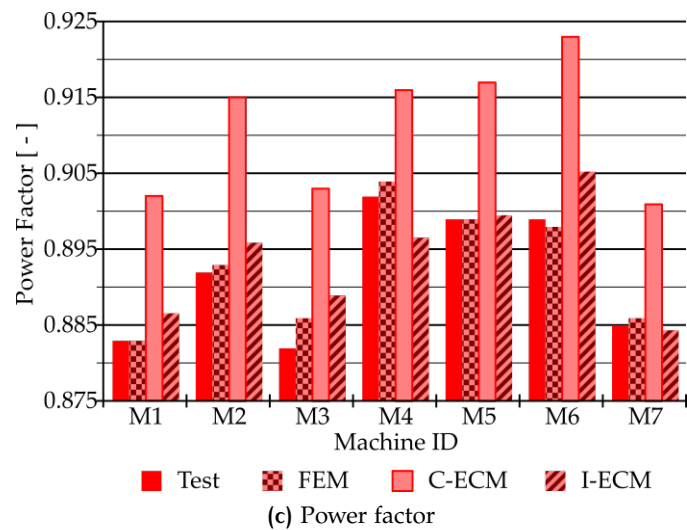
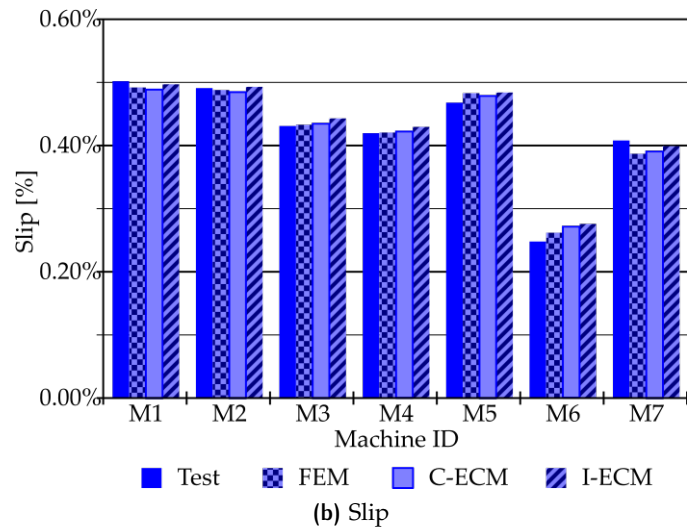
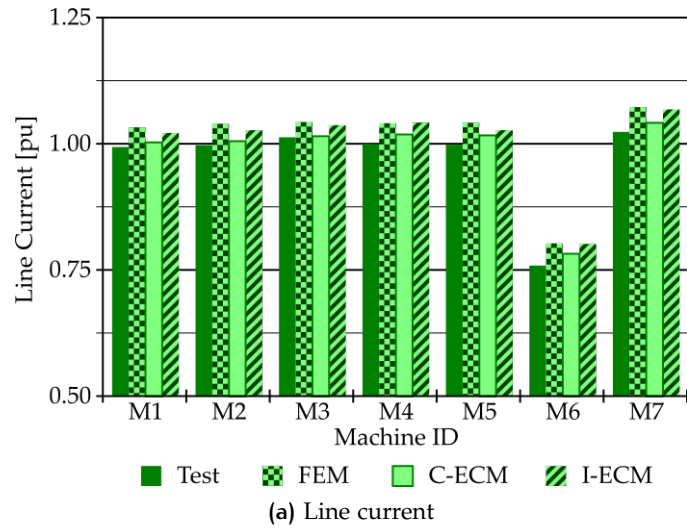


Figure 4.1: Experimental and calculated data for two-pole IMs

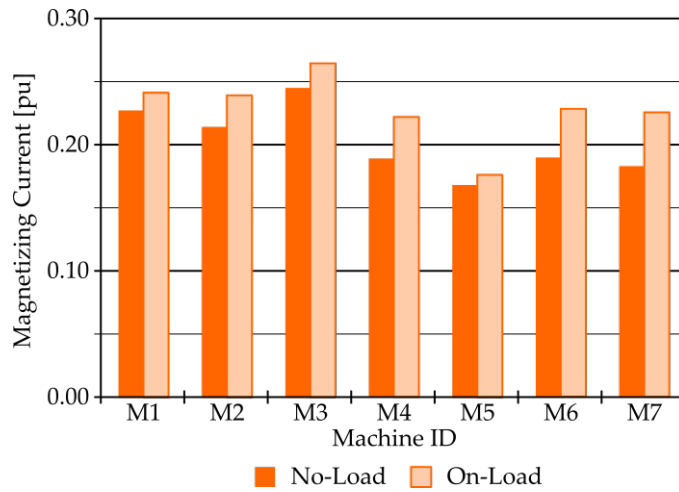


Figure 4.2: Magnetizing current from no-load test and from on-load improved equivalent circuit

Table 4.2: Power factor estimation errors for the motors in table 4.1

Machine	Tolerance	FEM	C-ECM	I-ECM
M1	2.21%	0.00%	2.15%	0.41%
M2	2.02%	0.11%	2.58%	0.44%
M3	2.23%	0.45%	2.38%	0.77%
M4	1.81%	0.22%	1.55%	0.60%
M5	1.87%	0.00%	1.11%	0.06%
M6	1.87%	0.11%	3.34%	0.70%
M7	2.17%	0.45%	2.37%	0.07%

every machine power factor, line current and slip are predicted through the three methods. Test and calculation results for the various quantities are shown in figure 4.1.

Figure 4.2 shows the comparison from the no-load current (obtained from factory no-load test) and the full load magnetizing current calculated accordingly to (3.43).

4.2 DISCUSSION

It can be noticed how the three calculation methods being compared in figure 4.1 are generally equivalent and in good accordance with experimental data as far as the line current and slip prediction is concerned. Conversely, the power factor value obtained with the C-ECM appears much higher than that estimated using FEM and I-ECM (see fig. 4.1c). The results obtained with FEM and I-ECM are in good accordance between them and with measurements as far as the power factor prediction is concerned. It is therefore confirmed that conventional analytical calculation techniques may lead to significant errors in the estimation of two-pole IMs equipped with solid-steel shaft, as pointed out in chapter 1.

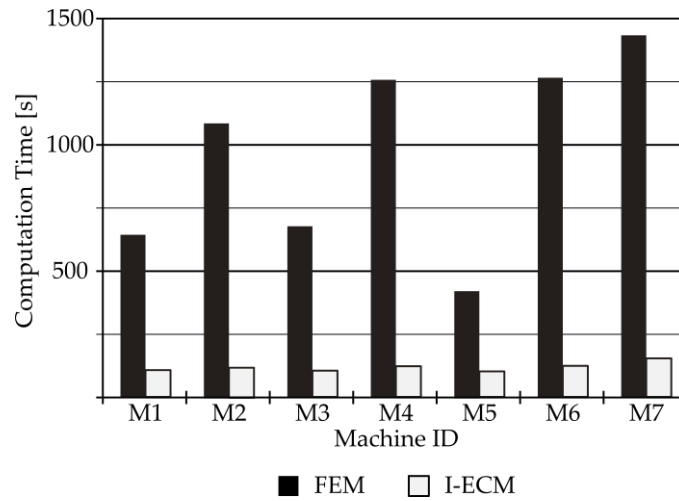


Figure 4.3: Computation time requested by FEM and I-ECM to evaluate the correct on-load working point for the motors in table 4.1

Table 4.3: Computational statistics

Machine label	FEM		I-ECM	
	Nodes	Iterations	Nodes	Iterations
M1	27 134	3	4183	1
M2	36 634	4	4165	2
M3	33 668	4	4208	1
M4	51 483	5	4161	2
M5	53 352	3	4174	2
M6	68 662	4	4176	3
M7	81 729	4	4183	1
Average	50 380	4	4179	2

In order to have a clearer assessment of the accuracy of the three compared methods, the percent errors in the prediction of the full-load power factor with respect to measurements are provided in table 4.2. This table also shows the tolerance, intended as the maximum error allowed in accordance to the IEC standard [6], calculated from the motor rated PF:

$$\varepsilon_{\%} < \frac{1}{6} \frac{1 - \cos \varphi_n}{\cos \varphi_n} \cdot 100 [\%] \quad (4.1)$$

It can be noticed that, for each of the sample motors taken into account in table 4.1, the C-ECM overestimates the power factor with an error which exceeds the IEC tolerance provided by (4.1) or, even if the error is within the tolerance, it is significantly larger than those affecting the other two computation methods.

Finally, figure 4.3 shows the total computation time for FEM and the I-ECM in order to provide a quantitative assessment of the computational benefit resulting from the use of a reduced IM model (as in section 3.2.2) instead of the complete one (from section 3.1). All calculations are performed on the same workstation equipped with an Intel Core™ i5-3470@3.20 GHz

processor and 16 GiB RAM, using a single-thread user-defined routine in Matlab™.

Table 4.3 reports other calculation statistics, i.e. the number of nodes of the 2D FE models (respectively complete and reduced) employed by the FEM and I-ECM for the various IMs from table 4.1, as well as the number of iterations required by the two methods to converge. In this regard, it is highlighted that, both for the FEM and the I-ECM, the iterative procedure starts with initial guess values (of the current, slip and flux per pole according to figures 3.2 and 3.3) obtained analytically by solution of the conventional equivalent circuit in figure 2.5. It is clear from figure 4.3 and table 4.3 that the I-ECM is much preferable to the FEM from a computational point of view, because it leads to the same level of accuracy (table 4.2) with an average 90 % saving in terms of computation time. Such feature makes the proposed improved equivalent circuit method more suitable than the FEM for being incorporated in genetic optimization programs for two-pole IM design optimization [16], where hundreds or thousands of iterations may be requested to identify optimal design solutions.

With respect to purely analytical algorithms [14, 15] the method suffers from the drawback of requiring a time-harmonic 2D FEA, but this is applied to a very simple reduced motor model which can be built, solved and processed very quickly and in a fully-automated way. The convenience of solving such reduced FE model is explained by two main reasons. Firstly, it makes the procedure suitable for including the effect of axial cooling vents in the rotor core [13], by simply adding them in the reduced FE model from figure 3.4. Secondly, it makes it possible to cope with the strongly non-uniform distribution of the magnetic-flux and eddy-current fields in the shaft and rotor yoke regions, as it has been shown in fig. 1.6. It is clear that the strongly non-uniform distribution of the magnetic field, flux density, magnetic permeability and eddy currents in the rotor core and solid-steel shaft is such that it would be extremely difficult to identify average or equivalent values for the mentioned quantities without a FEA (at least limited to the yoke and shaft domains as proposed in section 3.2).

Part II

STARTING PERFORMANCE OF DOL SYNCHRONOUS MOTORS

Oil&Gas industries adopt high-voltage electric motors with power ratings from few hundreds of kW up to 50 MW [33] and more to drive pumps and compressors in pipelines, refineries and processing systems. Wound field SMs have been increasingly used because of their sudden overload capability and higher power factor [34]. The main disadvantage of this kind of machines in their traditional form is that they are unable to start autonomously, i.e. they require a suitable starting system to reach the synchronous speed [35, 36].

One possibility for synchronous motor startup is to feed it through a variable-frequency converter [37], so as to control its speed and current. However, if the motor is designed to operate DOL at a fixed frequency, the converter would be needed only for start-up and this would decrease the overall drive system competitiveness. The use of a small-size converter for no-load starting may be a good compromise, but it still has the drawback of requiring a complex mechanical system for motor-load coupling; furthermore, it leads to a decreased reliability due to the presence of the static converter [38].

For these reasons several applications require synchronous motors with DOL-starting capability. A simple way to fulfill this requirement is using solid-rotor synchronous motors; in fact, the eddy currents that arise in the rotor core when the motor speed is lower than the synchronous speed provide a considerable starting torque, limiting the over-heating problems which would occur if a damper cage was used for start-up [39]. Furthermore, the solid rotor is mechanically stronger than a laminated one and, therefore, it has less vibrational and roto-dynamics issues.

The use of a solid rotor introduces a complexity in the machine modeling and design. Many approaches have been proposed in the literature to deal with this problem, some with analytical procedure [40–42] and other relying on numerical simulations [43–46]. Analytical methods are easy to implement but they often include semi-empirical formulas or suffer from strong simplifications (for example, iron saturation is frequently neglected). On the other hand, numerical methods are generally based on FEM and can well describe the machine behavior, but they suffer from high computational cost [47].

In this part the problem of starting performance prediction for a large synchronous motor with solid rotor is addressed. The general features of DOL SMs are firstly presented (chapter 5) and the theoretical background, focused on the starting up, is given (chapter 6). The motor is described through the two-axis equivalent circuit model, and its parameters are determined by means of a suitable set of time-harmonic FEAs performed on a simplified model (chapter 7), taking into account the frequency-dependent variability of the rotor field winding resistance as well. The calculated parameters are finally used to compute the machine current, average torque and pulsating torque as functions of the speed (chapter 8). The results are compared with experimental data collected during the machine acceptance test.

5

SYNCHRONOUS MOTORS WITH SOLID ROTOR

The general features of a synchronous motor with solid salient poles are presented in this chapter. The solid rotor gives mechanical strength against centrifugal force and realizes the DOL self-starting capability. Its main geometrical features are presented in section 5.1, limited to the rotor, since the stator is identical to the IMs one, presented in chapter 2.

The solid core is suitable for motor DOL starting because the eddy-currents that arise in the solid parts of the rotor interact with the armature rotating field and create a synchronizing torque that accelerates the rotor allowing for the asynchronous starting of the machine. However, because of the slotting effect, rotor eddy-currents may arise in the synchronous operation too, but in this case their effect is detrimental in terms of efficiency and overheating [48, 49]. Thus, to limit eddy currents at steady-state, rotor surface is circumferentially grooved [50]. Section 5.2 presents an experimental investigation on the impact of different groove geometry on losses and magnetizing current.

5.1 SYNCHRONOUS MOTOR ROTOR GEOMETRY

Figure 5.1 shows the main geometric characteristic of a synchronous machine rotor with salient poles. These kind of motors are usually adopted for machines with more than two poles. The solid rotor consists of a properly shaped forged shaft on which the solid pole shoes are bolted by means of screws (see also fig. 5.2). The field winding coils are directly wound around the pole body. They are usually built with a single elementary conductor per turn and, possibly, they have several adjacent layers of stacked conductors. The main geometric quantities that characterize a salient-pole solid rotor are collected in table 5.1. The stator data is identical to that of an induction machine (table 2.1).

Because of the pole-shoe curvature, the air-gap is not uniform, neither between direct (polar) and quadrature (inter-polar) axes, nor in the region in correspondance of the pole shoe. More in detail, the gap in the pole-shoe region varies accordingly to the following law, valid for $\theta \in [-\alpha_{ps}, \alpha_{ps}]$:

$$g(\theta) = D_{s,inn}/2 - \left[\delta_{ps} \cos(\theta) + \sqrt{r_{ps}^2 - \delta_{ps}^2 \sin^2(\theta)} \right] \quad (5.1)$$

The geometric justification of (5.1) is given in figure 5.3. The maximum and average gap are respectively given by:

$$g_{max} = g(\alpha_{ps}) = \frac{D_{s,inn}}{2} - \frac{1}{2} \sqrt{w_{ps} + [D_{r,out} - 2(h_{ps} - h'_{ps})]} \quad (5.2)$$

$$g_{avg} = \frac{1}{\alpha_{ps}} \int_0^{\alpha_{ps}} g(\theta) d\theta \quad (5.3)$$

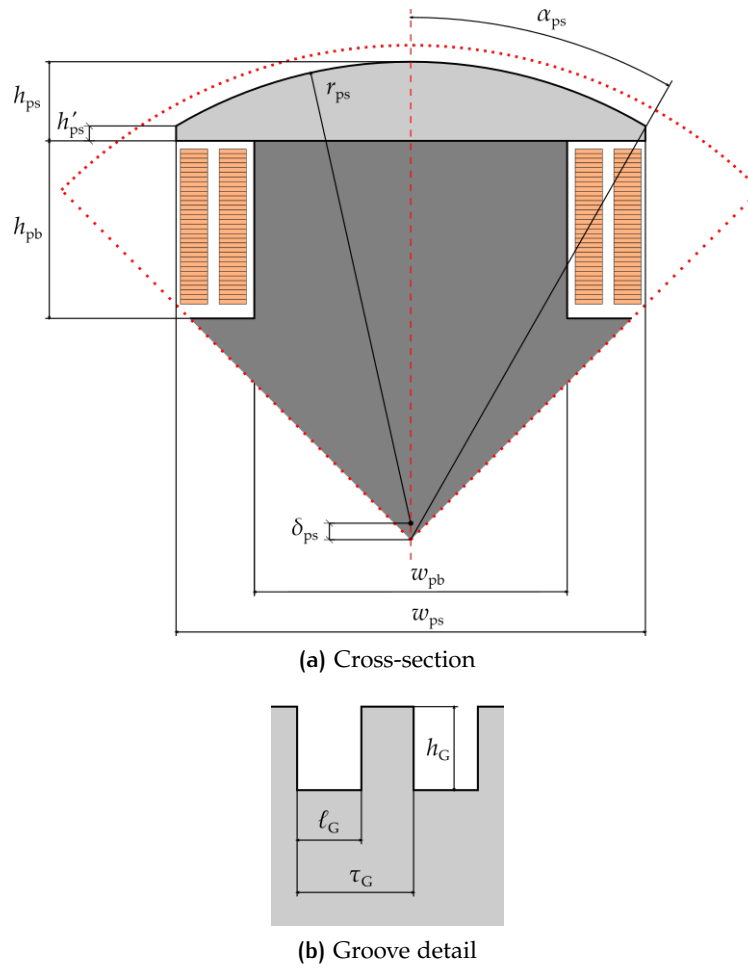


Figure 5.1: Rotor geometric sketch of a salient-pole synchronous motor



Figure 5.2: Example of manufactured salient-pole solid rotor (courtesy of Nidec-ASI, Monfalcone, Italy)

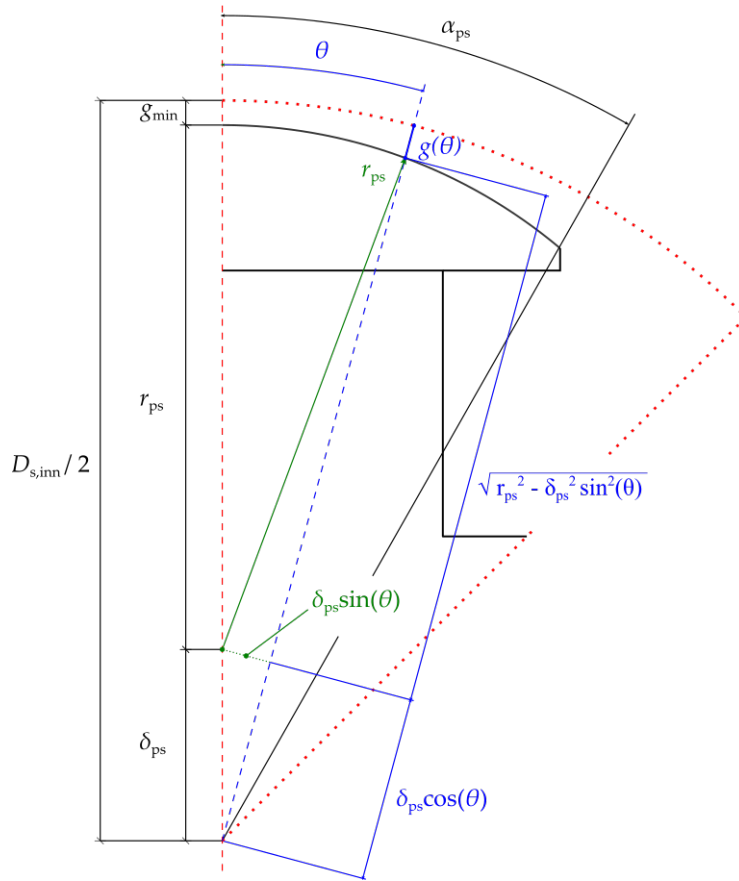


Figure 5.3: Air-gap variation for a salient-pole rotor

whereas the air-gap under the inter-pole axis is:

$$g_q = g_{\min} + h_{ps} + h_{pb} \quad (5.4)$$

The average gap in (5.3) is adopted to compute the equivalent core length according to (2.35).

Table 5.1: Salient-pole rotor characteristic data

Quantity	Symbol	Notes
GENERAL DATA		
Rotor core axial length	$\ell_{r,\text{tot}}$	
Rotor outer diameter	$D_{r,\text{out}}$	
Rotor diameter at pole base	$D_{r,\text{base}}$	1
Minimum air-gap length	g_{\min}	2
Average gap diameter	D_{gap}	3

(continued)

1 $D_{r,\text{base}} = D_{r,\text{out}} - 2(h_{ps} + h_{pb})$

2 $g_{\min} = (D_{s,\text{inn}} - D_{r,\text{out}})/2$

3 $D_{\text{gap}} = D_{s,\text{inn}} - g_{\min}$

<i>(continued)</i>		
Average pole pitch	τ_p	4
POLE DATA		
Pole shoe curvature radius	r_{ps}	
Pole shoe center offset	δ_{ps}	5
Pole shoe width	w_{ps}	
Pole shoe angular half width	α_{ps}	6
Pole shoe to pole pitch ratio	γ_{ps}	7
Pole shoe total height	h_{ps}	
Pole shoe side height	h'_{ps}	8
Pole body width	w_{pb}	
Pole body height	h_{pb}	
Pole pitch at pole base	τ'_p	9
FIELD WINDING DATA		
Elementary wire width	w_{rew}	
Elementary wire thickness	h_{rew}	
Elementary wire cross-section area	S_{rew}	
Number of elementary wires per turn	N_{rew}	
Number of overlaid turns per coil (pole)	$N_{rtc,h}$	
Number of adjacent layers per coil (pole)	$N_{rtc,w}$	
Number of turns per pole	N_{rtc}	10
Average turn length	ℓ_{rtu}	
Turn cross section area	S_{rtu}	11
Inter-turn insulation thickness	$b_{ins,rtu}$	
Pole-to-winding radial distance	d_{pwr}	
Pole-to-winding tangential distance	d_{pwt}	
Inter-layer tangential distance	d_{wwt}	
GROOVING DATA		
Number of grooves	N_G	
<i>(continued)</i>		

$$4 \quad \tau_p = \pi D_{gap} / N_p$$

$$5 \quad \delta_{ps} = D_{r,out} / 2 - r_{ps}$$

$$6 \quad \alpha_{ps} = \arcsin(0.5w_{ps} / r_{ps})$$

$$7 \quad \gamma_{ps} = 2r_{ps}\alpha_{ps} / \tau_p$$

$$8 \quad h'_{ps} = h_{ps} - r_{ps} [1 - \sqrt{1 - 0.25(w_{ps} / r_{ps})^2}]$$

$$9 \quad \tau'_p = \pi(D_{r,out} - 2h_{ps} - 2h_{pb}) / N_p$$

$$10 \quad N_{tr} = N_{tr,w} N_{tr,h} - 1$$

$$11 \quad S_{rtu} = N_{rew} S_{rew}$$

<i>(continued)</i>	
Groove axial pitch	τ_G
Groove depth	h_G
Groove width	l_G

5.2 EXPERIMENTAL STUDY OF ROTOR-GROOVE IMPACT

5.2.1 Testing procedure description

The impact of a given groove geometry can be experimentally assessed by means of the testing apparatus shown in figure 5.4. The testing apparatus is composed of three electric machines mechanically coupled into the same shaftline (fig. 5.4a):

1. the prime mover is a variable-speed driven induction motor;
2. the second machine is a two-pole wound rotor synchronous generator (SG), excited by an independent DC power source;
3. the final machine is the same testing prototype adopted in section 1.2 to study the on-load magnetizing current. The stator is the same of the prototype as in section 1.2, whose data are collected in table 1.1, whereas three different types of rotor are mounted, in order to perform different tests (fig 5.4b):
 - a solid smooth rotor;
 - a solid grooved rotor;
 - a laminated rotor;

The prototype is designed so that the rotor can be withdrawn and changed, allowing to identify the system losses, as explained in the following.

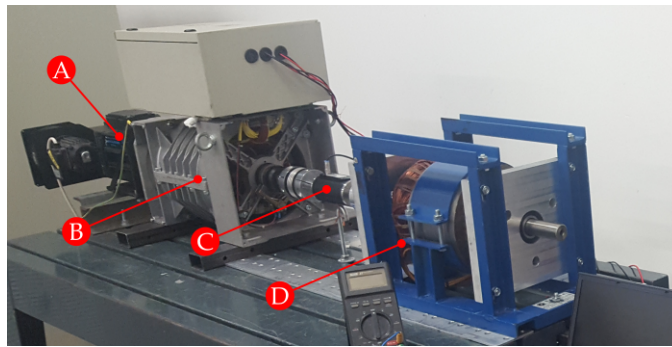
The prototype under test is electrically fed by the SG, so the stator field and the rotor are perfectly synchronous. As a result the prototype absorbs, from both the stator winding and the mechanical shaft, an amount of power that compensates for the losses of the prototype itself, i.e.:

$$P_{\text{mech,in}} + P_{\text{elt,in}} = P_{\text{loss,tot}} \quad (5.5)$$

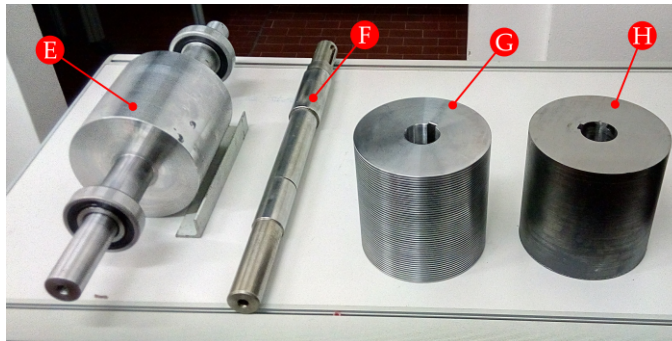
The electrical input power $P_{\text{elt,in}}$ is measured through a digital wattmeter (not shown in fig. 5.4), whereas the mechanical power $P_{\text{mech,in}}$ is obtained through a torque sensor placed between the SG and the testing prototype. Naturally, given the torque measurement \hat{T} and the system speed Ω then the mechanical power is simply $P_{\text{mech,in}} = \Omega\hat{T}$.

When the test is carried out on a solid rotor the following losses are dissipated inside the prototype:

- stator winding joule loss;



(a) Assembled test bench – A) Prime mover (VFD) B) Synchronous generator C) Torque sensor D) Testing prototype



(b) Rotor set – E) Smooth solid rotor F) Shaft G) Grooved solid rotor H) Laminated rotor

Figure 5.4: Experimental set for the investigation of rotor grooving impact

- stator core hysteresis and eddy current loss;
- mechanical loss;
- rotor eddy current loss.

The rotor eddy current is due to stator slotting effect and it is the loss that has to be reduced by the rotor grooving. This test procedure allows to identify such loss by measuring the total input power and separately identifying all the remaining losses. In fact:

- the stator joule loss is simply given by:

$$P_{js} = 3R_s I_s^2$$

where R_s is the DC measured resistance of a stator phase¹² and I_s is its current RMS-value;

- the mechanical loss is measured from the torque sensor performing the test with the prototype winding disconnected from the SG;
- the stator core loss is measured performing the test on the prototype equipped with the laminated rotor. In this situation no eddy currents arise in the rotor, so subtracting the remaining (known) losses from

¹² Since the prototype winding is made of round wire the skin effect is negligible, so the AC resistance is actually equal to the DC resistance

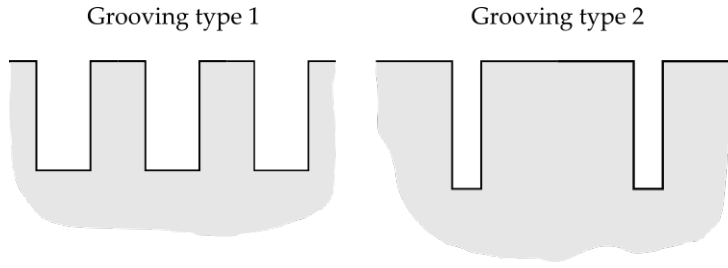


Figure 5.5: Different type of grooving for experimental investigation

Table 5.2: Solid rotor data for grooving investigation

Grooving type	1	2
Outer diameter	147 mm	
Axial length	150 mm	
Number of grooves	50	27
Groove pitch	3 mm	5 mm
Groove width	1.5 mm	0.8 mm
Groove depth	3 mm	3.5 mm

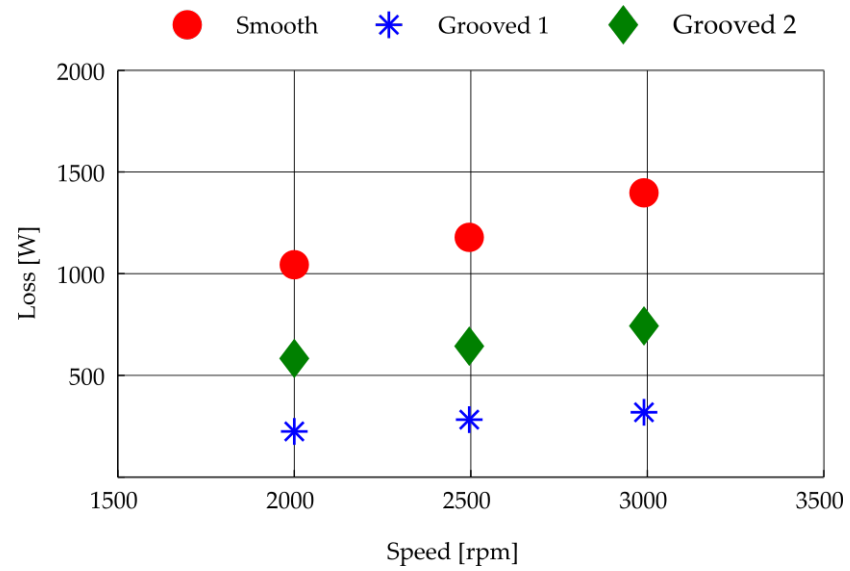
the total input the stator core loss is finally obtained. The rotor core loss is neglected because the rotor is at zero frequency, thanks to the synchronism guaranteed by the testing apparatus layout.

The core and mechanical losses are identified for a certain speed (frequency) and voltage pair, i.e. for a certain flux; performing the test on the prototype equipped with a solid rotor in the same voltage and speed conditions finally allows to determine the rotor eddy-current loss. Furthermore, the current absorbed by the prototype in this condition is the magnetizing current associated with the flux value under test. Thus the impact of the rotor grooving on these quantity can be experimentally assessed performing the procedure described above on a smooth solid rotor and on a grooved one.

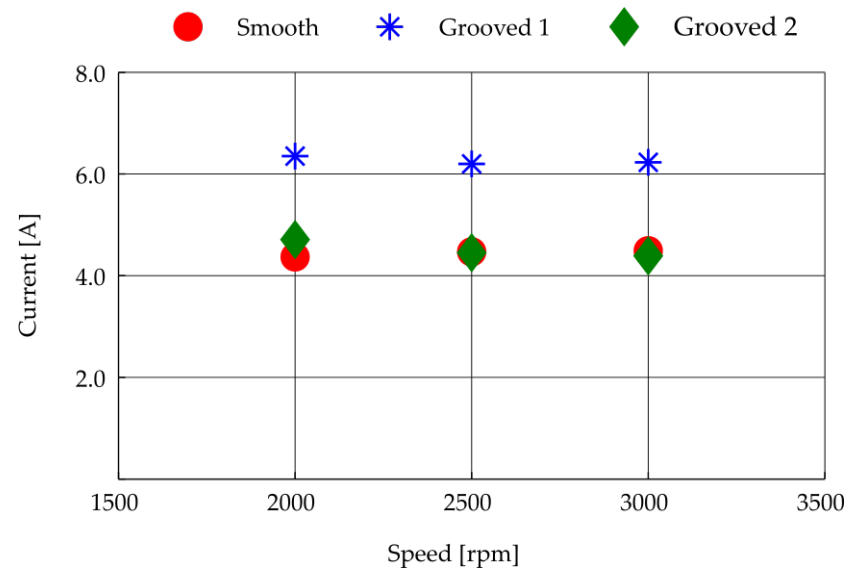
5.2.2 Example of grooving impact investigation

The testing procedure detailed in section 5.2.1 is applied to two different type of grooves, that are shown in figure 5.5. It can be noticed that the second groove-type is thinner and deeper than the first one. The groove characteristic dimensions are collected in table 5.2. The smooth solid rotor and the laminated one have the same outer diameter and axial length as the grooved rotors. All the solid rotor are made of C40 standard steel [12], whereas the laminated rotor and the stator are made of M530-65A electrical steel[11]. The stator data is the same as in table 1.1.

The test results are shown in figure 5.6. The tests have been conducted keeping the flux constant, i.e. choosing the voltage-speed values having the same ratio (153 V-2000 rpm, 192 V-2500 rpm and 230 V-3000 rpm). From figure 5.6a it can be noticed that groove 1 is more effective than groove 2 in terms of loss reduction, because it allows to limit the eddy-current loss at about 20% of the smooth case, whereas the groove 2 loss is more than



(a) Eddy-current losses



(b) Magnetizing current

Figure 5.6: Results from experimental assessment of grooving efficacy

50 % of the latter. On the other hand the groove type 2 practically does not influence the magnetizing current with respect to the smooth case, as it is shown in fig. 5.6b. The groove type 1, instead, increases the magnetizing current by about 40 %.

In this chapter the classic two-axis circuit model of the synchronous machine is recalled. The model is based on the Clarke-Park Transformation (CPT) [51], which allows to represent all the phase quantities (voltages, currents and flux-linkages) on a rotor attached-reference frame. This produces a simple linear model which can be associated with two lumped-parameter circuits. The circuit parameter calculation will be detailed in the next chapter. The two-axis model can be easily extended to the starting transient and, assuming a sufficiently slow start process, simplified into a couple of induction-machine like circuit, from which the starting performance is analytically computed (section 6.1). A brief introduction on how the model is identified from the experiments is also given (section 6.2).

6.1 SYNCHRONOUS MACHINE MODELING

6.1.1 Clarke-Park Transformation

The Clarke-Park Transformation [51] is a variable transformation that allows to represent a generic triplet of stator phase quantities from the static (actual) reference frame into a rotor-attached one. The variable transformation is realized through the following transformation matrix:

$$\mathcal{P}(\vartheta) = \sqrt{\frac{2}{3}} \begin{bmatrix} \cos(\vartheta) & \cos\left(\vartheta - \frac{2}{3}\pi\right) & \cos\left(\vartheta + \frac{2}{3}\pi\right) \\ -\sin(\vartheta) & -\sin\left(\vartheta - \frac{2}{3}\pi\right) & -\sin\left(\vartheta + \frac{2}{3}\pi\right) \\ \frac{1}{\sqrt{2}} & \frac{1}{\sqrt{2}} & \frac{1}{\sqrt{2}} \end{bmatrix} \quad (6.1)$$

where ϑ is the electric angular position of the rotor, i.e. $\vartheta = N_{pp}\vartheta_r$, being ϑ_r the mechanical angle between the rotor pole axis (direct axis) and the phase U stator axis. The generic triplet of phase quantities $\langle a \rangle_{UVW} = |a_U \ a_V \ a_W|^T$ is transformed into the dqo triplet $\langle a \rangle_{dqo} = |a_d \ a_q \ a_o|^T$:

$$\langle a \rangle_{dqo} = \mathcal{P}(\vartheta) \langle a \rangle_{UVW} \quad (6.2)$$

Here a_d is the direct-axis quantity, a_q is the quadrature-axis quantity and a_o is related to the zero sequence component of the phase quantity.

The expression of the CPT in (6.1) must be applied to the instantaneous value of a_U , a_V and a_W . However, assuming a steady-state AC system at angular frequency ω , the phasor notation can be employed and the triplet of stator phase quantities can be written as:

$$\langle a \rangle_{UVW} = \text{Re} \left\{ \begin{bmatrix} \bar{A}_U \\ \bar{A}_V \\ \bar{A}_W \end{bmatrix} e^{j\omega t} \right\} \quad (6.3)$$

The generic system is transformed into the sum of three symmetric system [52]. Letting $\check{\omega} = e^{j\frac{2}{3}\pi}$ the sequence components are then defined as:

$$\begin{cases} \bar{A}_0 = \frac{1}{3} (\bar{A}_U + \bar{A}_V + \bar{A}_W) \\ \bar{A}_1 = \frac{1}{3} (\bar{A}_U + \check{\omega}\bar{A}_V + \check{\omega}^2\bar{A}_W) \\ \bar{A}_2 = \frac{1}{3} (\bar{A}_U + \check{\omega}^2\bar{A}_V + \check{\omega}\bar{A}_W) \end{cases} \quad (6.4)$$

so that (6.3) becomes:

$$\langle a \rangle_{UVW} = \langle a^{(0)} \rangle_{UVW} + \langle a^{(1)} \rangle_{UVW} + \langle a^{(2)} \rangle_{UVW}$$

with:

$$\langle a^{(0)} \rangle_{UVW} = \text{Re} \left\{ \begin{array}{c} 1 \\ 1 \\ 1 \end{array} \middle| \bar{A}_0 e^{j\omega t} \right\} = \begin{array}{c} A_0 \cos(\omega t + \angle \bar{A}_0) \\ A_0 \cos(\omega t + \angle \bar{A}_0) \\ A_0 \cos(\omega t + \angle \bar{A}_0) \end{array} \quad (6.5a)$$

$$\langle a^{(1)} \rangle_{UVW} = \text{Re} \left\{ \begin{array}{c} 1 \\ \check{\omega}^2 \\ \check{\omega} \end{array} \middle| \bar{A}_1 e^{j\omega t} \right\} = \begin{array}{c} A_1 \cos(\omega t + \angle \bar{A}_1) \\ A_1 \cos(\omega t + \angle \bar{A}_1 - 2\pi/3) \\ A_1 \cos(\omega t + \angle \bar{A}_1 + 2\pi/3) \end{array} \quad (6.5b)$$

$$\langle a^{(2)} \rangle_{UVW} = \text{Re} \left\{ \begin{array}{c} 1 \\ \check{\omega} \\ \check{\omega}^2 \end{array} \middle| \bar{A}_2 e^{j\omega t} \right\} = \begin{array}{c} A_2 \cos(\omega t + \angle \bar{A}_2) \\ A_2 \cos(\omega t + \angle \bar{A}_2 + 2\pi/3) \\ A_2 \cos(\omega t + \angle \bar{A}_2 - 2\pi/3) \end{array} \quad (6.5c)$$

Thanks to the linearity of CPT the generic system on the dqo reference frame is obtained applying the CPT matrix in (6.1) to each of the components in (6.5) and superposing the effects, thus we can write:

$$\langle a \rangle_{dqo} = \langle a^{(0)} \rangle_{dqo} + \langle a^{(1)} \rangle_{dqo} + \langle a^{(2)} \rangle_{dqo} \quad (6.6)$$

with:

$$\begin{aligned} \langle a^{(0)} \rangle_{dqo} &= \mathcal{P}(\vartheta) \langle a^{(0)} \rangle_{UVW} \\ \langle a^{(1)} \rangle_{dqo} &= \mathcal{P}(\vartheta) \langle a^{(1)} \rangle_{UVW} \\ \langle a^{(2)} \rangle_{dqo} &= \mathcal{P}(\vartheta) \langle a^{(2)} \rangle_{UVW} \end{aligned}$$

Combining (6.1) and (6.5), after some algebraic transformations, we finally obtain:

$$\langle a^{(0)} \rangle_{dqo} = \begin{array}{c} 0 \\ 0 \\ \sqrt{3}A_0 \cos(\omega t + \angle \bar{A}_0) \end{array} = \text{Re} \left\{ \sqrt{3}\bar{A}_0 \begin{array}{c} 0 \\ 0 \\ 1 \end{array} \middle| e^{j\omega t} \right\} \quad (6.7a)$$

$$\langle a^{(1)} \rangle_{dqo} = \begin{array}{c} \sqrt{\frac{3}{2}}A_1 \cos(\omega t + \angle \bar{A}_1 - \vartheta) \\ \sqrt{\frac{3}{2}}A_1 \sin(\omega t + \angle \bar{A}_1 - \vartheta) \\ 0 \end{array} = \text{Re} \left\{ \sqrt{\frac{3}{2}}\bar{A}_1 \begin{array}{c} 1 \\ -j \\ 0 \end{array} \middle| e^{-j\vartheta} e^{j\omega t} \right\} \quad (6.7b)$$

$$\langle a^{(2)} \rangle_{dqo} = \begin{array}{c} \sqrt{\frac{3}{2}}A_2 \cos(\omega t + \angle \bar{A}_2 + \vartheta) \\ -\sqrt{\frac{3}{2}}A_2 \sin(\omega t + \angle \bar{A}_2 + \vartheta) \\ 0 \end{array} = \text{Re} \left\{ \sqrt{\frac{3}{2}}\bar{A}_2 \begin{array}{c} 1 \\ j \\ 0 \end{array} \middle| e^{j\vartheta} e^{j\omega t} \right\} \quad (6.7c)$$

and (6.6) becomes:

$$\langle a \rangle_{\text{dqo}} = \text{Re} \left\{ \sqrt{\frac{3}{2}} \begin{bmatrix} \bar{A}_1 e^{-j\theta} + \bar{A}_2 e^{j\theta} \\ -j(\bar{A}_1 e^{-j\theta} - \bar{A}_2 e^{j\theta}) \\ \sqrt{2}\bar{A}_0 \end{bmatrix} e^{j\omega t} \right\} \quad (6.8)$$

All these considerations allow to extend the CPT to the phasors as follows:

Given $\bar{A}_U, \bar{A}_V, \bar{A}_W$

$$\begin{aligned} & \downarrow \\ \begin{bmatrix} \bar{A}_0 \\ \bar{A}_1 \\ \bar{A}_1 \end{bmatrix} &= \frac{1}{3} \begin{bmatrix} 1 & 1 & 1 \\ 1 & \check{\omega} & \check{\omega}^2 \\ 1 & \check{\omega}^2 & \check{\omega} \end{bmatrix} \begin{bmatrix} \bar{A}_U \\ \bar{A}_V \\ \bar{A}_W \end{bmatrix} \end{aligned} \quad (6.9)$$

$$\begin{aligned} & \downarrow \\ \begin{bmatrix} \bar{A}_d \\ \bar{A}_q \\ \bar{A}_o \end{bmatrix} &= \sqrt{\frac{3}{2}} \begin{bmatrix} 0 & e^{-j\theta} & e^{j\theta} \\ 0 & -je^{-j\theta} & je^{j\theta} \\ \sqrt{2} & 0 & 0 \end{bmatrix} \begin{bmatrix} \bar{A}_0 \\ \bar{A}_1 \\ \bar{A}_2 \end{bmatrix} \end{aligned} \quad (6.10)$$

Clearly, if the three-phase system is already symmetric (positive sequence) then the transformation follows immediatly:

$$\begin{bmatrix} \bar{A}_U \\ \bar{A}_V \\ \bar{A}_W \end{bmatrix} = \begin{bmatrix} 1 \\ \check{\omega}^2 \\ \check{\omega} \end{bmatrix} \bar{A} \xrightarrow{\mathcal{P}} \begin{bmatrix} \bar{A}_d \\ \bar{A}_q \\ \bar{A}_o \end{bmatrix} = \sqrt{\frac{3}{2}} \bar{A} \begin{bmatrix} 1 \\ -j \\ 0 \end{bmatrix} e^{-j\theta}$$

All the phasors in (6.9) and (6.10) have to be intended as associated with the stator complex-frequency operator $e^{j\omega t}$, i.e. they rotate at angular speed equal to ω .

The inverse CPT allows to determine the actual stator triplet from a vector on the rotor-attached reference frame. The inverse transformation is obtained taking the inverse of the matrix in (6.1); since the latter is orthonormal then its inverse is equal to its transposed, so:

$$\langle a \rangle_{UVW} = \mathcal{P}(\vartheta)^T \langle a \rangle_{\text{dqo}} \quad (6.11)$$

The inverse transformation for phasors is obtained reverting (6.9) and (6.10):

Given $\bar{A}_d, \bar{A}_q, \bar{A}_o$

$$\begin{aligned} & \downarrow \\ \begin{bmatrix} \bar{A}_0 \\ \bar{A}_1 \\ \bar{A}_2 \end{bmatrix} &= \frac{1}{\sqrt{6}} \begin{bmatrix} 0 & 0 & \sqrt{2} \\ e^{j\theta} & je^{j\theta} & 0 \\ e^{-j\theta} & -je^{-j\theta} & 0 \end{bmatrix} \begin{bmatrix} \bar{A}_d \\ \bar{A}_q \\ \bar{A}_o \end{bmatrix} \end{aligned} \quad (6.12)$$

$$\begin{aligned} & \downarrow \\ \begin{bmatrix} \bar{A}_U \\ \bar{A}_V \\ \bar{A}_W \end{bmatrix} &= \begin{bmatrix} 1 & 1 & 1 \\ 1 & \check{\omega}^2 & \check{\omega} \\ 1 & \check{\omega} & \check{\omega}^2 \end{bmatrix} \begin{bmatrix} \bar{A}_0 \\ \bar{A}_1 \\ \bar{A}_2 \end{bmatrix} \end{aligned} \quad (6.13)$$

The orthonormality of the CPT matrix in (6.1) guarantees the preservation of the energetic quantities from the actual reference frame to the rotor

attached one and vice-versa. In fact the instantaneous power entering the three-phase system is given by:

$$\begin{aligned}
 P &= \langle \mathbf{U} \rangle_{UVW}^T \langle I \rangle_{UVW} \\
 &= \langle \mathbf{U} \rangle_{UVW}^T \mathcal{P}(\vartheta)^T \mathcal{P}(\vartheta) \langle I \rangle_{UVW} \\
 &= [\mathcal{P}(\vartheta) \langle \mathbf{U} \rangle_{UVW}]^T [\mathcal{P}(\vartheta) \langle I \rangle_{UVW}] \\
 &= \langle \mathbf{U} \rangle_{dqo}^T \langle I \rangle_{dqo}
 \end{aligned}$$

6.1.2 Standard dq dynamic model for synchronous motors

The introduction of the CPT allows to simplify the synchronous machine dynamic model in the rotor-attached reference frame as follows[53]:

$$U_d = R_s I_d + \dot{\Psi}_d - \vartheta \Psi_q \quad (6.14a)$$

$$U_q = R_s I_q + \dot{\Psi}_q + \vartheta \Psi_d \quad (6.14b)$$

$$0 = R_{kd} I_{kd} + \dot{\Psi}_{kd} \quad (6.14c)$$

$$0 = R_{kq} I_{kq} + \dot{\Psi}_{kq} \quad (6.14d)$$

$$U_f = R_f I_f + \dot{\Psi}_f \quad (6.14e)$$

with the flux-linkages given by:

$$\Psi_d = L_{ad}(I_d + I_{kd} + I_f) + L_s I_d \quad (6.15a)$$

$$\Psi_q = L_{aq}(I_q + I_{kq}) + L_s I_q \quad (6.15b)$$

$$\Psi_{kd} = L_{ad}(I_d + I_{kd} + I_f) + L_{kd} I_{kd} \quad (6.15c)$$

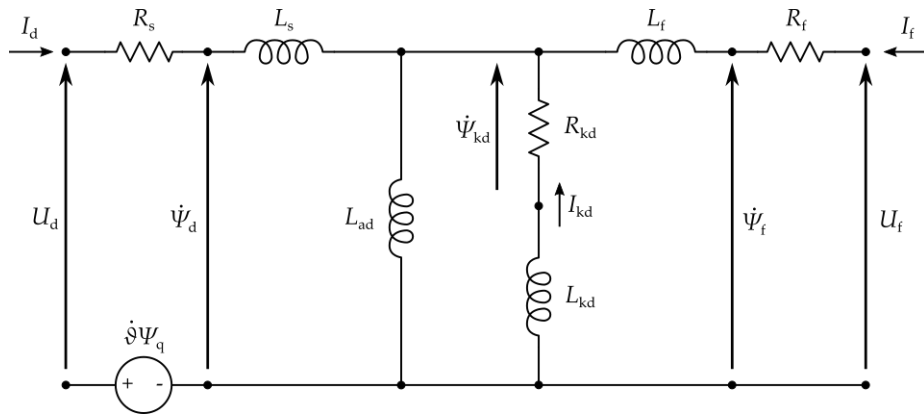
$$\Psi_{kq} = L_{aq}(I_q + I_{kq}) + L_{kq} I_{kq} \quad (6.15d)$$

$$\Psi_f = L_{ad}(I_d + I_{kd} + I_f) + L_f I_f \quad (6.15e)$$

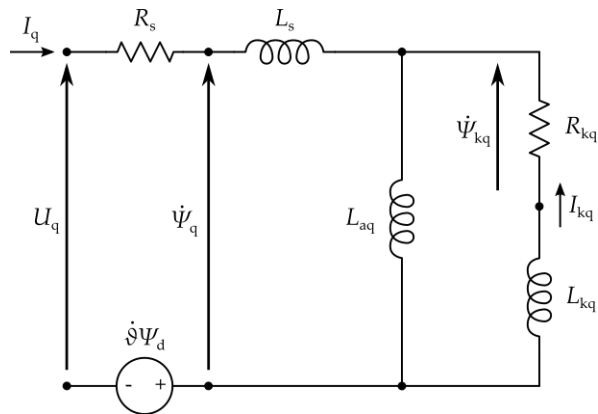
The term ϑ in (6.14) is related to the rotor speed by the relation $\vartheta = N_{pp}\Omega$.

This model assumes that the synchronous machine is equipped with three rotor windings, i.e. the field winding (on the direct-axis) and two (short-circuited) damping windings (one per each axis). In the equations (6.14) and (6.15) the zero-sequence terms are omitted, because these are independent of the d and q terms. In the case of solid rotor machines the model is still valid, but the rotor parameters are speed-dependant. The dynamic model in (6.14) and (6.15) is summarized in the two circuits in figure 6.1. The model can be also written in a matrix form; letting the phase variable arrays:

$$\mathbf{U} = \begin{bmatrix} U_d \\ U_q \\ 0 \\ 0 \\ U_f \end{bmatrix} \quad \mathbf{I} = \begin{bmatrix} I_d \\ I_q \\ I_{kd} \\ I_{kq} \\ I_f \end{bmatrix} \quad \mathbf{\Psi} = \begin{bmatrix} \Psi_d \\ \Psi_q \\ \Psi_{kd} \\ \Psi_{kq} \\ \Psi_f \end{bmatrix}$$



(a) Direct axis



(b) Quadrature axis

Figure 6.1: Synchronous machine dynamic circuits

and the parameter matrices:

$$[\mathbf{R}] = \begin{bmatrix} R_s & 0 & 0 & 0 & 0 \\ 0 & R_s & 0 & 0 & 0 \\ 0 & 0 & R_{kd} & 0 & 0 \\ 0 & 0 & 0 & R_{kq} & 0 \\ 0 & 0 & 0 & 0 & R_f \end{bmatrix}$$

$$[\mathbf{L}] = \begin{bmatrix} L_s + L_{ad} & 0 & L_{ad} & 0 & L_{ad} \\ 0 & L_s + L_{aq} & 0 & L_{ad} & 0 \\ L_{ad} & 0 & L_{kd} + L_{ad} & 0 & L_{ad} \\ 0 & L_{aq} & 0 & L_{kq} + L_{aq} & 0 \\ L_{ad} & 0 & L_{ad} & 0 & L_f + L_{ad} \end{bmatrix}$$

$$[\mathcal{J}] = \begin{bmatrix} 0 & -1 & 0 & 0 & 0 \\ 1 & 0 & 0 & 0 & 0 \\ 0 & 0 & 0 & 0 & 0 \\ 0 & 0 & 0 & 0 & 0 \end{bmatrix}$$

then (6.14) and (6.15) become, respectively:

$$\mathbf{U} = [\mathbf{R}]\mathbf{I} + \dot{\Psi} + \dot{\theta}[\mathcal{J}]\Psi \quad (6.16)$$

$$\Psi = [\mathbf{L}]\mathbf{I} \quad (6.17)$$

The machine dynamics is completed by the mechanical equation, given by:

$$T_{em} = T_{load} + K_f\Omega + J\dot{\Omega} \quad (6.18)$$

The expression for the motor electro-magnetic torque is obtained from the power balance. In fact it has to be:

$$P_{in} = \sum P_{loss} + \Omega T_{em} \quad (6.19)$$

The input power comes from (6.16); in fact, multiplying both members by \mathbf{I}^T it results:

$$\mathbf{I}^T\mathbf{U} = \mathbf{I}^T[\mathbf{R}]\mathbf{I} + \mathbf{I}^T\dot{\Psi} + \dot{\theta}\mathbf{I}^T[\mathcal{J}]\Psi \quad (6.20)$$

Considering that:

- $\mathbf{I}^T\mathbf{U} = U_d I_d + U_q I_q + U_f I_f$ is the total input power;
- $\mathbf{I}^T[\mathbf{R}]\mathbf{I} = R_s(I_d^2 + I_q^2) + R_{kd}I_{kd}^2 + R_{kq}I_{kq}^2 + R_f I_f^2$ is the total joule loss
- $\mathbf{I}^T\dot{\Psi} = I_d\dot{\Psi}_d + I_q\dot{\Psi}_q + I_{kd}\dot{\Psi}_{kd} + I_{kq}\dot{\Psi}_{kq} + I_f\dot{\Psi}_f$ is the variation of the energy stored in the magnetic circuit

then comparing (6.19) and (6.20) it has to be:

$$T_{em}\Omega = \dot{\theta}\mathbf{I}^T[\mathcal{J}]\Psi$$

and, finally:

$$T_{em} = N_{pp}\mathbf{I}^T[\mathcal{J}]\Psi = N_{pp}(\Psi_d I_q - \Psi_q I_d) \quad (6.21)$$

6.1.3 Quasi-stationary dq model for motor starting

The dq model for the study of SM starting is obtained from the standard model in section 6.1.2 considering that:

1. the motor is started with no rotor excitation and the field winding is generally short-circuited or closed on an additional resistor (called *discharge resistor*). For this reason, in the following, it will be assumed $U_f = 0$ and R_f will be intended as the proper winding resistance plus the (possible) discharge resistance;
2. the stator is fed with a three-phase symmetric voltage system with positive sequence, having amplitude $U_{\max} \leq U_{n,\max}$ ¹ and angular frequency ω_0 . From this hypothesis, accordingly to (6.7b), the feeding voltage system on the rotor-attached dq reference frame is

$$\begin{Bmatrix} U_d \\ U_q \end{Bmatrix} = \operatorname{Re} \left\{ \sqrt{\frac{3}{2}} U_{\max} \begin{Bmatrix} 1 \\ -j \end{Bmatrix} \right\} e^{j(\omega_0 t - \vartheta)} \quad (6.22)$$

3. the motor starting is a slow process, so it can be studied as a sequence of steady-state working points with the rotor spinning at a constant speed, given by:

$$\Omega = (1 - s)\Omega_0 = (1 - s) \frac{\omega_0}{N_{pp}}$$

so the rotor electric position at a generic instant t is given by:

$$\vartheta(t) = N_{pp}\Omega t = (1 - s)\omega_0 t \quad (6.23)$$

Here s is analogous to the slip for an induction motor, since we have $s = 1 - \Omega/\Omega_0$; the electrical dynamic in the transtion from a certain speed point to another can be ignored, so the starting performance can be intended as a function of the speed only, not involving the time.

At this point, combining (6.22) and (6.23) the final stator supply on the dq reference frame is obtained:

$$\begin{Bmatrix} U_d \\ U_q \end{Bmatrix} = \operatorname{Re} \left\{ \sqrt{\frac{3}{2}} U_{\max} \begin{Bmatrix} 1 \\ -j \end{Bmatrix} e^{js\omega_0 t} \right\} \quad (6.24)$$

Since the terms in (6.24) are the only source terms and the hypothesis of AC steady-state has been assumed, the two circuits on the dq reference frame can be studied at the slip frequency $s\omega_0$ and the phasor notation can be adopted. It is useful to re-define the phasors with respect to the rotor-referred frequency, i.e. the stator voltage system is:

$$\begin{Bmatrix} U_d \\ U_q \end{Bmatrix} = \operatorname{Re} \left\{ \begin{Bmatrix} \bar{U}_d \\ \bar{U}_q \end{Bmatrix} e^{js\omega_0 t} \right\} \quad (6.25)$$

being

$$\begin{Bmatrix} \bar{U}_d \\ \bar{U}_q \end{Bmatrix} = \begin{Bmatrix} 1 \\ -j \end{Bmatrix} \sqrt{\frac{3}{2}} U_{\max} \quad (6.26)$$

¹ $U_{n,\max}$ is the maximum value of the rated phase voltage, that it is usually expressed as RMS value, i.e. $U_{n,\max} = \sqrt{2}U_n$

With this assumption the explicit time dependency can be eliminated from the electric equations and, thus, expression (6.14) becomes:

$$\bar{U}_d = R_s \bar{I}_d + j s \omega_0 \bar{\Psi}_d - (1-s) \omega_0 \bar{\Psi}_q \quad (6.27a)$$

$$\bar{U}_q = R_s \bar{I}_q + j s \omega_0 \bar{\Psi}_q + (1-s) \omega_0 \bar{\Psi}_d \quad (6.27b)$$

$$0 = R_{kd} \bar{I}_{kd} + j s \omega_0 \bar{\Psi}_{kd} \quad (6.27c)$$

$$0 = R_{kq} \bar{I}_{kq} + j s \omega_0 \bar{\Psi}_{kq} \quad (6.27d)$$

$$0 = R_f \bar{I}_f + j s \omega_0 \bar{\Psi}_f \quad (6.27e)$$

Expression (6.15) is formally identical in the phasor notation, thus it is still valid.

It can be observed that, if the stator resistance is neglected in (6.27a) and (6.27b) then the cross-dependency of the two axis can be eliminated [54]. In fact we have:

$$\begin{aligned} \begin{vmatrix} \bar{U}_d \\ \bar{U}_q \end{vmatrix} &= \omega_0 \begin{bmatrix} j s & -(1-s) \\ (1-s) & j s \end{bmatrix} \begin{vmatrix} \bar{\Psi}_d \\ \bar{\Psi}_q \end{vmatrix} \\ &\Downarrow \\ \begin{vmatrix} \bar{\Psi}_d \\ \bar{\Psi}_q \end{vmatrix} &= \frac{1}{(1-2s)\omega_0} \begin{bmatrix} j s & (1-s) \\ -(1-s) & j s \end{bmatrix} \begin{vmatrix} \bar{U}_d \\ \bar{U}_q \end{vmatrix} \end{aligned}$$

and then, using (6.26):

$$\begin{aligned} \begin{vmatrix} \bar{\Psi}_d \\ \bar{\Psi}_q \end{vmatrix} &= \begin{vmatrix} -j \\ -1 \end{vmatrix} \sqrt{\frac{3}{2}} \frac{U_{\max}}{\omega_0} = -\frac{j}{\omega_0} \begin{vmatrix} \bar{U}_d \\ \bar{U}_q \end{vmatrix} \\ &\Downarrow \\ \begin{vmatrix} \bar{U}_d \\ \bar{U}_q \end{vmatrix} &= j \omega_0 \begin{vmatrix} \bar{\Psi}_d \\ \bar{\Psi}_q \end{vmatrix} \end{aligned}$$

As regards the rotor equations (6.27c), (6.27d) and (6.27e) they can be reduced to an analogous form dividing both sides of each equation by s . Finally, reintroducing the effect of stator resistance, equations in (6.27) are reduced to:

$$\bar{U}_d = R_s \bar{I}_d + j \omega_0 \bar{\Psi}_d \quad (6.28a)$$

$$\bar{U}_q = R_s \bar{I}_q + j \omega_0 \bar{\Psi}_q \quad (6.28b)$$

$$0 = \frac{R_{kd}}{s} \bar{I}_{kd} + j \omega_0 \bar{\Psi}_{kd} \quad (6.28c)$$

$$0 = \frac{R_{kq}}{s} \bar{I}_{kq} + j \omega_0 \bar{\Psi}_{kq} \quad (6.28d)$$

$$0 = \frac{R_f}{s} \bar{I}_f + j \omega_0 \bar{\Psi}_f \quad (6.28e)$$

or, making the flux linkage expressions explicit:

$$\bar{U}_d = R_s \bar{I}_d + j \omega_0 L_s \bar{I}_d + j \omega_0 L_{ad} (\bar{I}_d + \bar{I}_{kd} + \bar{I}_f) \quad (6.29a)$$

$$\bar{U}_q = R_s \bar{I}_q + j \omega_0 L_s \bar{I}_q + j \omega_0 L_{aq} (\bar{I}_q + \bar{I}_{kq}) \quad (6.29b)$$

$$0 = \frac{R_{kd}}{s} \bar{I}_{kd} + j \omega_0 L_{kd} \bar{I}_{kd} + j \omega_0 L_{ad} (\bar{I}_d + \bar{I}_{kd} + \bar{I}_f) \quad (6.29c)$$

$$0 = \frac{R_{kq}}{s} \bar{I}_{kq} + j \omega_0 L_{kq} \bar{I}_{kq} + j \omega_0 L_{aq} (\bar{I}_q + \bar{I}_{kq}) \quad (6.29d)$$

$$0 = \frac{R_f}{s} \bar{I}_f + j \omega_0 L_f \bar{I}_f + j \omega_0 L_{ad} (\bar{I}_d + \bar{I}_{kd} + \bar{I}_f) \quad (6.29e)$$

From (6.29) it can be noticed that all the inductances, with the previous assumptions and simplifications, are associated with the stator frequency ω_0 ; therefore the following reactances can be defined:

$$\begin{aligned} X_s &= \omega_0 L_s & X_{aq} &= \omega_0 L_{aq} & X_{kq} &= \omega_0 L_{kq} \\ X_{ad} &= \omega_0 L_{ad} & X_{kd} &= \omega_0 L_{kd} & X_f &= \omega_0 L_f \end{aligned}$$

and the resistance and reactance matrix can be defined as:

$$[\mathbf{R}_{dq}] = \begin{bmatrix} R_s & 0 & 0 & 0 & 0 \\ 0 & R_s & 0 & 0 & 0 \\ 0 & 0 & R_{kd}/s & 0 & 0 \\ 0 & 0 & 0 & R_{kq}/s & 0 \\ 0 & 0 & 0 & 0 & R_f/s \end{bmatrix}$$

$$[\mathbf{X}_{dq}] = \begin{bmatrix} X_s + X_{ad} & 0 & X_{ad} & 0 & X_{ad} \\ 0 & X_s + X_{aq} & 0 & X_{aq} & 0 \\ X_{ad} & 0 & X_{kd} + X_{ad} & 0 & X_{ad} \\ 0 & X_{aq} & 0 & X_{kq} + X_{aq} & 0 \\ X_{ad} & 0 & X_{ad} & 0 & X_f + X_{ad} \end{bmatrix}$$

so (6.29) can be expressed in a more compact way as:

$$\bar{\mathbf{U}} = ([\mathbf{R}_{dq}] + j[\mathbf{X}_{dq}]) \bar{\mathbf{I}} \quad (6.30)$$

The model in (6.30) leads also to the two-axes circuit in figure 6.2.

The impedance seen by each axis (excluding the stator resistance) is called *operatorial impedance* and, for the two axes, are given by:

$$\bar{Z}_d(s) = jX_s + \frac{1}{\frac{1}{jX_{ad}} + \frac{1}{\frac{R_{kd}}{s} + jX_{kd}} + \frac{1}{\frac{R_f}{s} + jX_f}} \quad (6.31a)$$

$$\bar{Z}_q(s) = jX_s + \frac{1}{\frac{1}{jX_{aq}} + \frac{1}{\frac{R_{kq}}{s} + jX_{kq}}} \quad (6.31b)$$

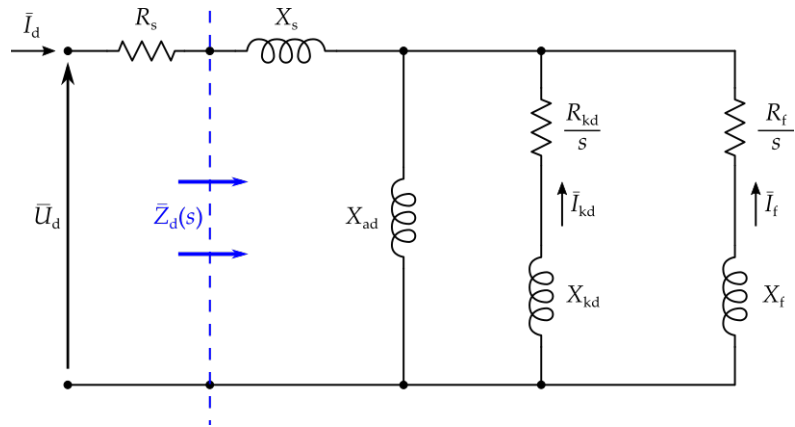
6.1.4 Starting performance calculation

The introduction of the operational impedances allow to easily calculate the stator currents on the dq reference frame:

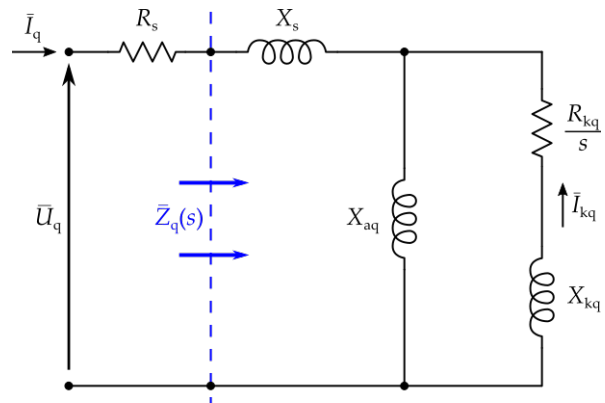
$$\bar{I}_d = \frac{\bar{U}_d}{R_s + \bar{Z}_d(s)} \quad \bar{I}_q = \frac{\bar{U}_q}{R_s + \bar{Z}_q(s)} \quad (6.32)$$

and the flux linkages are given as well:

$$\bar{\Psi}_d = \frac{\bar{Z}_d(s)\bar{I}_d}{j\omega_0} \quad \bar{\Psi}_q = \frac{\bar{Z}_q(s)\bar{I}_q}{j\omega_0} \quad (6.33)$$



(a) Direct axis



(b) Quadrature axis

Figure 6.2: Synchronous machine circuits for slow start-up

The phasors of current and flux-linkage are used to calculate the torque expression in accordingly to (6.21), similarly to what is proposed in [54]. Letting:

$$\begin{aligned}\bar{I}_d &= D_1 + jD_2 & \bar{Z}_d(s) &= R_d + jX_d \\ \bar{I}_q &= Q_1 + jQ_2 & \bar{Z}_q(s) &= R_q + jX_q\end{aligned}$$

then from (6.33) the flux-linkages are given:

$$\begin{aligned}\bar{\Psi}_d &= \frac{X_d D_1 + R_d D_2}{\omega_0} + j \frac{X_d D_2 - R_d D_1}{\omega_0} \\ \bar{\Psi}_q &= \frac{X_q Q_1 + R_q Q_2}{\omega_0} + j \frac{X_q Q_2 - R_q Q_1}{\omega_0}\end{aligned}$$

The torque expression in (6.21) must be evaluated using the instantaneous values of currents and fluxes, that are given by:

$$I_d(t) = \text{Re} \{ \bar{I}_d e^{js\omega_0 t} \} = D_1 \cos(s\omega_0 t) - D_2 \sin(s\omega_0 t) \quad (6.34a)$$

$$I_q(t) = \text{Re} \{ \bar{I}_q e^{js\omega_0 t} \} = Q_1 \cos(s\omega_0 t) - Q_2 \sin(s\omega_0 t) \quad (6.34b)$$

$$\begin{aligned}\Psi_d(t) &= \text{Re} \{ \bar{\Psi}_d e^{js\omega_0 t} \} = \frac{X_d D_1 + R_d D_2}{\omega_0} \cos(s\omega_0 t) \\ &\quad - \frac{X_d D_2 - R_d D_1}{\omega_0} \sin(s\omega_0 t)\end{aligned} \quad (6.34c)$$

$$\begin{aligned}\Psi_q(t) &= \text{Re} \{ \bar{\Psi}_q e^{js\omega_0 t} \} = \frac{X_q Q_1 + R_q Q_2}{\omega_0} \cos(s\omega_0 t) \\ &\quad - \frac{X_q Q_2 - R_q Q_1}{\omega_0} \sin(s\omega_0 t)\end{aligned} \quad (6.34d)$$

Substituting (6.34) into (6.21), after some algebraic transformations we obtain [54]:

$$\begin{aligned}T_{em}(t) &= \frac{1}{2} N_{pp} \left[(Q_1 D_1 + Q_2 D_2) \frac{X_d - X_q}{\omega_0} + (Q_1 D_2 - Q_2 D_1) \frac{R_d + R_q}{\omega_0} \right] \\ &\quad \frac{1}{2} N_{pp} \left[(Q_1 D_1 - Q_2 D_2) \frac{X_d - X_q}{\omega_0} + (Q_1 D_2 - Q_2 D_1) \frac{R_d - R_q}{\omega_0} \right] \cos(2s\omega_0 t) \\ &\quad \frac{1}{2} N_{pp} \left[(Q_1 D_2 + Q_2 D_1) \frac{X_q - X_d}{\omega_0} + (Q_1 D_1 - Q_2 D_2) \frac{R_d - R_q}{\omega_0} \right] \sin(2s\omega_0 t)\end{aligned}$$

Therefore the starting torque consists of the sum of a constant term (the *average torque*) plus a fluctuating term at double the slip frequency (the *torque pulsation*). The average torque can be written as:

$$T_{avg} = \frac{1}{2} \frac{N_{pp}}{\omega_0} \text{Im} \left\{ \bar{I}_d \bar{Z}_d(s) \bar{I}_q^* - \bar{I}_q \bar{Z}_q(s) \bar{I}_d^* \right\} \quad (6.35)$$

whereas the peak of the torque pulsation is

$$T_{pul} = \frac{1}{2} \frac{N_{pp}}{\omega_0} |\bar{I}_d| |\bar{Z}_d(s) - \bar{Z}_q(s)| |\bar{I}_q| \quad (6.36)$$

Similarly, the actual system of currents is calculated. Assuming:

$$\bar{I}_d = |\bar{I}_d| e^{j\angle I_d} \quad \bar{I}_q = |\bar{I}_q| e^{j\angle I_q}$$

then the instantaneous values of the currents in the dq reference frame is given by:

$$I_d(t) = \text{Re} \{ \bar{I}_d e^{js\omega_0 t} \} = |\bar{I}_d| \cos(s\omega_0 t + \angle \bar{I}_d) \quad (6.37a)$$

$$I_q(t) = \text{Re} \{ \bar{I}_q e^{js\omega_0 t} \} = |\bar{I}_q| \cos(s\omega_0 t + \angle \bar{I}_q) \quad (6.37b)$$

Applying the expressions in (6.37) to the inverse transformation in (6.11), assuming $I_o(t) = 0$ the current system on the stator reference frame is obtained:

$$\begin{aligned} I_U(t) &= \frac{1}{\sqrt{6}} \left[|\bar{I}_d| \cos(\vartheta + s\omega_0 t + \angle \bar{I}_d) - |\bar{I}_q| \sin(\vartheta + s\omega_0 t + \angle \bar{I}_q) \right. \\ &\quad \left. + |\bar{I}_d| \cos(\vartheta - s\omega_0 t - \angle \bar{I}_d) - |\bar{I}_q| \sin(\vartheta - s\omega_0 t - \angle \bar{I}_q) \right] \\ I_V(t) &= \frac{1}{\sqrt{6}} \left[|\bar{I}_d| \cos\left(\vartheta + s\omega_0 t + \angle \bar{I}_d - \frac{2}{3}\pi\right) - |\bar{I}_q| \sin\left(\vartheta + s\omega_0 t + \angle \bar{I}_q - \frac{2}{3}\pi\right) \right. \\ &\quad \left. + |\bar{I}_d| \cos\left(\vartheta - s\omega_0 t - \angle \bar{I}_d - \frac{2}{3}\pi\right) - |\bar{I}_q| \sin\left(\vartheta - s\omega_0 t - \angle \bar{I}_q - \frac{2}{3}\pi\right) \right] \\ I_W(t) &= \frac{1}{\sqrt{6}} \left[|\bar{I}_d| \cos\left(\vartheta + s\omega_0 t + \angle \bar{I}_d + \frac{2}{3}\pi\right) - |\bar{I}_q| \sin\left(\vartheta + s\omega_0 t + \angle \bar{I}_q + \frac{2}{3}\pi\right) \right. \\ &\quad \left. + |\bar{I}_d| \cos\left(\vartheta - s\omega_0 t - \angle \bar{I}_d + \frac{2}{3}\pi\right) - |\bar{I}_q| \sin\left(\vartheta - s\omega_0 t - \angle \bar{I}_q + \frac{2}{3}\pi\right) \right] \end{aligned}$$

Given the expression of ϑ in (6.23) it results that the system of current has two components:

- the fundamental component has the same frequency as the voltage system (ω_0) and its RMS value is given by:

$$I_{\text{avg}} = \frac{1}{2\sqrt{3}} |\bar{I}_d + j\bar{I}_q| \quad (6.38)$$

- the second component fluctuates at a frequency of $(1 - 2s)\omega_0$ and its RMS value is given by:

$$I_{\text{pul}} = \frac{1}{2\sqrt{3}} |\bar{I}_d - j\bar{I}_q| \quad (6.39)$$

All these expressions are used in IEEE Standard 1255 [55] for the calculation of the starting performance.

6.1.5 Per-unit reduction

The synchronous machine starting model can be expressed in *per-unit* using the base quantities provided in appendix C. This allows to furtherly simplify the structure of the equations written above.

The stator feeding voltage is assumed to have a *pu*-value equal to v , i.e. the RMS value of the stator voltage is vU_n . The phasors of phase voltage on the dq reference frame are:

$$\begin{bmatrix} \bar{u}_d \\ \bar{u}_q \end{bmatrix} = \begin{bmatrix} 1 \\ -j \end{bmatrix} \sqrt{3}v \quad (6.40)$$

The two-axis circuits are formally identical to figure 6.2, substituting the physical values with their corresponding pu values. The operational impedances are given by:

$$\bar{z}_d(s) = jx_s + \frac{1}{jx_{ad} + \frac{1}{\frac{r_{kd}}{s} + jx_{kd}} + \frac{1}{\frac{r_f}{s} + jx_f}} \quad (6.41a)$$

$$\bar{z}_q(s) = jx_s + \frac{1}{jx_{aq} + \frac{1}{\frac{r_{kq}}{s} + jx_{kq}}} \quad (6.41b)$$

The axis currents are, therefore:

$$\bar{i}_d = \frac{\bar{u}_d}{r_s + \bar{z}_d(s)} \quad \bar{i}_q = \frac{\bar{u}_q}{r_s + \bar{z}_q(s)} \quad (6.42)$$

and the torque and line current components are, finally:

$$\hat{T}_{avg} = \frac{1}{6} \frac{S_n}{P_n} \text{Im} \left\{ \bar{i}_d \bar{z}_d \bar{i}_q^* - \bar{i}_d^* \bar{z}_q \bar{i}_q \right\} \quad (6.43)$$

$$\hat{T}_{pul} = \frac{1}{6} \frac{S_n}{P_n} |\bar{i}_d| |\bar{z}_d - \bar{z}_q| |\bar{i}_q| \quad (6.44)$$

$$i_{avg} = \frac{1}{2\sqrt{3}} |\bar{i}_d + j\bar{i}_q| \quad (6.45)$$

$$i_{pul} = \frac{1}{2\sqrt{3}} |\bar{i}_d - j\bar{i}_q| \quad (6.46)$$

6.2 MODEL IDENTIFICATION FROM STAND-STILL TESTS

6.2.1 Stationary dq model at stand-still

If the rotor is not moving then the model presented in 6.1.3 is not valid. In this case, assuming the stator being fed with a generic three-phase voltage system at angular frequency ω the stator voltages on the dq reference frame are:

$$\begin{bmatrix} U_d(t) \\ U_q(t) \end{bmatrix} = \text{Re} \left\{ \begin{bmatrix} \bar{U}_{d,max}(t) \\ \bar{U}_{q,max} \end{bmatrix} e^{j(\omega t - \vartheta_0)} \right\} \quad (6.47)$$

where $\bar{U}_{d,max}$, $\bar{U}_{q,max}$ depend on the voltage system and ϑ_0 is the rotor electric angular position, that is assumed fixed. It can be noticed that the voltages pulsate on the rotor model with the same frequency as the stator model; thus the voltage phasors can be defined as usual:

$$\begin{bmatrix} \bar{U}_d(t) \\ \bar{U}_q \end{bmatrix} = \begin{bmatrix} \bar{U}_{d,max}(t) \\ \bar{U}_{q,max} \end{bmatrix} e^{-j\vartheta_0}$$

and, since $\dot{\vartheta} = 0$ the stand-still model directly follows from (6.16) and (6.17), using the phasor notation:

$$\bar{U} = [\mathbf{R}]\bar{I} + j\omega[\mathbf{L}]\bar{I} \quad (6.48)$$

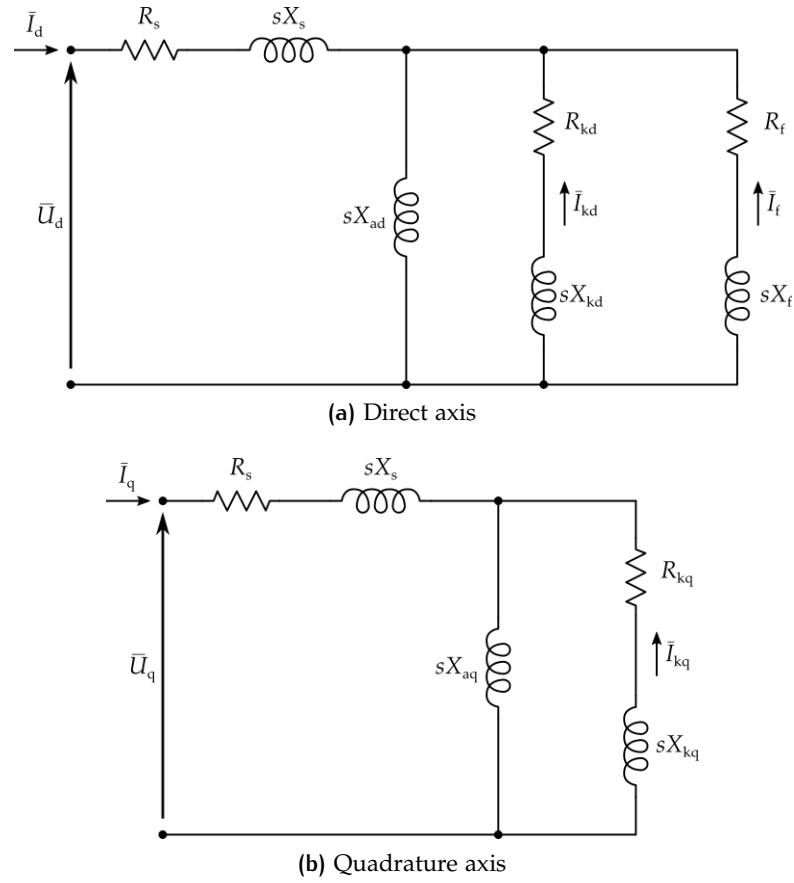


Figure 6.3: Synchronous machine circuits for still-rotor condition

Using the fact that the matrix of the reactances is defined with respect to the machine rated frequency ω_0 then (6.48) can be rewritten as:

$$\bar{U} = \left([\mathbf{R}] + j \frac{\omega}{\omega_0} [\mathbf{X}] \right) \bar{\mathbf{I}} \quad (6.49)$$

The matrix $[\mathbf{X}]$ is formally identical to the one introduced in (6.30), whereas $[\mathbf{R}]$ is equal to the matrix in (6.16), not the one in (6.30).

It is worth noticing that, if the feeding frequency at stand-still is equal to the slip frequency, i.e. $\omega = s\omega_0$ then (6.49) becomes:

$$\bar{U} = ([\mathbf{R}] + js[\mathbf{X}]) \bar{\mathbf{I}}$$

and the rotor equations are formally identical to (6.27c), (6.27d) and (6.27e) in the same slip conditions. This fact can be used to identify the rotor parameters at slip s through a series of suitable tests; after the relations between X_{ad} , R_{kd} , X_{kd} , R_f , X_f , X_{aq} , R_{kq} , X_{kq} and s are derived at stand-still, these parameters can be used in the moving-rotor model according to (6.30). This fact is also highlighted in figure 6.3; the parameters in these circuits are identical to the corresponding parameters in figure 6.2.

The operational impedances are defined as:

$$\bar{Z}_d(s) = jsX_s + \frac{1}{\frac{1}{jsX_{ad}} + \frac{1}{R_{kd} + jsX_{kd}} + \frac{1}{R_f + jsX_f}} \quad (6.50a)$$

$$\bar{Z}_q(s) = jsX_s + \frac{1}{\frac{1}{jsX_{aq}} + \frac{1}{R_{kq} + jsX_{kq}}} \quad (6.50b)$$

and the total axis admittances are introduced:

$$\bar{Y}_d(s) = \frac{1}{R_s + \bar{Z}_d(s)} \quad \bar{Y}_q(s) = \frac{1}{R_s + \bar{Z}_q(s)} \quad (6.51)$$

so the current components on the dq reference frame are simply given by:

$$\bar{I}_d = \bar{Y}_d(s)\bar{U}_d \quad \bar{I}_q = \bar{Y}_q(s)\bar{U}_q \quad (6.52)$$

6.2.2 Axis admittance identification

The axis admittances in (6.51) can be practically determined through two stand-still rotor tests:

- a locked-rotor test with the machine fed by a symmetric three-phase voltage system;
- a test with the machine fed by a single-phase voltage between one phase and the parallel of the other two.

Actually one test could be enough to identify both axes if the rotor position θ_0 is known; this situation is not always possible for large machines, because of the difficulty in the rotor handling; this section shows how the axis admittances (and, thus, the operational impedances) can be calculated from the combination of the two tests results, without the need of determining the rotor angle. An alternative to these tests is reported in IEEE Standard 115 [56] but this requires performing burdensome tests (like sudden short-circuit test) or multiple ones.

Stand-still test with three-phase supply

The stator is fed with a positive-sequence symmetric three-phase voltage system of amplitude U_{\max} (phase voltage). This excitation, clearly, produces a rotating air-gap field, so the rotor must be mechanically blocked to keep it still. According to (6.10) the voltage phasor on the dq reference frame in this condition are:

$$\begin{vmatrix} \bar{U}_d^{(3\phi)} \\ \bar{U}_q^{(3\phi)} \end{vmatrix} = \sqrt{\frac{3}{2}} U_{\max} \begin{vmatrix} 1 \\ -j \end{vmatrix} e^{j\theta_0} \quad (6.53)$$

This allows to determine the current dq components according to (6.52):

$$\bar{I}_d^{(3\phi)} = \bar{Y}_d \bar{U}_d^{(3\phi)} \quad \bar{I}_q^{(3\phi)} = \bar{Y}_q \bar{U}_q^{(3\phi)}$$

and the current sequence component on the stator reference frame are calculated according to (6.12). We have:

$$\begin{aligned}\bar{I}_1^{(3\phi)} &= \frac{1}{\sqrt{6}} \left(\bar{I}_d^{(3\phi)} + j\bar{I}_q^{(3\phi)} \right) e^{j\theta_0} = \frac{1}{2} (\bar{Y}_d + \bar{Y}_q) U_{\max} \\ \bar{I}_2^{(3\phi)} &= \frac{1}{\sqrt{6}} \left(\bar{I}_d^{(3\phi)} - j\bar{I}_q^{(3\phi)} \right) e^{-j\theta_0} = \frac{1}{2} (\bar{Y}_d - \bar{Y}_q) U_{\max} e^{-j2\theta_0}\end{aligned}$$

The *common mode admittance* and the *differential mode admittance* are introduced:

$$\bar{Y}_C = \frac{1}{2} (\bar{Y}_d + \bar{Y}_q) \quad \bar{Y}_\Delta = \frac{1}{2} (\bar{Y}_d - \bar{Y}_q) \quad (6.54)$$

so the stator current sequence components are given by:

$$\bar{I}_1^{(3\phi)} = \bar{Y}_C U_{\max} \quad \bar{I}_2^{(3\phi)} = \bar{Y}_\Delta U_{\max} e^{j2\theta_0} \quad (6.55)$$

It can be noticed that, from the current measurements, the common mode admittance can always be determined, whereas the differential mode one requires the prior determination of the rotor angle θ_0 .

Stand-still test with single-phase supply

The machine is supplied between phase U and phases V-W (connected together) with a single-phase voltage of amplitude V_{\max} . This configuration produces a pulsating air-gap along the phase U axis, so the rotor is naturally at stand-still. The line-voltage system can be decomposed into its positive and negative sequence component, according to (6.9):

$$\begin{vmatrix} \bar{V}_{UV}^{(1\phi)} \\ \bar{V}_{VW}^{(1\phi)} \\ \bar{V}_{WU}^{(1\phi)} \end{vmatrix} = \begin{vmatrix} V_{\max} \\ 0 \\ -V_{\max} \end{vmatrix} \rightarrow \begin{vmatrix} \bar{V}_1^{(1\phi)} \\ \bar{V}_2^{(1\phi)} \end{vmatrix} = \begin{vmatrix} \frac{(1 - \check{\omega}^2)}{3} V_{\max} \\ \frac{(1 - \check{\omega})}{3} V_{\max} \end{vmatrix} \quad (6.56)$$

The phase voltage sequence components are obtained considering that, by definition:

$$\bar{V}_1 = (1 - \check{\omega}^2) \bar{U}_1 \quad \bar{V}_2 = (1 - \check{\omega}) \bar{U}_2$$

so:

$$\bar{U}_1^{(1\phi)} = \bar{U}_2^{(1\phi)} = \frac{1}{3} V_{\max} \quad (6.57)$$

and thus the dq components of phase voltage are obtained, according to (6.10):

$$\begin{vmatrix} \bar{U}_d^{(1\phi)} \\ \bar{U}_q^{(1\phi)} \end{vmatrix} = \sqrt{\frac{3}{2}} \begin{bmatrix} e^{-j\theta_0} & e^{j\theta_0} \\ -je^{-j\theta_0} & je^{j\theta_0} \end{bmatrix} \begin{vmatrix} \bar{U}_1^{(1\phi)} \\ \bar{U}_2^{(1\phi)} \end{vmatrix} = \sqrt{\frac{2}{3}} V_{\max} \begin{vmatrix} \cos(\theta_0) \\ -\sin(\theta_0) \end{vmatrix} \quad (6.58)$$

The final expression in (6.58) has been obtained making use of the following identities:

$$\cos \alpha = \frac{e^{j\alpha} + e^{-j\alpha}}{2} \quad \sin \alpha = \frac{e^{j\alpha} - e^{-j\alpha}}{2j} \quad (6.59)$$

The dq components of current are obtained according to (6.52):

$$\bar{I}_d^{(1\phi)} = \bar{Y}_d \bar{U}_d^{(1\phi)} \quad \bar{I}_q^{(1\phi)} = \bar{Y}_q \bar{U}_q^{(1\phi)}$$

and so the current sequence components on the stator reference frame are calculated from (6.13)

$$\begin{aligned}\bar{I}_1^{(1\phi)} &= \frac{1}{3}V_{\max} (\bar{Y}_d \cos \vartheta_0 - j\bar{Y}_q \sin \vartheta_0) e^{j\vartheta_0} \\ \bar{I}_2^{(1\phi)} &= \frac{1}{3}V_{\max} (\bar{Y}_d \cos \vartheta_0 + j\bar{Y}_q \sin \vartheta_0) e^{-j\vartheta_0}\end{aligned}\quad (6.60)$$

From (6.54) it is obtained:

$$\bar{Y}_d = \bar{Y}_C + \bar{Y}_\Delta \quad \bar{Y}_q = \bar{Y}_C - \bar{Y}_\Delta \quad (6.61)$$

so (6.60) becomes:

$$\begin{aligned}\bar{I}_1^{(1\phi)} &= \frac{1}{3}V_{\max} (\bar{Y}_C + \bar{Y}_\Delta e^{j2\vartheta_0}) \\ \bar{I}_2^{(1\phi)} &= \frac{1}{3}V_{\max} (\bar{Y}_C + \bar{Y}_\Delta e^{-j2\vartheta_0})\end{aligned}\quad (6.62)$$

where the identities in (6.59) have been used again.

Admittance determination from tests

The common mode admittance can be directly determined from the three-phase test, according to (6.55):

$$\bar{Y}_C = \frac{\bar{I}_1^{(3\phi)}}{U_{\max}^{(3\phi)}} \quad (6.63)$$

where $\bar{I}_1^{(3\phi)}$ is the positive-sequence current phasor measured when the machine is supplied with a three phase voltage system, having phase voltage peak equal to $U_{\max}^{(3\phi)}$.

Rearranging the expression in (6.62) it can be written:

$$\bar{Y}_\Delta e^{j2\vartheta_0} = \frac{3\bar{I}_1^{(1\phi)}}{V_{\max}^{(1\phi)}} - \bar{Y}_C \quad \bar{Y}_\Delta e^{-j2\vartheta_0} = \frac{3\bar{I}_2^{(1\phi)}}{V_{\max}^{(1\phi)}} - \bar{Y}_C$$

and then, mutually multiplying these expression the rotor position dependency is eliminated, obtaining the differential mode admittance:

$$\bar{Y}_\Delta = \sqrt{\left[\frac{3\bar{I}_1^{(1\phi)}}{V_{\max}^{(1\phi)}} - \bar{Y}_C \right] \left[\frac{3\bar{I}_2^{(1\phi)}}{V_{\max}^{(1\phi)}} - \bar{Y}_C \right]} \quad (6.64)$$

Here $\bar{I}_1^{(1\phi)}$ and $\bar{I}_2^{(1\phi)}$ are, respectively, the positive and negative sequence component of the current measured when the machine is supplied between one phase terminal and the parallel connection of the remaining two with a sinusoidal voltage of peak amplitude equal to $V_{\max}^{(1\phi)}$.

Once the common and differential mode admittance are determined accordingly to (6.63) and (6.64) the axis admittances are calculated through (6.61) and, finally, the operational impedances are determined accordingly to (6.51).

7

STARTING MODEL CALCULATION

This chapter presents a FE-based method for the calculation of the synchronous motor starting circuit described in chapter 6. Particular focus is given to the case of solid rotor DOL SMs presented in chapter 5 and the calculation of their rotor equivalent cage parameters, because the analytical methods commonly found in the literature [40–42] are often heuristic and experience-based. Numerical methods, on the other hand, introduce an excessive computational burden [43–46], because the rotor eddy-current and the core saturation must be taken into account [57].

Despite what is commonly made in most of the literature FE-based methods, which focus on the complete starting simulation [46], the procedure herein described intends to calculate the starting circuit parameters, using a set of FEAs that reproduce the stand-still rotor tests described in section 6.2. More in detail, since the rotor angular position is known in this case, there is no need to perform the whole procedure presented in section 6.2.2 and the equivalent dq cage parameters can be identified through a simple three-phase excited model or a pair of single-phase excited models (one per axis). However, the single-phase excited models present an additional symmetry with respect to the three-phase excited one, so they can be further simplified, realizing a more efficient calculation procedure based on a half-pole model (whereas the three-phase excited model requires at least an entire pole geometry to be included in the problem domain). The equivalence of these two modeling strategy is discussed in section 7.1, whereas section 7.2 focuses on the precautions that have to be taken to simulate this complex problem with the simplest possible geometry. Finally, section 7.3 will verify the validity of the half-pole model strategy on a simple case (locked-rotor cage parameter calculation). The complete start-up simulation will be discussed in chapter 8.

7.1 METHOD OUTLINE

As pointed out in the previous chapter the SM start-up can be calculated through the two-axes circuit in figure 6.2, so the problem of starting performance calculation is reduced to determining the circuit parameters. Most of these parameters (R_s , X_s , X_{ad} , X_{aq} , R_f and X_f) can be analytically calculate through literature methods [58, 59], so this section is focused on the determination of the rotor cage parameters (R_{kd} , X_{kd} , R_{kq} and X_{kq}) by means of FEM.

The equivalent dq cage parameters can be calculated through a TH simulation at stand-still and open field winding, which allows to determine the operational impedances corresponding to the circuit from figure 6.3 (excluding the field-winding branch). The simulation frequency is sf_0 , with s the slip being investigated and f_0 the machine rated frequency. The cage

parameters variation during start-up is determined iterating the calculation procedure for different values of slip.

The practical calculation of operational impedances depends on the model excitation. The FE model is current-excited, as done for the IM case in section 3.1.3. Two current system can be adopted:

- a symmetric three-phase current system, that produce a rotating MMF field wave (see also section B.2 in appendix B);
- a single-phase current system between one phase terminal and the parallel connection of the others, that produce a pulsating MMF wave in the direction of the first phase axis (see also section B.3 in appendix B).

In both cases the operational impedances calculation depends on the stand-still current-excited model, which is slightly different from the one presented in section 6.2.2 (that is voltage-excited).

7.1.1 Three-phase excited model

If the three-phase current system is chosen as model excitation than, assuming a maximum value of current equal to I_{\max} then, accordingly to (6.10) the dq components of current are:

$$\begin{vmatrix} \bar{I}_d \\ \bar{I}_q \end{vmatrix} = \sqrt{\frac{3}{2}} \begin{vmatrix} 1 \\ -j \end{vmatrix} I_{\max} e^{-j\theta_0}$$

and thus the dq voltage components are obtained:

$$\bar{U}_d = (R_s + \bar{Z}_d) \bar{I}_d \quad \bar{U}_q = (R_s + \bar{Z}_q) \bar{I}_q$$

and the sequence components of stator phase voltage are calculated as per (6.13):

$$\bar{U}_1 = \left[R_s + \frac{\bar{Z}_d + \bar{Z}_q}{2} \right] I_{\max} \quad \bar{U}_2 = \left[\frac{\bar{Z}_d - \bar{Z}_q}{2} e^{j2\theta_0} \right] I_{\max}$$

and, finally, the U phase voltage is:

$$\bar{U} = \bar{U}_1 + \bar{U}_2 = \left[R_s + \bar{Z}_d \frac{1 + e^{-j2\theta_0}}{2} + \bar{Z}_q \frac{1 - e^{-j2\theta_0}}{2} \right] I_{\max}$$

This is the general expression for the phase voltage. However, since the rotor position is known in the FE model definition then it is useful assume $\theta_0 = 0$ and obtain:

$$R_s + \bar{Z}_d = \frac{\bar{U}}{I_{\max}} \Big|_{\theta_0=0} \quad (7.1)$$

whereas choosing $\theta_0 = \pi/2$ leads to:

$$R_s + \bar{Z}_q = \frac{\bar{U}}{I_{\max}} \Big|_{\theta_0=\frac{\pi}{2}} \quad (7.2)$$

Equations (7.1) and (7.2) show that the calculation of operational impedances can be made through two three-phase current-fed TH FEAs, one with the rotor aligned to phase U, the other one with rotor electrically orthogonal to

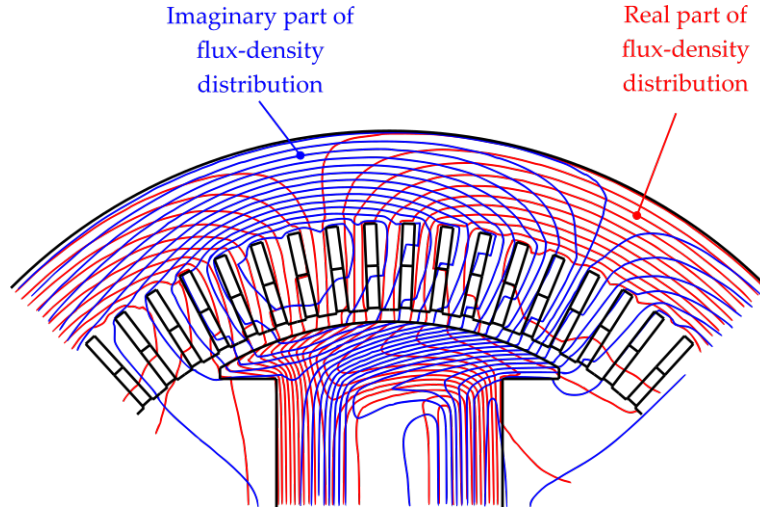


Figure 7.1: Flux-density complex distribution for a three-phase (rotating) system

phase U. Since all the parameters that define the operational impedances are known, except the cage parameters, then from the operational impedances the cage impedances are calculated as well. This procedure can be simplified observing that:

- the stator parameter R_s and X_s are known, so the stator geometry can be excluded from the FE model definition and the phase voltage \bar{U} can be calculated from the air-gap flux-density distribution;
- the temporal phase shift in a three-phase system corresponds to a spatial angular shift (see (B.26) in appendix B);
- the flux density distribution in a TH model is complex-valued.

The fact of excluding the stator geometry from the FE model will be discussed in section 7.2; for now is enough to notice that from this simplification the operational impedances given by equations (7.1) and (7.2) become:

$$\bar{Z}'_d = \frac{1}{\frac{1}{jsX_{ad}} + \frac{1}{R_{kd} + jsX_{kd}}} = \frac{\bar{U}}{I_{\max}} \Big|_{\theta_0=0} \quad (7.3a)$$

$$\bar{Z}'_q = \frac{1}{\frac{1}{jsX_{aq}} + \frac{1}{R_{kq} + jsX_{kq}}} = \frac{\bar{U}}{I_{\max}} \Big|_{\theta_0=\frac{\pi}{2}} \quad (7.3b)$$

so the cage parameters are simply given by:

$$R_{kd} + jsX_{kd} = \left(\frac{1}{\bar{Z}'_d} - \frac{1}{jsX_{ad}} \right)^{-1} \quad (7.4a)$$

$$R_{kq} + jsX_{kq} = \left(\frac{1}{\bar{Z}'_q} - \frac{1}{jsX_{aq}} \right)^{-1} \quad (7.4b)$$

The complex flux-density distribution is equivalent to two orthogonal (real) distributions, as shown in figure 7.1. As said before, in a rotating

MMF system, this orthogonality can be intended as temporal (i.e. the two distributions occur after a time shift of a quarter of period, that is the usual interpretation) or, equivalently, it can be assumed that they occur at the same time, but they are placed along orthogonal axes (in terms of electric angles). So, using this idea, a single model with the pole (direct) axis parallel to the first phase axis can be used to identify both axes impedances:

1. the *real* part of complex flux-density distribution is associated with the *direct* axis;
2. the *imaginary* part of complex flux-density distribution is associated with the *quadrature* axis.

More in detail, given the complex air-gap flux-density distribution its fundamental \bar{B}_g is obtained from the fundamental waves of real and imaginary part; assuming that the peak values of these fundamental are, respectively, $B_{g,Re}$ and $B_{g,Im}$ and they occur at an electric angle equal to $\alpha_{B,Re}$ and $\alpha_{B,Im}$, respectively, then it can be written:

$$\bar{B}_g(\alpha) = [B_{g,Re} \cos(N_{pp}\alpha - \alpha_{B,Re})] + j [B_{g,Im} \cos(N_{pp}\alpha - \alpha_{B,Im})] \quad (7.5)$$

assuming α as mechanical angle and $\alpha = 0$ on the phase U axis. Now, considering that for a spatial flux-density distribution like $B_{max} \cos(N_{pp}\alpha - \varphi_0)$ the total flux-linkage phasor is:

$$\bar{\Psi} = k_w N_{tph} \frac{2}{\pi} \tau_p \ell_{gap} B_{max} e^{j\varphi_0}$$

then, letting

$$K_\Psi = \frac{2}{\pi} k_w N_{tph} \tau_p \ell_{gap} \quad (7.6)$$

the phase voltages associated with the two axes are obtained from the FE model solution according to expression (7.5):

$$\bar{U} \Big|_{\vartheta_0=0} = j\omega_0 K_\Psi B_{g,Re} e^{j\alpha_{B,Re}} \quad (7.7a)$$

$$\bar{U} \Big|_{\vartheta_0=\frac{\pi}{2}} = j\omega_0 K_\Psi B_{g,Im} e^{j\alpha_{B,Im}} \quad (7.7b)$$

and so the operational impedances from the three-phase current excited model are calculated as:

$$\bar{Z}'_d = \frac{j\omega_0 K_\Psi B_{g,Re} e^{j\alpha_{B,Re}}}{I_{max}} \quad (7.8a)$$

$$\bar{Z}'_q = \frac{j\omega_0 K_\Psi B_{g,Im} e^{j\alpha_{B,Im}}}{I_{max}} \quad (7.8b)$$

and finally the cage impedances are calculated according to (7.4).

7.1.2 Single-phase excited model

The model excited by means of a single-phase system of currents is subjected to a pulsating magnetic field in the direction of the input phase¹. Supplying the machine with a maximum current I_{\max} entering the U terminal and assuming the current equally split between phases V and W then the positive and negative sequence of current are obtained:

$$\begin{bmatrix} \bar{I}_U \\ \bar{I}_V \\ \bar{I}_W \end{bmatrix} = \begin{bmatrix} 1 \\ -1/2 \\ -1/2 \end{bmatrix} I_{\max} \quad \longrightarrow \quad \bar{I}_1 = \bar{I}_2 = \frac{1}{2} I_{\max}$$

then from (6.10) the dq currents are obtained:

$$\begin{bmatrix} \bar{I}_d \\ \bar{I}_q \end{bmatrix} = \sqrt{\frac{3}{2}} \begin{bmatrix} e^{-j\vartheta_0} & e^{j\vartheta_0} \\ -je^{-j\vartheta_0} & je^{j\vartheta_0} \end{bmatrix} \begin{bmatrix} \bar{I}_1 \\ \bar{I}_2 \end{bmatrix} = \sqrt{\frac{3}{2}} \begin{bmatrix} \cos \vartheta_0 \\ -\sin \vartheta_0 \end{bmatrix} I_{\max}$$

and the corresponding phase voltage:

$$\bar{U}_d = (R_s + \bar{Z}_d) \bar{I}_d \quad \bar{U}_q = (R_s + \bar{Z}_q) \bar{I}_q$$

so from (6.13) the sequence component of the stator phase voltage are obtained:

$$\begin{aligned} \bar{U}_1 &= \frac{1}{2} I_{\max} \left[R_s + \frac{\bar{Z}_d + \bar{Z}_q}{2} + \frac{\bar{Z}_d - \bar{Z}_q}{2} e^{j2\vartheta_0} \right] \\ \bar{U}_2 &= \frac{1}{2} I_{\max} \left[R_s + \frac{\bar{Z}_d + \bar{Z}_q}{2} + \frac{\bar{Z}_d - \bar{Z}_q}{2} e^{-j2\vartheta_0} \right] \end{aligned}$$

and, finally, the phase U voltage is given by:

$$\bar{U} = \bar{U}_1 + \bar{U}_2 = I_{\max} \left[R_s + \frac{\bar{Z}_d + \bar{Z}_q}{2} + \frac{\bar{Z}_d - \bar{Z}_q}{2} \cos(2\vartheta_0) \right]$$

The axis impedances are determined by suitably choosing the rotor axis angle ϑ_0 , like in the three phase case:

1. the choice $\vartheta_0 = 0$ identifies the direct axis:

$$R_s + \bar{Z}_d = \left. \frac{\bar{U}}{I_{\max}} \right|_{\vartheta_0=0}$$

2. the choice $\vartheta_0 = \pi/2$ identifies the quadrature axis:

$$R_s + \bar{Z}_q = \left. \frac{\bar{U}}{I_{\max}} \right|_{\vartheta_0=\frac{\pi}{2}}$$

As for the three-phase case, the model can be simplified removing the stator, so the actual cage parameters are calculated accordingly to (7.3) and (7.4) as well.

In this case the equivalence between spatial angular displacement and time phase shift is not applicable (see (B.32) in appendix B) so two distinct models, with orthogonal axis configuration, must be adopted; however, in section 7.1.3 it will be shown that these models can be further reduced with respect to the three phase case, obtaining an overall improvement of the computational cost.

¹ Once again, a single phase system is realized by supplying the machine between one phase terminal, considered as input terminal, and the parallel connection of the remaining two phase terminals, i.e. the output terminal of the single phase circuit

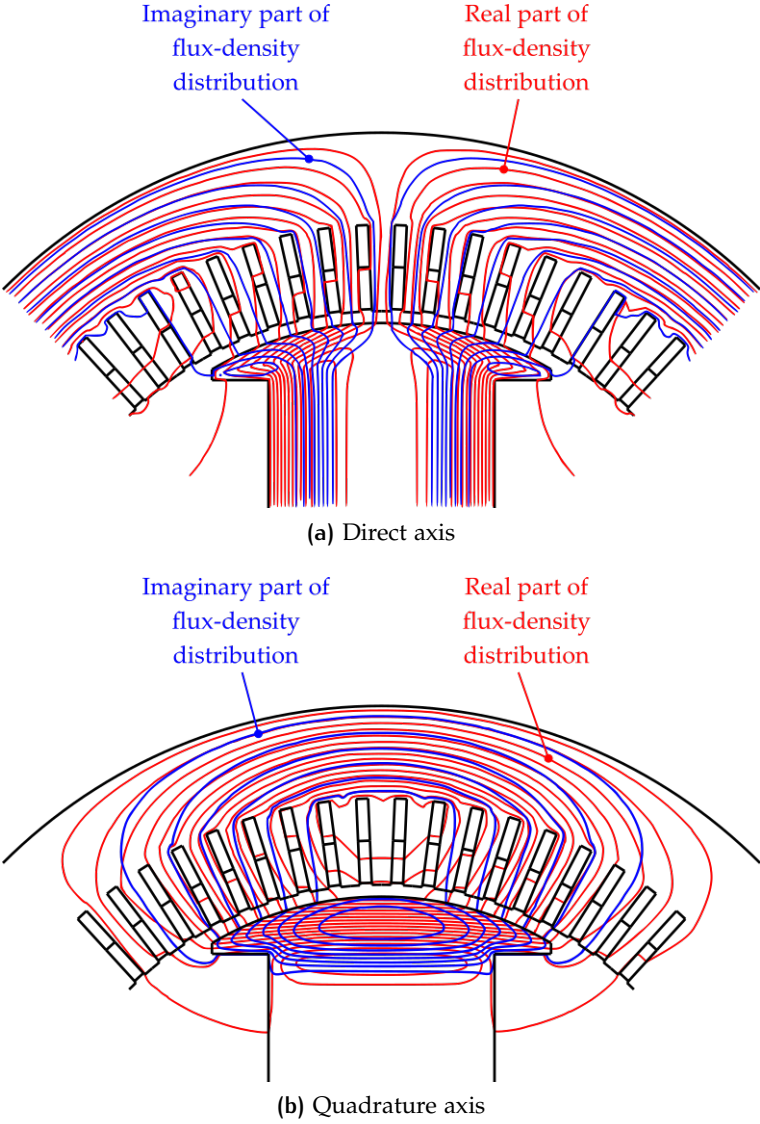


Figure 7.2: Flux-density complex distribution for a single-phase (pulsating) system

The flux-density distribution in the single-phase excited models is still complex and both real and imaginary air-gap distributions have their fundamental aligned with the input phase axis, as shown in figure 7.2; the fundamental for the two axes can be expressed as:

$$\bar{B}_{g,d}(\alpha) = [B_{d,Re} + jB_{d,Im}] \cos(N_{pp}\alpha) \quad (7.9a)$$

$$\bar{B}_{g,q}(\alpha) = [B_{q,Re} + jB_{q,Im}] \cos\left(N_{pp}\alpha - \frac{\pi}{2}\right) \quad (7.9b)$$

so the flux linkages are computed as:

$$\bar{\Psi}_d = j\omega_0 K_\Psi (B_{d,Re} + jB_{d,Im})$$

$$\bar{\Psi}_q = j\omega_0 K_\Psi (B_{q,Re} + jB_{q,Im})$$

with K_Ψ given by (7.6). The axis impedances from the reduced single-phase excited model are finally given by:

$$\bar{Z}'_d = \frac{j\omega_0 K_\Psi (B_{d,Re} + jB_{d,Im})}{I_{max}} \quad (7.10a)$$

$$\bar{Z}'_q = \frac{j\omega_0 K_\Psi (B_{q,Re} + jB_{q,Im})}{I_{max}} \quad (7.10b)$$

and, again, the cage impedances are calculated as per (7.4).

7.1.3 Model comparison

Observing figures 7.1 and 7.2 it can be noticed that the flux-density distribution in the three-phase excited model is not symmetric with respect to the rotor pole axis; in the case of single-phase excited model, instead, when the phase U axis is aligned with either the direct or the quadrature rotor axis, the flux-density distribution is symmetric with respect to the rotor pole axis. This fact implies that the single-phase excited models can be simplified, including just one half of the pole geometry in the model definition and suitably choosing the boundary conditions on the pole and inter-pole axes, in order to guarantee the solution symmetry. This fact will be further discussed in section 7.2. The symmetry makes the single-phase excited model more cost-efficient than the three-phase one, although the former requires two models to be solved. In fact, since the computation time for a FEA solution is approximately proportional to the square of the number of nodes in the FE model and the half-pole model has, approximately, half of the nodes of a full-pole model, than the proper choice of two half-pole single-phase excited models would lead to a computational cost of about 50% compared to the standard three-phase model. This justifies the introduction of the single-phase excitation strategy, as pointed out in figure 7.3. The two modeling strategies are also summarized and compared in table 7.1.

7.2 MODEL SET-UP

7.2.1 Excitation and boundary conditions

Figure 7.4 show a sketch of the stator-less FE models adopted for the identification of cage axes parameters. In particular, both the three-phase

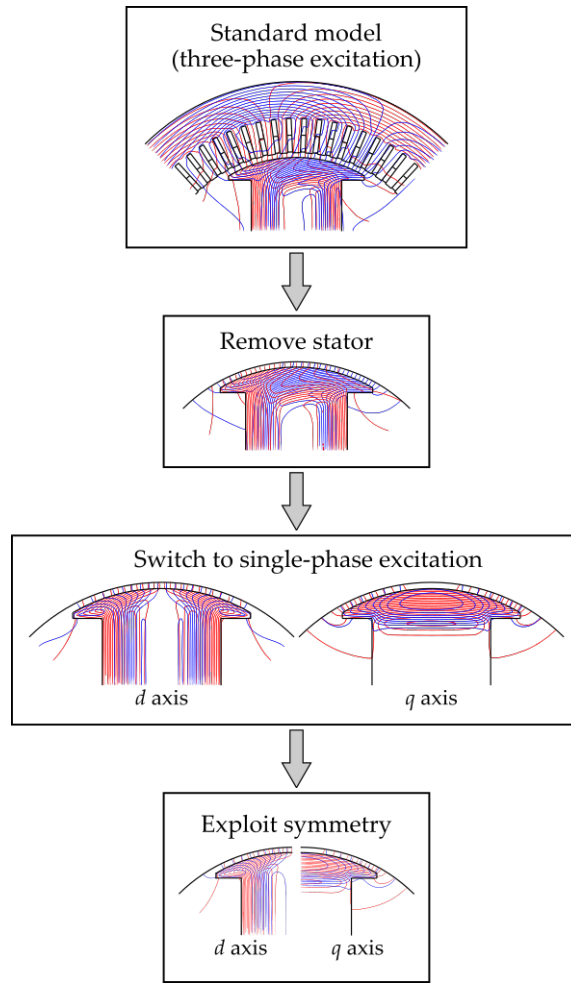
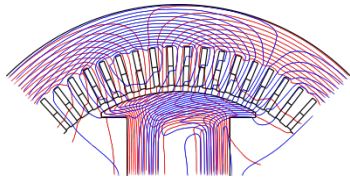
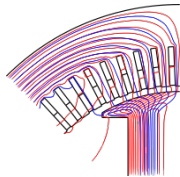
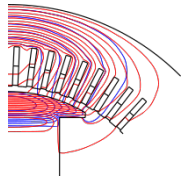
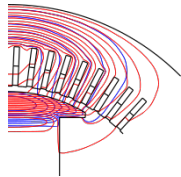


Figure 7.3: Logic simplification of synchronous machine FE modeling for cage parameters calculation

Table 7.1: Comparison between three-phase excited and single-phase excited FE models

Excitation	Three-phase		Single-phase	
	<i>d</i>	<i>q</i>	<i>d</i>	<i>q</i>
Axis				
Field	Rotating		Pulsating	
				
$\bar{F}(\alpha)$	$F_{\max} e^{-jN_{pp}\alpha}$		$F_{\max} \cos(N_{pp}\alpha)$	$F_{\max} \sin(N_{pp}\alpha)$
$\text{Re} \{ \bar{B}(\alpha) \}$	$B_1 \cos(N_{pp}\alpha - \alpha_1)$		$B_1 \cos(N_{pp}\alpha)$	$B_1 \sin(N_{pp}\alpha)$
$\text{Im} \{ \bar{B}(\alpha) \}$	$B_2 \cos(N_{pp}\alpha - \alpha_2)$		$B_2 \cos(N_{pp}\alpha)$	$B_2 \sin(N_{pp}\alpha)$
$\bar{\Psi}$	$K_{\Psi} B_1 e^{-j\alpha_1}$	$K_{\Psi} B_2 e^{-j\alpha_2}$	$K_{\Psi} [B_1 + jB_2]$	$K_{\Psi} [B_1 + jB_2]$

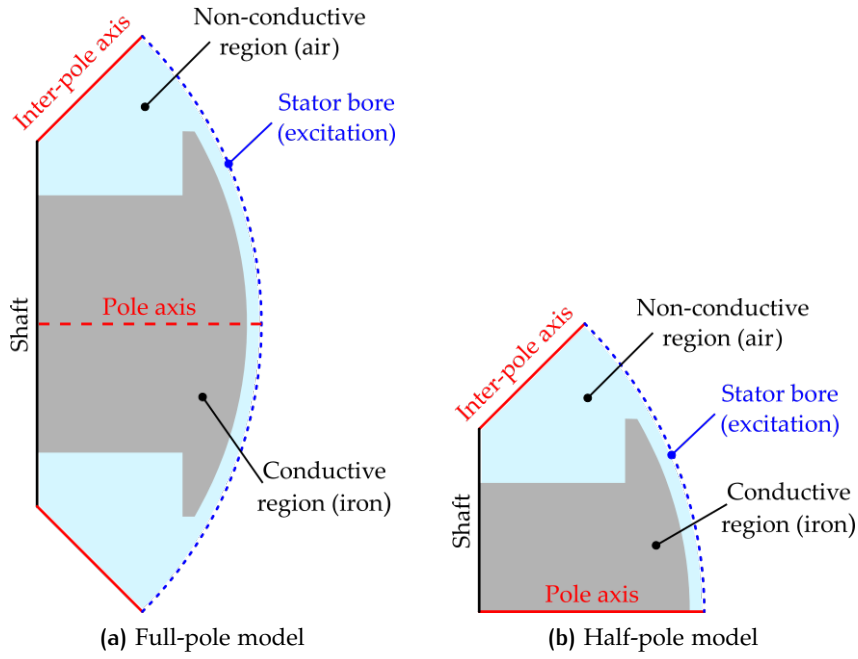


Figure 7.4: FE models for cage parameters calculation

excited model (7.4a) and the single-phase excited model (7.4b) are shown. These model share some similarities:

- on the shaft and bore boundaries a *Neumann BC* is assumed, i.e. the flux-lines are orthogonal to these contours, because they are an interface with regions at infinite permeability;
- the model excitation is provided through a suitable distribution of current points along the bore circumference, which realizes the stator MMF fundamental corresponding to a given stator current. The stator MMF is rotating, according to (B.23), if the full pole model is adopted, whereas it is pulsating, as in (B.32), in the case of half-pole model. In both cases, if the stator is supplied with a peak current equal to I_{\max} , the MMF fundamental peak value is given by:

$$F_{\max} = \frac{6}{\pi} \frac{k_w N_{\text{tph}}}{N_p} I_{\max} \quad (7.11)$$

so the rotating MMF spatial phasor is given by:

$$\bar{F}_{3\phi}(\alpha) = F_{\max} e^{-jN_{\text{pp}}\alpha} \quad (7.12)$$

whereas the pulsating MMF spatial phasor is:

$$\bar{F}_{1\phi}(\alpha) = F_{\max} \cos(N_{\text{pp}}\alpha - \varphi_0) \quad (7.13)$$

with $\varphi_0 = 0$ if the stator axis is aligned to pole axis (for direct axis parameters calculation) and $\varphi_0 = \pi/2$ if the stator axis is orthogonal to pole axis (for quadrature axis parameters calculation).

The MMF distribution is realized through a discrete set of current points. Assuming N equally-spaced points then the current in any point is given by:

$$I_\nu = \frac{\partial F(\alpha_\nu)}{\partial \alpha} d\alpha \quad \text{with } \nu = 1, 2, \dots, N$$

Table 7.2: Current point distribution expressions for different models

	Three-phase Full pole	Single-phase Full pole	Single-phase Half pole
ν	$1, 2, \dots, 2N$	$1, 2, \dots, 2N$	$1, 2, \dots, N$
F_{\max}		$\frac{6}{\pi} \frac{k_w N_{\text{tph}}}{N_p} I_{\max}$	
$F(\alpha)$	$F_{\max} e^{-jN_{\text{pp}}\alpha}$	$F_{\max} \cos(-jN_{\text{pp}}\alpha - \varphi_0)$	$F_{\max} \cos(-jN_{\text{pp}}\alpha - \varphi_0)$
α_ν	$\frac{2\nu - 2N - 1}{2N} \frac{\pi}{N_p}$	$\frac{2\nu - 2N - 1}{2N} \frac{\pi}{N_p}$	$\frac{2\nu - 2N - 1}{2N} \frac{\pi}{N_p}$
$I_{\nu, \max}$		$\frac{3}{N} \frac{k_w N_{\text{tph}}}{N_p} I_{\max}$	
I_ν	$-jI_{\nu, \max} e^{-jN_{\text{pp}}\alpha_\nu}$	$I_{\nu, \max} \sin(N_{\text{pp}}\alpha_\nu - \varphi_0)$	$I_{\nu, \max} \sin(N_{\text{pp}}\alpha_\nu - \varphi_0)$

with $d\alpha$ the angular distance between two adjacent points, that are placed at angles α_ν . The actual expression for the current point distribution is explicitated in table 7.2 for all the possible modeling strategies discussed in section 7.1 (three or single-phase excitation, full or half pole). It is worth noticing that, in order to have the same resolution for the models with full pole geometry is necessary double the points with respect to the half pole model. The rotor pole axis is assumed as reference direction for the α_ν angles.

The main difference between the single-pole model and the half-pole one regards the boundary conditions to be associated with the pole and inter-pole axes:

1. in the full-pole model an *anti-periodic BC* is imposed on both the inter-pole axes and no conditions are specified for the pole-axis;
2. in the single pole model the conditions on pole and inter-pole axes depend on the axis that is being considered:
 - for the d axis, as it can be seen in figure 7.2a, the flux lines are parallel to pole axis and orthogonal to the inter-pole one, so a *Dirichlet BC* must be chosen for the former axis, whereas a *Neumann BC* is assumed for the latter;
 - for the q axis the flux-lines distribution are parallel to inter-pole axis and orthogonal to the pole one, so the boundary conditions are switched with respect to the previous case.

7.2.2 Materials properties correction

The materials properties in the model have to be adjusted for considering the different regions axial length, as done for the induction motor study in table 3.1; furthermore, the pole conductivity has to be modified in order to take into account two additional effects:

- the rotor surface grooving (see chapter 5);

Table 7.3: Literature conductivity correction factors for finite length effects

Source	Expression	μ_r	$K_{\sigma,\ell}$	$K_{\sigma,\ell}K_{\sigma,G}$
Russell [61]	$\left(1 - \frac{1}{\zeta} \frac{\tanh \zeta}{1 + \tanh \zeta}\right)^2$	any	0.700	0.213
O'Kelly [62]	$\left(1 + \frac{\tau}{\ell_{r,\text{tot}}}\right)^{-2}$	any	0.436	0.133
Gibbs [63]	$\left(1 + \frac{1}{\zeta}\right)^{-2}$	any	0.567	0.173
Yee [64]	$\left\{ \frac{a\ell_{r,\text{tot}} \left[1 + \coth\left(\frac{\pi\ell_{r,\text{tot}}}{2\tau_p}\right) \right]^{-2}}{a\ell_{r,\text{tot}} \left[1 + \coth\left(\frac{\pi\ell_{r,\text{tot}}}{2\tau_p}\right) \right]} \right\}^2$	any	0.700	0.213
		1	0.437	0.133
Fu [65]	$\left(1 + \frac{\tau_p}{\ell_{r,\text{tot}}}\right)^{-2} \left(\frac{1 + \lambda^2 g_{\text{avg}} \mu_r \delta}{1 + a^2 g_{\text{avg}} \mu_r \delta}\right)^2$	5	0.441	0.134
		10	0.441	0.134
		50	0.482	0.147
		100	0.514	0.157
		500	0.614	0.187
		1000	0.648	0.197

- the finite length of the solid core.

Both effect are calculated using conductivity correction factor provided by the literature. The model core conductivity is finally given by:

$$\sigma' = K_{\sigma,G} K_{\sigma,\ell} \sigma \quad (7.14)$$

with σ being the actual core conductivity (corrected accordingly to table 3.1) and $K_{\sigma,G}$, $K_{\sigma,\ell}$ are the conductivity correction factors accounting for the surface grooving and the finite-length effects, respectively.

The groove correction factors for d and q axis are given by [60]:

$$K_{\sigma,G,d} = \left[1 + \frac{0.526\gamma_{ps}\tau_p + N_G(2h_G + \ell_G)}{\ell_{r,\text{tot}}} \right]^{-1} \quad (7.15a)$$

$$K_{\sigma,G,q} = \left[1 + \frac{2(h_{ps} + h_{pb}) + \tau'_p + N_G(2h_G + \ell_G)}{\ell_{r,\text{tot}}} \right]^{-1} \quad (7.15b)$$

$$(7.15c)$$

As total correction factor the average of the two values in (7.15) is assumed. For the salient-pole machine examined in chapter 8 we have:

$$K_{\sigma,G,d} = 0.316 \quad K_{\sigma,G,q} = 0.293 \quad K_{\sigma,G} = 0.305$$

Several finite-length correction factor are available in literature [66]; they are examined and collected in table 7.3, assuming the following definitions:

$$a = \frac{\pi}{\tau_p} \zeta = \frac{\pi \ell_{r,tot}}{2\tau_p}$$

$$\lambda = a \sqrt{1 + \left(\frac{\tau_p}{\ell_{r,tot}} \right)^2}$$

$$\delta = \sqrt{\frac{\sigma \mu_r \mu_0 \omega_0}{2}}$$

Table 7.3 also reports the total conductivity correction factors (calculated with different methods) for the reference salient-pole machine examined in chapter 8. It can be noticed that the total pole conductivity must be reduced to about 20% of the physical value, so hereinafter this correction factor will be considered for all the models.

7.3 MODEL EQUIVALENCE CHECK

In order to verify the simplification procedure described in figure 7.3 the dq axis cage parameters for the machine analyzed in chapter 8 are calculated using four different TH-FE strategies:

1. a single standard model, with the stator geometry included;
2. a single three-phase rotor-focused model, with a full pole geometry;
3. a pair of single-phase rotor-focused models, with full pole geometry;
4. a pair of single-phase rotor-focused models, with half pole geometry;

All these models are current-excited. The Locked-Rotor Current (LRC) obtained from a test on machine from chapter 8 has been considered as source current for the models. The test was performed at 25% of the machine rated voltage and the measured current was close to the rated one.

As a further validation of the proposed methods, the parameters obtained from FEM are used to compute the Locked-Rotor Torque (LRT) and LRC through (6.43) and (6.45) respectively; these results are compared with the experimental data.

Figure 7.5 and table 7.4 show the outcome of the four calculation methods. From figure 7.5 it can be noticed that all the calculated parameters are comparable and lead to LRT and LRC values close to the experimental ones. The torque error from the half-pole model method is higher than the other methods, but the current error is the least. Table 7.4 also reports the computation statistics. For the single-phase excited methods two models need to be solved; in order to make a better comparison with the full pole models the number of nodes and elements reported in table 7.4 correspond to a single model, but the computation time consider the total amount needed for the two models, as they are solved subsequently. It can be noticed that, even

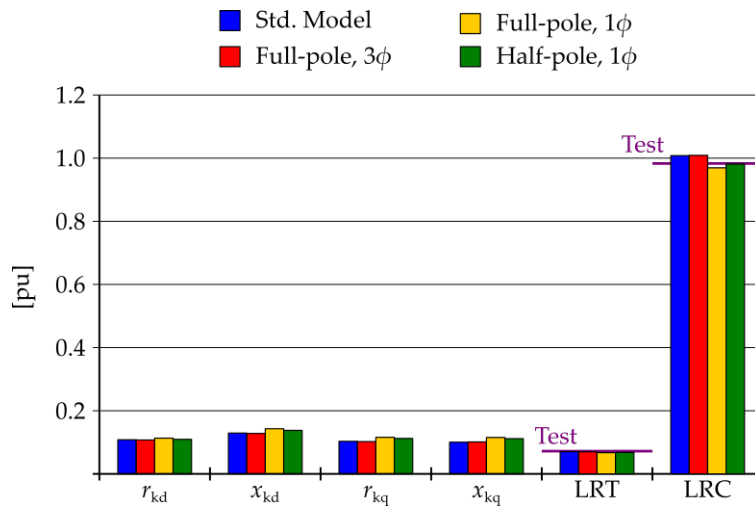


Figure 7.5: Locked-rotor parameters calculated with different methods

Table 7.4: Locked rotor test calculation results and statistics

	Standard model	Full-pole, 3φ	Full-pole, 1φ	Half-pole, 1φ
r_{kd}	0.108 pu	0.107 pu	0.113 pu	0.109 pu
x_{kd}	0.129 pu	0.128 pu	0.143 pu	0.138 pu
r_{kq}	0.103 pu	0.102 pu	0.116 pu	0.112 pu
x_{kq}	0.101 pu	0.101 pu	0.115 pu	0.112 pu
LRT	0.070 pu	0.070 pu	0.067 pu	0.068 pu
LRC	1.008 pu	1.009 pu	0.969 pu	0.981 pu
ε_{LRT}	-2.4 %	-3.1 %	-6.5 %	-5.8 %
ε_{LRC}	2.5 %	2.6 %	-1.4 %	-0.2 %
Nodes	8784	6552	6552 ^(a)	3138 ^(a)
Elements	17 300	12 664	12 664 ^(a)	6063 ^(a)
Computation time	23 s	19 s	24 s ^(b)	9 s ^(b)
	100 %	83 %	104 % ^(b)	39 % ^(b)

^(a) For a single model^(b) For the two models

though there are twice the models, the computation time is less than 40 % with respect to a standard model and about 50 % if compared to a stator-less three-phase model. Clearly, if the two half-pole models are solved simultaneously (i.e. parallel computing is employed) the time saving obtained performing the half-pole method is about 80 % with respect to the standard model computation time.

In this chapter the half-pole method to compute equivalent cage parameters presented in chapter 7 is applied to characterize the whole start-up of a 4-pole synchronous motor with solid salient-poles. The four cage parameters (resistance and reactance for the direct and quadrature axes) at different frequencies (i.e. at different rotor speeds) are evaluated, using this method, in section 8.1 The rotor field winding AC resistance is evaluated as well, by means of a suitable set of TH-FEAs. The problem of dealing with the calculation of these parameters at a given voltage using a current-excited model is solved considering an iterative method, similarly to what has been done for induction motors in section 3.1.3. The machine starting torque and current are then calculated (section 8.2) according to the two-axis model presented in chapter 6; two approaches have been considered:

- the cage parameters are used to determine line current, average torque and torque pulsation at different speed values through the quasi-steady-state approach in section 6.1.3;
- the cage parameters vs speed characteristic is embedded in a lumped-parameter time-domain model of the synchronous motor, based on the standard two-axis theory from section 6.1.2

The outcomes of these two calculation approaches are finally compared with the experimental data and with the results obtained from a transient FEA as well (section 8.3).

8.1 START-UP ROTOR PARAMETER CALCULATION

The calculation of the dq cage parameters for different speed values has been presented in chapter 7; it is worth noticing that this calculation method uses the stator current as input parameter; however, this value is usually expected as a result of the start-up calculation, whereas the voltage is assumed as input variable. Thus an iterative calculation procedure must be adopted, which assumes a first guess for the stator current, uses it to estimate the rotor parameters and, through the two-axis circuit solution, evaluates the voltage; the result is compared with the actual desired stator voltage U_{ref} and, if the difference is above a certain tolerance threshold, the input current is modified and the procedure is repeated until the voltage convergence is obtained.

The overall procedure is summarized in figure 8.1. The calculation of the cage parameters (R_{kd} , X_{kd} , R_{kq} , X_{kq}) has been extensively covered in the previous chapter, so in the following the remaining part of the flow chart will be explained.

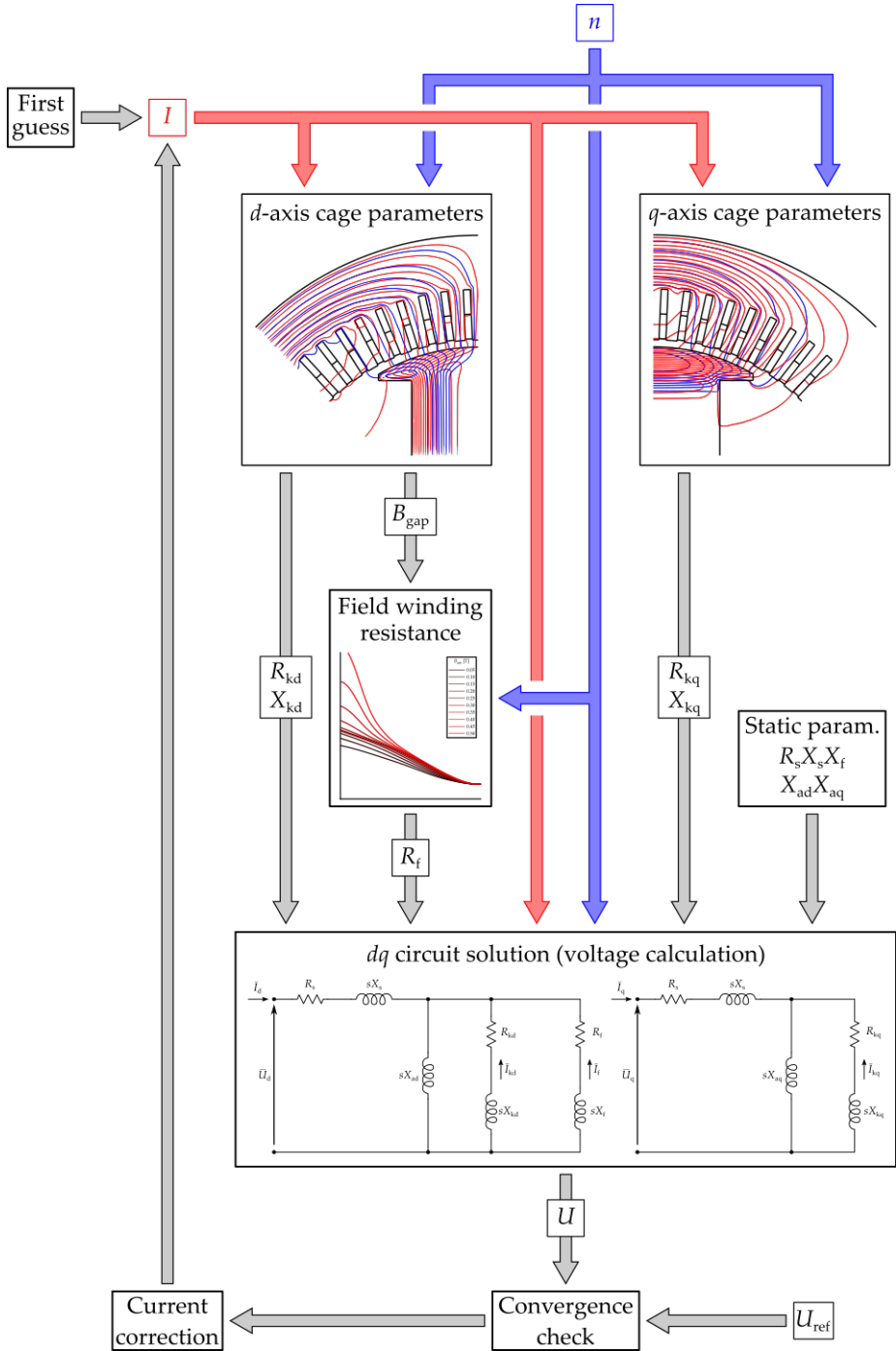


Figure 8.1: Calculation procedure for DOL synchronous machine dq circuit evaluation at speed n and stator voltage U_{ref}

8.1.1 Field winding resistance calculation

The AC field winding resistance is evaluated by means of a suitable set of TH FEAs. The FE model set-up is similar to the model for the d -axis cage identification discussed in section 7.2.1; in particular it has the same BCs on the shaft, pole and inter-pole boundaries and the same physical properties corrections. The main differences are the following:

- the field winding elementary conductor geometry was not explicitly drawn in the cage calculation model, but clearly it has to be included in this one, since we are interested in the winding AC resistance calculation;
- the new model excitation is not provided by the current-points distribution along the bore boundary, even if the *Neumann* condition is still assumed on this line; instead, a proper current value supplies the field winding and realizes the model excitation.

The field winding AC resistance is obtained considering the total joule loss on the elementary conductors and it is defined as the lumped resistance value that realizes the same power dissipation when it is supplied with the total winding current. The winding loss is evaluated from the FEA results, taking into account the fact that half of a pole is actually modeled, so:

$$P_{jr,AC} = 2N_p \ell_{rtu} \iint \rho J^2 dS$$

where the double integral is extended to all the wire sections included in the model. The resistance value is

$$R_{f,AC} = \frac{P_{jr,AC}}{I_f^2} \quad (8.1)$$

being I_f the RMS-value of the model excitation current (referred to the stator, so the calculated resistance is stator-referred as well).

It can be noticed that, actually, the field winding current is not known *a priori*, since it has to be obtained from the dq circuit solution, which, in turn, depends on the field winding AC resistance. Thus the proper value of current that has to be adopted in the model for taking into account the saturation effects should be determined through a non-linear iterative solution, as proposed per the cage parameters. This would complicate the overall procedure and increase the total computation time. However, such non-linearity can be bypassed defining a suitable look-up table prior to the main procedure solution.

The look-up table construction starts with an exploration grid of speed and field winding current values, at which the model is solved and the AC resistance is calculated accordingly to (8.1); the air-gap flux-density fundamental (B_{gap}) is evaluated at each node of the grid as well. The exploration grid should be constructed assuming a certain number of speed steps between zero and the rated speed value, whereas the current values should be chosen between the rated one and 6-8 times the latter. This assumption ensures that, most likely, the actual field current trajectory at start-up is included in the exploration grid of the look-up table.

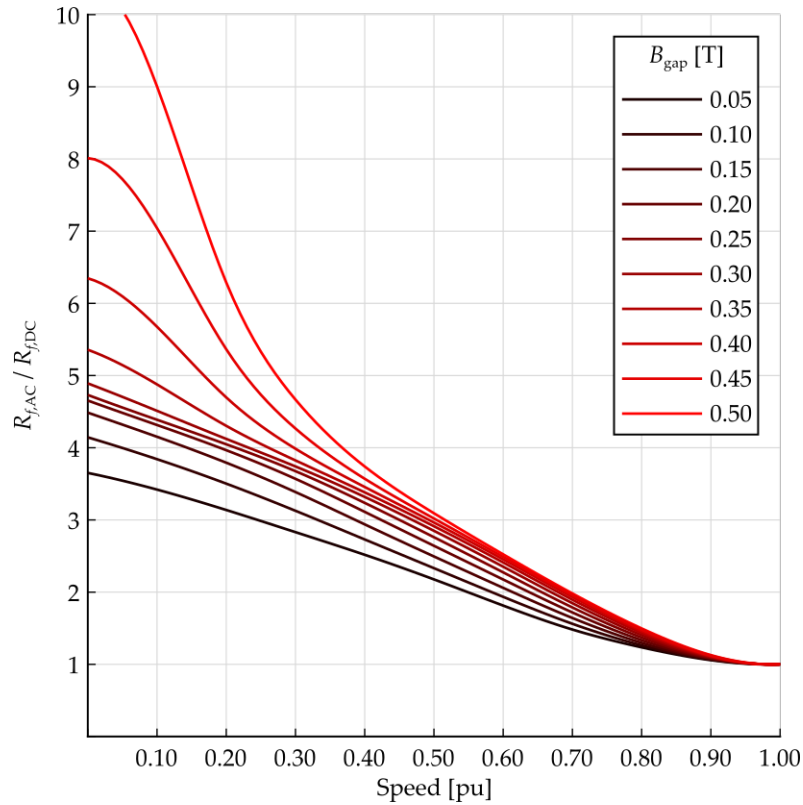


Figure 8.2: Field winding resistance vs Speed look-up table at different flux-density working points

Since, for any speed value, B_{gap} depends monotonically on the field winding current then the AC resistance surface determined from the exploration grid (which is speed and current dependent) can be re-defined as a function of speed and flux-density fundamental. Clearly the speed- B_{gap} matrix can be made more regular interpolating among the previously calculated points. A new look up table for the field winding resistance is therefore obtained, which maps any given speed-flux-density pair into a certain resistance value. Such look up table for the reference synchronous motor is drawn in figure 8.2 as a family of resistance-vs-speed plots parametrized with respect to the B_{gap} values.

This look-up table is used, in the start-up calculation process, to properly take into account the effect of saturation along direct axis on the field winding resistance; for any speed value being investigated the flux-density fundamental obtained from the d -cage model solution is used to determine the corresponding field winding resistance value, according to fig. 8.2.

8.1.2 Static parameters

Some of the parameters from the dq circuits in figure 6.2 can be assumed as static, i.e. they do not depend on the actual speed value. These parameters are:

- the stator parameters R_s and X_s ;
- the magnetization reactances X_{ad} and X_{aq} ;

Table 8.1: Static dq parameters for the reference DOL machine

Parameter	Symbol	Value [pu]
Stator resistance	r_s	0.0029
Stator leakage reactance	x_s	0.1494
Direct-axis magnetizing reactance	x_{ad}	2.2655
Quadrature-axis magnetizing reactance	x_{aq}	1.0868
Field winding leakage reactance	x_f	0.2347

- the field winding leakage reactance.

Their values can be calculated through well known literature methods [58, 59, 67]. The static parameters for the reference SM are collected in table 8.1.

8.1.3 Iterative calculation

As said before the starting parameter identification is an iterative procedure, which cycles on different values of current until the actual stator voltage is obtained. For any speed value being explored, the given current value I is used to compute the equivalent cage parameters according to the procedure presented in section 7.1.2, with the half-pole models; from the d -axis model the flux-density fundamental is obtained as well and, thus, the field winding resistance is evaluated as explained in section 8.1.1. Combining these results with the static parameters from section 8.1.2 the operational impedances are calculated according to (6.50) and then the stator voltage is obtained:

$$\bar{U}_d = (R_s + Z_d)I \quad \bar{U}_q = (R_s + Z_q)I \quad (8.2)$$

$$U = \frac{1}{2\sqrt{3}}|\bar{U}_d + j\bar{U}_q| \quad (8.3)$$

This value is compared with the actual desired reference voltage (for instance, the rated voltage) and if the difference is above a chosen tolerance threshold, the current value is adjusted through a quasi-Newton algorithm; Broyden method [30] can be employed in this case as well, to reduce the number of simulation that are performed. The above procedure is repeated until the convergence is obtained.

This calculation performed on the reference SM at rated voltage has given the results collected in table 8.2.

8.2 START-UP PERFORMANCE CALCULATION

Two methods can be adopted to predict the synchronous machine start-up performance:

1. the quasi-stationary dq -model from section 6.1.3 is solved for a sequence of speed values from zero to rated speed, like presented in [55];

Table 8.2: Rotor cage and field winding parameters for start-up at rated voltage

Speed [pu]	r_{kd} [pu]	x_{kd} [pu]	r_f [pu]	r_{kq} [pu]	x_{kq} [pu]
0.000	0.0698	0.0896	0.00465	0.0614	0.0515
0.150	0.0657	0.0935	0.00412	0.0572	0.0560
0.300	0.0605	0.1002	0.00351	0.0520	0.0618
0.450	0.0551	0.1073	0.00290	0.0478	0.0707
0.600	0.0490	0.1198	0.00225	0.0420	0.0835
0.750	0.0417	0.1417	0.00157	0.0350	0.1072
0.900	0.0317	0.2034	0.00104	0.0258	0.1883
0.925	0.0294	0.2264	0.00098	0.0235	0.2275
0.950	0.0268	0.2545	0.00095	0.0208	0.3011
0.975	0.0234	0.2376	0.00091	0.0175	0.5154

2. the standard model from section 6.1.2 is solved in the time domain, considering the circuit parameters as a function of the speed.

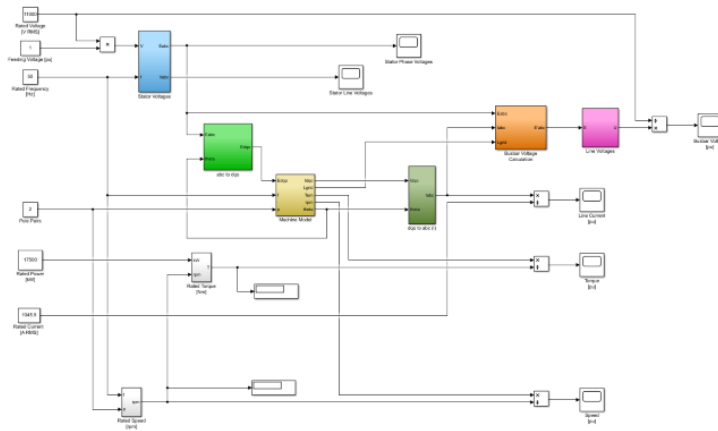
Both of these approaches require the preliminary identification of the rotor parameters at start up, using the numerical procedure described in section 8.1, that has to be performed for a proper discrete set of different speed values, from zero to rated speed. The quasi-stationary model has been extensively covered in section 6.1.3, so just the time-domain simulation will be quickly covered in the following.

Figure 8.3 shows the schematic representation of the complete start-up block-diagram. The machine is modeled by means of a Lumped Parameter (LP) circuit, whose parameters are considered as a function of the slip (see fig. 8.3c). The mechanical equation in (6.18) has to be included in the machine model as well. In order to take into account the supply voltage drop during the start-up the grid equivalent reactance has to be added to the stator reactance in both the quasi-stationary model and the time-domain simulation.

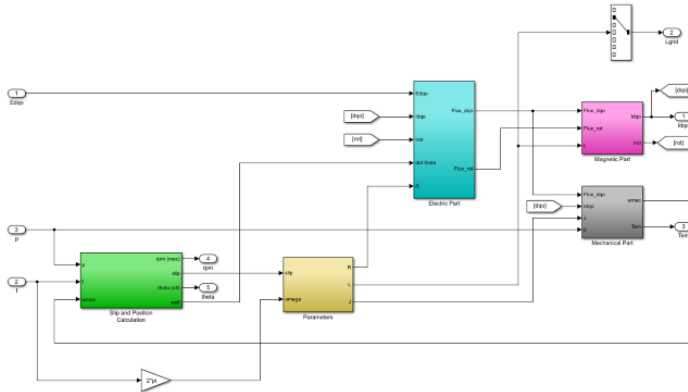
8.3 RESULTS

8.3.1 Reference solid salient pole machine

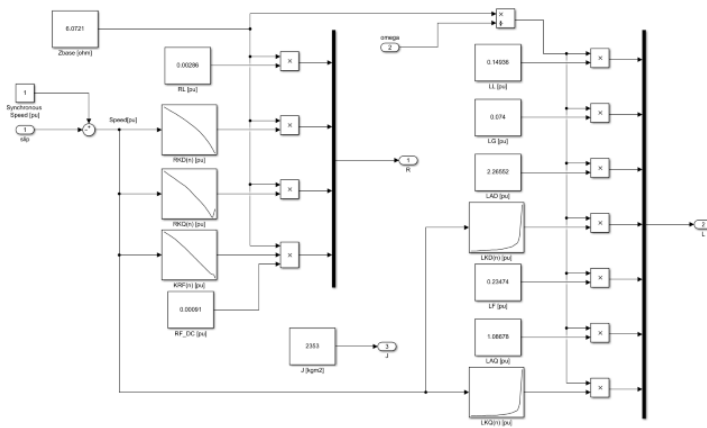
The machine used for the method validation is a 17.5 MW-11 kV-1500 rpm synchronous motor, with four solid salient poles, shown in figure 8.4. Table 8.3 lists the motor characteristic data. The machine is designed to drive a centrifugal compressor for Oil&Gas applications and its cooling system is a built-on heat exchanger mounted on the top of the motor, using ambient air as cooling medium. The machine has undergone an acceptance no-load starting test at full voltage [56]. The machine starting has also been simulated through a complete time-stepping FE model.



(a) Global model



(b) Machine electro-magnetic model



(c) Circuit parameters

Figure 8.3: Block diagram of the synchronous machine at start-up



Figure 8.4: Synchronous motor with DOL-starting capability (courtesy of Nidec-ASI, Monfalcone, Italy)

Table 8.3: Synchronous motor characteristic data

Quantity	Value
Rated voltage	11 kV
Rated current	1046 A
Rated power	17 500 kW
Rated speed	1500 rpm
Rated frequency	50 Hz
Rated torque	111.5 kN m
Rated power factor	0.9 (lag)
Shaft height	1120 mm
Gap diameter	1180 mm
Axial length	1800 mm
Total mass	80 000 kg
Cooling method	IC616 ^(a)
Mounting arrangement	IM1005 ^(b)
Degree of protection	IP55 ^(c)
Thermal class	F ^(d)

^(a) see [18]

^(b) see [68]

^(c) see [69]

^(d) see [31]

8.3.2 Results comparison

Figures 8.5, 8.6 and 8.7, respectively, show the comparison between current, voltage and torque diagrams obtained from the two time-domain simulations (lumped-parameter and finite-element) and from the experimental test. The torque diagrams are obtained with different approaches, depending on the corresponding methods:

- the LP-simulation diagram is calculated from the dq model, according to (6.21);
- the FE-simulation diagram is evaluated applying *virtual work method* to the solved model [10]
- the experimental torque diagram is indirectly determined through the *input power method*, as suggested by IEEE Std.1255 [55]:

$$T = \frac{1}{\Omega_0} \sum_{x=U,V,W} (U_x I_x - R_s I_x^2)$$

being U_x and I_x the instantaneous values of phase voltage and line current for the phase x .

In all the transient plots the speed diagram is shown as well, in order to visually identify when the starting transient is over. It can be noticed that, apart from a slight starting time over-estimation from the FE method, the calculation data is in accordance with the experimental results.

A more precise comparison can be made through the starting diagrams shown in figure 8.8; this figure includes the Current-vs-Speed, Voltage-vs-Speed Average Torque-vs-Speed and Torque Pulsation-vs-Speed diagrams obtained from the previous sources of data, plus the IEEE Std. 1255 (quasi-stationary dq model) method, which does not consider the time dependency, so it could not had been included in the plots from figures 8.5, 8.6 and 8.7.

It can be noticed that the three calculation method accuracy is comparable, as regards the current and voltage prediction (see fig. 8.8a and fig. 8.8b), whereas from fig. 8.8c it can be noticed that the best torque-prediction accuracy is obtained employing the half-pole model-based identification routine discussed in section 8.1, applied either to the IEEE Std.1255 method or the LP-simulation.

All the calculation methods are not accurate as regards the low-speed torque pulsation prediction, as it can be observed in fig. 8.8d, whereas the prediction accuracy is almost the same for the speed values above 40 % of the rated speed.

Finally, a few considerations about the computational cost are given next:

- the time-steeping simulation has taken ≈ 20 h to be solved;
- the rotor equivalent cage parameters have been calculated solving the iterative procedure described in figure 8.1 for a set of speed-voltage values; the cage impedance array used for the IEEE Std.1255 method application has been obtained through a 2D interpolation of the table of calculated values, at the actual speed and voltage values recorded

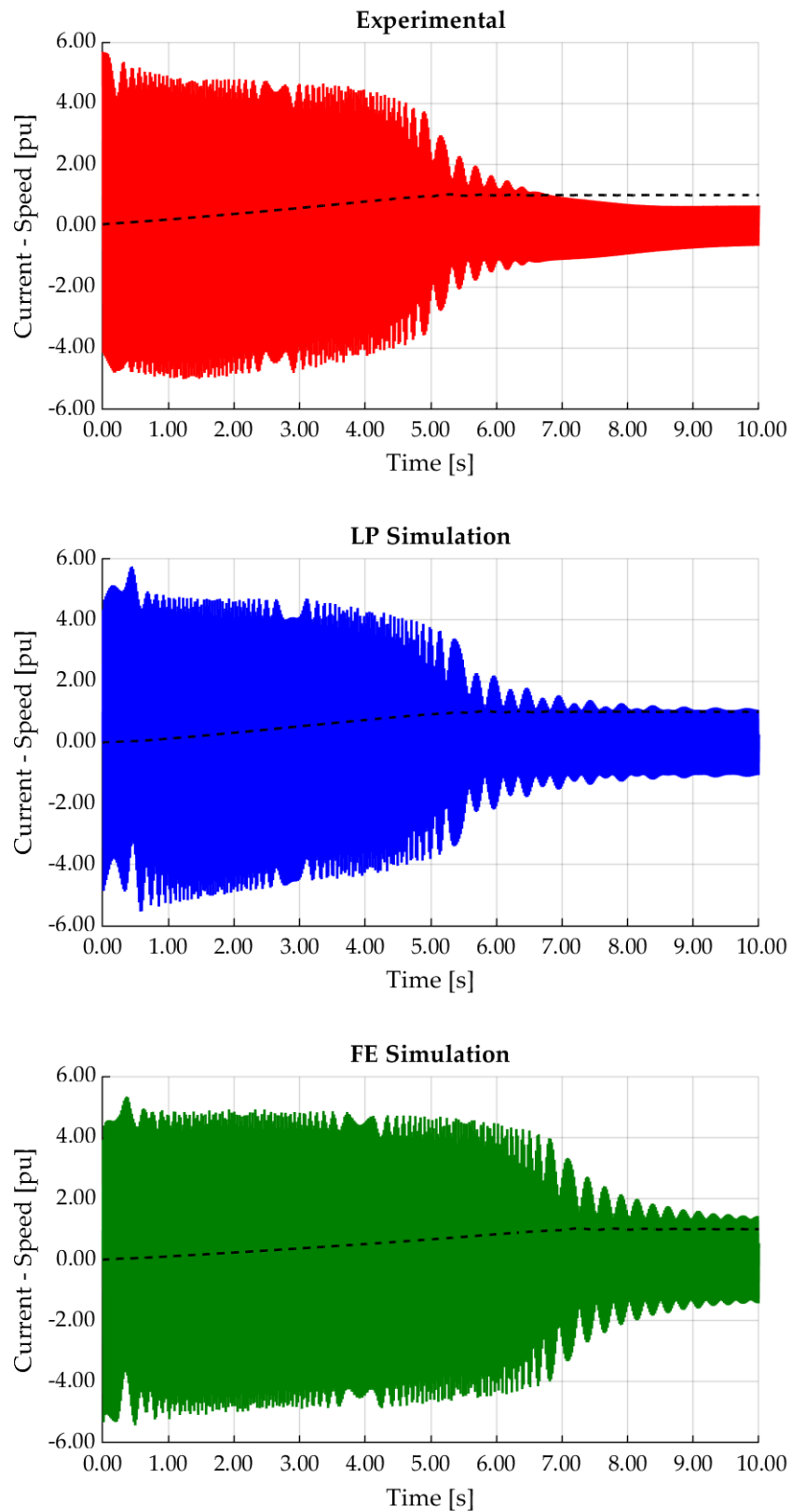


Figure 8.5: Current traces obtained from LP simulation, FE simulation and test

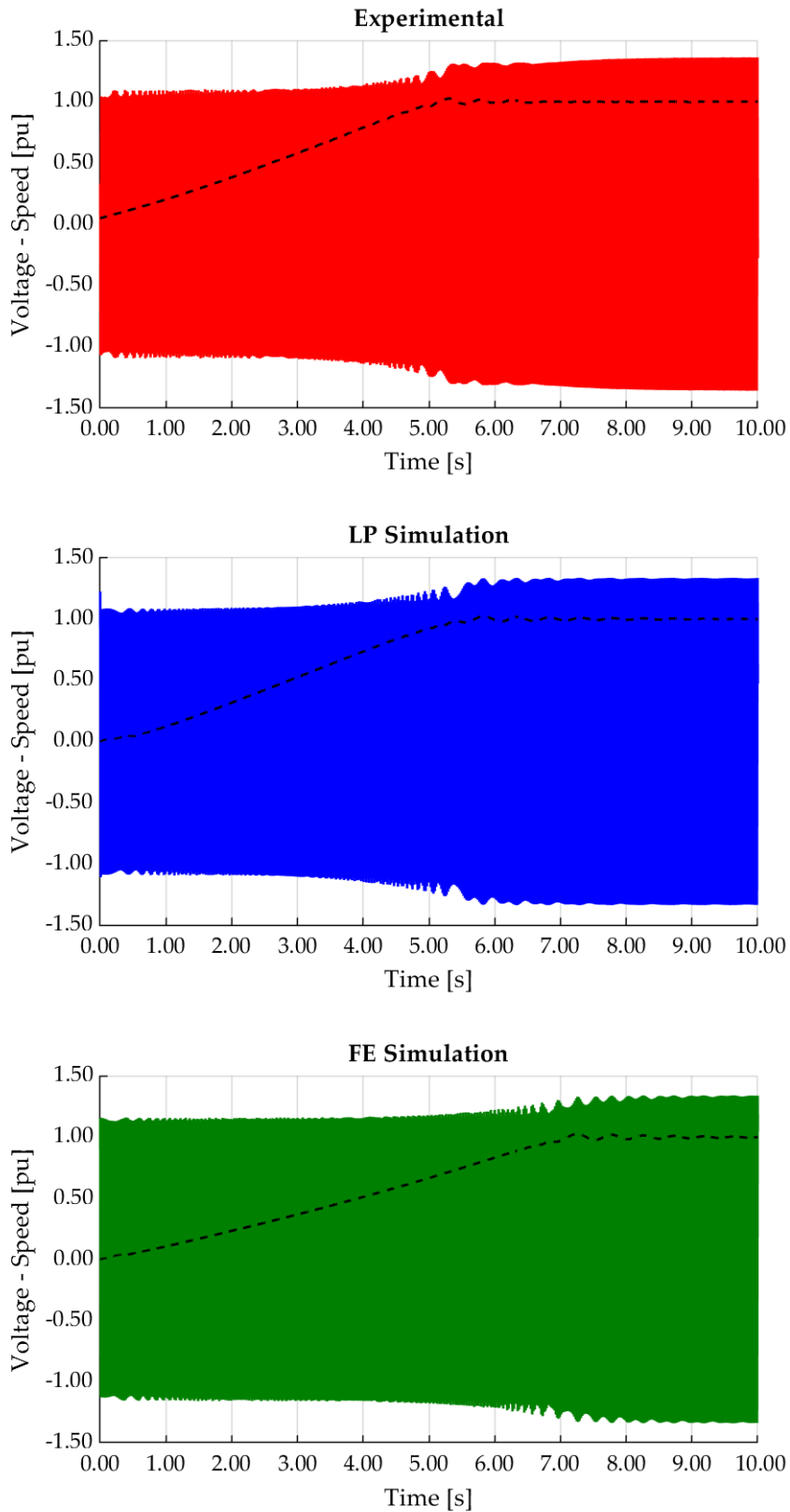


Figure 8.6: Voltage traces obtained from LP simulation, FE simulation and test

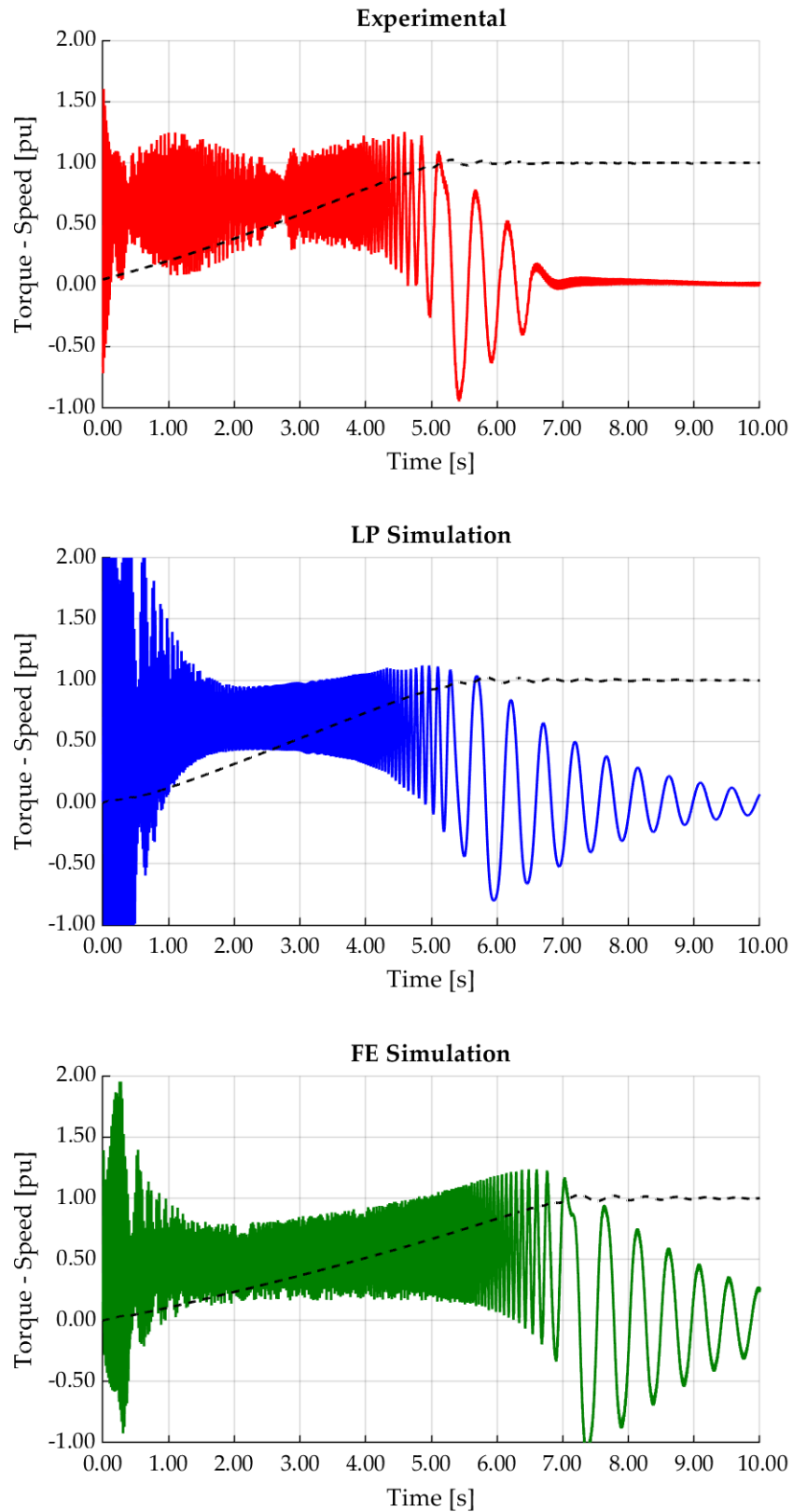


Figure 8.7: Torque traces obtained from LP simulation, FE simulation and test

Table 8.4: Calculation times for dq half pole models

Speed [pu]	Voltage [pu]		
	0.70	0.85	1.00
0.000	28 s	26 s	28 s
0.150	17 s	17 s	19 s
0.300	18 s	16 s	17 s
0.450	23 s	25 s	26 s
0.600	24 s	22 s	21 s
0.750	21 s	20 s	19 s
0.900	16 s	18 s	17 s
0.925	15 s	14 s	15 s
0.950	14 s	13 s	13 s
0.975	12 s	12 s	11 s

at start-up; similarly it has been done for the LP simulation. The time needed to solve each $d-q$ model pair for the cage identification is reported in table 8.4; the total computation time is less than 10 min;

- the field winding AC resistance has been computed separately, before the cage parameters calculation, using an explorative speed-current matrix made of 24 nodes, as described in section 8.1.1. The total computation time is around 40 min;
- the lumped parameter simulation is carried out in less than 1 min

Thus the total computation cost of the new proposed methods, whether through the circuit-based or the LP-simulation, are below 1 h, i.e. less than 5% if compared to the standard FE-based approach.

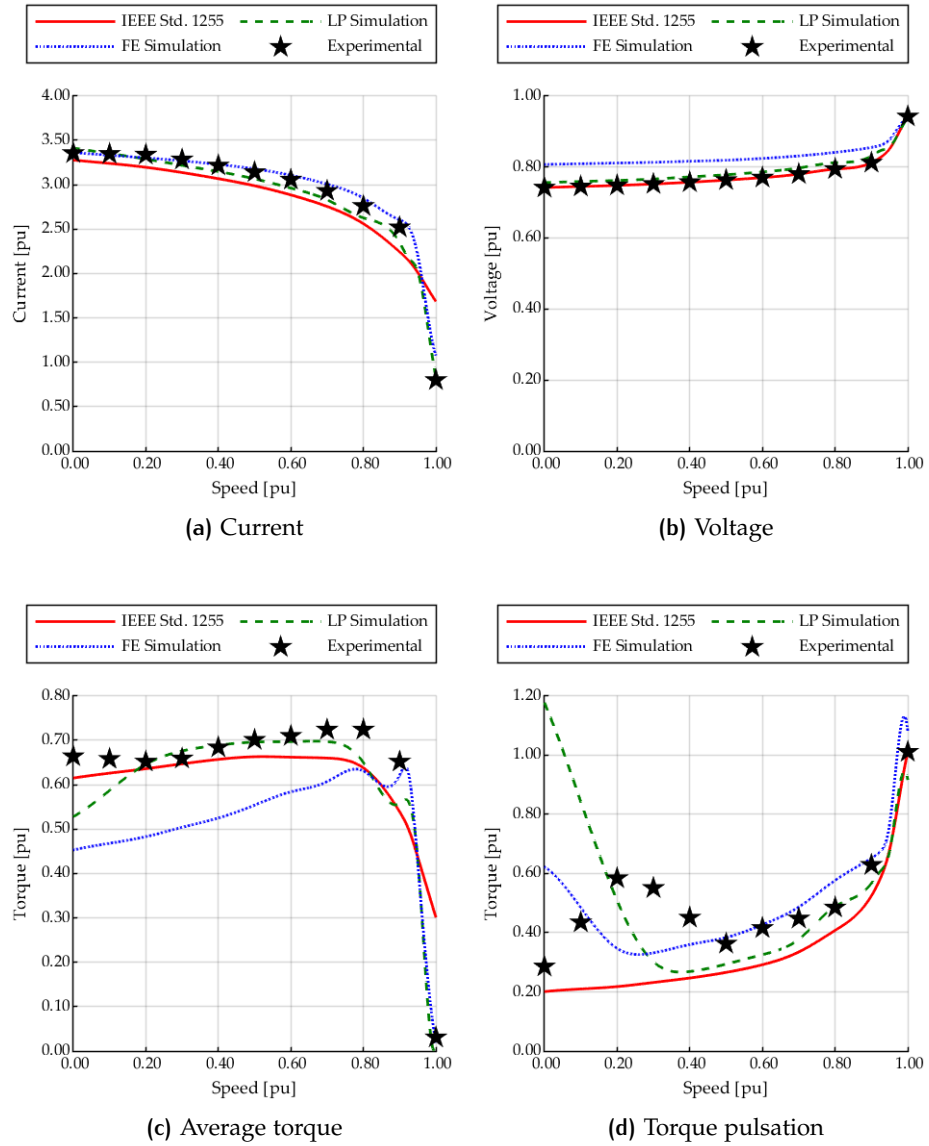


Figure 8.8: Starting diagrams for synchronous machine

CONCLUSIONS

In this PhD dissertation some aspects about the calculation of eddy-current effects in medium-voltage electric machines has been examined. Particular focus has been put on the definition of innovative calculation procedures, based on the limited use of finite-element method and their application to simplified or reduced models. The results of numerical simulations have been used to properly compute the lumped-parameters included in the machines equivalent circuits.

Out of the various investigations carried out throughout the PhD study course, two applications have been specifically detailed as follows.

- The effects of shaft eddy currents in two-pole induction motors have been investigated in the first part of this dissertation. It has been shown how the magnetic flux rejection from the shaft, caused by eddy currents, results in a worse measured power factor value than expected employig traditional literature methods. A new approach for the IM equivalent circuit calculation has been introduced; this method exploits a set of reduced shaft-focused FE models to properly evaluate the motor magnetizing reactance, accounting for the eddy current related saturation effects.
- the second part of the thesis has been focused on the study of solid-rotor eddy currents used for the DOL starting of large synchronous motors. The starting performance calculation from the two-axis equivalent circuit theory has been described. It has been shown that the equivalent rotor cage parameters can be calculated through FEM and, by properly defining the model boundary conditions and excitations, the analysis can be limited to half of a rotor pole.

In both cases the proposed calculation results have been compared with data coming from standard FEM-based calculations and with experimental measurements as well. The accuracy of the new methods has been proved and their computational burden has been assessed against conventional calculation procedures. It has been shown that, for both the IM and the SM applications, the new proposed methods reduce the computational time significantly without a loss in the accuracy of results.

APPENDICES

A

END-WINDING LEAKAGE CALCULATION

Reference [21] details the method to compute the end-winding reactances through Neumann integrals. The method is applied to multi-phase stator windings in [22] whereas the case of synchronous machines field winding is analyzed in [70]. The computation method is here detailed for the sake of completeness.

A.1 METHOD OUTLINE

To take into account the rotor core effect the mirror images method has to be adopted (figure A.1). Therefore the mutual inductance between an observer coil (Γ_0) and a generic source coil (Γ_ν) must include the contribution of the coil image (Γ'_ν) and the coil infinite extension ($\Gamma_\nu^{(\infty)}$). It is worth noticing that, for symmetry reasons, the characterization of a generic coil geometry allows to identify all the other coils, their images and all the infinite extensions by means of simple geometric transformations.

Each coil is discretized into N segments, numbered from 1 to N . Assuming an infinitely-permeable magnetic core the mutual inductance between the observer coil and the ν -th source coil is given by:

$$\begin{aligned} \mathcal{M}_{0,\nu} = \frac{\mu_0}{4\pi} \sum_{i=1}^N \left[\sum_{j=1}^N \mathcal{N}(\mathbf{S}_i^{(0)}, \mathbf{S}_j^{(\nu)}) \right. \\ - \mathcal{N}(\mathbf{S}_i^{(0)}, \mathbf{S}'_1^{(\nu)}) \\ + \sum_{j=2}^{N-1} \mathcal{N}(\mathbf{S}_i^{(0)}, \mathbf{S}'_j^{(\nu)}) \\ - \mathcal{N}(\mathbf{S}_i^{(0)}, \mathbf{S}'_N^{(\nu)}) \\ \left. + 2\mathcal{I}(\mathbf{S}_i^{(0)}, \mathbf{S}_\infty^{(\nu)}) \right] \end{aligned} \quad (\text{A.1})$$

where $\mathcal{N}(\mathbf{S}, \mathbf{s})$ and $\mathcal{I}(\mathbf{S}, \mathbf{s}_\infty)$ are the Neumann integrals between two finite-segments (\mathbf{S}, \mathbf{s}) and between a finite-segment and a pair of infinite-segments ($\mathbf{S}, \mathbf{s}_\infty$) respectively, given by:

$$\mathcal{N}(\mathbf{S}, \mathbf{s}) = \int_P^F \int_p^f \frac{d\vec{L} \cdot d\vec{\ell}}{\text{dist}(d\vec{L}, d\vec{\ell})} \quad (\text{A.2})$$

$$\mathcal{I}(\mathbf{S}, \mathbf{s}_\infty) = \int_P^F \int_\infty^f \frac{d\vec{L} \cdot d\vec{\ell}}{\text{dist}(d\vec{L}, d\vec{\ell})} + \int_P^F \int_p^\infty \frac{d\vec{L} \cdot d\vec{\ell}}{\text{dist}(d\vec{L}, d\vec{\ell})} \quad (\text{A.3})$$

The detailed calculation of these integral is presented in section A.3, accordingly to the coil geometry model given in section A.2. This allows to

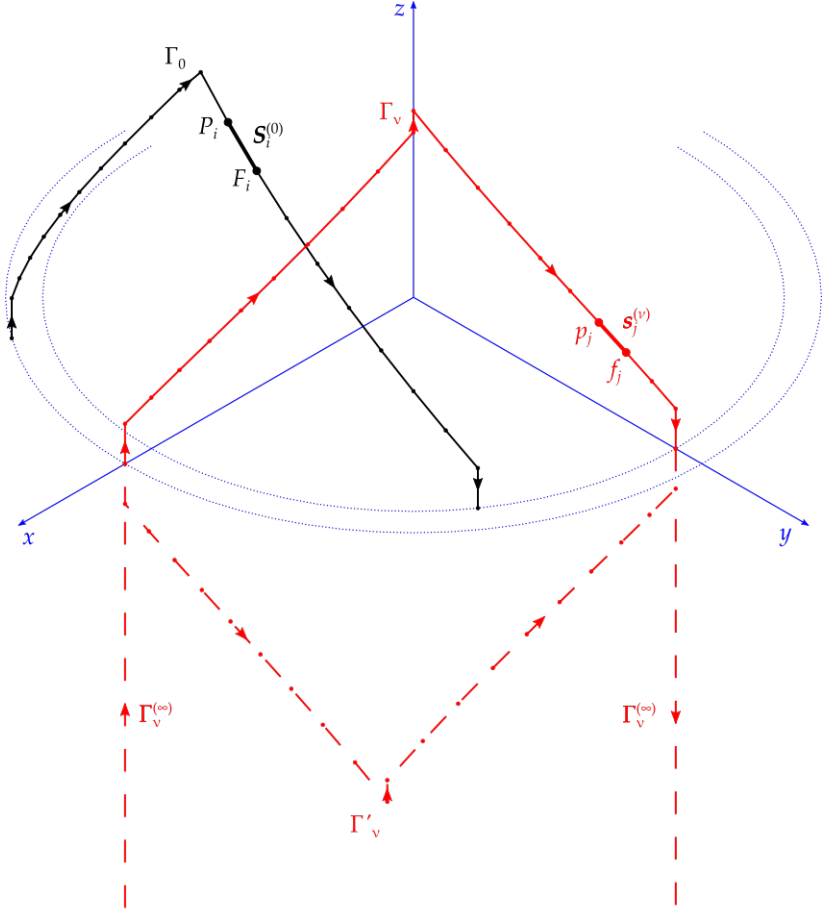


Figure A.1: Image method applied to end-coils mutual inductance computation

characterize the full matrix of inductances, whose generic element is the mutual inductance between a pair of coils from the winding. Once this task is done the phase end-winding inductance is calculated, distinguishing between the case of a multi-phase winding (stator winding, for instance) or a single phase winding (like rotor field winding).

A.1.1 End-winding inductance for a multi-phase winding

It is assumed a double-layer winding, so the winding is composed of Z coils¹ with N_{tc} turns each. The coils are numbered from 1 to Z and the mutual inductance between the first coil and the j -th coil has been calculated through (A.1) and it is equal to $\hat{\mathcal{M}}_j$, with $j = 1, 2, \dots, Z$. Thanks to the winding circular symmetry the full matrix of inductances is defined as:

$$\mathcal{M}_{i,j} = \hat{\mathcal{M}}_{|i-j|}$$

for any $i, j = 1, 2, \dots, Z$.

The winding is subdivided into N_p poles with m phases each. There are N_{pc} circuits per phase. The number of coils per phase in a single pole is given by:

$$q = \frac{Z}{N_p m}$$

The generic i -th coil of the k -th phase in the u -th pole is thus given by index $i + (k-1)q + (u-1)mq$ with $i = 1, \dots, q$ and $k = 1, \dots, m$ and $u = 1, \dots, N_p$.

It is firstly assumed that all the phases of the same pole are wound in the same directions, whereas two coils belonging to adjacent poles are opposite. With this assumption we considered the i -th coil of the k -th phase in the u -th pole. Its flux-linkage produced by a given current flowing in the j -th coil of the h -th phase in the v -th pole is given by:

$$\begin{aligned} \Psi_{k_i,u,h_j,v} &= (-1)^{u-v} N_{tc} \mathcal{M}_{i+(k-1)q+(u-1)mq,j+(h-1)q+(v-1)mq} N_{tc} \frac{I}{N_{pc}} \\ &= (-1)^{u-v} \frac{N_{tc}^2}{N_{pc}} \hat{\mathcal{M}}_{|i-j+(k-h)q+(u-v)mq|} I \end{aligned}$$

The term $(-1)^{u-v}$ accounts for the fact that two coils from evenly-spaced poles have the same orientation, but it is opposite if the pole are oddly-spaced. The term N_{tc}^2/N_{pc} is explained by considering that the observer coil is formed by N_{tc} coils that link the same flux and the actual amount of current flowing in the source coil is $N_{tc} I/N_{pc}$, with I assumed as the phase current.

The flux linkage in the observer coil due to the whole h -th phase being fed is obtained by adding the contributions of all the possible source coils of this phase.

$$\Psi_{k_i,u,h} = \sum_{j=1}^q \sum_{v=1}^{N_p} (-1)^{u-v} \frac{N_{tc}^2}{N_{pc}} \hat{\mathcal{M}}_{|i-j+(k-h)q+(u-v)mq|} I$$

¹ Z is also the number of slots.

Similarly the flux-linkage in the whole k -th phase due to the h -th phase being fed is obtained by summing all the contributions from every possible observer coil in the former phase. Bear in mind that the total contribution has to be divided by N_{cp} to take into account the presence of multiple circuits per phase. The k -to- h phase end-winding inductance is finally given by:

$$\tilde{L}_{k,h} = 2 \left(\frac{N_{tc}}{N_{pc}} \right)^2 \sum_{i,j=1}^q \sum_{u,v=1}^{N_p} (-1)^{u-v} \hat{\mathcal{M}}_{|i-j+(k-h)q+(u-v)mq|} \quad (\text{A.4})$$

where the term 2 accounts for the fact that there are two coil ends. The matrix of the inductance is defined as well

$$\tilde{\mathbf{L}} = [L_{k,h}]_{\substack{k=1,\dots,m \\ h=1,\dots,m}}$$

To obtain the matrix of the leakage inductances for the actual phases of the winding we introduce a mapping matrix (\mathcal{P}) which permutes the fictitious phases of a pole into the actual system of phases. For instance, in a three-phase system, the actual phase sequence in a pole is +U,-W,+V, whereas the fictitious system of phases is given by +U,+V,+W, so the mapping matrix is defined as:

$$\mathcal{P} = \begin{bmatrix} 1 & 0 & 0 \\ 0 & 0 & -1 \\ 0 & 1 & 0 \end{bmatrix} \quad \text{so that} \quad \begin{bmatrix} +\text{U} \\ -\text{W} \\ +\text{V} \end{bmatrix} = \begin{bmatrix} 1 & 0 & 0 \\ 0 & 0 & -1 \\ 0 & 1 & 0 \end{bmatrix} \begin{bmatrix} +\text{U} \\ +\text{V} \\ +\text{W} \end{bmatrix}$$

It is worth noticing that the mapping matrix is anti-symmetric and its inverse is equal to its transpose. This is valid for any symmetric phase arrangement [22]. The matrix \mathcal{P} applied to any array of fictitious phase quantities rearrange it to the actual array of phase quantities. Thus it can be written:

$$\begin{aligned} \tilde{\Psi} &= \tilde{\mathbf{L}} \tilde{\mathbf{I}} \\ \mathcal{P} \tilde{\Psi} &= \mathcal{P} \tilde{\mathbf{L}} \mathcal{P}^T \mathcal{P} \tilde{\mathbf{I}} \\ \Psi &= (\mathcal{P} \tilde{\mathbf{L}} \mathcal{P}^T) \mathbf{I} \end{aligned}$$

so the matrix of leakage inductances is defined as

$$\mathbf{L} = \mathcal{P} \tilde{\mathbf{L}} \mathcal{P}^T \quad (\text{A.5})$$

For a three-phase winding it results:

$$\begin{aligned} L_{U,U} &= L_{V,V} = L_{W,W} = L \\ L_{U,V} &= L_{V,W} = L_{W,V} = -L/2 \end{aligned}$$

so the end-winding flux leakage for a phase is:

$$\Psi_U = LI_U - \frac{1}{2}L(I_V + I_W)$$

so, considering that $I_V + I_W = -I_U$ the equivalent leakage inductance for a phase is finally defined:

$$L_{s,\text{end}} = \frac{3}{2}L \quad (\text{A.6})$$

A.1.2 End-winding inductance for a single-phase winding

In this case the coil arrangement is complicated, so it is better to directly calculate the whole matrix of mutual inductances accordingly to (A.1). Assuming Z coils with N_{tc} turns each the mutual inductance matrix is given by:

$$\mathcal{M} = \begin{bmatrix} \mathcal{M}_{1,1} & \mathcal{M}_{1,2} & \dots & \mathcal{M}_{1,Z} \\ \mathcal{M}_{2,1} & \mathcal{M}_{2,2} & \dots & \mathcal{M}_{2,Z} \\ \vdots & \vdots & \ddots & \vdots \\ \mathcal{M}_{Z,1} & \mathcal{M}_{Z,2} & \dots & \mathcal{M}_{Z,Z} \end{bmatrix}$$

For symmetry reasons only half of this matrix has to actually be computed, because $\mathcal{M}_{i,j} = \mathcal{M}_{j,i}$.

Assuming N_p poles, the number of coils per pole is $Q = Z/N_p$. The i -th coil in the u -th pole is identified by index $i + u - 1$. The flux-linkage of the i -th coil of the u -th pole when the j -th coil of the v -th pole is fed by a given current I is:

$$\Psi_{u_i,v_j} = (-1)^{u-v} N_{tc} \mathcal{M}_{u+i-1,v+j-1} N_{tc}^2 I$$

The terms in this expression have the same justification of the multi-phase case. It is assumed that all the coils are connected in series, i.e. $N_{pc} = 1$. By summing all the contributions of any possible combination of observer and source coils the total leakage inductance is finally obtained:

$$L_{\text{end}} = 2N_{tc}^2 \sum_{u,v=1}^{N_p} \sum_{i,j=1}^Q (-1)^{u-v} \mathcal{M}_{u+i-1,v+j-1} \quad (\text{A.7})$$

A.2 COIL GEOMETRY MODEL

The mutual inductance between two end-coils is calculated by means of the Neumann integrals in (A.1). These integrals are calculated along the average line of the end coils (see figure A.1) so this part of the machine has to be geometrically identified precisely. Two geometries are considered:

1. diamond-shaped coil, adopted in stator double-layer windings (section A.2.1);
2. rectangular coils, adopted in synchronous machines field winding (section A.2.2);

A.2.1 Stator-winding geometry

Figure A.2 shows a detail of the end-coil geometry. The coil is divided into five elementary lines:

- two straight lines (Σ_1 and Σ_2). These are the closest elements to the active core. Each line has length ℓ ;
- two cylindrical helixes (ε_1 and ε_2). Each elix has height h , angular width α and radius R and r respectively;

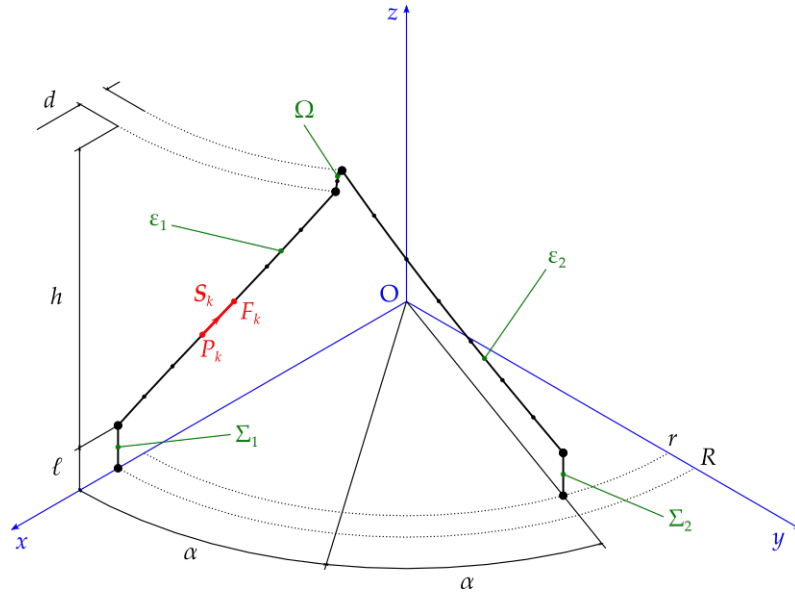


Figure A.2: Detail of a stator end-coil geometry

- a semi-circumference (Ω) in the eye part. The circumference diameter is equal to d .

Each of these lines (except for the two straight lines) are divided into a certain number of elementary segments. If each helix is divided into n_h segments and the eye line is divided into n_0 segments then the end-coil average line is defined by $N = 2n_h + n_0 + 2$ segments², denoted by S_k , with $k = 1, \dots, N$. Each segment is identified by its endpoints P_k and F_k ³. It is assumed that each segment is oriented from P to F . It is worth noticing that the first end-point of any segment (except the first one) is the final end-point of the previous one. So the end-coil geometry is completely characterized once the coordinates of all the points P_k is known.

The coil is placed in a three-dimensional orthogonal reference frame O_{xyz} , as shown in figure A.2. The z -axis is the machine axis and the xy -plane is one of the core-end faces. Furthermore the x -axis is chosen to intersect the first straight part of the coil. With these assumptions the coil reference points are obtained through simple geometric considerations. Table A.1 collects the reference points for the coil shown in figure A.2. In this table k is the numbering of the whole coil line, whereas i denote the numbering of the elementary line. For the eye-part expression the following quantities are assumed:

$$r_{\text{avg}} = \frac{R + r}{2}$$

$$r_x = \frac{d}{2} \cos(\alpha)$$

$$r_y = \frac{d}{2} \sin(\alpha)$$

² To ensure a symmetric segmenting the number N should be odd, i.e. n_0 should be odd.

³ The notation P, F is used to refer to the geometric objects, whereas \mathbf{P}, \mathbf{F} denote the arrays of the coordinates of the points

Table A.1: Characteristic points of a stator end-coil

k	Line	i	P_k		
			x	y	z
1	Σ_1	1	R	0	0
$2, \dots, n_h + 1$	ε_1	$1, \dots, n_h$	$R \cos\left(\frac{i-1}{n_h}\alpha\right)$	$R \sin\left(\frac{i-1}{n_h}\alpha\right)$	$\ell + \frac{i-1}{n_h}h$
$n_h + 2, \dots$ $N - n_h - 2$	Ω	$1, \dots, n_0$	$r_{\text{avg}} \cos(\alpha) +$ $+r_x \cos\left(\frac{i-1}{n_0}\pi\right)$	$r_{\text{avg}} \sin(\alpha) +$ $+r_y \cos\left(\frac{i-1}{n_0}\pi\right)$	$\ell + h +$ $+\frac{d}{2} \sin\left(\frac{i-1}{n_0}\pi\right)$
$N - n_h - 1, \dots, N - 1$	ε_2	$1, \dots, n_h$	$r \cos\left(\frac{n_h+i-1}{n_h}\alpha\right)$	$r \sin\left(\frac{n_h+i-1}{n_h}\alpha\right)$	$\ell + \frac{n_h+i-1}{n_h}h$
N	Σ_2	1	$r \cos(2\alpha)$	$r \sin(2\alpha)$	ℓ

The points in table A.1 provide the starting endpoints of the elementary segments. The final endpoints for any $k = 1, \dots, N$ are given by:

$$\mathbf{F}_k = \begin{cases} \mathbf{P}_{k+1} & \text{for } k < N \\ \begin{vmatrix} R \cos(2\alpha) \\ R \sin(2\alpha) \\ 0 \end{vmatrix} & \text{for } k = N \end{cases}$$

Furthermore if this coil is assumed as reference for a winding with Z coils, the rest of the winding is simply obtained through a geometric rotation. Thus, denoting the array of the coordinates of the endpoints for the k -th segment in the ν -th coil with $\mathbf{P}_k^{(\nu)}$ and $\mathbf{F}_k^{(\nu)}$ respectively, the rotation matrix is defined:

$$\mathcal{R}_\nu = \begin{bmatrix} \cos\left((\nu-1)\frac{2\pi}{Z}\right) & -\sin\left((\nu-1)\frac{2\pi}{Z}\right) & 0 \\ \sin\left((\nu-1)\frac{2\pi}{Z}\right) & \cos\left((\nu-1)\frac{2\pi}{Z}\right) & 0 \\ 0 & 0 & 1 \end{bmatrix}$$

and finally, for any $\nu = 1, \dots, Z$ and $k = 1, \dots, N$ it results:

$$\mathbf{P}_k^{(\nu)} = \mathcal{R}_\nu \mathbf{P}_k^{(1)} \quad \mathbf{F}_k^{(\nu)} = \mathcal{R}_\nu \mathbf{F}_k^{(1)}$$

Similarly, the coil image (figure A.1) is obtained through a flipping matrix, defined as:

$$\mathcal{F} = \begin{bmatrix} 1 & 0 & 0 \\ 0 & 1 & 0 \\ 0 & 0 & -1 \end{bmatrix}$$

so that the end-points of the k -th segment in the ν -th coil image are given by:

$$\mathbf{P}'_k^{(\nu)} = \mathcal{F} \mathbf{P}_k^{(\nu)} \quad \mathbf{F}'_k^{(\nu)} = \mathcal{F} \mathbf{F}_k^{(\nu)}$$

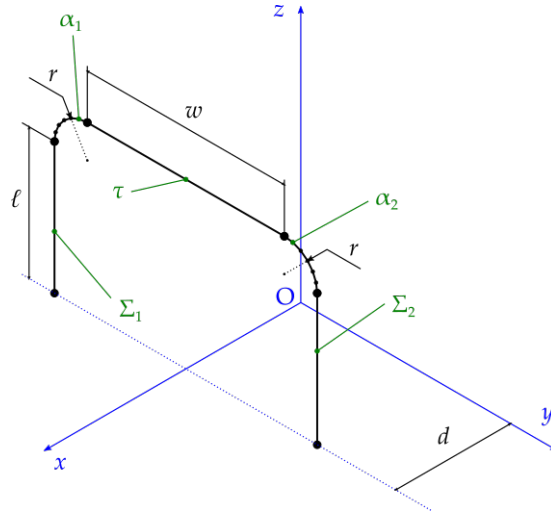


Figure A.3: Detail of a rotor end-coil geometry

Finally, it is worth noticing that the infinite extension of the ν -th coil image is identified by the two points:

$$\mathbf{P}_\infty^{(\nu)} = \mathcal{F}\mathbf{P}_N^{(\nu)} \quad \mathbf{F}_\infty^{(\nu)} = \mathcal{F}\mathbf{F}_1^{(\nu)}$$

and the orientation of the infinite segments is accordingly to $-\vec{e}_z$ and \vec{e}_z respectively, where \vec{e}_z is the versor of the z axis.

A.2.2 Rotor-winding geometry

The coil geometry here considered is shown in figure A.3. It is composed as follows:

- two straight parts parallel to the machine axis, denoted by Σ_1 and Σ_2 . Each segment has length ℓ ;
- one straight segment orthogonal to the machine axis, denoted by τ and with length w ;
- the coil corners are round and have radius r . Each line is denoted by α_1 and α_2 .

Furthermore the coil plane is placed at a distance d from the machine axis. The coil winding is composed of N_p poles with N_c coils each, i.e. there are N_p groups of N_c coils like the one in figure A.3, whose axes are placed with a central symmetry. The planes of coils within the same pole are parallel, placed at different distances d or with different dimensions.

As done for the stator case a three-dimensional reference frame O_{xyz} is introduced (see figure A.3). The z -axis is the machine axis and x -axis is the coil axis. The coil is also symmetric with respect to plane xz . The coil average line is subdivided into elementary segments. Actually, since the only non-straight parts are the corners α_1 and α_2 , it is sufficient to approximate these quarters of circumference with a sequence of n_a segments each, so the total coil is made from $N = 2n_a + 3$ segments. Again, the coil geometry is identified if the starting end-point P_k of every segment S_k is defined. Table A.2 collects the characteristic points of the coil for any $k = 1, \dots, N$.

Table A.2: Characteristic points of a rotor end-coil

k	Line	i	P_k		
			x	y	z
1	Σ_1	1	d	$-w/2 - r$	0
$2, \dots, n_a + 1$	α_1	$1, \dots, n_a$	d	$-w/2 + r \cos\left(\frac{2n_a - i + 1}{2n_a} \pi\right)$	$\ell + r \sin\left(\frac{2n_a - i + 1}{2n_a} \pi\right)$
$n_a + 2$	τ	1	d	$-w/2$	ℓ
$N - n_a - 1, \dots, N - 1$	α_2	$1, \dots, n_a$	d	$w/2 + r \cos\left(\frac{n_a - i + 1}{2n_a} \pi\right)$	$\ell + r \sin\left(\frac{n_a - i + 1}{2n_a} \pi\right)$
N	Σ_2	1	d	$w/2 + r$	ℓ

The final endpoints of the segments are given as well:

$$\mathbf{F}_k = \begin{cases} \mathbf{P}_{k+1} & \text{for } k < N \\ \begin{pmatrix} d \\ w/2 + r \\ 0 \end{pmatrix} & \text{for } k = N \end{cases}$$

All the coils in the first pole are identified through this approach. Remember that there are N_c coils in N_p poles. The k th segment endpoints of the ν -th coil in the p -th pole are denoted as $P_k^{(\nu,p)}$ and $F_k^{(\nu,p)}$. Their coordinates are obtained from the first-pole coils through a proper rotation matrix:

$$\mathcal{R}_p = \begin{bmatrix} \cos\left(\left(p-1\right)\frac{2\pi}{N_p}\right) & -\sin\left(\left(p-1\right)\frac{2\pi}{N_p}\right) & 0 \\ \sin\left(\left(p-1\right)\frac{2\pi}{N_p}\right) & \cos\left(\left(p-1\right)\frac{2\pi}{N_p}\right) & 0 \\ 0 & 0 & 1 \end{bmatrix}$$

so that:

$$\mathbf{P}_k^{(\nu,p)} = \mathcal{R}_p \mathbf{P}_k^{(\nu,1)} \quad \mathbf{F}_k^{(\nu,p)} = \mathcal{R}_p \mathbf{F}_k^{(\nu,1)}$$

for any $k = 1, \dots, N$ and $\nu = 1, \dots, N_c$ and $p = 1, \dots, N_p$. As regards the calculation of the coil images and their infinite extension the considerations made in the stator-winding case are still valid.

A.3 NEUMANN INTEGRALS CALCULATION

To properly compute the Neumann integrals in (A.2) and (A.3) three cases have to be considered

1. the two segments are both finite and they do not intersect (section A.3.1);

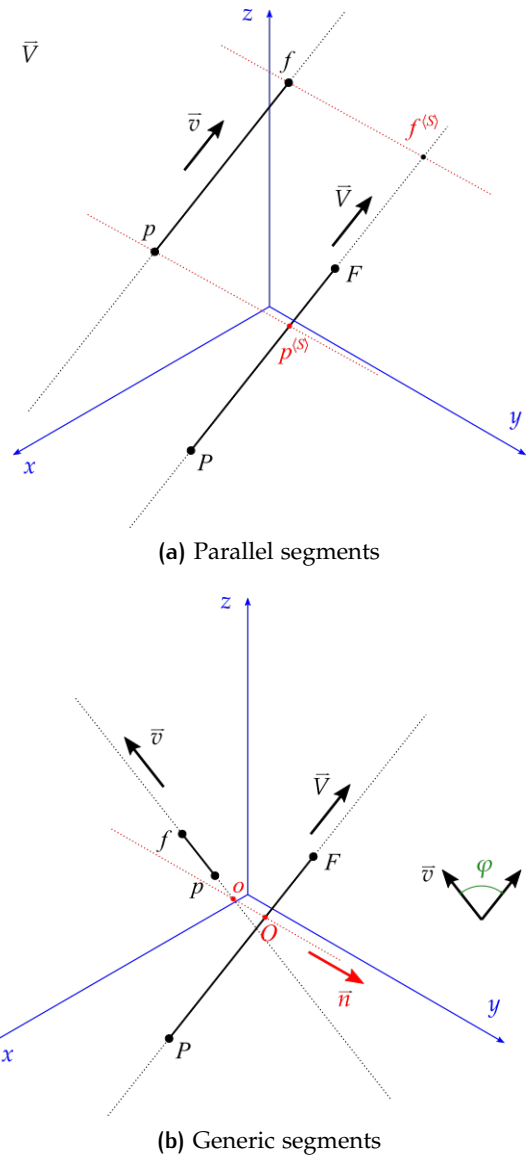


Figure A.4: Reference nomenclature for the calculation of Neumann integral between two non-intersecting finite segments

2. the two segments are both finite and they overlap, i.e. the self-inductance of a segment is being computed (section A.3.2);
3. one segment is finite and the other is a pair of infinite parallel segments with opposite orientation. The finite segment do not intersect any of the infinite segments (section A.3.3).

A.3.1 Neumann integral between finite segments

The solution of this case is taken from [21]. The pair of segments S and s is identified through the pair of endpoints of each segment, i.e. $S \leftrightarrow P, F$ and $s \leftrightarrow p, f$ (see figure A.4). The length of each segment respectively is given by:

$$\Lambda = \|F - P\| \quad \lambda = \|f - p\|$$

and the unit vectors are also given by:

$$\vec{V} = \frac{\mathbf{F} - \mathbf{P}}{\Lambda} \quad \vec{v} = \frac{\mathbf{f} - \mathbf{p}}{\lambda}$$

These vectors identify two straight lines passing through the segments. The angle between the line is obtained from the dot product of the vectors:

$$\cos \varphi = \vec{V} \cdot \vec{v}$$

Three sub-cases must be distinguished:

1. $\cos \varphi = 0$, i.e. $\vec{V} \perp \vec{v}$; in this case the Neumann integral is always equal to zero

$$\mathbf{S} \perp \mathbf{s} \implies \mathcal{N}(\mathbf{S}, \mathbf{s}) = 0$$

2. $\cos \varphi = \pm 1$, i.e. $\vec{V} \parallel \vec{v}$; in this case the projections of points \mathbf{p} and \mathbf{f} on the straight line identified by \mathbf{S} are determined (figure A.4a):

$$\begin{aligned} \mathbf{p}^{(S)} &= \mathbf{P} + [(\mathbf{p} - \mathbf{P}) \cdot \vec{V}] \vec{V} \\ \mathbf{f}^{(S)} &= \mathbf{P} + [(\mathbf{f} - \mathbf{P}) \cdot \vec{V}] \vec{V} \end{aligned}$$

and the Neumann integral is computed:

$$\begin{aligned} \mathcal{N}(\mathbf{S}, \mathbf{s}) &= \|\mathbf{P} - \mathbf{p}\| + \|\mathbf{F} - \mathbf{f}\| - \|\mathbf{P} - \mathbf{f}\| - \|\mathbf{F} - \mathbf{p}\| \\ &+ \Lambda \ln \frac{\|\mathbf{F} - \mathbf{p}\| + (\mathbf{F} - \mathbf{p}^{(S)}) \cdot \vec{V}}{\|\mathbf{F} - \mathbf{f}\| + (\mathbf{F} - \mathbf{f}^{(S)}) \cdot \vec{V}} \\ &+ [(\mathbf{P} - \mathbf{p}^{(S)}) \cdot \vec{V}] \frac{\|\mathbf{F} - \mathbf{p}\| + (\mathbf{F} - \mathbf{p}^{(S)}) \cdot \vec{V}}{\|\mathbf{P} - \mathbf{p}\| + (\mathbf{P} - \mathbf{p}^{(S)}) \cdot \vec{V}} \quad (\text{A.8}) \\ &- [(\mathbf{P} - \mathbf{f}^{(S)}) \cdot \vec{V}] \frac{\|\mathbf{F} - \mathbf{f}\| + (\mathbf{F} - \mathbf{f}^{(S)}) \cdot \vec{V}}{\|\mathbf{P} - \mathbf{f}\| + (\mathbf{P} - \mathbf{f}^{(S)}) \cdot \vec{V}} \end{aligned}$$

Some of the terms in (A.8) may not be defined if the two segments lay on the same line, so this special case will be insighted later;

3. finally, if $0 < |\cos \varphi| < 1$ the two segments are in a generic position, so the solution of Neumann integrals require to determine the common perpendicular to segments \mathbf{S} and \mathbf{s} and its intersections with the straight lines passing through each of these segments, denoted as O and o respectively (figure A.4b). It can be noticed that:

- the perpendicular direction is given by:

$$\vec{n} = \vec{V} \times \vec{v}$$

and, thanks to the properties of the vector product, it results $\|\vec{n}\| = |\sin \varphi| = \sqrt{1 - \cos^2 \varphi}$;

- the points O and o lie on the lines passing through \mathbf{S} and \mathbf{s} respectively, so it can be written:

$$\begin{aligned} \mathbf{O} &= \mathbf{P} + \alpha \vec{V} \\ \mathbf{o} &= \mathbf{p} + \beta \vec{v} \end{aligned}$$

for a proper α, β pair. It also results:

$$\mathbf{O} - \mathbf{o} = (\mathbf{P} - \mathbf{p}) + \alpha \vec{V} - \beta \vec{v}$$

- Since $\mathbf{O} - \mathbf{o}$ lies on the perpendicular to both \mathbf{S} and \mathbf{s} it will result:

$$(\mathbf{O} - \mathbf{o}) \cdot \vec{V} = (\mathbf{P} - \mathbf{p}) \cdot \vec{V} + \alpha - \beta \cos \varphi = 0$$

$$(\mathbf{O} - \mathbf{o}) \cdot \vec{v} = (\mathbf{P} - \mathbf{p}) \cdot \vec{v} + \alpha \cos \varphi - \beta = 0$$

and:

$$\begin{bmatrix} 1 & -\cos \varphi \\ \cos \varphi & -1 \end{bmatrix} \begin{bmatrix} \alpha \\ \beta \end{bmatrix} = - \begin{bmatrix} (\mathbf{P} - \mathbf{p}) \cdot \vec{V} \\ (\mathbf{P} - \mathbf{p}) \cdot \vec{v} \end{bmatrix}$$

- Solving the previous equation the values for α and β are obtained

$$\alpha = \frac{1}{|\sin \varphi|^2} (\mathbf{P} - \mathbf{p}) \cdot [\vec{v} \cos \varphi - \vec{V}]$$

$$\beta = \frac{1}{|\sin \varphi|^2} (\mathbf{P} - \mathbf{p}) \cdot [\vec{v} - \vec{V} \cos \varphi]$$

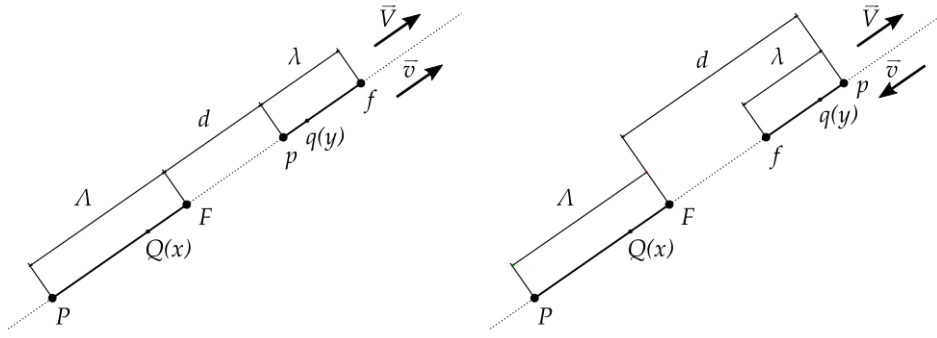
and, finally:

$$\mathbf{O} = \mathbf{P} + [(\mathbf{p} - \mathbf{P}) \cdot (\vec{V} - \vec{v} \cos \varphi)] \frac{\vec{V}}{1 - \cos^2 \varphi}$$

$$\mathbf{o} = \mathbf{p} + [(\mathbf{P} - \mathbf{p}) \cdot (\vec{v} - \vec{V} \cos \varphi)] \frac{\vec{v}}{1 - \cos^2 \varphi}$$

At this point the Neumann integral is given by:

$$\mathcal{N}(\mathbf{S}, \mathbf{s}) = \mathcal{N}_1 \cos \varphi - \mathcal{N}_2 \|\mathbf{O} - \mathbf{o}\| \cot \varphi \quad (\text{A.9})$$



(a) Equal directions

(b) Opposite directions

Figure A.5: Calculation of Neumann integral for two aligned and not overlapping finite segments

with:

$$\begin{aligned}
 \mathcal{N}_1 &= [(\mathbf{F} - \mathbf{O}) \cdot \vec{V}] \ln \frac{\|\mathbf{F} - \mathbf{p}\| + \|\mathbf{F} - \mathbf{f}\| + \lambda}{\|\mathbf{F} - \mathbf{p}\| + \|\mathbf{F} - \mathbf{f}\| - \lambda} \\
 &\quad - [(\mathbf{P} - \mathbf{O}) \cdot \vec{V}] \ln \frac{\|\mathbf{P} - \mathbf{p}\| + \|\mathbf{P} - \mathbf{f}\| + \lambda}{\|\mathbf{P} - \mathbf{p}\| + \|\mathbf{P} - \mathbf{f}\| - \lambda} \\
 &\quad + [(\mathbf{f} - \mathbf{o}) \cdot \vec{v}] \ln \frac{\|\mathbf{f} - \mathbf{P}\| + \|\mathbf{f} - \mathbf{F}\| + \Lambda}{\|\mathbf{f} - \mathbf{P}\| + \|\mathbf{f} - \mathbf{F}\| - \Lambda} \\
 &\quad - [(\mathbf{p} - \mathbf{o}) \cdot \vec{v}] \ln \frac{\|\mathbf{p} - \mathbf{P}\| + \|\mathbf{p} - \mathbf{F}\| + \Lambda}{\|\mathbf{p} - \mathbf{P}\| + \|\mathbf{p} - \mathbf{F}\| - \Lambda} \\
 \\
 \mathcal{N}_2 &= \arctan \left[\frac{\|\mathbf{O} - \mathbf{o}\|}{\|\mathbf{F} - \mathbf{f}\|} \cot \varphi + \frac{[(\mathbf{f} - \mathbf{o}) \cdot \vec{v}] [(\mathbf{F} - \mathbf{O}) \cdot \vec{V}]}{\|\mathbf{O} - \mathbf{o}\| \|\mathbf{F} - \mathbf{f}\|} \sin \varphi \right] \\
 &\quad + \arctan \left[\frac{\|\mathbf{O} - \mathbf{o}\|}{\|\mathbf{P} - \mathbf{p}\|} \cot \varphi + \frac{[(\mathbf{p} - \mathbf{o}) \cdot \vec{v}] [(\mathbf{P} - \mathbf{O}) \cdot \vec{V}]}{\|\mathbf{O} - \mathbf{o}\| \|\mathbf{P} - \mathbf{p}\|} \sin \varphi \right] \\
 &\quad - \arctan \left[\frac{\|\mathbf{O} - \mathbf{o}\|}{\|\mathbf{P} - \mathbf{f}\|} \cot \varphi + \frac{[(\mathbf{f} - \mathbf{o}) \cdot \vec{v}] [(\mathbf{P} - \mathbf{O}) \cdot \vec{V}]}{\|\mathbf{O} - \mathbf{o}\| \|\mathbf{P} - \mathbf{f}\|} \right] \\
 &\quad - \arctan \left[\frac{\|\mathbf{O} - \mathbf{o}\|}{\|\mathbf{F} - \mathbf{p}\|} \cot \varphi + \frac{[(\mathbf{p} - \mathbf{o}) \cdot \vec{v}] [(\mathbf{F} - \mathbf{O}) \cdot \vec{V}]}{\|\mathbf{O} - \mathbf{o}\| \|\mathbf{F} - \mathbf{p}\|} \right]
 \end{aligned}$$

Special case - Parallel segments lying on the same line

Figure A.5 show a special case for the computation of Neumann integral for two parallel finite segments, i.e. the case in which the two segments are

lying on the same straight line. In this case the projections of the endpoints second segments are coinciding with the endpoints itself:

$$\mathbf{p}^{(S)} \equiv \mathbf{p} \quad \mathbf{f}^{(S)} \equiv \mathbf{f}$$

From figure A.5 it can also be noticed that most of the denominators in (A.8) are equal to zero, so this formula is not applicable. The Neumann integral must be calculated by direct applying the definition given in (A.2). Two cases may occur:

- the two segments are oriented in the same direction (figure A.5a);
- the two segments are oriented in opposite directions (figure A.5b);

In both cases it is defined the distance between the starting endpoint of the second segment and the final end-point of the first one:

$$d = (\mathbf{p} - \mathbf{F}) \cdot \vec{V} = \|\mathbf{p} - \mathbf{F}\|$$

It is worth noticing that, in order to ensure the non-overlapping of the two segments, it results $d \geq 0$ in the case of equally-oriented segments and $d \geq \lambda > 0$ for reversely-oriented segments.

The parametric equations of the two segments are given by:

$$\begin{aligned} Q \in \overline{PF} &\implies \mathbf{Q} = \mathbf{P} + x\vec{V} && \text{with } x \in [0, \Lambda] \\ q \in \overline{pf} &\implies \mathbf{q} = \mathbf{P} + (\Lambda + d + \kappa y)\vec{V} && \text{with } y \in [0, \lambda], \kappa = \vec{V} \cdot \vec{v} \end{aligned}$$

and, since the Neumann integral is given by:

$$\mathcal{N}(\overline{PF}, \overline{pf}) = \int_{\mathbf{P}}^{\mathbf{F}} \int_{\mathbf{p}}^{\mathbf{f}} \frac{d\mathbf{Q} \cdot d\mathbf{q}}{\|\mathbf{Q} - \mathbf{q}\|}$$

the following quantities are calculated:

$$\begin{aligned} d\mathbf{Q} &= \vec{V}dx \\ d\mathbf{q} &= \kappa\vec{V}dy \\ \|\mathbf{Q} - \mathbf{q}\| &= |\Lambda + d + \kappa y - x| \end{aligned}$$

It is worth noticing that the hypothesis on the bounds of d guarantees that the argument of the absolute value in the $\|\mathbf{Q} - \mathbf{q}\|$ definition is always positive. The Neumann integral is calculated by double integration:

$$\begin{aligned} \mathcal{N}(\overline{PF}, \overline{pf}) &= \int_0^\Lambda \int_0^\lambda \frac{\kappa dy dx}{\Lambda + d - x + \kappa y} = \int_0^\Lambda \left[\int_0^\lambda \frac{\kappa dy}{\Lambda + d - x + \kappa y} \right] dx \\ &= \int_0^\Lambda \left[\ln(\Lambda + d + \kappa\lambda - x) - \ln(\Lambda + d - x) \right] dx \\ &= (\Lambda + \kappa\lambda + d) \ln \frac{\Lambda + \kappa\lambda + d}{\kappa\lambda + d} \\ &\quad - (\Lambda + d) \ln \frac{\Lambda + d}{d} \\ &\quad + \Lambda \ln \frac{\kappa\lambda + d}{d} \end{aligned}$$

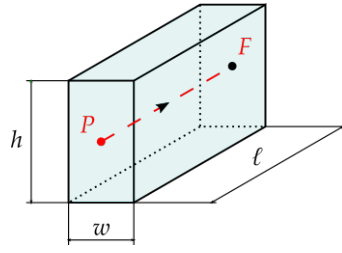


Figure A.6: Computation of the self inductance associated with a finite straight segment

where the following elementary integrals have been used:

$$\int_0^a \frac{\kappa \, du}{K + \kappa u} = \ln \frac{K + \kappa a}{K}$$

$$\int_0^b \ln(K - v) \, dv = K \ln \frac{K}{K - b} + b \ln(K - b) - b$$

The Neumann integral expression can be rewritten using the usual notations for segments. It results:

$$\begin{aligned} \Lambda + \kappa \lambda + d &= \| \mathbf{f} - \mathbf{P} \| \\ \kappa \lambda + d &= \| \mathbf{f} - \mathbf{F} \| \\ \Lambda + d &= \| \mathbf{p} - \mathbf{P} \| \\ d &= \| \mathbf{p} - \mathbf{F} \| \end{aligned}$$

and, finally:

$$\mathcal{N}(\mathcal{S}, s) = \| \mathbf{f} - \mathbf{P} \| \ln \frac{\| \mathbf{f} - \mathbf{P} \|}{\| \mathbf{f} - \mathbf{F} \|} - \| \mathbf{p} - \mathbf{P} \| \ln \frac{\| \mathbf{p} - \mathbf{P} \|}{\| \mathbf{p} - \mathbf{F} \|} + \Lambda \ln \frac{\| \mathbf{f} - \mathbf{F} \|}{\| \mathbf{p} - \mathbf{F} \|} \quad (\text{A.10})$$

A.3.2 Self-inductance of a finite segment

In this case neither the expressions in (A.8) nor in (A.10) are applicable. A proper Neumann function \mathcal{S} is introduced, so that:

$$\mathcal{N}(\mathcal{S}, \mathcal{S}) = \mathcal{S}(\mathcal{S})$$

for any segment \mathcal{S} . The expression for \mathcal{S} depends on the whole coil volume associated with \mathcal{S} and it is given in [22]:

$$\begin{aligned} \mathcal{S}(\mathcal{S}) = \ell \left[2 \ln(2\ell) - \left(1 - \frac{h^2}{6w^2} - \frac{w^2}{6h^2} \right) \ln(h^2 + w^2) + \frac{11}{6} \right. \\ \left. - \frac{4}{3} \frac{h}{w} \arctan\left(\frac{w}{h}\right) - \frac{4}{3} \frac{w}{h} \arctan\left(\frac{h}{w}\right) \right. \\ \left. - \frac{w^2}{3h^2} \ln w - \frac{h^2}{3w^2} \ln h \right] \end{aligned}$$

where w , h and ℓ are, respectively, the width, the height and the length of the coil segment associated with \mathcal{S} (see also A.6).

The expression for \mathcal{S} can be furtherly simplified if the width to height ratio ζ is defined:

$$\zeta = \frac{w}{h} < 1$$

With some algebraic passages the expression of \mathcal{S} can be transformed into:

$$\begin{aligned} \mathcal{S}(\mathcal{S}) = \ell \left[2 \ln \left(\frac{2\ell}{h} \right) - \frac{1}{3} \zeta^2 \ln \zeta + \frac{11}{6} \right. \\ \left. - \left(1 - \frac{1}{6\zeta^2} - \frac{1}{6}\zeta^2 \right) \ln(1 + \zeta^2) \right. \\ \left. - \frac{4}{3} \left(\frac{1}{\zeta} \arctan \zeta + \zeta \arctan \frac{1}{\zeta} \right) \right] \end{aligned}$$

and, considering the Taylor series expansion of transcendental functions:

$$\begin{aligned} \ln(1 + \zeta^2) &= \sum_{n=1}^{+\infty} \frac{(-1)^{n+1}}{n} \zeta^{2n} = \zeta^2 - \frac{1}{2}\zeta^4 + \frac{1}{3}\zeta^6 + \dots \\ \arctan(\zeta) &= \sum_{n=1}^{+\infty} \frac{(-1)^{n+1}}{2n-1} \zeta^{2n-1} = \zeta - \frac{1}{3}\zeta^3 + \frac{1}{5}\zeta^5 + \dots \\ \arctan\left(\frac{1}{\zeta}\right) &= \frac{\pi}{2} + \sum_{n=1}^{+\infty} \frac{(-1)^n}{2n-1} \zeta^{2n-1} = \frac{\pi}{2} - \zeta + \frac{1}{3}\zeta^3 - \frac{1}{5}\zeta^5 + \dots \end{aligned}$$

the expression of Neumann integral for the self-inductance becomes:

$$\mathcal{S}(\mathcal{S}) = \ell \left[2 \ln \frac{2\ell}{h} - K(\zeta) + \frac{2}{3} \right] \quad (\text{A.11})$$

with:

$$K(\zeta) = 0.333\zeta^2 \ln \zeta + 0.083\zeta^6 - 0.011\zeta^4 - 0.694\zeta^2 + 2.094\zeta$$

A.3.3 Neumann integral between infinite segments

The solution of this case is taken from [21] as well. The finite segment \mathcal{S} is identified through the pair of endpoints \mathbf{P} and \mathbf{F} , which give the length of the segment and the unit vector:

$$\begin{aligned} \Lambda &= \|\mathbf{F} - \mathbf{P}\| \\ \vec{\mathbf{V}} &= \frac{\mathbf{F} - \mathbf{P}}{\Lambda} \end{aligned}$$

As regards the pair of infinite segments \mathbf{s}_∞ it is identified through the finite endpoints \mathbf{p} , \mathbf{f} and the reference unit vector $\vec{\mathbf{v}}$. It is assumed that the first segment is oriented from \mathbf{p} to infinity, accordingly to $\vec{\mathbf{v}}$, whereas the second is oriented from infinity to \mathbf{f} , i.e. accordingly to $-\vec{\mathbf{v}}$ (figure A.7).

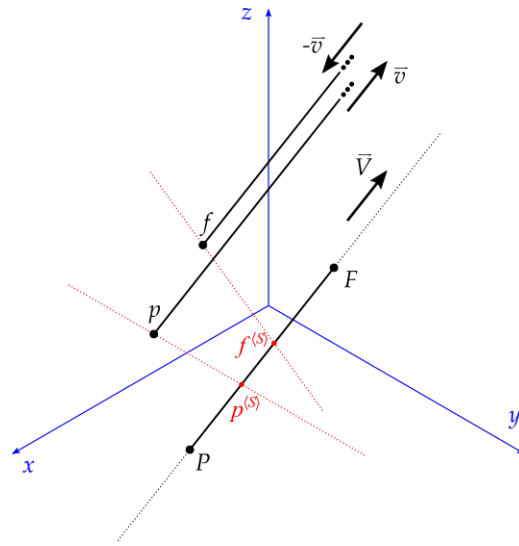
The angle between vectors is defined as usual

$$\cos \varphi = \vec{\mathbf{V}} \cdot \vec{\mathbf{v}}$$

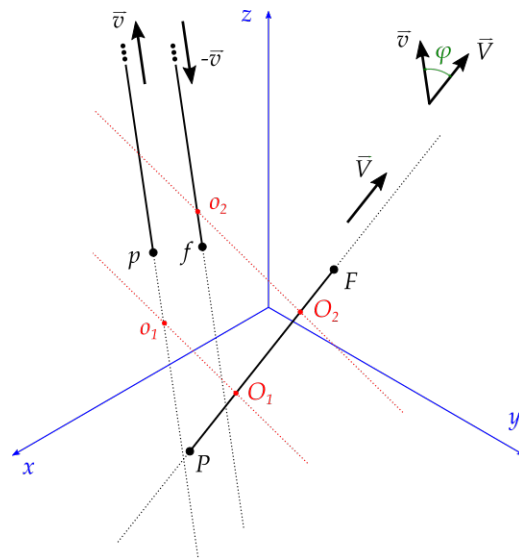
and three cases are possible:

1. $\cos \varphi = 0$, i.e. $\vec{\mathbf{V}} \perp \vec{\mathbf{v}}$ and the Neumann integral is equal to zero:

$$\mathcal{S} \perp \mathbf{s}_\infty \quad \implies \quad \mathcal{I}(\mathcal{S}, \mathbf{s}_\infty) = 0$$



(a) Parallel segments



(b) Generic segments

Figure A.7: Reference nomenclature for the calculation of Neumann integral between a segment and a pair of parallel infinite segments

2. $\cos \varphi = \pm 1$, i.e. $\vec{V} \parallel \vec{v}$. The projections of the infinite segment end-points on segment S are determined (figure A.7a):

$$\begin{aligned} \mathbf{p}^{(S)} &= \mathbf{P} + [(\mathbf{p} - \mathbf{P}) \cdot \vec{V}] \vec{V} \\ \mathbf{f}^{(S)} &= \mathbf{P} + [(\mathbf{f} - \mathbf{P}) \cdot \vec{V}] \vec{V} \end{aligned}$$

and the Neumann integral is given by:

$$\begin{aligned} \mathcal{I}(\mathbf{S}, \mathbf{s}_\infty) &= \|\mathbf{P} - \mathbf{p}\| + \|\mathbf{F} - \mathbf{f}\| - \|\mathbf{P} - \mathbf{f}\| - \|\mathbf{F} - \mathbf{p}\| \\ &+ \Lambda \ln \frac{\|\mathbf{F} - \mathbf{p}\| + (\mathbf{F} - \mathbf{p}^{(S)}) \cdot \vec{V}}{\|\mathbf{F} - \mathbf{f}\| + (\mathbf{F} - \mathbf{f}^{(S)}) \cdot \vec{V}} \\ &+ [(\mathbf{P} - \mathbf{p}^{(S)}) \cdot \vec{V}] \frac{\|\mathbf{F} - \mathbf{p}\| + (\mathbf{F} - \mathbf{p}^{(S)}) \cdot \vec{V}}{\|\mathbf{P} - \mathbf{p}\| + (\mathbf{P} - \mathbf{p}^{(S)}) \cdot \vec{V}} \\ &- [(\mathbf{P} - \mathbf{f}^{(S)}) \cdot \vec{V}] \frac{\|\mathbf{F} - \mathbf{f}\| + (\mathbf{F} - \mathbf{f}^{(S)}) \cdot \vec{V}}{\|\mathbf{P} - \mathbf{f}\| + (\mathbf{P} - \mathbf{f}^{(S)}) \cdot \vec{V}} \end{aligned} \quad (\text{A.12})$$

3. if $0 < |\cos \varphi| < 1$ the two common perpendiculars between the finite segment S and each of the infinite segments of the pair \mathbf{s}_∞ have to be determined. The procedure is analogous to the finite segments case and the intersection between the perpendiculars and S and \mathbf{s}_∞ are determined (figure A.7b):

$$\begin{aligned} \mathbf{O}_1 &= \mathbf{P} + [(\mathbf{p} - \mathbf{P}) \cdot (\vec{V} - \vec{v} \cos \varphi)] \frac{\vec{V}}{1 - \cos^2 \varphi} \\ \mathbf{O}_2 &= \mathbf{P} + [(\mathbf{f} - \mathbf{P}) \cdot (\vec{V} - \vec{v} \cos \varphi)] \frac{\vec{V}}{1 - \cos^2 \varphi} \\ \mathbf{o}_1 &= \mathbf{P} + [(\mathbf{P} - \mathbf{p}) \cdot (\vec{v} - \vec{V} \cos \varphi)] \frac{\vec{v}}{1 - \cos^2 \varphi} \\ \mathbf{o}_2 &= \mathbf{P} + [(\mathbf{P} - \mathbf{f}) \cdot (\vec{v} - \vec{V} \cos \varphi)] \frac{\vec{v}}{1 - \cos^2 \varphi} \end{aligned}$$

The Neumann integral is given by:

$$\mathcal{I}(\mathbf{S}, \mathbf{s}_\infty) = \mathcal{I}_1 \cos \varphi - \mathcal{I}_{2,1} \|\mathbf{O}_1 - \mathbf{o}_1\| \cot \varphi + \mathcal{I}_{2,2} \|\mathbf{O}_2 - \mathbf{o}_2\| \cot \varphi \quad (\text{A.13})$$

being:

$$\begin{aligned} \mathcal{I}_1 = & \left[(\mathbf{P} - \mathbf{O}_1) \cdot \vec{V} \right] \ln \frac{\|\mathbf{P} - \mathbf{p}\| - \left[(\mathbf{P} - \mathbf{O}_1) \cdot \vec{V} \right] \cos \varphi + (\mathbf{p} - \mathbf{o}_1) \cdot \vec{v}}{\|\mathbf{P} - \mathbf{f}\| - \left[(\mathbf{P} - \mathbf{O}_2) \cdot \vec{V} \right] \cos \varphi + (\mathbf{f} - \mathbf{o}_2) \cdot \vec{v}} \\ & + \left[(\mathbf{F} - \mathbf{O}_1) \cdot \vec{V} \right] \ln \frac{\|\mathbf{F} - \mathbf{f}\| - \left[(\mathbf{F} - \mathbf{O}_2) \cdot \vec{V} \right] \cos \varphi + (\mathbf{f} - \mathbf{o}_2) \cdot \vec{v}}{\|\mathbf{F} - \mathbf{p}\| - \left[(\mathbf{F} - \mathbf{O}_1) \cdot \vec{V} \right] \cos \varphi + (\mathbf{p} - \mathbf{o}_1) \cdot \vec{v}} \\ & + \left[(\mathbf{O}_1 - \mathbf{O}_2) \cdot \vec{V} \right] \ln \frac{\|\mathbf{F} - \mathbf{f}\| - \left[(\mathbf{F} - \mathbf{O}_2) \cdot \vec{V} \right] \cos \varphi + (\mathbf{f} - \mathbf{o}_2) \cdot \vec{v}}{\|\mathbf{P} - \mathbf{f}\| - \left[(\mathbf{P} - \mathbf{O}_2) \cdot \vec{V} \right] \cos \varphi + (\mathbf{f} - \mathbf{o}_2) \cdot \vec{v}} \end{aligned}$$

$$\begin{aligned} \mathcal{I}_{2,1} = & \arctan \left[\frac{(\mathbf{F} - \mathbf{O}_1) \cdot \vec{V}}{\|\mathbf{O}_1 - \mathbf{o}_1\|} \sin \varphi \right] - \arctan \left[\frac{(\mathbf{P} - \mathbf{O}_1) \cdot \vec{V}}{\|\mathbf{O}_1 - \mathbf{o}_1\|} \sin \varphi \right] \\ & + \arctan \left[\frac{\|\mathbf{O}_1 - \mathbf{o}_1\|}{\|\mathbf{P} - \mathbf{p}\|} \cot \varphi + \frac{[(\mathbf{p} - \mathbf{o}_1) \cdot \vec{v}][(\mathbf{P} - \mathbf{o}_1) \cdot \vec{V}]}{\|\mathbf{O}_1 - \mathbf{o}_1\| \|\mathbf{P} - \mathbf{p}\|} \sin \varphi \right] \\ & - \arctan \left[\frac{\|\mathbf{O}_1 - \mathbf{o}_1\|}{\|\mathbf{F} - \mathbf{p}\|} \cot \varphi + \frac{[(\mathbf{p} - \mathbf{o}_1) \cdot \vec{v}][(\mathbf{F} - \mathbf{o}_1) \cdot \vec{V}]}{\|\mathbf{O}_1 - \mathbf{o}_1\| \|\mathbf{F} - \mathbf{p}\|} \sin \varphi \right] \end{aligned}$$

$$\begin{aligned} \mathcal{I}_{2,2} = & \arctan \left[\frac{(\mathbf{F} - \mathbf{O}_2) \cdot \vec{V}}{\|\mathbf{O}_2 - \mathbf{o}_2\|} \sin \varphi \right] - \arctan \left[\frac{(\mathbf{P} - \mathbf{O}_2) \cdot \vec{V}}{\|\mathbf{O}_2 - \mathbf{o}_2\|} \sin \varphi \right] \\ & + \arctan \left[\frac{\|\mathbf{O}_2 - \mathbf{o}_2\|}{\|\mathbf{P} - \mathbf{f}\|} \cot \varphi + \frac{[(\mathbf{f} - \mathbf{o}_2) \cdot \vec{v}][(\mathbf{P} - \mathbf{o}_2) \cdot \vec{V}]}{\|\mathbf{O}_2 - \mathbf{o}_2\| \|\mathbf{P} - \mathbf{f}\|} \sin \varphi \right] \\ & - \arctan \left[\frac{\|\mathbf{O}_2 - \mathbf{o}_2\|}{\|\mathbf{F} - \mathbf{f}\|} \cot \varphi + \frac{[(\mathbf{f} - \mathbf{o}_2) \cdot \vec{v}][(\mathbf{F} - \mathbf{o}_2) \cdot \vec{V}]}{\|\mathbf{O}_2 - \mathbf{o}_2\| \|\mathbf{F} - \mathbf{f}\|} \sin \varphi \right] \end{aligned}$$

B | MMF AND FLUX-LINKAGE CALCULATION

The MMF distribution of an electric machine winding is important, because it links the winding current, the air-gap flux density distribution and the flux-linkage. This appendix details the calculation of the MMF distribution for a distributed double-layer three-phase winding. The winding function is determined (section B.1) and applied to determine the MMF distribution and flux-linkage for two notable cases:

- a three-phase system of currents, which produces a rotating MMF wave (B.2);
- a single-phase system of currents, which produces a pulsating MMF wave (B.3).

B.1 WINDING FUNCTION EXPRESSION

B.1.1 Winding structure

The winding is made of $2Z$ active coilsides distributed in Z slots equally-spaced along a circumference. Each slot contains two coil-sides and each coilside is made of N_{tc} conductors. The winding is also subdivided into $2p$ poles and each pole is subdivided into three phase belts, one per phase. The number of coilsides per each layer in a phase belt is:

$$q = \frac{Z}{6p}$$

thus the number of coils per pole-pair per phase for two layer is $2q$.

The actual coilsides of a given coil belong to different layers, for manufacturing reasons. Furthermore the coil pitch is usually shorter than the pole pitch and the coil-to-pole pitch ratio is r . However a winding of this kind is magnetically equivalent to two independent single-layer full-pitch windings, having their axes shifted of an angle equal to pitch shortening. The half-width of this (mechanical) angle is:

$$\zeta = \frac{1}{2}(1-r)3q\frac{2\pi}{Z} = (1-r)\frac{\pi}{2p}$$

so if a double-layer winding phase has its axis at a given electric angle α the two single-layer phases are placed at $\alpha \pm p\zeta$.

Each phase belt in a pole-pair is made of q coils shifted by a mechanical angle ε given by:

$$\varepsilon = \frac{2\pi}{Z} = \frac{\pi}{3pq}$$

so a phase whose axis is at electrical angle ζ is actually made by coils whose axes are placed between $\zeta - p(q-1)\varepsilon/2$ and $\zeta + p(q-1)\varepsilon/2$ and shifted by

an electrical angle equal to $p\varepsilon$. Considering the expression for ε given above, the coil axes limits are, in terms of electrical angle, $\xi \mp (q-1)/q\pi/6$, and the coil shift is $\pi/(3q)$.

B.1.2 Winding function expression

The MMF associated with a generic full-pitch turn having its axis at electric angle α_0 is obtained through the multiplication of the turn current by a proper function given by:

$$\hat{w}(\alpha, \alpha_0) = \begin{cases} \frac{1}{2} & \text{if } \alpha \in \left[\alpha_0 + (4k-1)\frac{\pi}{2}, \alpha_0 + (4k+1)\frac{\pi}{2} \right], \quad k \in \mathbb{Z} \\ -\frac{1}{2} & \text{otherwise} \end{cases} \quad (\text{B.1})$$

The angles in (B.1) are electric angles. \mathbb{Z} is the set of integer numbers. This expression can be expressed as its Fourier series expansion, obtaining:

$$w(\alpha, \alpha_0) = \sum_{h=1}^{+\infty} \frac{2}{h\pi} \sin\left(h\frac{\pi}{2}\right) \cos(h(\alpha - \alpha_0)) \quad (\text{B.2})$$

The term $\sin(h\frac{\pi}{2})$ is always zero for even harmonics, whereas becomes alternatively 1 and -1 for odd harmonics. The expression in (B.2) can be rewritten as:

$$w(\alpha, \alpha_0) = \sum_{k=0}^{+\infty} \frac{2}{(4k+1)\pi} \cos((4k+1)(\alpha - \alpha_0)) - \sum_{k=1}^{+\infty} \frac{2}{(4k-1)\pi} \cos((4k-1)(\alpha - \alpha_0))$$

The total MMF of a phase is obtained by summing all the contributions of the turns in the two layers. Each coil is made of N_{tc} turns and if the phase has N_{pc} parallel circuits then the turn current is i/N_{pc} , being i the total phase current. The MMF for a layer with its axis placed at electric angle ξ is:

$$\hat{F}(\alpha, \xi, i) = \sum_{n=0}^{q-1} \frac{N_{tc}i}{N_{pc}} w\left(\alpha, \xi - \frac{q-1}{q}\frac{\pi}{6} + n\frac{\pi}{3q}\right) \quad (\text{B.3})$$

Considering the expression for w given in (B.2) then the h -th harmonic of \hat{F} becomes:

$$\hat{F}_h(\alpha, \xi, i) = \frac{2}{h\pi} \frac{N_{tc}i}{N_{pc}} \sin\left(h\frac{\pi}{2}\right) \sum_{n=0}^{q-1} \cos\left(h\alpha - h\xi + h\frac{q-1}{q}\frac{\pi}{6} - hn\frac{\pi}{3q}\right) \quad (\text{B.4})$$

Considering that:

$$\begin{aligned} \cos\left(h\alpha - h\xi + h\frac{q-1}{q}\frac{\pi}{6} - hn\frac{\pi}{3q}\right) &= \text{Re} \left\{ e^{jh\left(\alpha - \xi + \frac{q-1}{q}\frac{\pi}{6} - n\frac{\pi}{3q}\right)} \right\} \\ &= \text{Re} \left\{ e^{jh\left(\alpha - \xi + \frac{q-1}{q}\frac{\pi}{6}\right)} \left(e^{-jh\frac{\pi}{3q}} \right)^n \right\} \end{aligned}$$

and

$$\sum_{n=0}^{N-1} x^n = \frac{1 - x^N}{1 - x}$$

then

$$\begin{aligned} \sum_{n=0}^{q-1} \left(e^{-jh \frac{\pi}{3q}} \right)^n &= \frac{1 - e^{-jh \frac{\pi}{3}}}{1 - e^{-jh \frac{\pi}{3q}}} \\ &= \frac{e^{-jh \frac{\pi}{6}} \left(e^{jh \frac{\pi}{6}} - e^{-jh \frac{\pi}{6}} \right)}{e^{-jh \frac{\pi}{6q}} \left(e^{jh \frac{\pi}{6q}} - e^{-jh \frac{\pi}{6q}} \right)} \\ &= e^{-jh \frac{q-1}{q} \frac{\pi}{6}} \frac{\sin \left(h \frac{\pi}{6} \right)}{\sin \left(h \frac{\pi}{6q} \right)} \end{aligned}$$

and, finally:

$$\sum_{n=0}^{q-1} \cos \left(h\alpha - h\xi + h \frac{q-1}{q} \frac{\pi}{6} - hn \frac{\pi}{3q} \right) = \frac{\sin \left(h \frac{\pi}{6} \right)}{\sin \left(h \frac{\pi}{6q} \right)} \cos (h(\alpha - \xi))$$

The distribution factor for the h -th harmonic is defined as:

$$k_{d,h} = \frac{\sin \left(h \frac{\pi}{6} \right)}{q \sin \left(h \frac{\pi}{6q} \right)} \quad (\text{B.5})$$

and the h -th harmonic of the MMF for a single layer becomes:

$$\hat{F}_h(\alpha, \xi, i) = \frac{2}{h\pi} q k_{d,h} \frac{N_{tc} i}{N_{pc}} \sin \left(h \frac{\pi}{2} \right) \cos (h(\alpha - \xi)) \quad (\text{B.6})$$

Letting

$$\hat{f}_h(i) = \frac{2}{h\pi} q k_{d,h} \frac{N_{tc} i}{N_{pc}}$$

then the total MMF for a single layer is:

$$\hat{F}(\alpha, \xi, i) = \sum_{h=1}^{+\infty} \hat{f}_h(i) \sin \left(h \frac{\pi}{2} \right) \cos (h(\alpha - \xi)) \quad (\text{B.7})$$

The MMF of the phase is obtained combining the contributions in (B.7) for the two layers. Remembering that for a phase with axis in α_0 the two layers have their axes in $\alpha_0 \mp (1-r)\pi/2$ the h -th harmonic for the phase MMF is given:

$$\begin{aligned} F(\alpha, \alpha_0, i) &= \hat{F} \left(\alpha, \alpha_0 - (1-r) \frac{\pi}{2}, i \right) + \hat{F} \left(\alpha, \alpha_0 + (1-r) \frac{\pi}{2}, i \right) \\ &= \sum_{h=1}^{+\infty} \hat{f}_h(i) \sin \left(\frac{h\pi}{2} \right) \cos \left(h(\alpha - \alpha_0) + (1-r)h \frac{\pi}{2} \right) \\ &\quad + \sum_{h=1}^{+\infty} \hat{f}_h(i) \sin \left(\frac{h\pi}{2} \right) \cos \left(h(\alpha - \alpha_0) - (1-r)h \frac{\pi}{2} \right) \end{aligned} \quad (\text{B.8})$$

Using the angle sum trigonometric identities:

$$\cos(x + y) = \cos x \cos y - \sin x \sin y$$

$$\cos(x - y) = \cos x \cos y + \sin x \sin y$$

$$\cos(x + y) + \cos(x - y) = 2 \cos x \cos y$$

then

$$F(\alpha, \alpha_0, i) = \sum_{h=1}^{+\infty} 2\hat{f}_h(i) \sin\left(\frac{h\pi}{2}\right) \cos(h(\alpha - \alpha_0)) \cos\left((1-r)h\frac{\pi}{2}\right)$$

Using the angle sum identity again we obtain

$$\cos\left((1-r)h\frac{\pi}{2}\right) = \cos\left(h\frac{\pi}{2}\right) \cos\left(rh\frac{\pi}{2}\right) + \sin\left(h\frac{\pi}{2}\right) \sin\left(rh\frac{\pi}{2}\right)$$

The terms $\sin(h\pi/2)$ and $\cos(h\pi/2)$ from this equation combine with the term $\sin(h\pi/2)$ from (B.8). In particular:

$$\sin\left(h\frac{\pi}{2}\right) \cos\left(h\frac{\pi}{2}\right) = \frac{1}{2} \sin(h\pi) = 0 \quad \forall h$$

$$\sin\left(h\frac{\pi}{2}\right) \sin\left(h\frac{\pi}{2}\right) = \sin^2\left(h\frac{\pi}{2}\right) = \begin{cases} 1 & \text{if } h \text{ is odd} \\ 0 & \text{if } h \text{ is even} \end{cases}$$

The pitch factor for the h -th harmonic is defined:

$$k_{p,h} = \sin\left(rh\frac{\pi}{2}\right) \quad (\text{B.9})$$

and the expression for the phase MMF is finally obtained

$$F(\alpha, \alpha_0, i) = \sum_{\substack{h=2k+1 \\ k \in \mathbb{N}}} \frac{4}{h\pi} k_{d,h} k_{p,h} \frac{q N_{tc}}{N_{pc}} i \cos(h(\alpha - \alpha_0)) \quad (\text{B.10})$$

The expression in (B.10) can be furtherly transformed considering that:

$$\frac{q N_{tc}}{N_{pc}} = \frac{Z N_{tc}}{32p N_{pc}} = \frac{N}{2p}$$

where N is the number of turns per phase. Furthermore the winding factor for the h -th harmonic is defined:

$$k_{w,h} = k_{d,h} k_{p,h} = \sin\left(rh\frac{\pi}{2}\right) \frac{\sin\left(h\frac{\pi}{6}\right)}{q \sin\left(\frac{h\pi}{q6}\right)} \quad (\text{B.11})$$

With these assumption the phase MMF becomes

$$F(\alpha, \alpha_0, i) = \mathcal{W}(\alpha, \alpha_0) i \quad (\text{B.12})$$

where the phase winding function has been introduced

$$\mathcal{W}(\alpha, \alpha_0) = \sum_{\substack{h=2k+1 \\ k \in \mathbb{N}}} \frac{4}{h\pi} \frac{k_{w,h} N}{2p} \cos(h(\alpha - \alpha_0)) \quad (\text{B.13})$$

B.1.3 Flux-linkage expression

Let consider a certain air-gap flux-density spatial wave. Without losing of generality we can consider this wave harmonically-dependending from the spatial coordinate, i.e.

$$\mathcal{B}_\kappa(\alpha) = B_\kappa \cos(\kappa\alpha - \phi_\kappa)$$

with α an electrical angle and κ a positive integer giving the wave harmonic order, i.e. the number of periods in a full pole-pair pitch. B_κ and ϕ_κ are proper expressions not depending from α . The flux-density expression can be also expressed using the complex notation:

$$\mathcal{B}_\kappa(\alpha) = \text{Re} \{ \tilde{B}_\kappa e^{j\kappa\alpha} \}$$

where $\tilde{B}_\kappa = B_\kappa e^{-j\phi_\kappa}$ is the spatial phasor of flux-density.

The flux linkage of a turn with axis in α_0 is given by integration of the elementary flux along the turn angular span, whose limits are $\alpha_0 \mp \pi/2$:

$$\begin{aligned} \bar{\psi}_\kappa(\alpha_0, \tilde{B}_\kappa) &= \int_{\alpha_0 - \frac{\pi}{2}}^{\alpha_0 + \frac{\pi}{2}} \tilde{B}_\kappa e^{j\kappa\alpha} R \ell d\alpha \\ &= \frac{R\ell}{j\kappa} \tilde{B}_\kappa \left[e^{j\kappa(\alpha_0 + \frac{\pi}{2})} - e^{j\kappa(\alpha_0 - \frac{\pi}{2})} \right] \\ &= \frac{2R\ell}{\kappa} \tilde{B}_\kappa e^{j\kappa\alpha_0} \frac{e^{j\kappa\frac{\pi}{2}} - e^{-j\kappa\frac{\pi}{2}}}{2j} \\ &= \frac{2R\ell}{\kappa} \sin\left(\kappa\frac{\pi}{2}\right) \tilde{B}_\kappa e^{j\kappa\alpha_0} \end{aligned} \quad (\text{B.14})$$

where R and ℓ are the air-gap average radius and length, respectively.

The flux-linkage of the coils in a layer is obtained by adding all the turn contributions from (B.14). As before, we consider the layer axis placed at electric angle ζ ; the corresponding turns axes cover the span $\zeta \mp (q-1)/q \pi/6$ and are equally shifted by an angle equal to $\pi/(3q)$:

$$\begin{aligned} \hat{\Psi}_\kappa(\zeta, \tilde{B}_\kappa) &= \sum_{n=0}^{q-1} N_{\text{tc}} \bar{\psi}_\kappa\left(\zeta - \frac{q-1}{q}\frac{\pi}{6} + n\frac{\pi}{3q}, \tilde{B}_\kappa\right) \\ &= \frac{2}{\kappa} \tilde{B}_\kappa R \ell N_{\text{tc}} \sin\left(\kappa\frac{\pi}{2}\right) \sum_{n=0}^{q-1} e^{j\kappa\left(\zeta - \kappa\frac{q-1}{q}\frac{\pi}{6} + n\frac{\pi}{3q}\right)} \\ &= \frac{2}{\kappa} \tilde{B}_\kappa R \ell N_{\text{tc}} \sin\left(\kappa\frac{\pi}{2}\right) e^{j\kappa\zeta} e^{j\kappa\frac{q-1}{q}\frac{\pi}{6}} \sum_{n=0}^{q-1} \left(e^{j\kappa\frac{\pi}{3q}}\right)^n \\ &= \frac{2}{\kappa} \tilde{B}_\kappa R \ell k_{d,\kappa} N_{\text{tc}} \sin\left(\kappa\frac{\pi}{2}\right) e^{j\kappa\zeta} \end{aligned} \quad (\text{B.15})$$

where the distribution factor from (B.5) has been used.

Finally, the phase flux linkage is obtained by summing the contribution from the two layers. Bear in mind that the expression in (B.15) assumes that

all the coils are connected in series but, actually, the phase winding has N_{pc} parallel circuits, so the phase flux-linkage must be divided by this quantity:

$$\begin{aligned}
\bar{\Psi}_\kappa(\alpha_0, \tilde{B}_\kappa) &= \frac{\hat{\Psi}_\kappa(\alpha_0 - (1-r)\frac{\pi}{2}, \tilde{B}_\kappa) + \hat{\Psi}_\kappa(\alpha_0 + (1-r)\frac{\pi}{2}, \tilde{B}_\kappa)}{N_{pc}} \\
&= \frac{2}{\kappa} \tilde{B}_\kappa R \ell k_{d,\kappa} \frac{q N_{tc}}{N_{pc}} \sin\left(\kappa \frac{\pi}{2}\right) e^{j\kappa\alpha_0} \left[e^{-j\kappa(1-r)\frac{\pi}{2}} + e^{j\kappa(1-r)\frac{\pi}{2}} \right] \\
&= \frac{4}{\kappa} \tilde{B}_\kappa R \ell k_{d,\kappa} \frac{q N_{tc}}{N_{pc}} \sin\left(\kappa \frac{\pi}{2}\right) \cos\left(\kappa(1-r)\frac{\pi}{2}\right) e^{j\kappa\alpha_0} \\
&= \frac{4}{\kappa} \tilde{B}_\kappa R \ell k_{d,\kappa} k_{p,\kappa} \frac{q N_{tc}}{N_{pc}} \sin^2\left(\kappa \frac{\pi}{2}\right) e^{j\kappa\alpha_0}
\end{aligned} \tag{B.16}$$

where α_0 is the phase-axis electric angle and the definition of pitch factor from (B.9) has been used again. It is worth noticing that, because of the term $\sin^2(\kappa \frac{\pi}{2})$, the flux-linkage is zero for all the even harmonics, similarly to what has been shown for the MMF.

An alternative expression for $\bar{\Psi}_\kappa$ could be obtained if it is considered that the term \tilde{B}_κ represent a spatial sine-wave. The flux-per-pole of this spatial wave is given by:

$$\Phi_\kappa = \frac{2}{\pi} |\tilde{B}_\kappa| \tau_\kappa \ell$$

where $|\tilde{B}_\kappa|$ is the peak of the flux-density spatial wave and τ_κ is the pole-pitch length for the flux-density wave. Since κ is the number of wave periods in a machine pole-pair pitch, the wave pole-pitch and the actual machine pole-pitch are bonded by the equation $\tau_p = \kappa \tau_\kappa$. As regards the argument of complex \tilde{B}_κ it represents the position at which the wave peak actually occurs. Thus, if a turn has its axis aligned with this angle, it will experience the maximum flux-linkage. Therefore it is legit considering the following complex expression of the κ -th flux-density wave flux per pole:

$$\check{\Phi}_\kappa = \frac{2}{\pi} \tilde{B}_\kappa \tau_\kappa \ell$$

At this point we can observe that:

$$\tilde{B}_\kappa R \ell = \frac{4\pi}{4\pi} \tilde{B}_\kappa R \ell = \frac{1}{4} \frac{2}{\pi} \tilde{B}_\kappa 2p\kappa\tau_\kappa\ell = \frac{2p\kappa}{4} \check{\Phi}_\kappa$$

where the fact that, clearly, $2\pi R = 2p\kappa\tau_\kappa$ has been used. Finally, remembering that it holds:

$$\begin{aligned}
\frac{q N_{tc}}{N_{pc}} &= \frac{N}{2p} \\
k_{p,\kappa} k_{d,\kappa} &= k_{w,\kappa} = \sin\left(\kappa r \frac{\pi}{2}\right) \frac{\sin\left(\kappa \frac{\pi}{6}\right)}{q \sin\left(\frac{\kappa}{q} \frac{\pi}{6}\right)}
\end{aligned}$$

expression (B.16) can be transformed into:

$$\bar{\Psi}_\kappa(\alpha_0, \check{\Phi}_\kappa) = k_{w,\kappa} N \check{\Phi}_\kappa e^{j\kappa\alpha_0} \tag{B.17}$$

or, switching back to the real notation:

$$\Psi_\kappa(\alpha_0) = k_{w,\kappa} N |\check{\Phi}_\kappa| \cos(\kappa\alpha_0 + \arg(\check{\Phi}_\kappa)) \tag{B.18}$$

B.2 ROTATING SYSTEM OF MMF AND FLUX LINKAGE

A three-phase symmetric system of currents is given by:

$$\begin{cases} i_U(t) = \sqrt{2} I \cos(\omega t) \\ i_V(t) = \sqrt{2} I \cos(\omega t - \frac{2}{3}\pi) \\ i_W(t) = \sqrt{2} I \cos(\omega t + \frac{2}{3}\pi) \end{cases} \quad (\text{B.19})$$

being I the RMS value of phase current and ω the angular frequency. The phase axis are placed at electric angles:

$$\begin{cases} \alpha_U = 0 \\ \alpha_V = \frac{2}{3}\pi \\ \alpha_W = -\frac{2}{3}\pi \end{cases} \quad (\text{B.20})$$

The total three-phase winding MMF is obtained summing the phase MMF from (B.12):

$$\mathcal{F}(\alpha, t) = \mathcal{W}(\alpha, \alpha_U) i_U(t) + \mathcal{W}(\alpha, \alpha_V) i_V(t) + \mathcal{W}(\alpha, \alpha_W) i_W(t) \quad (\text{B.21})$$

and, accordingly to (B.13), (B.19) and (B.20), we obtain :

$$\begin{aligned} \mathcal{F}(\alpha, t) = \sum_{h=1,3,5,1\dots} \frac{4\sqrt{2} k_{w,h} N}{h\pi} \frac{I}{2p} & \left[\cos(h\alpha) \cos(\omega t) \right. \\ & + \cos(h\alpha - h\frac{2}{3}\pi) \cos(\omega t - \frac{2}{3}\pi) \\ & \left. + \cos(h\alpha + h\frac{2}{3}\pi) \cos(\omega t + \frac{2}{3}\pi) \right] \end{aligned} \quad (\text{B.22})$$

Applying the angle sum trigonometric identities the terms inside the summatory in (B.22) become:

$$\begin{aligned} \cos(h\alpha) \cos(\omega t) &= \frac{1}{2} \cos(\alpha - \omega t) + \frac{1}{2} \cos(\alpha + \omega t) \\ \cos(h\alpha - h\frac{2}{3}\pi) \cos(\omega t - \frac{2}{3}\pi) &= \frac{1}{2} \cos\left(\alpha - \omega t - (h-1)\frac{2}{3}\pi\right) \\ & \quad + \frac{1}{2} \cos\left(\alpha + \omega t - (h+1)\frac{2}{3}\pi\right) \\ \cos(h\alpha + h\frac{2}{3}\pi) \cos(\omega t + \frac{2}{3}\pi) &= \frac{1}{2} \cos\left(\alpha - \omega t + (h-1)\frac{2}{3}\pi\right) \\ & \quad + \frac{1}{2} \cos\left(\alpha + \omega t + (h+1)\frac{2}{3}\pi\right) \end{aligned}$$

and, applying again the trigonometric identities, expression (B.22) becomes

$$\begin{aligned} \mathcal{F}(\alpha, t) = \sum_{h=1,3,5,1\dots} \frac{4\sqrt{2} k_{w,h} N}{h\pi} \frac{I}{2p} & \left\{ \left[\frac{1}{2} + \cos\left((h-1)\frac{2}{3}\pi\right) \right] \cos(h\alpha - \omega t) \right. \\ & \left. + \left[\frac{1}{2} + \cos\left((h+1)\frac{2}{3}\pi\right) \right] \cos(h\alpha + \omega t) \right\} \end{aligned}$$

Now, considering that:

$$\begin{aligned}\cos\left((h-1)\frac{2}{3}\pi\right) &= -\frac{1}{2}\cos\left(h\frac{2}{3}\pi\right) + \frac{\sqrt{3}}{2}\sin\left(h\frac{2}{3}\pi\right) \\ \cos\left((h+1)\frac{2}{3}\pi\right) &= -\frac{1}{2}\cos\left(h\frac{2}{3}\pi\right) - \frac{\sqrt{3}}{2}\sin\left(h\frac{2}{3}\pi\right)\end{aligned}$$

and, for $k \in \mathbb{N}$:

$$\begin{aligned}\cos\left(h\frac{2}{3}\pi\right) &= \begin{cases} -\frac{1}{2} & \text{if } h = 6k + 1 = 1, 7, 13, \dots \\ 1 & \text{if } h = 6k + 3 = 3, 9, 15, \dots \\ -\frac{1}{2} & \text{if } h = 6k + 5 = 5, 11, 17, \dots \end{cases} \\ \sin\left(h\frac{2}{3}\pi\right) &= \begin{cases} \frac{\sqrt{3}}{2} & \text{if } h = 6k + 1 = 1, 7, 13, \dots \\ 0 & \text{if } h = 6k + 3 = 3, 9, 15, \dots \\ -\frac{\sqrt{3}}{2} & \text{if } h = 6k + 5 = 5, 11, 17, \dots \end{cases}\end{aligned}$$

then the expression for the winding MMF becomes:

$$\begin{aligned}\mathcal{F}(\alpha, t) &= \sum_{\substack{h=6k+1 \\ k \in \mathbb{N}}} \frac{6\sqrt{2} k_{w,h} N}{h\pi} \frac{I}{2p} \cos(\omega t - \alpha) \\ &+ \sum_{\substack{h=6k-1 \\ k \in \mathbb{N} \setminus \{0\}}} \frac{6\sqrt{2} k_{w,h} N}{h\pi} \frac{I}{2p} \cos(\omega t + \alpha)\end{aligned}\tag{B.23}$$

The three-phase MMF peak is $3/2$ times the single-phase MMF peak. The MMF wave has only odd harmonics that are not multiples of 3. Furthermore the harmonics are alternatively counter-rotating, i.e. the $(6k+1)$ -th harmonics rotate Counter-Clock-Wise (CCW), whereas the $(6k-1)$ -th harmonics rotate Clock-Wise (CW).

The air-gap flux-density spatial wave is given by:

$$\mathcal{B}(\alpha, t) = \mu_0 \frac{\mathcal{F}(\alpha, t)}{g}\tag{B.24}$$

where g is the air-gap length. Considering the expression for \mathcal{F} given in (B.23) the peak value of the h -th harmonic of the flux-density spatial wave is given:

$$B_h = \mu_0 \frac{6\sqrt{2} k_{w,h} N}{h\pi} \frac{I}{2p} \frac{1}{g}\tag{B.25}$$

and the expression for the flux-density total distribution becomes:

$$\mathcal{B}(\alpha, t) = \sum_{h=6k+1} B_h \cos(h\alpha - \omega t) + \sum_{h=6k-1} B_h \cos(h\alpha + \omega t)\tag{B.26}$$

The flux per pole associated with the h -th harmonic is

$$\Phi_h = \frac{2}{\pi} B_h \frac{\tau_p}{h} \ell\tag{B.27}$$

and the flux-phasor is given by:

$$\tilde{\Phi}_h = \begin{cases} \Phi_h e^{-j\omega t} & \text{if } h = 6k + 1 \\ \Phi_h e^{j\omega t} & \text{if } h = 6k - 1 \end{cases}$$

so the complex flux linkages for the three phases are:

$$\begin{cases} \tilde{\Psi}_U(t) = \sum_{h=6k+1} k_{w,h} N \Phi_h e^{-j\omega t} + \sum_{h=6k-1} k_{w,h} N \Phi_h e^{j\omega t} \\ \tilde{\Psi}_V(t) = \sum_{h=6k+1} k_{w,h} N \Phi_h e^{-j(\omega t + h\frac{2}{3}\pi)} + \sum_{h=6k-1} k_{w,h} N \Phi_h e^{j(\omega t + h\frac{2}{3}\pi)} \\ \tilde{\Psi}_W(t) = \sum_{h=6k+1} k_{w,h} N \Phi_h e^{-j(\omega t - h\frac{2}{3}\pi)} + \sum_{h=6k-1} k_{w,h} N \Phi_h e^{j(\omega t - h\frac{2}{3}\pi)} \end{cases}$$

It is worth noticing that, since the actual expression for flux-linkages is the real part of these complex value, each term can be substituted with its conjugate, if this is convenient. Furthermore it can be observed that:

$$h\frac{2}{3}\pi = \begin{cases} 4k\pi + \frac{2}{3}\pi \equiv \frac{2}{3}\pi & \text{if } h = 6k + 1 \\ 4k\pi - \frac{2}{3}\pi \equiv -\frac{2}{3}\pi & \text{if } h = 6k - 1 \end{cases}$$

so the phase flux-linkages are:

$$\begin{cases} \Psi_U(t) = \sum_{h=6k+1} k_{w,h} N \Phi_h e^{j\omega t} + \sum_{h=6k-1} k_{w,h} N \Phi_h e^{j\omega t} \\ \Psi_V(t) = \sum_{h=6k+1} k_{w,h} N \Phi_h e^{j(\omega t - \frac{2}{3}\pi)} + \sum_{h=6k-1} k_{w,h} N \Phi_h e^{j(\omega t - \frac{2}{3}\pi)} \\ \Psi_W(t) = \sum_{h=6k+1} k_{w,h} N \Phi_h e^{j(\omega t + \frac{2}{3}\pi)} + \sum_{h=6k-1} k_{w,h} N \Phi_h e^{j(\omega t + \frac{2}{3}\pi)} \end{cases}$$

and, finally:

$$\begin{cases} \Psi_U(t) = \sum_{h=6k\pm 1} k_{w,h} N \Phi_h \cos(\omega t) \\ \Psi_V(t) = \sum_{h=6k\pm 1} k_{w,h} N \Phi_h \cos(\omega t - \frac{2}{3}\pi) \\ \Psi_W(t) = \sum_{h=6k\pm 1} k_{w,h} N \Phi_h \cos(\omega t + \frac{2}{3}\pi) \end{cases} \quad (\text{B.28})$$

B.2.1 Extention to a generic three-phase system

It is well-known that a generic (non symmetric) three-phase system of currents (with the same frequency) can be studied as the superposition of three symmetric systems [52]:

- zero-sequence
- positive sequence (or sequence 1)
- negative sequence (or sequence 2)

Thus, given a generic system of currents $\langle I_{UVW} \rangle$ it is assumed that:

$$\langle I_{UVW} \rangle = \begin{vmatrix} \bar{I}_U \\ \bar{I}_V \\ \bar{I}_W \end{vmatrix} = \bar{I}_0 \begin{vmatrix} 1 \\ 1 \\ 1 \end{vmatrix} + \bar{I}_1 \begin{vmatrix} 1 \\ \check{\omega}^2 \\ \check{\omega} \end{vmatrix} + \bar{I}_2 \begin{vmatrix} 1 \\ \check{\omega} \\ \check{\omega}^2 \end{vmatrix} \quad (\text{B.29})$$

where $\check{\omega}$ is the sequence-shift operator, defined as:

$$\check{\omega} = e^{j\frac{2\pi}{3}} \quad \text{so that} \quad \check{\omega}^n = \begin{cases} 1 & \text{if } n = 3k \\ \check{\omega} & \text{if } n = 3k + 1 \\ \check{\omega}^* & \text{if } n = 3k + 2 \end{cases}$$

and \bar{I}_0 , \bar{I}_1 and \bar{I}_2 are the phasors of the sequence currents, for whose it results:

$$\bar{I}_0 = \sqrt{2}I_0e^{j\phi_0} \quad \bar{I}_1 = \sqrt{2}I_1e^{j\phi_1} \quad \bar{I}_2 = \sqrt{2}I_2e^{j\phi_2}$$

If the system is linear the MMF and the flux linkages produced by an arbitrary system of currents can be determined superposing the effects of each symmetric system acting singularly. The case examined above for a symmetric three phase system is actually the positive sequence system. Proceeding in a similar way, the expression of the winding MMF for the three sequences can be calculated:

$$\mathcal{F}_0(\alpha, t) = \sum_{h=6k+3} \frac{12\sqrt{2}}{h\pi} \frac{k_{w,h}N}{2p} I_0 \cos(h\alpha) \cos(\omega t + \phi_0)$$

$$\begin{aligned} \mathcal{F}_1(\alpha, t) &= \sum_{h=6k+1} \frac{6\sqrt{2}}{h\pi} \frac{k_{w,h}N}{2p} I_1 \cos(\omega t + \phi_1 - h\alpha) \\ &+ \sum_{h=6k-1} \frac{6\sqrt{2}}{h\pi} \frac{k_{w,h}N}{2p} I_1 \cos(\omega t + \phi_1 + h\alpha) \end{aligned}$$

$$\begin{aligned} \mathcal{F}_2(\alpha, t) &= \sum_{h=6k+1} \frac{6\sqrt{2}}{h\pi} \frac{k_{w,h}N}{2p} I_2 \cos(\omega t + \phi_2 + h\alpha) \\ &+ \sum_{h=6k-1} \frac{6\sqrt{2}}{h\pi} \frac{k_{w,h}N}{2p} I_2 \cos(\omega t + \phi_2 - h\alpha) \end{aligned}$$

The flux-density spatial harmonics for the three sequences are given by:

$$\begin{cases} B_h^{(0)} = \mu_0 \frac{12\sqrt{2}}{h\pi} \frac{k_{w,h}N}{2p} \frac{I_0}{g} \\ B_h^{(1)} = \mu_0 \frac{6\sqrt{2}}{h\pi} \frac{k_{w,h}N}{2p} \frac{I_1}{g} \\ B_h^{(2)} = \mu_0 \frac{6\sqrt{2}}{h\pi} \frac{k_{w,h}N}{2p} \frac{I_2}{g} \end{cases}$$

and the corresponding fluxes per pole are:

$$\begin{cases} \Phi_h^{(0)} = \frac{2}{\pi} B_h^{(0)} \frac{\tau_p}{h} \ell \\ \Phi_h^{(1)} = \frac{2}{\pi} B_h^{(1)} \frac{\tau_p}{h} \ell \\ \Phi_h^{(2)} = \frac{2}{\pi} B_h^{(2)} \frac{\tau_p}{h} \ell \end{cases}$$

and, finally, the flux-linkage systems:

$$\begin{aligned}\langle \Psi^{(0)} \rangle &= \begin{vmatrix} 1 \\ 1 \\ 1 \end{vmatrix} \sum_{h=6k+3} k_{w,h} N \Phi_h^{(0)} e^{j\phi_0} \\ \langle \Psi^{(1)} \rangle &= \begin{vmatrix} 1 \\ \check{\omega}^2 \\ \check{\omega} \end{vmatrix} \sum_{h=6k\pm 1} k_{w,h} N \Phi_h^{(1)} e^{j\phi_1} \\ \langle \Psi^{(2)} \rangle &= \begin{vmatrix} 1 \\ \check{\omega} \\ \check{\omega}^2 \end{vmatrix} \sum_{h=6k\pm 1} k_{w,h} N \Phi_h^{(2)} e^{j\phi_2}\end{aligned}$$

B.3 PULSATING SYSTEM OF MMF AND FLUX-LINKAGE

A pulsating system of MMF can be obtained by feeding the three-phase winding between one phase (say, U) and the parallel of the remaining two (V-W). It is assumed that the current of the first phase is equally splitted between the remaining two. Therefore the current system is given by:

$$\begin{cases} i_U(t) = \sqrt{2} I \cos(\omega t) \\ i_V(t) = -\frac{\sqrt{2}}{2} I \cos(\omega t) \\ i_W(t) = -\frac{\sqrt{2}}{2} I \cos(\omega t) \end{cases} \quad (\text{B.30})$$

The phase angles are the same as the three-phase case, given in (B.20). The winding MMF is given by:

$$\begin{aligned}\mathcal{F}(\alpha, t) = \sum_{h=1,3,5,\dots} \frac{4\sqrt{2} k_{w,h} N}{h\pi} \frac{1}{2p} I \left[\cos(h\alpha) \right. \\ \left. -\frac{1}{2} \cos\left(h\alpha - h\frac{2}{3}\pi\right) \right. \\ \left. -\frac{1}{2} \cos\left(h\alpha + h\frac{2}{3}\pi\right) \right] \cos(\omega t)\end{aligned} \quad (\text{B.31})$$

and, considering that:

$$\cos\left(h\alpha - h\frac{2}{3}\pi\right) + \cos\left(h\alpha + h\frac{2}{3}\pi\right) = 2 \cos(h\alpha) \cos\left(h\frac{2}{3}\pi\right)$$

and

$$\cos\left(h\frac{2}{3}\pi\right) = \begin{cases} -1/2 & \text{if } h = 6k \pm 1 \\ 1 & \text{if } h = 6k + 3 \end{cases}$$

then (B.31) becomes

$$\mathcal{F}(\alpha, t) = \sum_{h=6k\pm 1} \frac{6\sqrt{2} k_{w,h} N}{h\pi} \frac{1}{2p} I \cos(h\alpha) \cos(\omega t) \quad (\text{B.32})$$

As regards the flux linkage the flux-density harmonics and the corresponding fluxes per pole are defined as per (B.26) and (B.27) respectively. The flux phasor is real and is given by:

$$\tilde{\Phi}_h = \Phi_h \cos(\omega t)$$

so, accordingly to (B.18) the instantaneous values of the flux-linkages for the phases placed at angles as per (B.20) are given by

$$\begin{cases} \Psi_U(t) = \sum_{h=6k\pm 1} k_{w,h} N \Phi_h \cos(\omega t) \\ \Psi_V(t) = \sum_{h=6k\pm 1} k_{w,h} N \Phi_h \cos\left(h\frac{2}{3}\pi\right) \cos(\omega t) \\ \Psi_W(t) = \sum_{h=6k\pm 1} k_{w,h} N \Phi_h \cos\left(-h\frac{2}{3}\pi\right) \cos(\omega t) \end{cases}$$

and, considering that for $h = 6k \pm 1$ it results:

$$\cos\left(-h\frac{2}{3}\pi\right) = \cos\left(h\frac{2}{3}\pi\right) = \cos\left(4k\pi \pm \frac{2}{3}\pi\right) = -\frac{1}{2}$$

the pulsating system of flux-linkages is finally obtained:

$$\begin{vmatrix} \Psi_U(t) \\ \Psi_V(t) \\ \Psi_W(t) \end{vmatrix} = \begin{vmatrix} 1 \\ -1/2 \\ -1/2 \end{vmatrix} \sum_{h=6k\pm 1} k_{w,h} N \Phi_h \cos(\omega t) \quad (\text{B.33})$$

C

PER-UNIT BASE QUANTITIES

This appendix recaps the main concepts about the per-unit expression of the equations for electrical machine analysis. A generic physical quantity Q is expressed in *per-unit* (short: *pu*) of a certain (arbitrary) base value Q_{base} by simply relativizing the former with respect to the latter:

$$q = \frac{Q}{Q_{\text{base}}}$$

Vice-versa, given a certain *pu* value q the corresponding actual value in physical units is simply:

$$Q = q Q_{\text{base}}$$

Although the base choice is completely arbitrary, it is useful to properly assume some base quantities depending on some other, which values are still arbitrary. The following is a set of base quantities commonly adopted for the study of three-phase rotating electrical machines:

Quantity	Base for...	Definition
U_{base}	Phase voltages	U_{n}
V_{base}	Line voltages	$\sqrt{3}U_{\text{base}}^1$
I_{base}	Line currents	I_{n}
S_{base}	Electric powers	$3U_{\text{base}}I_{\text{base}}$
Z_{base}	Impedances, reactances, resistances	$U_{\text{base}}/I_{\text{base}}$
f_{base}	Electric frequencies	f_{n}
ω_{base}	Angular frequencies	$2\pi f_{\text{base}}$
L_{base}	Inductances	$Z_{\text{base}}/\omega_{\text{base}}^2$
Ψ_{base}	Fluxes, flux linkages	$U_{\text{base}}/\omega_{\text{base}}$
P_{base}	Mechanical powers	P_{n}^3
Ω_{base}	Angular speeds	$\omega_{\text{base}}N_{\text{pp}}$
T_{base}	Torques	$P_{\text{base}}/\Omega_{\text{base}}$
J_{base}	Moments of inertia	$T_{\text{base}}t_{\text{start}}/\Omega_{\text{base}}^4$

¹ This choice guarantees that, for any winding, the *pu* value of phase and line voltage is the same.

² With this definition the *pu* value of reactances and inductances is the same, since usually the reactance is defined at the rated frequency.

³ This choice implicitly assumes that the machine is a motor, so the rated power actually is the mechanical output. A good choice for generators could be the rated power of the prime mover.

⁴ t_{start} is the motor starting time.

The proper definition of the base system preserves the formal structure of most of the equations written for physical units when the pu notation is employed. On the other hand, the relativization of such equations simplifies their structure (for instance, the factors 3 and $\sqrt{3}$ are cancelled when switching from the physical to the pu notation) and levels up the numeric value of the quantities to a quite small range.

BIBLIOGRAPHY

GENERAL BIBLIOGRAPHY

- [1] D. F. Alexander, "Recent improvements in large induction motors", *Journal of the American Institute of Electrical Engineers*, vol. 46, no. 11, pp. 1167–1175, Nov. 1927.
- [2] P. Zhang, Y. Du, T. G. Habetler, and B. Lu, "A survey of condition monitoring and protection methods for medium-voltage induction motors", *IEEE Transactions on Industry Applications*, vol. 47, no. 1, pp. 34–46, Jan. 2011.
- [3] A. T. de Almeida, F. J. T. E. Ferreira, and G. Baoming, "Beyond induction motors: Technology trends to move up efficiency", *IEEE Transactions on Industry Applications*, vol. 50, no. 3, pp. 2103–2114, May 2014.
- [4] M. K. Yoon, C. S. Jeon, and S. K. Kauh, "Efficiency increase of an induction motor by improving cooling performance", *IEEE Transactions on Energy Conversion*, vol. 17, no. 1, pp. 1–6, Mar. 2002.
- [5] J. Parrish, S. Moll, and R. C. Schaefer, "Synchronous versus induction motors: Plant efficiency benefits resulting from the use of synchronous motors", *IEEE Industry Applications Magazine*, vol. 12, no. 2, pp. 61–70, Mar. 2006.
- [6] "Rotating electrical machines, part 1: Ratings and performance", *IEC Std. 60034-1*, pp. 1–148, May 2017.
- [7] A. Boglietti, A. Cavagnino, and M. Lazzari, "Computational algorithms for induction-motor equivalent circuit parameter determination, part 1: Resistances and leakage reactances", *IEEE Transactions on Industrial Electronics*, vol. 58, no. 9, pp. 3723–3733, Sep. 2011.
- [8] —, "Computational algorithms for induction motor equivalent circuit parameter determination, part 2: Skin effect and magnetizing characteristics", *IEEE Transactions on Industrial Electronics*, vol. 58, no. 9, pp. 3734–3740, Sep. 2011.
- [9] L. Alberti, N. Bianchi, and S. Bolognani, "A very rapid prediction of induction motor performance combining analytical and finite-element analysis", *IEEE Transactions on Industry Applications*, vol. 44, no. 5, pp. 1505–1512, Sep. 2008.
- [10] N. Bianchi, *Electrical Machine Analysis Using Finite Elements*. CRC Press, 2017.
- [11] "Cold rolled non-oriented electrical steel strip and sheet delivered in the fully processed state", *DIN-EN Std. 10106*, pp. 1–24, Mar. 2016.
- [12] "Heat-treatable steels, alloy steels and free-cutting steels, part 1: Non-alloy steels for quenching and tempering", *ISO Std. 683-1*, pp. 1–39, Jul. 2016.

- [13] R. D. Findlay, B. Szabados, S. H. Lie, S. J. Spencer, R. J. Belmans, and M. Poloujadoff, "Placement of vents to reduce shaft flux in two pole induction motors with a comment on heating effects", *IEEE Transactions on Energy Conversion*, vol. 7, no. 3, pp. 483–490, Sep. 1992.
- [14] M. Reinlein, T. Hubert, A. Kremser, and T. Bauer, "Magnetic flux distribution between rotor and shaft in two-pole induction machines with axial cooling vents", in *V International Conference on Power Engineering, Energy and Electrical Drives (POWERENG)*, (Riga, Latvia), May 2015, pp. 485–490.
- [15] M. Dems, K. Komezka, and J.-P. Lecoq, "Influence of massive ferromagnetic shaft on the distribution of electromagnetic field and magnetising current for two- and four-pole induction motors at frequencies of 50 and 200 Hz", *IET Electric Power Applications*, vol. 12, no. 7, pp. 1407–1416, Nov. 2018.
- [16] M. De Martin, F. Luise, S. Pieri, A. Tassarolo, and C. Poloni, "Numerical multi-objective optimization of a squirrel cage induction motor for industrial application", in *International Conference on Optimization of Electrical and Electronic Equipment (OPTIM)*, Sep. 2015, pp. 170–175.
- [17] L. Alberti, N. Bianchi, and S. Bolognani, "Variable-speed induction machine performance computed using finite-element", *IEEE Transactions on Industry Applications*, vol. 47, no. 2, pp. 789–797, Apr. 2011.
- [18] "Rotating electrical machines, part 6: Methods of cooling", *IEC Std. 60034-6*, pp. 1–44, Oct. 1991.
- [19] J. Pyrhonen, T. Jokinen, and V. Hrabovcova, "Resistances", in *Design of Rotating Electrical Machines*. John Wiley & Sons, 2009, pp. 255–280.
- [20] ———, "Flux leakage", in *Design of Rotating Electrical Machines*. John Wiley & Sons, 2009, pp. 225–253.
- [21] D. Ban, D. Zarko, and I. Mandic, "Turbogenerator end-winding leakage inductance calculation using a three-dimensional analytical approach based on the solution of Neumann integrals", *IEEE Transactions on Energy Conversion*, vol. 20, no. 1, pp. 98–105, Mar. 2005.
- [22] A. Tassarolo and F. Luise, "An analytical-numeric method for stator end-coil leakage inductance computation in multi-phase electric machines", in *IEEE Industry Applications Society Annual Meeting*, (Edmonton, Alberta, Canada), Oct. 2008, pp. 1–8.
- [23] J. Pyrhonen, T. Jokinen, and V. Hrabovcova, "Heat transfer", in *Design of Rotating Electrical Machines*. John Wiley & Sons, 2009, pp. 457–496.
- [24] F. W. Carter, "The magnetic field of the dynamo-electric machine", *Journal of the Institution of Electrical Engineers*, vol. 64, no. 359, pp. 1115–1138, Nov. 1926.
- [25] J. Pyrhonen, T. Jokinen, and V. Hrabovcova, "Design of magnetic circuits", in *Design of Rotating Electrical Machines*. John Wiley & Sons, 2009, pp. 153–224.
- [26] S. J. Salon, *Finite Element Analysis of Electrical Machines*. Springer US, 1995.

- [27] D. Meeker, *Finite element method magnetics user's manual*, 2018.
- [28] D. J. Griffiths, *Introduction to Electrodynamics*. Pearson, 2013.
- [29] E. W. Weisstein. (2019). Prosthaphaeresis formulas, from MathWorld—A Wolfram Web Resource, [Online]. Available: <http://mathworld.wolfram.com/ProsthaphaeresisFormulas.html>.
- [30] C. G. Broyden, "A class of methods for solving nonlinear simultaneous equations", *Mathematics of computation*, vol. 19, no. 92, pp. 577–593, 1965.
- [31] "Electrical insulation – Thermal evaluation and designation", *IEC Std. 60085*, pp. 1–16, Nov. 2007.
- [32] "Standard test procedure for polyphase induction motors and generators", *IEEE Std. 112-2017 (Revision of IEEE Std. 112-2004)*, pp. 1–115, Feb. 2018.
- [33] A. Tessarolo, G. Zocco, and C. Tonello, "Design and testing of a 45 MW 100 Hz quadruple-star synchronous motor for a liquefied natural gas turbo-compressor drive", *IEEE Transactions on Industry Applications*, vol. 47, no. 3, pp. 1210–1219, May 2011.
- [34] J. Parrish, S. Moll, and R. C. Schaefer, "Plant efficiencies benefit by selection of synchronous motor", in *IEEE Industry Applications Society Annual Meeting*, (New Orleans, Louisiana, USA), Sep. 2007, pp. 1229–1237.
- [35] K. LeDoux, P. W. Visser, J. D. Hulin, and H. Nguyen, "Starting large synchronous motors in weak power systems", *IEEE Transactions on Industry Applications*, vol. 51, no. 3, pp. 2676–2682, May 2015.
- [36] J. C. Das and J. Casey, "Characteristics and analysis of starting of large synchronous motors", in *IEEE Industrial and Commercial Power Systems Technical Conference*, (Sparks, Nevada, USA), May 1999.
- [37] S.-H. Park, S.-H. Hwang, J.-M. Kim, H.-S. Ryu, and J.-H. Lee, "A starting-up control algorithm of large synchronous generation motor for gas turbosets", in *IEEE International Symposium on Industrial Electronics*, (Cambridge, UK), Jun. 2008, pp. 502–508.
- [38] V. R. Khrushin, R. R. Khrushin, V. A. Zhilina, O. I. Karandaeva, and K. E. Odintsov, "Methods of electric drive reliability calculation at introduction of frequency converters", in *IEEE North-West Russia Young Researchers in Electrical and Electronic Engineering Conference (El-ConRusNW)*, (St. Petersburg, Russia), Feb. 2016, pp. 590–595.
- [39] D. Na, L. Yingli, and Z. Jian, "Performance calculation and analysis on line-start solid rotor PMSM", in *International Conference on Electrical Machines and Systems (ICEMS)*, (Beijing, China), Aug. 2011, pp. 1–4.
- [40] K. Oberretl, "Eddy current losses in solid pole shoes of synchronous machines at no-load and on load", *IEEE Transactions on Power Apparatus and Systems*, vol. PAS-91, no. 1, pp. 152–160, Jan. 1972.
- [41] G. F. T. Widger and B. Adkins, "Starting performance of synchronous motors with solid salient poles", *Proceedings of the Institution of Electrical Engineers*, vol. 115, no. 10, pp. 1471–1484, Oct. 1968.

- [42] K. J. Binns and M. R. Lloyd, "Method for evaluating the starting characteristics of solid salient-pole synchronous motors", *IEE Journal on Electric Power Applications*, vol. 1, no. 4, pp. 127–135, Nov. 1978.
- [43] K. Shima, K. Fujinuki, T. Matsumoto, and T. Fukami, "Measurement of surface losses in solid poles of synchronous machines under load conditions", in *IEEE International Magnetism Conference (INTERMAG)*, (Beijing, China), May 2015.
- [44] Y. B. Li, S. L. Ho, W. N. Fu, and W. Y. Liu, "An interpolative finite-element modeling and the starting process simulation of a large solid pole synchronous machine", *IEEE Transactions on Magnetism*, vol. 45, no. 10, pp. 4605–4608, Oct. 2009.
- [45] H. Yamada, K. Fujibayashi, K. Ito, M. Nakano, and H. Kanai, "Calculation of loss in solid-salient-pole machine", *IEEE Transactions on Power Apparatus and Systems*, vol. PAS-103, no. 6, pp. 1355–1362, Jun. 1984.
- [46] R. Son and M. Jeon, "A study for starting characteristic analysis method of salient pole synchronous motors", *IEEE Transactions on Industry Applications*, vol. 53, no. 2, pp. 1627–1634, Mar. 2017.
- [47] C. C. Mi, Y. Li, and H. Karmaker, "Modeling of the starting performance of large solid-pole synchronous motors using equivalent circuit approach", *IEEE Transactions on Magnetism*, vol. 45, no. 12, pp. 5399–5404, Dec. 2009.
- [48] K. C. Mukherji, P. J. Lawrenson, P. Reece, M. C. Ralph, J. H. Walker, and M. C. Ralph, "Tooth-ripple losses in solid poles", *Proceedings of the Institution of Electrical Engineers*, vol. 114, no. 2, pp. 275–276, Feb. 1967.
- [49] W. Z. Fam, "Direct measurement of the fundamental and harmonic tooth-ripple losses in solid poles part 1: Theory", *IEEE Transactions on Power Apparatus and Systems*, vol. PAS-90, no. 2, pp. 597–601, Mar. 1971.
- [50] S. Moriyasu and K. Endo, "The ripple loss at the rotor surface of synchronous machines", *IEEE Transactions on Power Apparatus and Systems*, vol. PAS-99, no. 6, pp. 2393–2399, Nov. 1980.
- [51] R. H. Park, "Two-reaction theory of synchronous machines generalized method of analysis – part 1", *Transactions of the American Institute of Electrical Engineers*, vol. 48, no. 3, pp. 716–727, Jul. 1929.
- [52] C. Fortescue, "Method of symmetrical co-ordinates applied to the solution of polyphase networks", *Transactions of the American Institute of Electrical Engineers*, vol. 37, no. 2, pp. 1027–1140, Jul. 1918.
- [53] C. Concordia, *Synchronous Machines: Theory and Performance*. Wiley, 1951.
- [54] E. L. Owen, H. D. Snively, and T. A. Lipo, "Torsional coordination of high speed synchronous motors, part 2", *IEEE Transactions on Industry Applications*, vol. IA-17, no. 6, pp. 572–580, Nov. 1981.
- [55] "Guide for evaluation of torque pulsations during starting of synchronous motors", *IEEE Std 1255-2000*, pp. 1–26, Aug. 2000.
- [56] "Test procedures for synchronous machines – Part 1: Acceptance and performance testing – Part 2: Test procedures and parameter determination for dynamic analysis", *IEEE Std 115-1995*, pp. 1–198, Apr. 1996.

- [57] P. Barret, "Computation of electromagnetic, thermal and mechanical quantities during asynchronous starting up of solid salient pole synchronous machines and experimental verification", *IEEE Transactions on Power Apparatus and Systems*, vol. PAS-100, no. 1, pp. 190–202, Jan. 1981.
- [58] A. Tassarolo and D. Giulivo, "Analytical methods for the accurate computation of stator leakage inductances in multi-phase synchronous machines", in *XX International Symposium on Power Electronics, Electrical Drives, Automation and Motion (SPEEDAM)*, (Pisa, Italy), Jun. 2010, pp. 845–852.
- [59] O. Laldin, S. D. Sudhoff, and S. Pekarek, "Magnetizing end-effects in salient pole machines", *IEEE Transactions on Energy Conversion*, vol. 30, no. 3, pp. 1135–1136, Sep. 2015.
- [60] W. J. Gibbs, "Induction and synchronous motors with unlaminated rotors", *Journal of the Institution of Electrical Engineers - Part II: Power Engineering*, vol. 95, no. 46, pp. 411–420, Aug. 1948.
- [61] R. L. Russell and K. H. Norsworthy, "Eddy currents and wall losses in screened-rotor induction motors", *Proceedings of the IEE - Part II: Power Engineering*, vol. 105, no. 20, pp. 163–175, Apr. 1958.
- [62] D. O'Kelly, "Theory and performance of solid - rotor induction and hysteresis machines", *Proceedings of the Institution of Electrical Engineers*, vol. 123, no. 5, pp. 421–428, May 1976.
- [63] W. J. Gibbs, "Theory and design of eddy current slip couplings", *BEAMA J*, vol. 10, pp. 123–128, 1946.
- [64] H. Yee, "Effects of finite length in solid-rotor induction machines", *Proceedings of the Institution of Electrical Engineers*, vol. 118, no. 8, pp. 1025–1033, Aug. 1971.
- [65] T. Xiaogao and F. Fengli, *Solid rotor induction motor and its application*. China Machine Press, 1991.
- [66] S. Wang, Z. Huang, Y. Sun, and H. Cao, "Rotor end factors for 2D FEA of induction motors with smooth or slitted solid rotor", *CES Transactions on Electrical Machines and Systems*, vol. 1, no. 2, pp. 132–139, Jul. 2017.
- [67] J. Pyrhonen, T. Jokinen, and V. Hrabovcova, *Design of Rotating Electrical Machines*. John Wiley & Sons, 2009.
- [68] "Rotating electrical machines, part 7: Classification of types of constructions and mounting arrangements", *IEC Std. 60034-7*, pp. 1–45, Dec. 1992.
- [69] "Degree of protection provided by enclosures", *IEC Std. 60529*, pp. 1–73, Nov. 1989.
- [70] M. Bortolozzi, A. Tassarolo, and C. Bruzzese, "Analytical computation of end-coil leakage inductance of round-rotor synchronous machines field winding", *IEEE Transactions on Magnetics*, vol. 52, no. 2, pp. 1–10, Feb. 2016.

PUBLICATIONS BY AUTHOR

- [P1] M. Olivo, A. Tassarolo, and M. Bortolozzi, "On the use of conformal mapping in the analysis of electric machines", in *XXII International Conference on Electrical Machines (ICEM)*, (Lausanne, Switzerland), Sep. 2016, pp. 492–498.
- [P2] A. Tassarolo and M. Olivo, "A new method for the analytical determination of the complex relative permeance function in linear electric machines with slotted air gap", in *XXIII International Symposium on Power Electronics, Electrical Drives, Automation and Motion (SPEEDAM)*, (Anacapri, Italy), Jun. 2016, pp. 1330–1335.
- [P3] M. Bortolozzi, N. Barbini, M. Olivo, and A. Tassarolo, "A new method for the analytical determination of the complex relative permeance function in slotted electrical machines", in *XIX International Conference on Power Electronics, Machines and Drives (PEMD)*, (Liverpool, UK), Apr. 2018.
- [P4] M. Bortolozzi, M. Olivo, N. Barbini, and A. Tassarolo, "Analytical flux density determination in spm slotless machine stator core", in *XIX International Conference on Power Electronics, Machines and Drives (PEMD)*, (Liverpool, UK), Apr. 2018.
- [P5] M. Olivo, N. Barbini, A. Tassarolo, S. Cicutto, and G. Zocco, "Start-up performance prediction of line-fed solid-rotor salient-pole synchronous motors", in *XXIII International Conference on Electrical Machines (ICEM)*, (Alexandroupolis, Greece), Sep. 2018, pp. 407–413.
- [P6] A. Tassarolo, M. Olivo, and N. Barbini, "Curvature effects on permanent magnet harmonic losses of surface-mounted permanent magnet machines", in *XXIII International Conference on Electrical Machines (ICEM)*, (Alexandroupolis, Greece), Sep. 2018, pp. 615–621.
- [P7] N. Elloumi, M. Bortolozzi, A. Masmoudi, M. Mezzarobba, M. Olivo, and A. Tassarolo, "Numerical and analytical approaches to the modeling of a spoke type ipm machine with enhanced flux weakening capability", *IEEE Transactions on Industry Applications*, vol. 55, no. 5, pp. 4702–4714, Sep. 2019.
- [P8] M. Olivo, M. Bortolozzi, A. Tassarolo, and F. Luise, "A new method for the accurate prediction of on-load power factor in two-pole induction motors considering shaft eddy currents", *IEEE Transactions on Energy Conversion*, 2019, submitted.